



Delft University of Technology

Innovative low-melting glass compositions containing fly ash and blast furnace slag

Justino de Lima, Clarissa

DOI

[10.4233/uuid:ea63ca9c-5db2-4e9e-ab63-db5b068ee327](https://doi.org/10.4233/uuid:ea63ca9c-5db2-4e9e-ab63-db5b068ee327)

Publication date

2020

Document Version

Final published version

Citation (APA)

Justino de Lima, C. L. (2020). Innovative low-melting glass compositions containing fly ash and blast furnace slag. <https://doi.org/10.4233/uuid:ea63ca9c-5db2-4e9e-ab63-db5b068ee327>

Important note

To cite this publication, please use the final published version (if applicable). Please check the document version above.

Copyright

Other than for strictly personal use, it is not permitted to download, forward or distribute the text or part of it, without the consent of the author(s) and/or copyright holder(s), unless the work is under an open content license such as Creative Commons.

Takedown policy

Please contact us and provide details if you believe this document breaches copyrights. We will remove access to the work immediately and investigate your claim.

**INNOVATIVE LOW-MELTING GLASS COMPOSITIONS
CONTAINING FLY ASH AND BLAST FURNACE SLAG**

INNOVATIVE LOW-MELTING GLASS COMPOSITIONS CONTAINING FLY ASH AND BLAST FURNACE SLAG

Proefschrift

ter verkrijging van de graad van doctor
aan de Technische Universiteit Delft,
op gezag van de Rector Magnificus Prof. dr. ir. T. H. J. J. van der Hagen,
voorzitter van het College voor Promoties,
in het openbaar te verdedigen op maandag 30 maart 2020 om 15:00 uur

door

Clarissa Luiza JUSTINO DE LIMA

Master of Science in Materials Science and Engineering,
Federal University of Alfenas, Brazilië.
geboren te Monte Santo de Minas, Brazilië.

Dit proefschrift is goedgekeurd door de

promotoren:

Dr. ir. F.A. Veer

Prof. ir. R. Nijse

copromotor:

Dr. O. Copuroglu

Samenstelling promotiecommissie:

Rector Magnificus,

Dr. ir. F.A. Veer,

Dr. O. Copuroglu,

Prof. ir. R. Nijse,

voorzitter

Technische Universiteit Delft

Technische Universiteit Delft

Technische Universiteit Delft

Onafhankelijke leden:

Prof. dr. F. Castro Cassanjes,

Prof. dr. R.J. Hand,

Prof. dr. ir. H.E.J.G. Schlangen,

Prof.dr.ir. R. Benedictus,

Prof.dr. M. Overend,

Federal University of Alfnas

University of Sheffield

Technische Universiteit Delft

Technische Universiteit Delft

Technische Universiteit Delft, reserverlid

This research was funded by the National Council for Scientific and Technological Development (CNPq), Brazil, Grant no. 202950/2014-0.

Keywords: Glasses, Phosphate, Fly Ash, Blast Furnace Slag, Nanoindentation, Crystallization.

Copyright © 2020 by C. L. Justino de Lima.

An electronic version of this dissertation is available at

<http://repository.tudelft.nl/>.

CONTENTS

1	Introduction	1
1.1	General Introduction	2
1.2	The demand for new glass compositions	2
1.3	Aim of this thesis	4
1.4	Outline of the thesis.	4
2	Advances and challenges in glass concepts, manufacturing and applications	7
2.1	Glass origins and applications along the years	8
2.2	Glass strengthening and composition.	13
2.3	The definition of glass.	15
2.4	Glass in construction	21
2.5	Discussion and results	22
2.6	Conclusions.	25
3	Creating the new glass compositions	29
3.1	Designing compositions containing slag and fly ash	30
3.1.1	Slag and ash	30
3.1.2	Phosphate glasses	33
3.2	Experimental	35
3.3	Composition of the samples	38
3.4	Crystallinity of the sample	41
3.5	Chemical durability.	43
3.6	Discussion and conclusions.	47
4	Thermal, crystallization and coloration studies of the glasses	53
4.1	Thermal analysis of the samples	54
4.1.1	Thermal analysis of samples containing slag.	54
4.1.2	Thermal analysis of samples containing fly ash	57
4.2	Thermal analysis of commercial glasses	58
4.3	Coloration of samples.	59
4.3.1	Factors determining the color of a glass	59
4.3.2	Visual aspect of the glasses containing wastes and their melting conditions	62
4.3.3	Optical spectroscopy, mass loss and gas release of the glasses	64
4.4	Crystallization studies	72
4.5	Discussion and Conclusions	76

5	Compositional dependence of the coefficient of thermal expansion of the glasses	81
5.1	Preparation of the samples	82
5.2	Experimental setup	83
5.3	Discussion and conclusions.	90
6	Mechanical properties of the produced glasses: elastic modulus, hardness and indentation toughness	95
6.1	Elastic modulus and hardness	96
6.2	Indentation toughness	98
6.3	Materials and methods	98
6.4	Results and discussion	102
6.5	Conclusions.	116
7	Conclusion and perspectives for future work	121
7.1	Summarizing the properties	122
7.2	Anisotropic glasses	124
7.3	Low-melting point glasses, colorless glasses and compositions produced with pure reagents	126
7.4	High expansion glasses	128
	Acknowledgements	131
A	Appendix A	133
B	Appendix B	141
C	Appendix C	147
D	Appendix D	163
E	Appendix E	173
	Summary	195
	Samenvatting	197
	Curriculum Vitæ	199
	List of Publications	201

1

INTRODUCTION

1.1. GENERAL INTRODUCTION

INDUSTRIAL waste management is an urgent issue in a society that witnesses growing industrial production. Expanding populations, rising urbanization and increased wealth are ramping up the global production of solid waste. Factors like population and per capita gross domestic product (GDP) are used to measure the total global municipal solid waste (MSW) production [1]. Some predictions about the world population suggest that it will reach its highest point during this century. The waste production rates per capita usually grow with wealth, despite the fact that there is a tendency toward anti-materialism in the wealthiest countries. The junction of these aspects points to a scenario in which over the next decades the global waste generation will probably peak [1].

About 5 to 7% of global greenhouse gas emissions originate from the manufacture of ordinary Portland cement (OPC), constituting a huge burden on the global environment [2]. Geopolymer is a promising technology; an ecological binding material that functions as an alternative binder to Portland cement. Usually, the geopolymer is formed by the reaction of a geologically generated aluminosilicate compound, like clay and metakaolin, or of industrial by-products, like fly ash and ground granulated blast furnace slag with an alkaline solution [3]. The two principal environmental advantages that derive from substituting the geopolymer binder for the Portland cement are the significant decrease in greenhouse gas emissions and the use of industrial by-products to develop building materials. Using slag cement or ground granulated blast furnace slag (GGBS) is another way to develop building materials. As a concrete additive, the slag confers many benefits. Slag is also useful in road construction and porous asphalt concrete.

Despite large number of products developed from waste materials, most of them consist of non-transparent materials, partly because it is a challenge to get transparent materials in reasonable temperatures from these waste products. Slag and fly ash contain many elements that are also present in typical glass formulas. For instance, the elements found in higher amounts in the chemical systems of standard silicate glasses are SiO_2 , Na_2O , CaO , K_2O , MgO , Al_2O_3 , Fe_2O_3 [4]. All those elements are found both in slag and in fly ash compositions. Some of those elements are highly refractory and their presence in complex compositions means they are highly likely to crystallize and have high working temperatures. Glass is a material that allows large amounts of various elements in solution, being suitable to assimilate complex compounds in its compositions.

The use of recycled raw materials in glass fusion makes it possible to reduce energy consumption. This reduction is accompanied by reduction in CO_2 emissions, which leads glass manufacturing process to become more sustainable.

1.2. THE DEMAND FOR NEW GLASS COMPOSITIONS

THE earliest glasses used by humans were found in nature. The ease of forming sharp edges on obsidians, for example, allowed for the production of knives and other cutting tools. These natural glasses, which result from the cooling of molten rock, or lava, contain a wide variety of components, including alkali, alkaline earth, and transition metal oxides. In every case, however, silica is the major constituent of these materials [5].

As naturally occurring glasses proved to be so useful to early humans, it is not unexpected that the desire to produce glass also began thousands of years ago. And as all known glasses were based on silica, it is not surprising to find that the earliest synthesized glasses were silicates as well [5]. Even ancient glasses have much the same composition as many of those used today. Analysis of very old bottles and window glasses shows similarities to modern compositions that are certainly more than coincidence. The reasons for this can be found in the fundamental character of glass. From a modern viewpoint, usable commercial compositions must satisfy these stringent requirements [6]:

- The batch materials must be as inexpensive as possible, consistent with the fulfillment of other prerequisites.
- The materials must be fused and become fluid at a reasonable industrial temperature, and the liquid usually must be free of gas bubbles.
- The glass must be sufficiently viscous that it can be manipulated at temperatures above its freezing range without devitrification, yet not so viscous that workability must be sacrificed. In other words, must be very viscous in and below its freezing range so that it will not devitrify during the cooling.
- The glass must be chemically durable.
- It must have the desired physical properties for its intended application, such as high crack resistance or high hardness.

The glasses that have survived the centuries represent the very best product of the old glassmakers: they are fundamentally soda-lime-silica glasses [6]. Until today, silica has been the main glass former. Most commercial glasses, which must satisfy the requirements already listed, are silicate glasses.

Another common variety is borosilicate glass. The first important group of such glasses was manufactured by Corning Glass Works, under the trademark Pyrex. These borosilicate glasses have roughly one-third the expansion of the ordinary lime glass, great resistance to thermal shock, high electrical resistance, and excellent chemical stability. Although they are more expensive to manufacture than lime glass, these superior characteristics have led to the success of borosilicate glass in fields from which glass was previously excluded, like kitchenware [6].

In recent years more advanced glasses like the aluminosilicate “Gorilla Glass” have been introduced into niche areas, such as like mobile telephone displays. Standard soda-lime glass works well for bottles and lightbulbs, but not so much for other applications, because it can shatter into sharp pieces. Borosilicate glasses, such as Pyrex, are resistant to thermal shock, but they take a lot of energy to melt. At the same time, there are only two ways to produce flat glass on a large scale: the fusion draw and the float glass process. One challenge that a glass company faces is to match a composition, with all its desired traits, to the manufacturing process [7].

Aluminosilicate compositions like “Gorilla Glass” contain silicon dioxide, aluminium, magnesium, and sodium. When the glass is dipped in a hot bath of molten salt, it heats up and expands. Sodium and potassium are in the same column on the periodic table of elements, so they behave similarly. The heat from the bath increases the migration of the sodium ions out of the glass, and the similar potassium ions easily float in and take their place. But because potassium ions are larger than sodium, they get packed

into space more tightly. With the cooling of the glass, they are compressed together in this now-cramped space, and a layer of compressive stress on the surface of the glass is formed. Compared with thermally strengthened glass, the "crowding" effect in chemically strengthened glass results in higher surface compression, making it up to four times as strong. This process can be applied to glass of any thickness or shape [7].

These new glass types have interesting properties for architectural engineering, opening the question of whether more advanced glasses can be specifically developed. Moreover, these new compositions could match contemporary demands, such as sustainability.

Waste management efforts chiefly to reduce the quantities of production waste created. Of secondary concern is the recovery of production waste internally, followed by the development of external recovery industries, such as reuse and recycling. The combustion of fossil fuels and chemical reactions, such as the de-carbonization of carbonates in glass fusion, results in high CO₂ emissions. High rates of energy consumption are another fundamental production issue, and electricity acquisition is indirectly related to CO₂ emission. Using recycled raw materials in glass fusion makes it possible to reduce energy consumption. In the case of flat glass, energy consumption is reduced by 3% when the percentage of cullet is increased from 20% to 30% of raw materials. Furthermore, new glass recipes can incorporate industrial wastes, such as the slag discharged from blast furnaces in the steel industry [8].

1.3. AIM OF THIS THESIS

IN this work, we aimed to create new glass recipes incorporating by-products in their compositions, while keeping transparency and relatively low working temperatures. The optical, mechanical and thermal properties of the samples were measured, evaluating their potential applications as building materials and compared to the standard borosilicate and soda-lime glasses. To reach properties like high crack-resistance, transparency, resistance against thermal shock and high chemical durability, the amount of chemical elements as well as the melting conditions were optimized. Besides these properties, the ease of recycling and the inexpensive production of these glasses make them good candidates to new technologies, remarkably for the 3D glass printing.

1.4. OUTLINE OF THE THESIS

CHAPTER 1 provides a general introduction to the thesis.

Chapter 2 is a literature review, discussing the changes in glass definition, manufacturing and composition over the years. It examines how these innovations helped to consolidate the importance of glass as a building material, expanding its range of applications. Relevant advancements over millennia of the history of glass are reviewed and the challenges and questions that remain unanswered are debated. The chapter clarifies why there is currently a demand for a more sustainable glass manufacturing process.

Chapter 3 reinforces the idea that the valorization of by-products is an important social and ecological issue. It explains how waste reuse and recycling could help to aggregate value to these products. It demonstrates that it is a challenge to produce transparent materials at reasonable temperatures using these materials. New glass compositions

containing slag and fly ash are described. These compositions have phosphorus oxide as a glass former, instead of the silicon oxide, typically used for building engineering. Glass forming domains are determined by melt-quenching of the starting nominal compositions. The main drawback of phosphate glasses is the fact that they are hygroscopic. For this reason, we test and improve the water resistance of the glasses via changes in their formulas.

Chapter 4 reports the results from the thermal characterization of the glasses, performed by DSC. The glasses with the highest amounts of waste present a very dark colouration. In order to clarify the structure and origin of colouration of these materials, they are characterized by X-ray diffraction (XRD) and their spectral transmission are determined with a UV-VIS spectrophotometer. The results from the DSC and XRD are correlated, enabling the identification of possible crystalline phases.

Chapter 5 describes the measurement of the thermal expansion coefficient of the developed glasses. We report the preparation of the setup using strain gauges and analyse the results, correlating them with the compositions and comparing themselves with each other. Different applications are suggested for different glasses, according to their thermal expansion coefficients.

Chapter 6 reports the mechanical properties of the glasses, obtained via the nanoindentation technique. The Oliver and Pharr method is the base of the measurements of both elastic modulus and hardness, and the crack resistance is determined using high indentation loads. We discuss the results as a function of the compositions.

Chapter 7 discusses the applications for the developed glasses, such as 3d printing, based on their measured properties. Furthermore, it suggests some directions for future research.

REFERENCES

- [1] Hoornweg, D., Bhada-Tata, P. and Kennedy, C. (2015). Peak Waste: When Is It Likely to Occur?. *Journal of Industrial Ecology*, 19: pp.117–128.
- [2] Hendriks, C.A., Worrel, E., De Jager, D., Riemer, P. (1998). Emission reduction of greenhouse gases from the cement industry. *Proceedings of the 4th International Conference on Greenhouse Gas Control Technologies*, Interlaken, Austria, Aug. 30–Sept. 2, IEA GHG R&D Programme, UK.
- [3] Neupane, K. (2016). Fly Ash and GGBFS Based Powder-Activated Geopolymer Binders: A Viable Sustainable Alternative of Portland Cement in Concrete Industry. *Mechanics of Materials*, 103, pp.110–122.
- [4] Zschimmer, E. (2013). *Chemical technology of glass*. Sheffield: Society of Glass Technology.
- [5] Shelby, J.E. (2005). *Introduction to Glass Science and Technology*. 2nd edition.
- [6] Philips, C.J. (1948). *Glass, the miracle maker. Its history, technology, manufacture and applications*. 2nd edition. Pitman, London.
- [7] Gardiner, B., *Glass works: how corning created the ultrathin, ultrastrong material of the future*. *Wired Magazine*. Retrieved August 3, 2015, from: <http://www.wired.com/2012/09/ff-corning-gorilla-glass/>
- [8] Xu, Y., Zhang, Y. Z., Hou, L. Y., and Lu, X. (2014). Preparation of CaO–Al₂O₃–SiO₂ system glass from molten blast furnace slag. *International Journal of Minerals, Metallurgy,*

and Materials. v.21, Issue 2, pp. 169–174.

2

ADVANCES AND CHALLENGES IN GLASS CONCEPTS, MANUFACTURING AND APPLICATIONS

This chapter introduces the discussion around changes in glass definition, manufacturing and composition in history, and how these innovations contributed to the consolidation of the current importance of glass as a building material. Relevant advancements over the millennia of glass production will be reviewed and the challenges and questions that have remained unanswered will be debated.

The earliest known man-made glass was produced around 4000 BC in Egypt and Mesopotamia. Until very recently, scientific analysis of ancient glass has been conducted to estimate the elemental composition of vestigial remnants. Since its early production, the glass manufacturing process has constantly evolved: between the arrival of glass blowing around 50 BC to the float process patented in 1953, critical steps in the development of glass technology can be traced through individual innovations.

As the scientific knowledge of glass has improved, the way in which it is defined and classified has also evolved over the years. In 1932, Zachariassen [1] stated that it must be frankly admitted that we know practically nothing about the atomic arrangement of glass. Despite recent advances, this statement still remains largely true in the modern day, as the structural understanding of glass - one of the earliest materials used by man - is still quite limited. Ancient glass types are very similar in composition to most of the architectural glass used today, meaning that even with intense research activity and new glass compositions being investigated every day, there has been little innovation nor evolution in the composition of architectural glass. This is partially explained by the fact that a substantial part of glass research is not relevant to practical large scale applications.

2.1. GLASS ORIGINS AND APPLICATIONS ALONG THE YEARS

GLASS has been a material present in everyday life since primitive times. Originating from volcanic activity, Obsidian glass (Figure 2.1) was used to make cutting tools due to its hardness. This organic form of glass results from the cooling of molten rock, or lava, and contains a wide variety of components, including alkali, alkaline earth, and transition metal oxides. There is still no consensus about which ancient civilization made glass for the first time. In every case, however, silica is found to be the major constituent of these materials [2]. During more than 5000 years of glassmaking, glass applications have vastly expanded and today it is an indispensable material in modern society, used in fields such as communication, automotive engineering and architecture.

The discovery of glass has been a controversial issue, as historians do not have accurate data relating to its origin. Pliny, the great Roman naturalist, credits the discovery of glass making to the Phoenicians. In his encyclopedia "Naturalis Historia", [3] Pliny writes that when the Phoenicians landed in Syria, around 5000 BC, they built improvised stoves using blocks of saltpeter on the sand. After some time, the appearance of a bright substance was noted. This liquid solidified quickly, leading to the Phoenicians devoting a lot of time to reproducing this phenomenon. The resulting materials were used for utilitarian purposes. Among the few existing records, there is a recipe belonging to the ancient library of the Assyrian king Ashurbanipal: "Take 60 parts of sand, 180 parts of ash from sea plants, and 5 parts of chalk and you obtain glass" [4].

It is supposed that manual glass production arrived around 1500 BC by the covering of a clay mold with molten glass. Small objects were formed by pressing the hot glass

into the clay molds. However, ornamental stone beads with a vitreous glaze had already appeared long before, in around 4000 BC [5].

The earliest glass was found in Egypt and Mesopotamia, however, there is no consensus on the exact geographical location where glass was first made. An ongoing project is currently reinvestigating glass remains initially found in the 1920's and 1930's in the city of Nuzi, Northern Iraq [6], using Scanning Electron Microscope-Wavelength Dispersive Spectroscopy (SEM-WDS) analysis to estimate the elemental compositions of these vestigial remnants. As part of the analysis, strontium and neodymium isotope ratios were measured to support the identification of the original silica sources. While the Nuzi glass is mainly tinted blue as it contains traces of copper, the Egyptian glass samples exhibits a broad range of colorants, as shown in Figure 2.2. While this does not answer the question of which civilization made the first glass, it does suggest that early Egyptian civilizations mastered a more developed technique.



Figure 2.1: Obsidian: naturally occurring glass.



Figure 2.2: Ancient glass from Egypt. Petrie Museum of Egyptian Archaeology, London.

The introduction of glass blowing around 50 BC by Syrian craftsmen, revolutionized glassware. Using this technique, glass could be produced on a large scale, thus vastly expanding its availability and popularity. The expansion of the Roman Empire caused the dissemination of this technique, as the practice of blowing and moulding glasses was

popularized by the empire wide demand for vessels and windows. Pieces were also cut, engraved and painted. The Romans dominated the plastic character of heat-softened glass, which is important to modern processes [7]. After the decline of the Western Roman Empire, glass manufacturing diffused to different sites in Western Europe. Around 1300, Venice led the renascent glass industry, becoming a pioneer in the manufacturing of glass used for lenses, mirrors, and colored glass for ornamental purposes. At this point, glassmaking became a recognized art form, and as a consequence, glassmakers had their lives strictly controlled as a way to preserve the monopoly artistic glass-making techniques. As time passed, Venice lost its position as a leader in glass production and around 1700 glassmakers had spread all over Europe [7].

In the Middle Ages, the use of glass for windows and stained glass had been disseminated throughout Europe, still principally made by blowing. Around 1700, sparkling glasses and jars coming from Venice - so-called "crystals" - became famous. Despite the name, these glasses technically do not qualify as crystals due their amorphous structure. Automation in glass production only arrived at the beginning of the last century, chiefly in the production of flat glass containers, tubes and fibers. Before invention of the float process, the main processes underlying the fabrication of flat sheets of glass were the window glass and the plate glass processes. The window glass process involved stretching a lump of molten glass [8] by spinning, blowing or pulling. This process can be classified as a crown, cylinder or drawn sheet, and is used to make windows with a bright fire finish. As a result, inhomogeneities in the glass structure appeared, creating distortions. Such distortions were not tolerable for the production of car windows or, later, for the large distortion free shop windows, which became popular around 1850 [8]. The plating process came as an answer to these demands.

Distortion-free glass was created by melting composite materials in pots and pouring it onto a casting table. Using a heavy roller, the glass was flattened to the required thickness, before being ground and polished. Approximately 50% of the original thickness of the cast glass was removed by grinding and polishing [9]. The Bicheroux process was introduced in Germany, after the First World War. In this process, the glass was melted in pots and rolled between two rollers, instead of on a table. Continuous grinding and polishing activities were developed by the Ford Motor Company of America and by Pilkington Brothers Limited of England [9]. From 1688, when the process of casting plate-glass was refined, with the introduction of the semi-continuous Bicheroux process, plate glass fabrication evolved very slowly, despite accelerating innovation in craftsmanship and technology in the 20th century. In 1935, the twin grinding and polishing process was developed by Pilkington. In this process, glass was rolled from the tank in a continuous ribbon. After having been annealed in the lehr, this ribbon crossed a twin grinder, in which both sides were ground simultaneously, and later through a twin polisher [9]. The importance of the twin grinder machine is undeniable. Nevertheless, this process was expensive and therefore required heavy capital investment, as well as a high glass wastage of around 20% [8].

The float process, patented in 1953 by Pilkington, allowed flat glass production on a large-scale, at a relatively low cost and producing a significantly higher quality product than any process known before. In this process, an uninterrupted ribbon of glass moves out of the melting furnace and floats along the surface of an enclosed bath of molten tin.

This ribbon is kept in a chemically controlled inert atmosphere at high temperature for a relatively long time, which allows irregularities to melt out and the surface to become flat and parallel [10]. The glass becomes flat due to the flat surface of the molten tin. As the ribbon is cooled down, the glass is still advanced across the molten tin until the surfaces become hard enough to be taken out of the bath without the rollers marking the bottom surface. In this way, a ribbon is produced with uniform thickness and bright fire-polished surfaces without any exigency for grinding and polishing [8]. This process is illustrated in Figure 2.3.

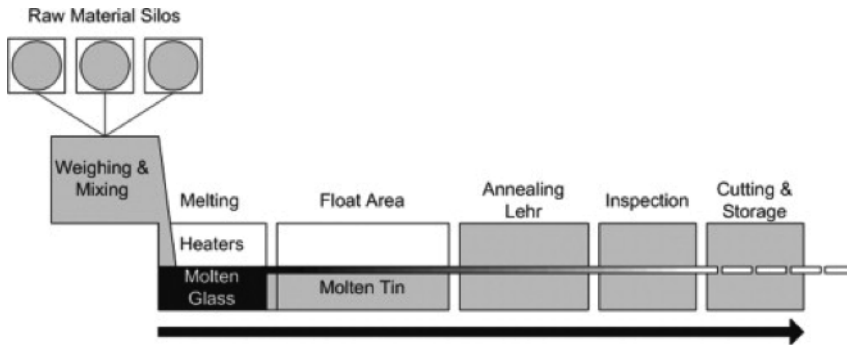


Figure 2.3: The basic float glass manufacturing process consists of melting raw material, cooling and flattening molten glass, annealing and cutting flat glass on rollers [10].

Industrially manufactured glass blocks were introduced to the mass market in 1932, made from Pyrex, a heat-resistant borosilicate glass. However, for a long time they were relegated to something less than first-class status as a building material. They were more commonly used commercially, and some attempts to introduce it residentially were not successful [11]. The Manhattan Laundry building, constructed in 1936 in Washington D.C (Figure 2.4) illustrates the use of a glass block curtain wall in a commercial context. Glass blocks boomed in the 1970's, gaining acceptance in both public and private spaces. Because the bricks were translucent, but not transparent, they were able to provide light and visual privacy at the same time. Around that time, most glass blocks were about twice as expensive as regular masonry bricks. They were hollow, not used to support heavy loads and were mainly used for exteriors as they were able to provide significant insulation [11]. In relation to the plate glass sheets, glass blocks were cheap and easy to assemble.

During the last decades of the twentieth century, many new glazing techniques were conceived in order to realize the idea of the all-glass building [12]. Among the technological advancements that supported the structural glass industry, were the invention of new adhesives, fundamental to glass-to-glass bonds. In 1931, the German company Glasbau-Hahn was responsible for the production of the first glass-cement and first all-glass construction by bonding glass-to-glass. Later, in 1958, the same company introduced double-sided glass stiffeners, also known as the glass fin. Glass fins can be placed perpendicular to a glass curtain wall along the vertical joints, helping to stabilize all-glass shop fronts and entrances without the use of vertical mullions and eliminating the need

to introduce an opaque structural material such as steel [12]. In 1965, Glasbau-Hahn introduced suspended glazing - structures wherein glass sheets are hung from fixtures at the top of a facade, allowing glass panels to be installed theoretically at an unlimited height. This development notably influenced architecture in Europe over the following decades. The new facades developed since then have a dematerialized appearance in relation to the noticeable structures exhibited by a traditional curtain wall [12]. An example of the modern application of glass blocks is the Crystal House built in 2016 in Amsterdam (Figure 2.5). Its construction involved adhesively bonded cast low iron soda lime glass blocks as an answer to the demand for structural transparency. The adhesive was applied in a 0.2-0.3 mm thick layer, which required extreme precision in each construction layer [13].



Figure 2.4: Manhattan Laundry,1936 [12].



Figure 2.5: The Crystal Houses, 2016 [13].

2.2. GLASS STRENGTHENING AND COMPOSITION

As mentioned above, ancient glass remnants have much the same composition as most glass used today. Analysis of very old bottles and window glass show a striking similarity to modern compositions, which is certainly not a coincidence. Since its discovery, silica has been used as the main glass former due to its easy availability (sand) and low cost. Most modern commercial glass, which must satisfy certain requirements of price, chemical durability, and viscosity, is typically silicate in composition. Another family of glass that is used on a large scale is borosilicate. This glass has roughly one-third of the expansion of ordinary soda lime glass, which provides resistance to thermal shock, high electrical resistance, and good chemical stability. Nevertheless, this type of glass is more expensive to manufacture than soda lime glass [14].

The constituent elements of oxide glasses are grouped into three distinct categories: glass formers, modifiers and intermediates. Vitreous formers are elements that alone are capable of forming a three-dimensional random network, which is the basic structure of glass. The covalent tendency of the Si-O, Ge-O, P-O, As-O and Sb-O bonds enables these oxides to form an amorphous solid. Modifiers are cations that make ionic bonds with the anions of the glass network. These modifying ions – for example K^+ , Na^+ and Fe^{2+} – have the ability to bind to the oxygen atoms attached to only one forming cation. The introduction of modifiers may alter some of the physical and chemical properties of glass. The intermediates may act as both modifiers and formers, since though they do not form glassy structures when present in isolation, they can enter the glass structure and replace a former, such as Fe^{3+} and Al^{3+} . The structural effect of each network former and modifier on the glass is dependent on both its chemical composition and its thermal history [15].

In 19th century, the industrial revolution heralded a new era in glassmaking. Synthetic raw materials were used for the first time and glass with controlled properties became available. In 1875, special glass was developed in Germany by Abbe, Schott and Carl Zeiss, and as a result, The University of Jena, Germany, has become a center of glass science and engineering [16]. First studies on the property-composition of glass for the construction of optical instruments, such as the microscope, date from 1881 [16]. Here, the chemistry of glass was in its infancy. The first department dedicated to glass teaching and research was inaugurated in 1915 at the University of Sheffield, England. Since the 1960's, there has been a remarkable scientific and technological advancements in the development of special glass [17].

Glasses can be formed by various processes, including chemical vapor deposition, pyrolysis, neutron irradiation, and sol-gel. Nowadays, new glass-forming technologies such as 3D printing have the potential to enable large-scale manufacturing of glass articles with complex geometries in the future. In spite of this, conventional glass is almost exclusively produced by the melting-quenching method. This method involves the melting of a mixture of starting materials, generally at high temperatures, followed by rapid cooling. Currently, the manufacturing process is optimized to almost completely avoid the formation of bubbles, inclusions and other defects in the glass, however, these defects do still occur on occasion, making the glass prone to structural failure. The processes of physical tempering and chemical tempering are alternatives to minimize the effects of these defects on the strength of glass.

Theoretically, glass is a strong material with a theoretical strength around 7000 MPa [18]. However, when factoring in defects, glass has a practical strength of approximately 35-70 MPa, only around 1% of the theoretical value. A standard borosilicate glass has an elastic modulus of approximately 63 GPa and a hardness of 6.4 GPa while for a soda-lime glass these values are 74 GPa and 5.5 GPa, respectively [19]. Physical tempering is related to quick cooling of the glass from above the T_g . The surface cools down much faster than the center, and at a certain point, the surface becomes an elastic solid while the center undergoes thermoelastic stress relaxation. Contraction occurs in the center as the surface enters a state of compression. This way, a balancing tensile stress is created at the center of the glass. Generally, this tensile stress corresponds to half of the value of the compressive stress. This process requires a minimum glass thickness of 2 mm. Otherwise, the introduced stress is not enough to increase its strength. This is a relatively inexpensive process and applicable to flat glass, enabling a uniform cooling process. Chemical tempering is related to the modification of surface composition. This occurs below the glass transition temperature, T_g , and is an ion exchange process. In general, a soda lime glass is submerged in a hot molten potassium salt bath and the heat from the bath increases the migration of the sodium ions out of the glass, while the similar potassium ions easily float in and take their place. As potassium ions are larger than sodium, they get packed into space more tightly, as shown in Figure 2.6. With the cooling of the glass, potassium ions get compressed together in this now-cramped space, and a layer of compressive stress on the surface layer of the glass is formed. Compared with thermally strengthened glass, the "crowding" effect in chemically strengthened glass results in a higher surface compression in a very thin layer [20]. It is a relatively expensive process and is suitable for unusual and complex glass shapes. By applying chemical strengthening, it is possible to influence the pattern of the stress profile, which can be adjusted in order to improve the fracture behavior. It is possible to chemically strengthen samples as thin as 0.5-15mm, improving transmission while also reducing weight and costs related to mounting and transport [18].

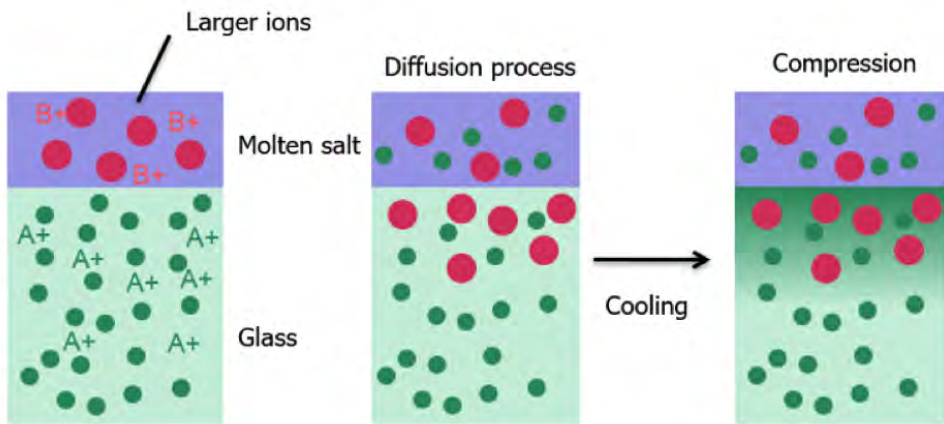


Figure 2.6: Scheme of ion-exchange (adapted from Uhlmann [21]).

The fusion drawing process is another innovative technique. Developed by Corning, this technique consists of pouring molten glass into a V-shaped trough and letting it overflow down the sides of the trough, clinging and running down the sides as treacle might cling to and run down the outside of a pot. When the two streams of glass meet at the bottom of the V-shaped trough, their internal surfaces fuse into a single sheet. The outside surfaces of each stream do not make contact with a production surface, thus they are free of any contamination or damage, and emerge flat and devoid of defects [22].

2.3. THE DEFINITION OF GLASS

OVER the years, the definition of glass has also changed in response to new developments and discoveries in the scientific understanding of glass and its properties. In the literature, there are several definitions for glass. In 1830, Michael Faraday, defined glass as a material "more related to a solution of different substances than a compound per se". In 1932, Zachariasen published an article entitled "The Atomic Arrangement in Glass", in which he contends that "it must be frankly admitted that we know practically nothing about the atomic arrangement in glasses" [1]. The structural basis for the formation of glass by the melting-quenching process was established by Zachariasen, who proposed that the "atomic arrangement in glasses was characterized by an extended three-dimensional network, which lacks symmetry and periodicity" and that "interatomic forces were comparable to those of the corresponding crystal." Still, according to Zachariasen, the presence or absence of periodicity and symmetry in a three-dimensional network would be the differentiating factor between crystal and glass [1]. Figure 2.7 shows the symmetrical and periodic crystal arrangement of a crystal of composition SiO_2 and the network of a glass of the same composition, in which is characterized by the absence of symmetry and periodicity.

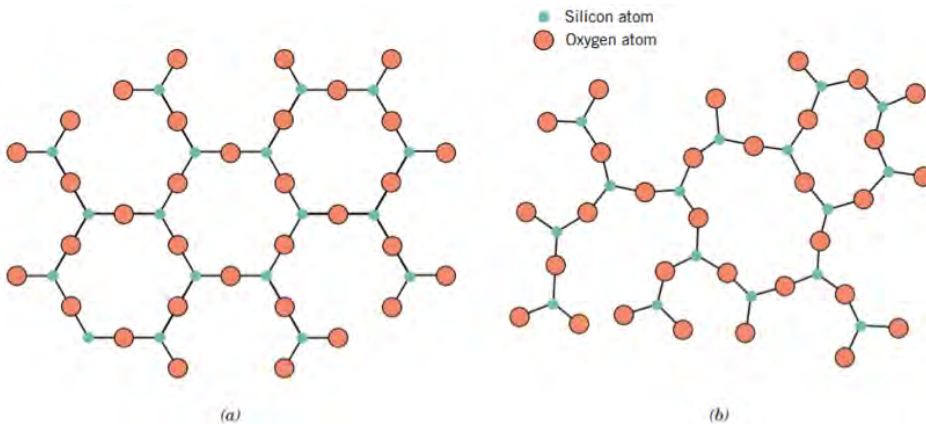


Figure 2.7: Structure of (a) crystalline SiO_2 and (b) non-crystalline SiO_2 [23].

Characterization techniques, as X-ray diffraction (XRD), provide information about the atomic structure of materials, enabling differentiation between amorphous and crystalline structures. The result of an XRD measurement is a diffractogram, in which the

peak positions indicate the phases present, the peak heights indicate the phase concentrations, presence of background bump corresponds to the amorphous content and the peak widths are related to the crystallite size or strain. The size and geometry of the unit cell can be determined from the angular positions of the diffraction peaks, while the arrangement of the atoms within the unit cell is associated with the relative intensities of those peaks. In Figure 2.8 it is possible to compare the diffractograms of glass-ceramic (KN), exhibiting peaks and halos, and a crystalline material (N), which exhibits peaks. Large crystallites create sharp peaks and the peak width increases as the crystallite size decreases. Figure 2.9 highlights the structure of glass, which presents characteristic halos.

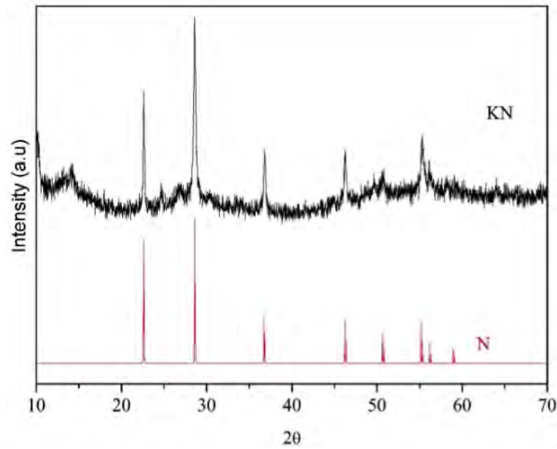


Figure 2.8: Diffraction patterns for a glass-ceramic (KN) and a crystal (N).

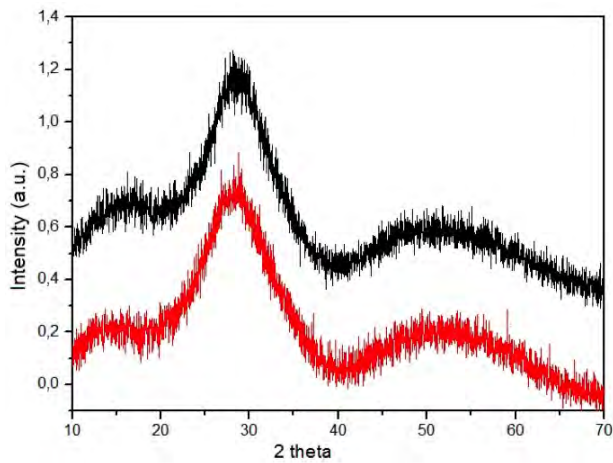


Figure 2.9: Diffraction patterns of vitreous samples, exhibiting characteristic halos.

Adding his “Random Network Theory” to the accepted scientific understanding of glass at the time of the publication of the paper, Zachariasen offered the following definition:

"glass is a fused inorganic product, based mainly on silica, which has been cooled to a rigid condition without crystallization, forming a three-dimensional random network, that is, with absence of symmetry and periodicity" [1].

As a result of modern scientific discoveries, this definition has again been adapted to reflect the discovery of an almost unlimited number of inorganic glass types which do not contain silica. In modern definitions of glass, the use of non-crystalline solids, amorphous solids, or vitreous materials is typically given. Such expressions are usually used as synonyms. In 1995, Gupta published an article entitled “Non-crystalline Solids: Glasses and Amorphous Solids”, in which it is suggested that each of these expressions implies a specific physio-chemical concept and, therefore, cannot be taken as synonyms [24]. As reported by Gupta, a non-crystalline solid can be thermodynamically divided into two distinct classes: glass and amorphous solids. Non-crystalline solids would be all those materials that present an extended and random three-dimensional network, in other words, solids without translational symmetry and periodicity. Considering the thermodynamic aspect, a non-crystalline solid would be a glass when it presented the glass transition phenomenon. Accordingly, amorphous solids would be non-crystalline solids which did not exhibit the glass transition [24].

By definition, vitreous materials do not solidify in the same way as crystalline materials. As glass cools, it becomes increasingly more viscous. There is no set temperature at which the liquid becomes a solid. In fact, one of the distinctions between crystalline and non-crystalline materials is the dependency on the specific volume (or volume per unit mass) in relation to the temperature. Crystalline materials solidify at the melting temperature T_m . A characteristic of the non-crystalline state is the glass transition temperature (T_g). In the case of crystalline materials, there is a discontinuous decrease in volume when the melting temperature (T_m) is reached [23]. However, in the case of vitreous materials, the volume decreases continuously as a function of the reduction in temperature. There is a small decrease in the slope of the curve in a range of temperatures, which is also known as glass transition temperature. Below this temperature, the material is considered to be a glass; above it, the material is first a supercooled liquid, and finally, a liquid [23]. This relation between specific volume and temperature is shown in Figure 2.10.

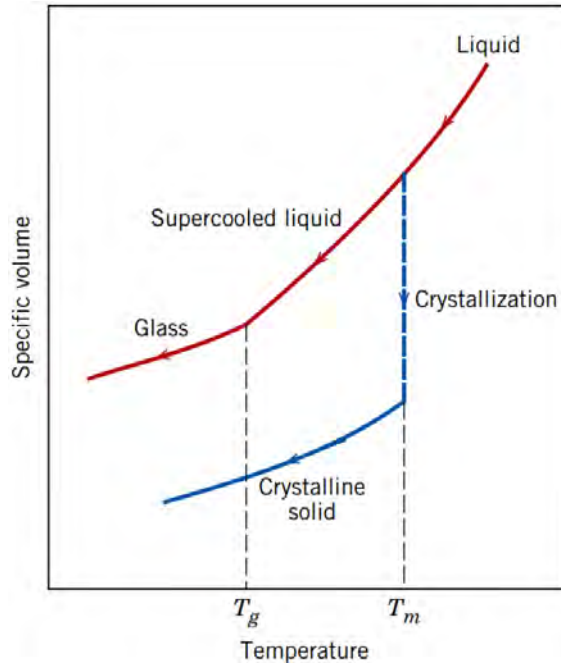


Figure 2.10: The contrast of specific volume versus-temperature behavior of crystalline and non-crystalline materials [23].

The glass transition region can be detected using thermo-analytical techniques, such as Differential Scanning Calorimetry (DSC), which are based on the thermal properties of materials. Changes in heat flow with temperature indicating physical changes such as crystallization or melting in the material investigated. The first phenomenon to appear on a DSC curve of glass is the glass transition (T_g), which corresponds to a baseline change. Next, exothermic peaks can be noted relative to crystallization, and an endothermic peak, which may be related to the melting of the crystalline phase (T_m). The onset crystallization temperature is called T_x , while the peak crystallization temperature is known as T_c . Figure 2.11 shows a typical DSC curve of a glass, where it is possible to note its characteristic temperatures. The identification of these temperatures is fundamental to the glass manufacturer and glass processor. Melting temperature is not the only figure of importance, as other temperatures can be of significant importance. Indeed, crystallization temperatures have a “danger zone”. During this range of temperatures, the glass cooling rate should be high enough to avoid the growth of crystals. The glass transition region helps to determine the annealing temperature. Annealing is a process of relaxation of internal stresses, which are introduced during glass cooling. The annealing temperature is located below the T_g because structural changes in the glass should not occur when it is treated below these temperatures.

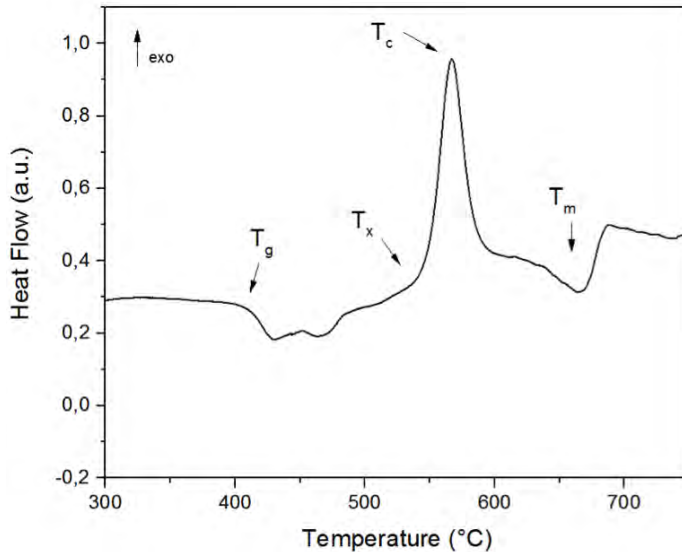


Figure 2.11: A typical curve of a DSC glass.

Given these considerations, a more complete glass definition was proposed by Shelby in 1997. Shelby defines glass as an amorphous solid with a complete absence of order and periodicity in the long range, exhibiting a glass transition region. According to Shelby, glass is any material - inorganic, organic or metal - formed by a technique which exhibits a glass transition phenomenon [2]. A definition proposed in 2017 criticizes some points proposed by Shelby and others. The first problem would be that the concept of the glass transition phenomenon lacks a widely-accepted and consensus-based understanding. Another issue is the fact that previous definitions label glass as a solid, while its structure is more comparable to a supercooled liquid. Glass resembles a solid on a human timescale, as it can flow at any temperature under the action of gravity, relaxing toward a supercooled liquid state [25]. Furthermore, it has been suggested that as a result of a long period of thermal treatment, or over a significant period of time, glass will solidify and crystallize. As a result of these developments, an updated definition was proposed:

“Glass is a nonequilibrium, non-crystalline condensed state of matter that exhibits a glass transition. The structure of types of glasses is similar to that of their parent supercooled liquids, and they spontaneously relax toward the supercooled state. Their ultimate fate, in the limit of infinite time, is to crystallize” [25].

According to Callister, some specific points on the viscosity scale are important in the fabrication and processing of glass, which are shown in Figure 2.12. These points are:

1. The melting point corresponds to the temperature at which the viscosity is $10 \text{ Pa}\cdot\text{s}$ (100 P); the glass is fluid enough to be considered a liquid.

2. The working point represents the temperature at which the viscosity is $10^3 \text{ Pa}\cdot\text{s}$ (10^4 P); the glass is easily deformed at this viscosity.

3. The softening point, the temperature at which the viscosity is $4 \times 10^6 \text{ Pa}\cdot\text{s}$ ($4 \times 10^7 \text{ P}$), is the maximum temperature at which a glass piece may be handled without causing significant dimensional alterations.

4. The annealing point is the temperature at which the viscosity is $10^{12} \text{ Pa}\cdot\text{s}$ (10^{13} P); at this temperature, atomic diffusion is sufficiently rapid that any residual stresses may be removed within about 15 min.

5. The strain point corresponds to the temperature at which the viscosity becomes $3 \times 10^{13} \text{ Pa}\cdot\text{s}$ ($3 \times 10^{14} \text{ P}$); for temperatures below the strain point, fracture will occur before the onset of plastic deformation. The glass transition temperature will be above the strain point [23].

Most glass-forming operations are carried out within the working range, in general between the working and softening temperatures. The temperature at which each of these points occurs is strongly related to the composition of the glass. Figure 2.12 shows that the softening points for soda-lime and 96% silica glass are respectively 700°C and 1550°C . This means that forming operations may be carried out at significantly lower temperatures for soda-lime glass [23].

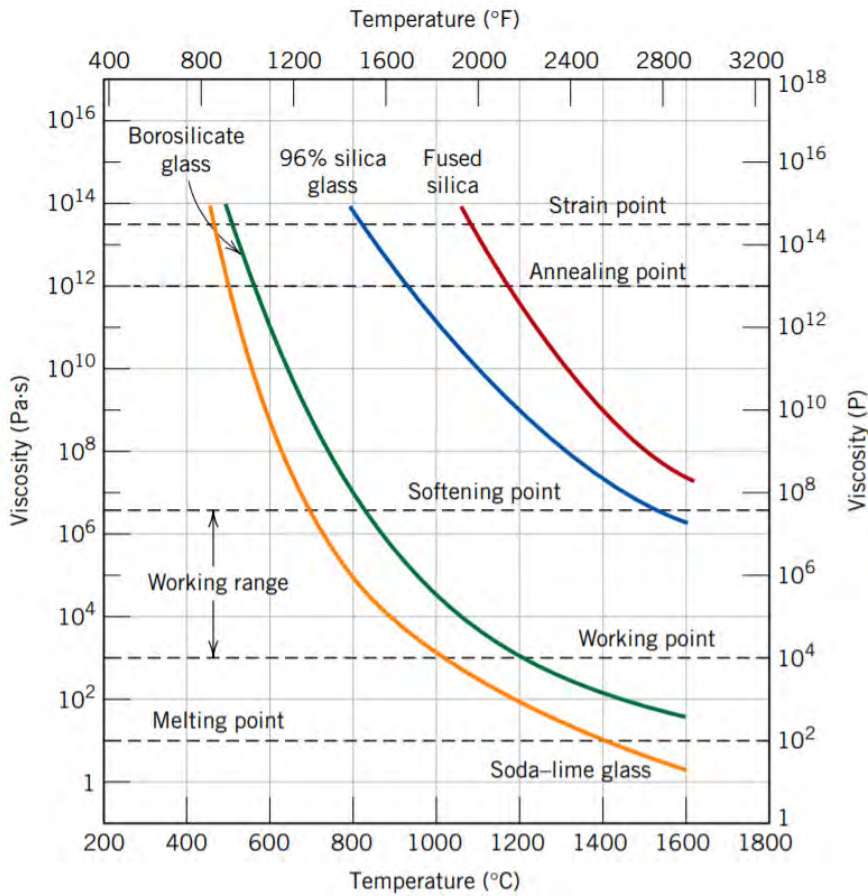


Figure 2.12: Logarithm of viscosity versus temperature for fused silica and three silica glasses [26].

2.4. GLASS IN CONSTRUCTION

IT was only a few decades ago that glass was introduced in the field of structural engineering. It is used in different branches of engineering because it is rigid but also transparent. Nowadays, most part of the glass production is float. However, simply using panels of float glass just as they are is not enough to create safe structures [27].

The tendency in modern buildings to increase the amount of glass used has resulted in the need of employing glass in a load bearing manner. However, when in tension, glass fails unpredictably. The strength of glass can be represented in certain cases by Weibull statistics and probabilistic strengths calculated. However, considerable uncertainty exists in the literature about the exact parameters and the allowable design strength [28]. The tensile strength cannot be correctly determined as in direct tensile test the glass will break in or at the grip. Bending test results provide a scattered value for the bending strength, with a spread varying between 30 and 50% of the mean strength [29]. To develop a safe structure, it is required to make the structure redundant, capable of carrying

after failure of a major part. Ductility indicates that if a structure is gradually reaching the limits of its carrying capacity it breaks or collapses all of a sudden [30].

Brittle materials, when subjected to stress, break without significant plastic deformation. From an engineering point of view, it is desirable that structures warn that a fatal loss of integrity is forthcoming. As glass does not present an evident deformation under high loads, cracking abruptly, strategies have been conceived in order to change this brittle behavior. The toughening of the glass, already discussed in this chapter, is one of these strategies. It consists of the artificial introduction of compression in the outside layer of a glass panel, closing existing cracks and compensating the tensile stresses. The tensile peak stress of impact loads is also compensated by the compression introduced during the toughening.

Another improvement to the brittleness of glass is the lamination process. A virtually transparent layer of glue holds separate glass panels together. This layer prevents the pane from falling apart upon breach. Then, laminating three layers of glass to form a beam it is possible to create a safe structure. Even if the two outside layers broke, from instance impacted by a stone, the glue keeps their broken parts glued to the central panel, protecting the remaining beam. If the central beam was adequately projected for carrying normal loads, with a safety factor of 1.1, nothing, except extra elastic deformation, should happen [27].

2.5. DISCUSSION AND RESULTS

THE definition of glass has changed over the years, reflecting an evolution in the scientific understanding of glass and its material properties. Previously, it was believed that all glass should be based on silica. Later it was proved that it is possible to form an almost unlimited number of inorganic glasses which do not contain silica. In fact, an enormous range of compositions can be formed into glass, as long as they are subject to a suitable process. The nature of the material cannot be used to formulate a definition, as both glass and crystal can have the same composition while showing different structures. Another past thought stated that glass was formed exclusively by a process of fusion. This concept was also corrected when it was found that glasses can be formed by innumerable processes. For instance, sodium silicate glass can be created through the evaporation of an aqueous solution of sodium silicate (known as "liquid glass") followed by heat treatment. The structure of the end-product obtained by this process is the same as the sodium silicate glass produced by the classical melting-quenching method. Therefore, it is not possible to define a type of glass based on its formation process, nor is it possible to distinguish different types of glass formed by different processes. It is therefore likely that the current commonly accepted definition of glass, proposed in 2017, will need to change again in the near future, as the structural understanding of glass is still being developed further.

Scientists produce thousands of new formulations of glass every year. A small part of these findings become commercialized or find a practical application. For example, one recent discovery was fluoride glass developed in France in the eighties. Fluoride glasses were promoted by their potential use for long distance repeaterless telecommunication links [31]. However, soda-lime-silica and borosilicate glass remain as the only options for architectural glass. New glass compositions have repeatedly demonstrated better prop-

erties than standard glass, being almost as tough as steel, having a much lower transition temperature, or a lighter and tougher glass. While new glass compositions can be beneficial in isolation, in their totality of properties, these types of glass are typically out of balance and thus disadvantageous in relation to standard glass.

A newly reported glass composition, claimed as almost as tough as steel, possesses one of the highest elastic moduli and hardness for an oxide glass. The measured Young's modulus and Vickers hardness were 158.3 GPa and 9.1 GPa, respectively [32]. However, its composition contains Al_2O_3 and Ta_2O_5 , which melt only at very high temperatures and can only be produced as small samples some 2mm in diameter, thus requiring special production techniques that are not suitable for a mass production [32]. Furthermore, the price of the process and the high price of the Ta_2O_5 make the final product expensive. Some special glass compositions, such as phosphate glasses containing titanium, can melt at temperatures lower than 400°C. However, in relation to standard glass, these compositions present a low hardness combined with a high thermal expansion coefficient. Previously, phosphate glasses demonstrated very poor chemical durability. The TiO_2 incorporation in the glass not only improves the chemical durability of phosphate glass, but also increases its nonlinear refractive index. As a result, phosphate glass is not used for architectural nor automotive purposes but is broadly utilized for nonlinear optical applications [33]. Gorilla glass, manufactured by Corning, is ultra-thin and ultra-strong glass made from an alkali-aluminosilicate composition that allows for a deep layer of chemical strengthening. The exceptional strength can be credited to a combination of the composition, a mixture of silica, aluminium oxide and sodium oxide, and the manufacturing process, as the glass is submitted to ion exchange process [22]. The ion exchange-strengthened glass is expensive in relation to the thermal tempering processed product. Furthermore, Gorilla glass is made by a fusion drawing process, which prevents warping after chemical strengthening. Float-produced glass is cheaper but suffers from warping after chemical strengthening as a result of varying amounts of tin on the two surfaces creating an unequal alkali-ion interdiffusion [34]. For these reasons, Gorilla glass is used on more than one billion electronic devices but is just starting to be considered for architectural lightweight solutions.

It is possible to conceive of a bright future where chemically strengthened float glass is used in building and interior constructions, where strength, design and shape prevent thermal strengthening. One way in which these material properties could be achieved is by applying ion strengthening to glass locally at a critical area. The achievement of local strengthening of the glass could initiate new prospects for glass in construction. This could be achieved by combining chemical strengthening with a mechanical treatment process in the production of glass. This would greatly facilitate the manufacture of glass for certain applications, as thermal strengthening cannot be applied in some situations, for instance, chemical strengthening around a drilled hole in a bolt fixed flat glass in a balustrade [18].

Approximately 650,000 papers of research in glass science and technology have been published in the last two centuries, and the publication rate has increased exponentially since 1945. Nowadays, oxide glasses, metallic glasses, amorphous carbon, and amorphous silicon have drawn the most research attention [35]. A recent review of the current status of glass research in the United States, considering papers published from 2007 to

2013 in each of the six main journals under study, found that silicate glasses and glass ceramics, are among the most important materials for the industry, represented less than one-quarter of the publications (Figure 2.13). At the same time, 17% of the publications were concerned with model glasses, for instance, theoretical glasses not based on any real chemistry [35]. The category “model” does not include modeling studies of real-world glass-forming systems. For instance, a molecular dynamics study of silicate glasses would be classified as focusing on “silicate” rather than “model” glasses. One of the causes of this discrepancy could be the fact that investigations of purely model systems require considerably less funding.

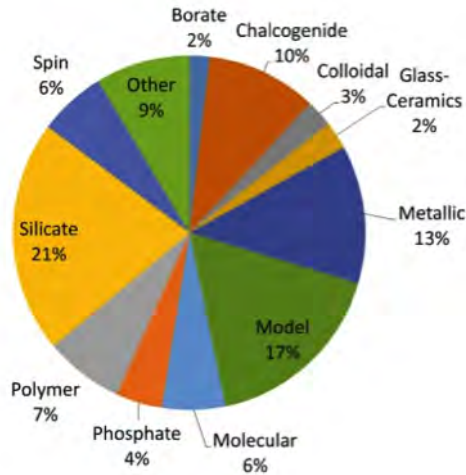


Figure 2.13: Breakdown of glass science-related journal publications by the primary type of glass under study [35].

If research on glass does not adequately focus on areas of technical relevance for future industrial applications, it will become increasingly difficult to meet the challenges faced by the glass industry and to form qualified researchers with the required expertise to work on these challenges [35]. The same report lists some topics that are not currently given sufficient attention by the global glass research community, including glass brittleness and breakage. This area deserves analytical attention in order to discover how to make glass with increased fracture toughness to avoid brittle failure. Another under-investigated factor is crystallization behavior, glass surfaces, and questions related to glass melting. Analyses of these phenomena could help uncover the fundamental reactions between glass melting and different types of refractory materials, leading to a minimization of the refractory dissolution process [35].

Despite the slow progress of industrial glass research, many technological advancements have already been developed, mainly during the end of the twentieth century, such as those which are helping to realize the concept of the all-glass building [12]. New adhesives and glass fins have boosted this desire to become reality. Issues from contemporary society bring new demands for glass. Now, in the twenty-first century, the

challenge is to create an all-glass building which is as sustainable as possible. An example of a prosperous and sustainable solution for all-glass, load-bearing structures is the development of interlocking cast units. Research is already being conducted on the development of such a system that eliminates the use of adhesives by employing dry connections instead. The total weight of the construction in combination with the unit's interlocking geometry secure the overall stability, providing constraints against lateral movement [36]. This could facilitate the recycling of glass, as it eliminates the contamination introduced by the adhesives, and also optimizes the building process, getting rid of the precise application of the adhesive.

In the scenario where environmental concerns become more and more demanding, industrial waste and recycled resources assist the growth of the material basis of the glass industry. The demand for new types of glass made from non-traditional materials is stimulated not only by economic conditions (i.e. energy conservation and fewer industrial materials) but also environmental conditions, such as air and environmental pollution. For these reasons, industrial waste is being increasingly used in the fabrication of glass. This industry utilizes mineral rocks and products of their processing, waste from ferrous and nonferrous metallurgical manufacturing in the form of ash and slime, and chemical wastes, such as alkaline-earth metals and technical sodium sulfate in the production of glass [37]. The priority of waste management efforts is to reduce the quantity of production waste created. Secondly, waste management concerns the recovery of production waste internally, followed by the development of external recovery industries such as reuse and recycling [38]. The combustion of fossil fuels and chemical reactions - such as the de-carbonization of carbonates in the glass fusion - results in high rates of CO₂ emissions. High rates of energy consumption are another fundamental production issue, and electricity acquisition is indirectly related to CO₂ emission. The use of recycled raw materials in glass fusion makes it possible to reduce energy consumption. In the case of flat glass, energy consumption is reduced by 3% when the amount of cullet used in production is increased from 20% to 30% of the raw materials. This reduction in energy consumption is accompanied by a reduction in CO₂ emissions [38]. New glass recipes can be developed incorporating industrial wastes, such as the slag discharged from blast furnaces in the steel industry [39]. The chain emission also impacts the environment, stimulating the development of new products. Glasses becoming continually lighter also reduces CO₂ emissions related with the transportation. Glass furnaces can emit substances that contribute to the acidification of the environment, such as sulfur dioxide (SO₂) and nitrogen oxides (NO_x). Some decades ago, there was little concern nor awareness of the impact of these effects, however, nowadays the optimization of equipment and processes is fundamental to decreasing these harmful emissions.

2.6. CONCLUSIONS

THE correct definition of glass is still an open issue. The current definition states that the structure of glass is more comparable to that of a supercooled liquid, while previous definitions have labelled glass as a solid. Despite various definitions that have been suggested over the years, it can be said with a certain degree of certitude that a universally accepted definition of glass remains elusive. As the structure of glass is still not fully clarified, the current definition can still be updated.

The introduction of the blowing technique around 50 BC expanded the popularity and usages of glass, and the expansion of the Roman Empire allowed for the dissemination of this process. It was still popular during the Middle Ages, however, the presence of inhomogeneities motivated the search for a technique free of distortions. Continuous grinding and polishing, highlighting the twin grinder machine, contributed to the achievement of the homogeneous glass, but with a high operational cost. Therefore, the float process was developed in 1953, facilitating the mass production of glass sheets at a relatively low cost and a better quality than any process known. Glass blocks boomed in the 1970's. In relation to the plate glass sheets, blocks were cheap and easy to assemble. But some advances were still necessary in order to realize the concept of an all-glass building. Adhesives, strengthening processes, suspended glass systems and other developments contributed to the achievement of this ambition. Traditional glass block curtain walls, which exhibited a noticeable structure, became obsolete in relation to the new facades, which demonstrate a dematerialized appearance. Analyzing all these cases along the course of history, innovation seems always to be the answer to contemporary demands.

The current demand is for the creation of all-glass buildings which are as sustainable as possible. Glass research focused on issues of practical relevance is key to facing this challenge. While this research requires funding, it is necessary in order to create a high impact product in a long-term. For this reason, optimization of equipment and processes, glass compositions containing waste, lighter glasses, recycling strategies and others, are fields that should receive more attention.

REFERENCES

- [1] Zachariasen, W.H. (1932). The atomic arrangement in glass. *Journal of the American Chemical Society*. v. 54, pp.3841-3851.
- [2] Shelby, J.E. (2005). *Introduction to Glass Science and Technology*. 2nd edition, Royal Society of Chemistry.
- [3] Rasmussen, S.C. (2012). *How Glass Changed the World: The history and the chemistry of glass from antiquity to the 13th century*. Springer: Berlin/Heidelberg, Germany.
- [4] Gerhard, C. (2017). *Optics Manufacturing: Components and Systems*. CRC Press.1st edition. Boca Raton.
- [5] Miller, J. (2015). *Glass: Miller's field guide*. Octopus Publishing.
- [6] Ball, P. (2017). Material witness: Who made the first glass? *Nature materials* 16, No.12, pp.1172.
- [7] Nascimento, M. L. F. (2014). Brief History of the Flat Glass Patent- Sixty Years of the Float Process. *World Patent Info*. 38, pp.50- 56.
- [8] Pilkington, L.A.B. (1969). Review Lecture: The float glass process. *Proceedings of the Royal Society of London. Series A, Mathematical and Physical Sciences*, v. 314, No. 1516, pp. 1-25.
- [9] Persson, R. (1969). *Flat Glass Technology*. Springer US, Springer Science+Business Media New York.
- [10] Na, B., Ahmed, S., Nemhauser, G.L., and Sokol, J. (2013). Optimization of automated float glass lines. *International Journal of Production Economics*, v.145, Issue 2, pp.561-572.

- [11] Horsley, C.B. (1977). Glamorous glass bricks are booming. *The New York times*. Edition of November 17, 1977. pp. 59.
- [12] Eskilson, S. (2018). *The age of glass: A cultural history of glass in modern and contemporary architecture*. Bloomsbury Academic.
- [13] Oikonomopoulou, F., Bristogianni, T., Veer, F., and Nijse, R. (2017). The construction of the crystal houses facade: challenges and innovations. *Glass Structures and Engineering*. pp.1-22.
- [14] Philips, C.J. (1948). *Glass, the miracle maker. Its history, technology, manufacture and applications*. 2nd edition. Pitman, London.
- [15] Mauro, J., Philip, C., Vaughn, D., and Pambianchi, M. (2014). *Glass Science in the United States: Current Status and Future Directions*. *International journal of applied glass science*. v.5, pp. 2-14.
- [16] Alves, O.L., Gimenez, I.F., Mazali, I.O. (2011). Vidros. *Cadernos temáticos- Química na nova escola*.
- [17] Zanotto, E.D. (1989). Vidros: arte, ciência e tecnologia de 4000A.C. a 2000 D.C. *Engenharia de Materiais, Artigo técnico*, v.1. pp.33-36.
- [18] Karlsson, S., Jonson, B., and Stålhandske, C. (2010). The technology of chemical glass strengthening- a review. *European Journal of glass science and technology Part A*, v.51, *Society of Glass Technology*, pp.41-54.
- [19] Chorfa, A., Madjoubi, M.A., Hamidouche, M., Bouras, N., Rubio, J., Rubio, F. (2010). Glass hardness and elastic modulus determination by nanoindentation using displacement and energy methods. *Ceramic-Silikaty*, v.54, pp. 225-234.
- [20] Gardiner, B. (2010). Glass works: how corning created the ultrathin, ultrastrong material of the future. *Wired Magazine*.
- [21] Uhlmann, D.R., and Kreidl, N.J. (1980). *Science and technology*, vol. 5, Academic Press, New York.
- [22] *The Economist*. (2017). One of the world's oldest products faces the digital future. *Science and Technology*. Edition Oct. 12th 2017.
- [23] Callister, W.D. (2007). *Materials Science and Engineering An Introduction*. 7th Edition, John Wiley & Sons, New York.
- [24] Gupta, P.K. (1996). Non-crystalline solids: glasses and amorphous solids. *Journal of Non-Crystalline Solids*, v. 195, Issues 1–2, pp.158–164.
- [25] Zanotto, E.D., and Maro, J.C. (2017). The glassy state of matter: Its definition and ultimate fate. *Journal of Non-Crystalline Solids*, v.471, pp.490-495.
- [26] Shand, E.B. (1968). *Engineering Glass, Modern materials*, vol.6, academic press, New York.
- [27] Nijse, R. (2003). *Glass in structures: Elements, concepts, designs*. Birkhäuser.
- [28] Veer, F., Zuidema, J., Bos, F.P. (2005). *The Strength and Failure of Glass in Bending*. *Glass processing days 2005*.
- [29] Veer, F., Rodichev, Y. (2016). The strength of glass, hidden damage. *Challenging Glass Conference Proceedings*, v.2, pp.395-404.
- [30] Oikonomopoulou, F., van den Broek, E.A.M., Bristogianni, T., Veer, F.A., Nijse, R. (2017). Design and experimental testing of the bundled glass column. *Glass Structures & Engineering*, v. 2, Issue 2, pp. 183-200.

- [31] Lucas, J. (1997). Fluoride glasses. *Current opinion in solid state and materials science*. 2: pp. 405-411.
- [32] Rosales-Sosa, G.A., Masuno, A., Higo, Y., Inoue, H., Yanaba, Y., Mizoguchi, T., Umada, T., Okamura, K., Kato, K., and Watanabe, Y. (2015). High elastic moduli of a 54Al₂O₃-46Ta₂O₅ glass fabricated via containerless processing. *Scientific Reports*. pp. 1-8.
- [33] Tiwari, B., Dixit, A., Kothiyal, G.P., Pandey, M., and Deb, S.K. (2007). Preparation and characterization of phosphate glasses containing titanium. *Barc. Newsletter*, No.285, pp. 177-173.
- [34] Varshneya, A.K., and Bihuniak, P.P. (2017). Cover screens for personal electronic devices: Strengthened glass or sapphire? *American Ceramic Society Bulletin*, v. 96, No. 5.
- [35] Mauro, J. C., and Zanutto, E. D. (2014). Two centuries of glass research: historical trends, current status, and grand challenges for the future. *International journal of applied glass science*. v.5, pp. 313-327.
- [36] Oikonomopoulou, F., Bristogianni, T., Barou, L., Jacobs, E., Frigo, G., Veer, F.A., Nijse, R. (2018). Interlocking cast glass components, Exploring a demountable dry-assembly structural glass system. *Heron*. v. 63. No. 1/2. pp.103-138.
- [37] Babadzhanova, O.F., Yashchishin, I.N. (2000). Low-melting glasses based on phosphate ore processing products. *Glass and ceramics*. v.57. n.5, pp.3-5.
- [38] Saint-Gobain (2017). Saint-Gobain corporate publications. 2017 Annual report.
- [39] Xu, Y., Zhang, Y. Z., Hou, L. Y., and Lu, X. (2014). Preparation of CaO-Al₂O₃-SiO₂ system glass from molten blast furnace slag. *International Journal of Minerals, Metallurgy, and Materials*. v.21, Issue 2, pp. 169-174.

3

CREATING THE NEW GLASS COMPOSITIONS

Despite a large number of products developed from by-products, most of them are non-transparent. This is partly because it is difficult to obtain transparent materials at reasonable temperatures from these waste products. Transparent glass samples incorporating slag and fly ash into a phosphate glass matrix were produced to study making a transparent glass from waste material. The compositions were adjusted to circumvent the typical drawbacks of phosphate glasses, such as low chemical durability. The use of phosphate as a glass former instead of silicate is a remarkable innovation, and according to the knowledge of the author, no other work reports its utilization for building engineering purposes. This novel method of producing glass, incorporates amounts up to 35% (in weight) of blast furnace slag or fly ash. The resulting glass possesses a low melting temperature in relation to standard soda-lime and borosilicate glasses, melting at temperatures between 1100 °C and 1350 °C. This drastic reduction of the melting temperature allows significant amounts of energy to be saved during the manufacturing process. Furthermore, using waste materials reduces costs and gas emissions. This is a promising development in the endeavor to fill the need for a more sustainable process of manufacturing glass.

3.1. DESIGNING COMPOSITIONS CONTAINING SLAG AND FLY ASH

3.1.1. SLAG AND ASH

THE utilization of industrial by-products in manufacturing building materials has increased considerably due to concerns over the amount of waste produced and the huge environmental problems caused by its disposal. Expanding populations, urbanization and increased wealth are ramping up the global production of solid waste. Factors like population and per capita gross domestic product (GDP) are used to measure total global municipal solid waste (MSW) production [1]. The waste production rates per capita usually grow with wealth, despite the fact that there is a tendency toward anti-materialism in wealthier countries. When combined, these aspects indicate a scenario in which, over the next decades, global waste generation will go beyond our capacity to control it [1].

Fly ash is a by-product from burning pulverized coal in electric power generating plants, it can be used in Portland Cement Concrete (PCC) pavement, paving roads, regular structural concrete, among others. The disposal of fly ash is becoming an increasing economic and environmental burden, creating demand for applications of fly ash other than in the cement industry [2].

Steel slag is a mixture of metal oxides and silicon dioxide, which can include metal sulphides along with metals in their elemental form. Steel slag output comprises approximately 20% of the mass of crude steel output. In 2014, global slag production was 250 Mt from the 1.6 bn tons of steel production [3].

Ground-granulated blast-furnace slag (GGBFS) is formed by quenching molten iron slag from a blast furnace in water, to produce a glassy, granular product that is then dried and ground into a fine powder. Slag is becoming a value-added engineering material, utilized in the manufacture of materials like ceramics. New low-cost ceramics, without traditional fluxes and containing 30, 50 and 70% blast furnace slag have already been synthesized at temperatures between 1200 °C and 1220 °C. The obtained samples present

good degrees of sintering and mechanical properties, which outperform the properties of the conventional building and tiling materials [4]. The blast furnace slag, used to produce glasses in the work, will be from now on simply referred as “slag”.

Despite the large number of products that can be developed from waste materials, most are non-transparent materials. This is partly because it is a challenge to get transparent materials at reasonable temperatures from these waste products. Slag and fly ash contain many elements that are also present in typical glass formulas. For instance, the compounds found in higher amounts in the compositions of standard silicate glasses are SiO_2 , Na_2O , CaO , K_2O , MgO , Al_2O_3 , Fe_2O_3 [5], all of which are found in different concentrations in both slag and fly ash compositions. The presence of oxides like Na_2O and CaO also produces fewer harmful emissions because for the traditional production of glass these oxides are obtained using thermal decomposition. Sodium oxide is often obtained from the thermal decomposition of sodium carbonate (Na_2CO_3) according to reaction 1, which takes place around 1000 °C. Calcium oxide (CaO) is mainly obtained from the decomposition of calcium carbonate (CaCO_3), as illustrated in reaction 2. During decomposition, both carbonates also form CO_2 (carbon dioxide). Thus, the incorporation of wastes into the glass composition allows for the addition of Na_2O and CaO already in the form of oxides, while their additions obtained from raw carbonates result in significant CO_2 emission.



The compositions of blast furnace slag and fly ash are listed in Table 3.1. They are expressed as a function of the concentrations of silicon dioxide (SiO_2), aluminum oxide (Al_2O_3), calcium oxide (CaO), magnesium oxide (MgO), iron (III) oxide (Fe_2O_3), Sulfur trioxide (SO_3), Sodium oxide (Na_2O), Potassium oxide (K_2O), Titanium dioxide (TiO_2) and Phosphorus pentoxide (P_2O_5). Some of these elements are highly refractory and their presence in complex compositions means they are highly likely to crystallize and have high working temperatures. However, glass is a material that allows for large amounts of various elements in its solution, and is thus suitable for assimilating complex materials within its composition.

Table 3.1: Chemical compositions of fly ash (FA) and blast furnace slag (BFS) deduced from X-ray fluorescence and expressed in weight%.

	SiO_2	Al_2O_3	CaO	MgO	Fe_2O_3	SO_3	Na_2O	K_2O	TiO_2	P_2O_5	L.O.I.
BFS	34.40	11.53	39.17	7.81	1.42	1.6	0.23	0.58	-	-	1.15
FA	54.28	23.32	4.23	1.62	8.01	0.64	0.85	1.97	1.23	0.54	3.37

The materials listed in Table 3.1 had their structures analyzed by X-ray diffraction (XRD). The diffractogram of the slag is presented in Figure 3.1. The experimental details of all the characterization performed in this work can be found in Appendix A. The identified crystalline phase is Quartz (SiO_2), but the sample is mostly amorphous. The red sticks give the peak positions and intensities of the crystalline phase identified as SiO_2 . The X-ray diffraction pattern of fly ash is presented in Figure 3.2. Besides compound quartz, the analysis also identified mullite ($3\text{Al}_2\text{O}_3 \cdot 2\text{SiO}_2$) in the fly ash. The red sticks give the peak positions and intensities of the crystalline phase identified as SiO_2 and the blue sticks give the peak positions and intensities of the crystalline phase identified as $3\text{Al}_2\text{O}_3 \cdot 2\text{SiO}_2$, mullite. This can be explained by the high concentration of Al_2O_3 in the composition of the fly ash. As illustrated in Table 3.1, Al_2O_3 corresponds to 23.32% of the mass of fly ash, while for the slag it consists of only 11.53% of the mass.

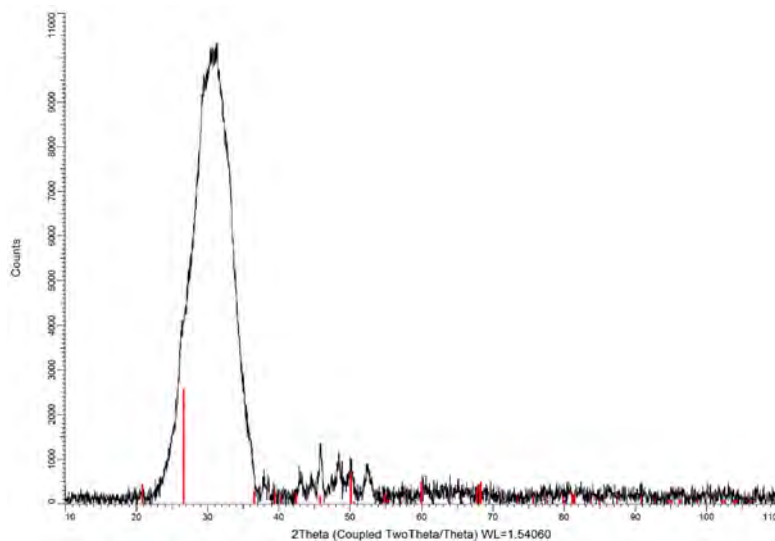


Figure 3.1: X-ray diffraction pattern of slag after background subtraction.

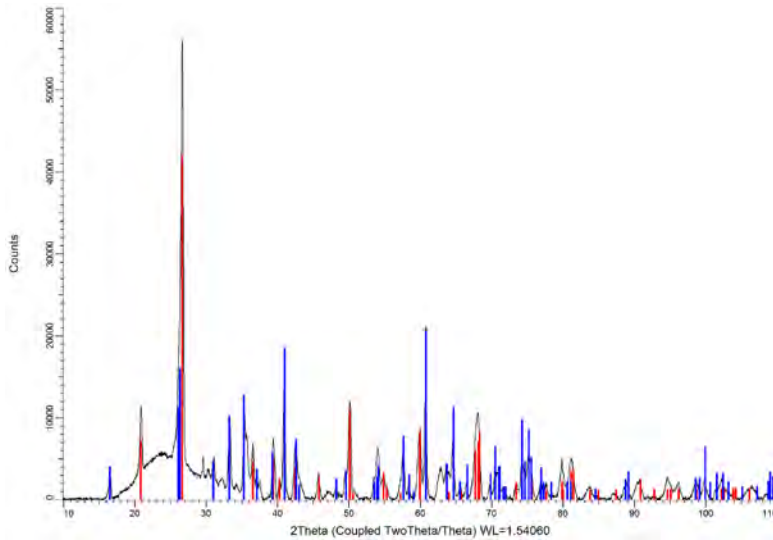


Figure 3.2: X-ray diffraction pattern of fly ash after background subtraction.

3.1.2. PHOSPHATE GLASSES

PHOSPHATE glass is one of the most important and technologically advanced types of glass. Originally developed in the 1950s [6], phosphate glass had poor chemical durability which vastly limited its application. However, in the 1980s, its properties were greatly improved with the use of intermediates and modifier elements. Initially, lead-iron phosphate glass was developed as a new waste form for the safe immobilization of high-level commercial radioactive waste [7]. In relation to borosilicate nuclear waste glass, which were at that time the standard waste form for the long-term disposal of nuclear waste, lead-iron phosphate glasses presented several advantages, for instance:

- (i) an aqueous corrosion rate approximately 1000 times lower
- (ii) a processing temperature which is 100 °C to 250 °C lower
- (iii) a much lower melt viscosity in the temperature range from 800 °C to 1000 °C

Since then, the potential applications of phosphate glasses have been largely expanded.

Phosphates are defined as phosphorus compounds in which each phosphorus atom is surrounded by four oxygen atoms positioned at the vertices of a tetrahedron $[\text{PO}_4]$. In the same way as pure phosphate glasses, binary and more complex compositions possess fundamental structures with tetrahedral coordination $(\text{PO}_4)^{3-}$. Phosphate glass, like silicate, has a tetrahedral structure in which each tetrahedron can be connected to another, sharing the atoms of oxygen, while the difference stands in the fact that phosphorus has three single bonds, named bridges, which bind to other $(\text{PO}_4)^{3-}$ units and a double bond, with an oxygen atom, named non-bridge. This occurs due to the excess charge associated with P^{5+} , which possesses a less cross-linked structure than the Si^{4+} . In the structure of silicates, a tetrahedral structure is formed by a Si atom in the center and four atoms at the vertices, connected to each other by the four vertices. The Figure 3.3 shows the two-dimensional schemes of the tetrahedral structure of silicate and phosphate glass

containing sodium (Na) as a modifying element. The tetrahedra of silicate glass presents a high degree of symmetry due to the absence of a double bond, while the tetrahedra of the phosphate glass is asymmetric [8]. The extra bridging oxygen related to the SiO_4 tetrahedra is responsible for the higher polymerized structure, affecting properties such as chemical durability and glass transition temperature.

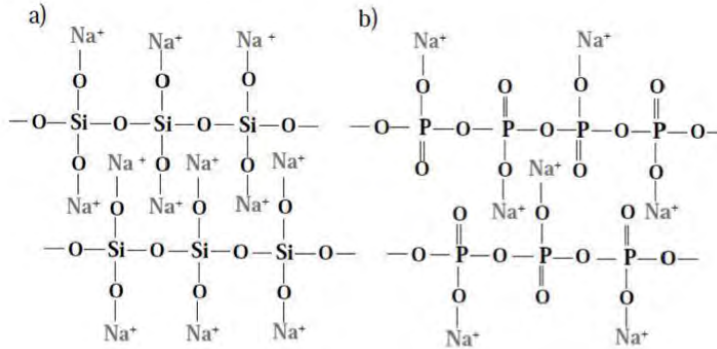


Figure 3.3: Two-dimensional representation of structures for: a) a silicate glass b) a phosphate glass [8].

Phosphate glasses separate into four different classifications and their structures can be illustrated by $Q^{[n]}$ where n represents the number of neighboring P-tetrahedra linked through common bridging oxygens. The four basic units are shown in Figure 3.4. The single P_2O_5 glass possesses a structure based on 3D interconnected chains of Q^3 tetrahedra that have three bridging oxygens and one non-bridging oxygen ($\text{P}=\text{O}$). These glasses are highly hygroscopic. Through the addition of a second oxide (modifier), bridging oxygens ($\text{P}-\text{O}-\text{P}$) are replaced by non-bridging oxygens to form an ultraphosphate based on Q^2 and Q^3 tetrahedra.

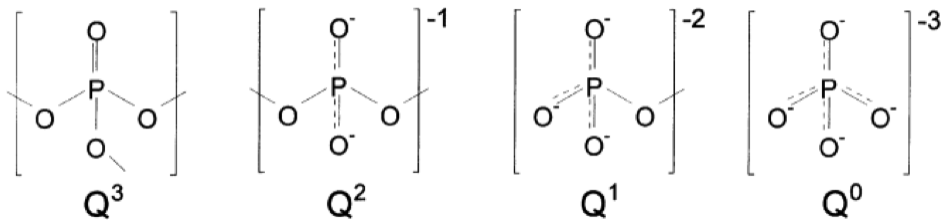


Figure 3.4: Phosphate tetrahedral sites that can exist in phosphate glasses [9].

At the metaphosphate, Q^2 tetrahedra bonds to form chains and rings which themselves are tied-together [10]. Further increases in the modifier content produce shorter polyphosphate chains that are terminated by Q^1 tetrahedra. At the pyrophosphate stoichiometry, the network is formed by Q^1-Q^1 dimers [10]. Finally, the orthophosphate glasses (Q^0) contain an isolated $(PO_4)^{-3}$ [8].

3.2. EXPERIMENTAL

ALMOST all elements in the periodic table could hypothetically be incorporated into the composition of glass. Consequently, choosing random elements to prepare glass is not an efficient option. The many possible combinations could lead to very variable properties far from those desired in this research. Two main methodologies are currently used for glass production.

The so-called “cook and look” technique has been used for a long time. Using this technique, a starting composition is developed based on available data, compositions previously reported and intuition. This composition is experimentally prepared at the laboratory and its properties are characterized and measured. The determined properties are compared with the desired ones; based on the difference, the researcher develops more samples in an attempt to finetune the composition and get closer to the target characteristics [11]. On the one hand, this technique has been used to create a wide variety of types of glass with a number of commercial applications. On the other hand, the large number of tested compositions can be expensive and protracted, especially if the choice of the starting composition is made without careful criteria and if its properties are considerably different to the target.

Another technique is based on the use of predictive modelling tools to facilitate the design of new glass compositions. Precise, quantitative models have already been developed for different properties. However, each model is only appropriate to solve a certain type of problem. There is still no model that is able to address every property simultaneously [11]. Topological constraint theory and atomistic simulations are examples of cases in which precise predictions of properties have been made based on the chemical makeup of the glass. However, as glass is a non-crystalline material, its atomic positions are not known with absolute certainty. They should be described using probability density distribution functions, which makes predictions more complex. An ideal application of this approach would require modelers working closely with experimentalists. Although the use of predictive modelling becomes each day more unavoidable the selection and implementation of the models is still a long process that requires interdisciplinary work. Collaboration among professionals skilled in chemistry, physics, and materials can facilitate the selection and implementation of models.

In this study we used the first technique, starting with an initial glass composition. The elements were weighted using an analytical balance and ground using a ceramic mortar. This mixture was transferred to a platinum crucible and kept molten for 1 hour. Melting temperatures ranged from 1100 °C to 1350 °C, depending on the glass composition. The melted mixtures were poured into a stainless steel mold preheated to around 450 °C and were annealed at this temperature for 3 hours before cooling to room temperature inside the furnace. These glass samples were then ground and polished. The steps of this process are illustrated in Figure 3.5.



Figure 3.5: Scheme of the glass samples production: preparation of the batch, melting, quenching and annealing.

Phosphate was used as a glass former, being obtained from KH_2PO_4 (potassium dihydrogen phosphate), which at temperatures around $250\text{ }^\circ\text{C}$ decomposes into KPO_3 (potassium metaphosphate) and H_2O , as presented in reaction 3 below. In turn, KH_2PO_4 results from the synthesis of K_2O (Potassium Oxide), P_2O_5 (Phosphorus pentoxide) and H_2O , as shown in reaction 4.



Usually, metaphosphate formers such as sodium polyphosphate (NaPO_3) and potassium metaphosphate (KPO_3) are known for their capacity to dissolve very large amounts of transition metal oxides. This capacity is due to the insertion of the MO_x polyhedra inside the linear phosphate chains, resulting in higher network connectivities that lead to higher viscosities and thermal stabilities against devitrification [12]. Potassium metaphosphate does not vitrify by itself but forms a white non-transparent ceramic under melt quenching. The addition of modifier elements allows for vitrification [13]. Aluminum oxide (Al_2O_3) was added in order to improve the chemical durability of the glass types. Fly ash and blast furnace slag were also incorporated, in amounts as high as possible. These waste materials were used in the powder form, as shown in Figure 3.6.



Figure 3.6: The raw waste materials, fly ash and slag.

Initially, attempts were made to produce glass in an alumina crucible, due to the relatively low cost of this crucible. However, analysis of XRF found that alumina crucibles led to alumina being incorporated into the melt. Moreover, the Al_2O_3 content of the glass increased as the melting temperature increased. Alumina is attacked by phosphate glass melt, leading to high amounts of aluminum being incorporated into the network of the glass [14]. At the same time, glasses prepared in a platinum crucible had a measured composition very close to their nominal composition. Thus, the theoretical composition for these glass types can only be achieved using a Pt crucible. As a result, all samples analyzed were prepared using a Pt crucible.

The first attempts at melting aimed to obtain samples from a binary mixture of KPO_3 and slag or fly ash, however produced non-transparent materials, as can be observed in Figure 3.7. The addition of aluminum oxide (Al_2O_3) yielded transparent glass samples. DiBoron trioxide (B_2O_3) was added to some samples in an attempt to decrease the thermal expansion coefficient of the glasses. The composition of a glass type is calculated in weight% or mole% and is usually expressed in oxides. In this case, the compositions were calculated in weight% and due to the complex composition of the waste, which contained 10 different oxides and were therefore simply named slag or FA (fly ash). Another reason to simplify the nomination is the uncertainty regarding the composition of wastes, which are not homogeneous. This could lead to a wrong representation of the amounts of oxides, based on estimation instead of precise composition.



Figure 3.7: Non-transparent samples containing 80KPO₃.20Slag and 70KPO₃.30Slag, respectively.

3.3. COMPOSITION OF THE SAMPLES

THE composition of some samples was checked using X-ray fluorescence (XRF). Details of the measurements can be found in Appendix A. The concentration of the compounds was determined by the percentage of overall weight before being manually converted to molar concentration based on the molecular weight of the elements. Details of the process of conversion are shown in Appendix B. Both concentrations are listed in Tables 3.2 and 3.3. In samples containing B₂O₃, the concentration of B₂O₃ could not be determined because boron cannot be measured by XRF. Thus, the concentration of this element was predicted based on the concentrations of the other elements.

Due to the fact that the waste was not homogeneous in composition, differences between samples with the same nominal composition were anticipated. In an attempt to quantify this difference, two samples with the same nominal composition but from different batches had their compositions analyzed (Table 3.4). The samples showed significant differences between their actual compositions. The main compounds of the samples were P₂O₅, K₂O, Al₂O₃, SiO₂ and CaO. Each one of these compounds had a mass corresponding to at least 7% of the total weight of the sample. Among these main elements, the difference between the concentrations of the two batches varied up to 18%. For the compounds present in small amounts (less than 1% of the total weight) the variation was wide. For instance, one of the batches had 0.01% of ZrO₂, while the other batch had a concentration 14x higher. Other compounds, the ZnO and BaO, were present in small amounts in one batch while traces of them are not found in the other batch.

Table 3.3: Compositions of the samples containing slag, expressed in wt% and mol%.

Sample:	60KPO ₃ - 20slag- 20Al ₂ O ₃		70KPO ₃ - 15slag- 15Al ₂ O ₃		50KPO ₃ - 15Slag- 15Al ₂ O ₃ - 20B ₂ O ₃		75KPO ₃ - 12.5slag- 12.5Al ₂ O ₃ 1150C		75KPO ₃ - 12.5slag- 12.5Al ₂ O ₃ 1250C	
	wt%	mol%	wt%	mol%	wt%	mol%	wt%	mol%	wt%	mol%
SiO ₂	7.48	12.06	5.19	8.78	5.49	8.15	4.46	7.81	4.29	7.53
B ₂ O ₃					17.77	22.79				
Al ₂ O ₃	18.95	18.01	17.58	17.52	22.50	19.71	14.39	14.86	14.68	15.19
Na ₂ O	0.06	0.10	0.05	0.09	0.06	0.09			0.05	0.09
K ₂ O	26.65	27.42	28.40	30.63	21.18	20.08	28.98	32.39	29.83	33.42
MgO	1.70	4.08	1.22	3.07	1.26	2.80	0.98	2.56	1.02	2.68
CaO	7.87	13.60	5.85	10.59	6.52	10.39	4.71	8.84	4.89	9.21
SrO	0.01	0.01	0.01	0.01	0.01	0.01	0.01	0.01	0.01	0.01
BaO	0.03	0.02			0.03	0.02	0.32	0.22	0.30	0.20
ZrO ₂	0.01	0.01	0.14	0.12	0.01	0.01	0.01	0.01	0.01	0.01
ZnO	0.09	0.10					0.09	0.12		
F							0.34	1.87		
Cl							0.02	0.05		
TiO ₂	0.21	0.26	0.17	0.22	0.18	0.20	0.15	0.19	0.14	0.18
MnO	0.06	0.09	0.04	0.06	0.05	0.06	0.04	0.06	0.04	0.06
SO ₃	0.08	0.10	0.06	0.08	0.02	0.02	0.04	0.04	0.03	0.04
Fe ₂ O ₃	0.15	0.09	0.11	0.07	0.12	0.07	0.12	0.08	0.10	0.06
P ₂ O ₅	35.19	24.02	40.17	28.74	24.77	15.58	41.61	30.86	42.10	31.30
I			0.02	0.02						
NiO	0.01	0.01	0.01	0.01	0.01	0.01	0.01	0.01	0.01	0.02

Table 3.4: Differences in the compositions of samples from different batches.

Compound	Batch 1 (wt%)	Batch 2 (wt%)	Absolute difference(%)
P ₂ O ₅	35.19	41.69	18%
K ₂ O	26.65	22.4	16%
Al ₂ O ₃	18.95	18.69	1%
SiO ₂	7.48	7.77	4%
CaO	7.87	7.01	11%
MgO	1.7	1.64	4%
Fe ₂ O ₃	0.15	0.11	27%
SO ₃	0.08	0.12	50%
Na ₂ O	0.06	0.11	83%
TiO ₂	0.21	0.22	5%
ZrO ₂	0.01	0.14	1300%
MnO	0.06	0.07	17%
ZnO	0.09	-	-
SrO	0.01	0.01	0%
BaO	0.04	-	-

3.4. CRYSTALLINITY OF THE SAMPLE

IN order to confirm the presence of an amorphous structure, the samples containing the most waste materials had their structures analyzed by X-ray diffraction (XRD). This analysis confirmed the amorphous character of the samples by showing the large hump in their XRD patterns characteristic of amorphous materials, as can be observed in Figures 3.8 and 3.9.

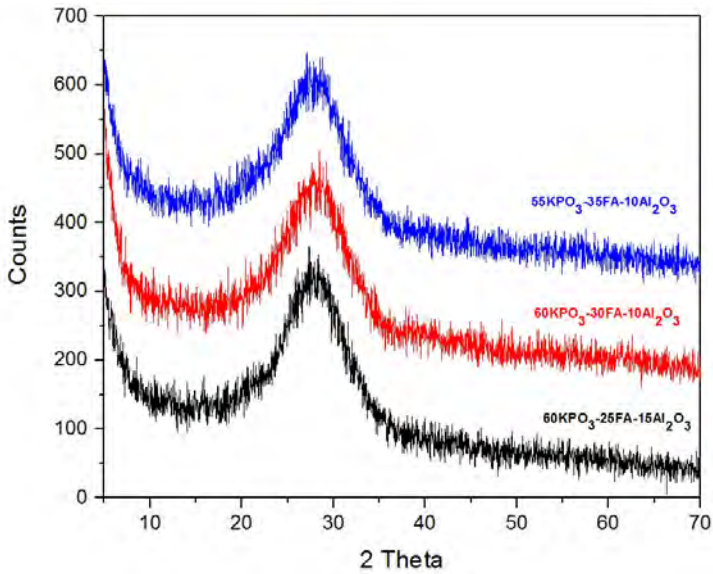


Figure 3.8: X-ray diffraction pattern of the samples with a high concentration of fly ash.

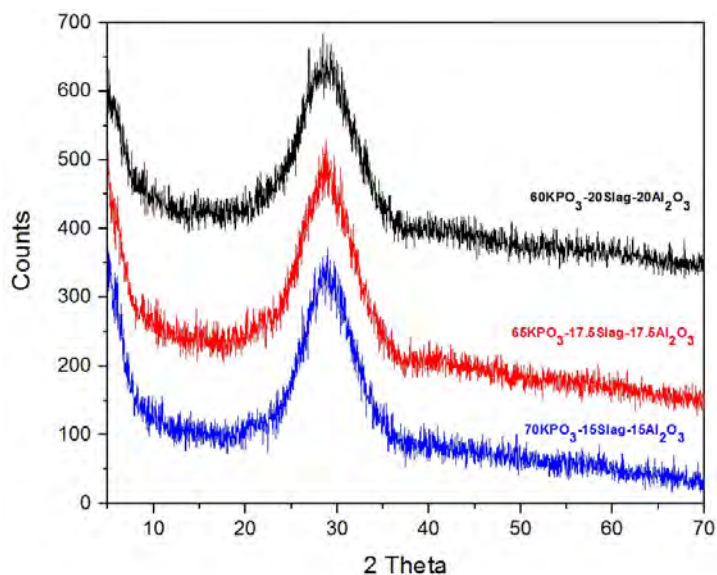


Figure 3.9: X-ray diffraction pattern of the samples with a high concentration of slag.

The samples containing 20% of B_2O_3 also had their structures analyzed by XRD, which proved that they are both amorphous, as shown in Figures 3.10 and 3.11.

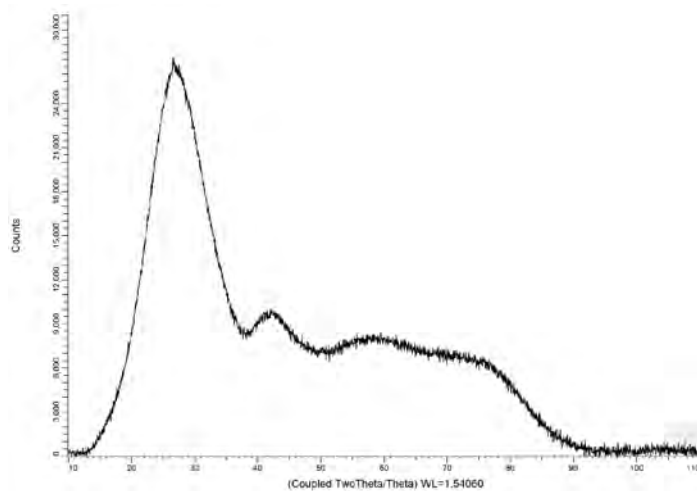


Figure 3.10: X-ray diffraction pattern of the sample $40\text{KPO}_3\text{-}25\text{FA-}15\text{Al}_2\text{O}_3\text{-}20\text{B}_2\text{O}_3$

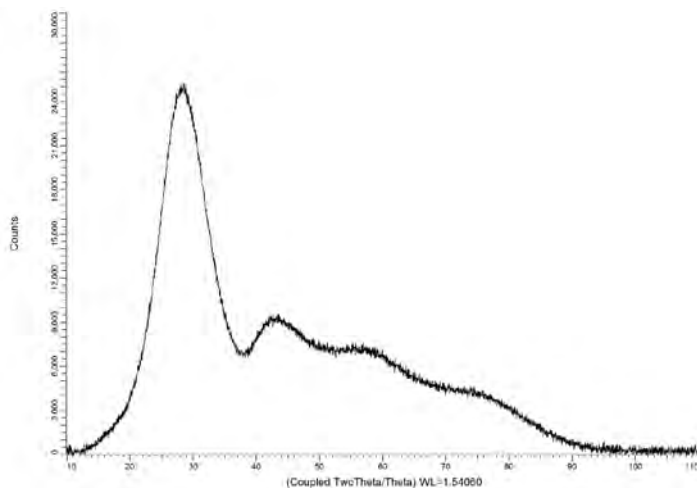


Figure 3.11: X-ray diffraction pattern of the sample 50KPO₃-15Slag-15Al₂O₃-20B₂O₃.

3.5. CHEMICAL DURABILITY

IN the past, the low chemical durability of phosphate glass limited its practical application. The term “chemical durability” has been commonly used to indicate the resistance offered by a glass type towards attack by aqueous solutions and atmospheric agents [15]. Nowadays, it is known that the addition of some elements to phosphate glass helps overcome this drawback, resulting in high chemical durability. For this reason, it is important to measure the chemical durability of the samples and how the introduction of different elements affects this property. Existing literature suggests that the incorporation of Al₂O₃ is linked to higher chemical durability in the samples [16]. This conclusion is reinforced by the water resistance tests conducted in this study.

There is no absolute measure of chemical durability and glass types are generally graded relative to one another after subjecting them to similar experimental conditions, i.e. the nature of the experiment usually determines the relative order or durability. On the one hand, accelerated tests can be performed in a controlled environment, however, the validity of the experiment can be compromised by not reflecting real-life conditions. On the other hand, long-term tests can be conducted, however, these present a challenge to continuity and experimental logistics. Long-term tests are generally conducted under a less controlled environment and are more representative of real conditions. Other test conditions can also change: the protocols (static or dynamic) and the sample preparation can be altered, while the glass itself can be tested as a whole article or as a powder. The MCC-1 static test is an example of a patterned test. It was developed as a standard leach test for nuclear waste forms and tests monolithic samples kept in PFA Teflon vessels under leaching solutions (deionized water, reference silicate solution or reference brine) for 28 days at 90 °C, 70 °C or 40 °C [17]. In our work, samples were tested statically and the tests did not follow a standard. The samples were tested under demineralized water and ambient temperature (around 20 °C) in plastic vessels (Figure 3.12).

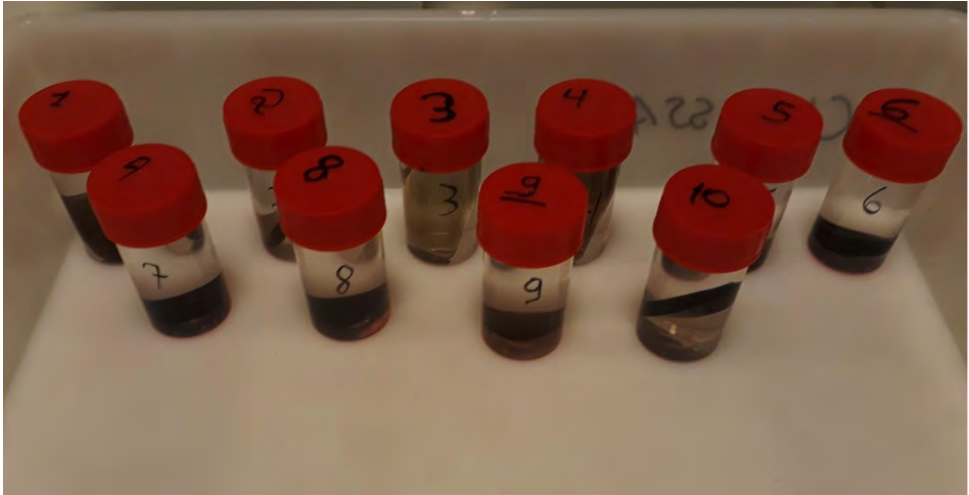


Figure 3.12: The samples were kept in plastic vessels under demineralized water and ambient temperature.

The results of the first tests (Series 1), in which samples were kept underwater for just 24 hours, can be found in Table 3.5. The results show the binary samples or ternary samples with a very low Al_2O_3 content had the lowest durability. At the end of the test, the binary samples containing 10% of slag or Al_2O_3 presented a total loss of their mass.

Table 3.5: Samples of series 1 that remained 24h under demineralized water.

Sample	Final Mass
*B270	100%
75KPO ₃ -12.5Slag-12.5Al ₂ O ₃	100%
77.5KPO ₃ -10Slag-12.5Al ₂ O ₃	100%
80KPO ₃ -10Slag-10Al ₂ O ₃	96.7%
80KPO ₃ -20Al ₂ O ₃	99.78%
85KPO ₃ -10Slag-5Al ₂ O ₃	42.59%
90KPO ₃ -10Slag	0%
90KPO ₃ -10Al ₂ O ₃	0%

*B270 is a commercial Borosilicate glass used here as a reference.

Concentrations of Al_2O_3 lower than 12.5% do not improve the chemical durability. Therefore, the Al_2O_3 was added to the samples in concentrations between 12.5% and 20%. These samples are labeled Series 2. The samples listed in Table 3.6 had their water resistance tested for a period longer than that of the first test. They were kept under demineralized water for 30 days without any mass loss. These glass types demonstrated high water resistance in relation to general phosphate glass types. As an example, the reported compositions 54.5P₂O₅-20.5K₂O-20.5Cs₂O-4.5Al₂O₃ and 50P₂O₅-16.7Na₂O-16.7K₂O-16.7Cs₂O respectively had a mass loss of 19.3% and 100% when dipped in water at 18 °C for 1 hour [16].

Table 3.6: Nominal compositions (weight %) of samples of series 2 that remained under demineralized water for 30 days with no mass loss.

KPO ₃	Fly Ash	Slag	Al ₂ O ₃	B ₂ O ₃
60	25	-	15	-
70	15	-	15	-
75	12.5	-	12.5	-
60	20	-	20	-
55	35	-	10	-
65	20	-	15	-
60	30	-	10	-
70	-	15	15	-
60	-	20	20	-
65	-	17.5	17.5	-
40	25	-	15	20
50	25	-	15	10
60	-	15	15	10
50	-	15	15	20

Phosphate glass types typically have poor water durability due to the presence of easily hydrated phosphate chains. However, current studies have shown it is possible to develop phosphate glass types with excellent resistance to aqueous corrosion by incorporating metal oxides with high valence cations like Fe₂O₃, Al₂O₃, etc. This process also results in a significant increase of the T_g. The rate at which phosphate-based glass types hydrolyze varies broadly [18]. Sodium phosphate glass types deteriorate within hours, while high iron content phosphate glass types have dissolution rates even slower than that of window glass [14]. The addition of iron or aluminum oxide to phosphate glass is known to result in a lower dissolution rate, increasing its chemical durability. In iron phosphate glass, the increase in chemical durability has been attributed to the formation of Fe-O-P type bonds in the glass structure at the expense of the more easily hydrated P-O-P bonds [19].

When alkali and alkaline-earth phosphate glasses are in contact with aqueous solutions, phosphate anions are quickly hydrated and dissolve into the solution. For instance, the structure of alkali metaphosphate (50 mol% alkali oxide, 50 mol% P₂O₅) glass, like KPO₃ or NaPO₃, is formed by Q² linkages, in which each bridging oxygen bond strength is 1.0 valence units (VU), and each nonbridging oxygen bond strength is 1.5 VU [20]. Therefore, the remaining charge on the nonbridging oxygen is compensated by neighboring alkali ions. The originated chainlike phosphate structures produce glass vulnerable to aqueous attack. The water resistance of these glasses can be improved by the addition of Al₂O₃ which cross-links neighboring phosphate anions with more hydration-resistant Al-O-P bonds. The Al³⁺ ions are included into phosphate glasses with 4-, 5- and 6-coordination, depending on composition [21]. The Al³⁺ is responsible for 0.75 UV, and the P⁵⁺ tetrahedron supplies 1.25 VU to fill the formal charge on the oxygen in each Al-O-P bond, as in the case for crystalline AlPO₄. Nonetheless, Al(4) is not favored in most aluminophosphate glasses. Previous studies confirm that Al(6) prevails

in the glass structure when up to 15 mol% Al_2O_3 is added to NaPO_3 and tetrahedral Al are formed at higher amounts of Al_2O_3 [20].

The addition of B_2O_3 to phosphate glass improves not only chemical durability, but also the thermal and mechanical stability of pure phosphate glass. In contrast to the PO_4 tetrahedra linked through covalent bridging oxygens which form a network of pure phosphate glass, the basic units of pure borate glass are trigonal BO_3 glass types [22]. The increase in the chemical durability as the B_2O_3 content is increased is associated to the replacement of the P-O-P bonds by P-O-B bonds generally forming a BPO_4 tetrahedral structure, which possesses a highly cross-linked structure. As in the case of the Al_2O_3 , it is also accompanied by an increase in T_g [22]. This is in accordance with the higher strength of the chemical bonds in the diatomic molecules of B-O (808 KJ/mol), compared to P-O (599.1KJ/mol) [23]. Due to this increase in the strength of the bonds, it is also expected that the addition of B_2O_3 will decrease the thermal expansion coefficient of the glass.

Previous studies have proven that phosphorous pentoxide (P_2O_5) content and O/P ratio exhibit a strong correlation to weight loss in water. It is assumed that the corrosion of phosphate glasses takes place by decomposition of phosphorous pentoxide in water. According to some studies, the ideal O/P ratio is 3.76 (Figure 3.13), which corresponds to the optimum phosphorous pentoxide percentage of 33 mol% in terms of durability [24]. According to other authors, the ideal rate is closer to 3.5 [25], corresponding to the structure Q1 in which there is one oxygen bridging two PO_4 tetrahedra.

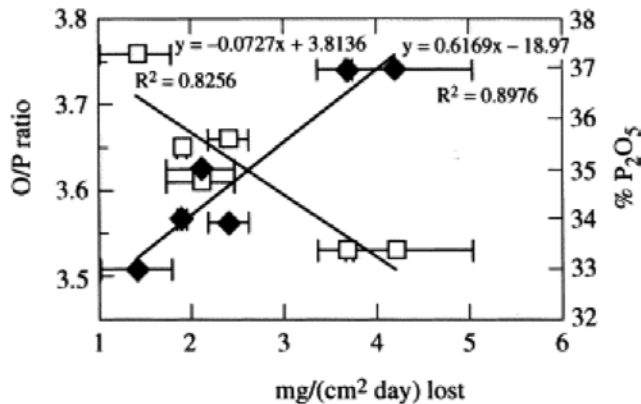


Figure 3.13: Phosphorus pentoxide and O/P ratio versus durability [24].

High contents of both network intermediates (Al_2O_3 , B_2O_3 , ZnO) and modifiers (Na_2O , K_2O , CaO) produce shorter polyphosphate chains that are terminated by Q^1 tetrahedra. This is because the modifiers offer enough non-bridging oxygen molecules for the glass network while the intermediates act as glass network formers, decreasing the real O/P ratio and developing a Q^1 structure.

3.6. DISCUSSION AND CONCLUSIONS

THE choice of the element used as glass former is the first step in designing a glass composition. Phosphate glasses possess relatively low working temperatures, low liquidus viscosity, high UV transparency and high solubility for other glass modifiers or intermediaries. For this reason, phosphate was used as a glass former in this study. The compound KPO_3 was chosen as the phosphate source. Like other alkali metal ions, Potassium can be incorporated between the chains, each formed from PO_4 tetrahedron. Alkali metal ions have a small electric field intensity and a small electronegativity. Consequently, the bonding strength between the alkali metal ion and an oxygen ion is small, while linear chains formed from PO_4 tetrahedra can be connected to each other by weak bonding strength through alkali metal ions [16]. The effect of these weak bonds is reflected in the low melting temperature of the glass, but also in its poor chemical durability.

Since binary alkali phosphate glasses have poor chemical durability, it is necessary to add more elements into the formula of the glass, namely, polyvalent element oxides. Cations of polyvalent elements can inhibit the penetration of water into a glass structure by increasing the bonding strength between the chains of a metaphosphate glass [16]. Among the polyvalent element oxides, there are divalent elements, which can improve water resistance to a certain extent, as they have a relatively small electric field intensity and electronegativity and have a relatively small bonding strength compared to an oxygen ion. Among these oxides, there is MgO and CaO, present in higher amounts in the compositions containing slag than in the ones containing fly ash (Tables 3.2 and 3.3). The concentration of MgO in these glasses varied between 2.5% and 4.1% in mol, while the concentration of CaO ranged from 8.8% to 13.6% in mol.

Other oxides, such as B_2O_3 , Al_2O_3 and Fe_2O_3 , are more present in higher concentrations in the glass containing fly ash than in the ones containing slag (Tables 3.2 and 3.3). This glass contained between 14-21 mol% of SiO_2 , 19-24 mol% of Al_2O_3 and 0.8-1.4 mol% of B_2O_3 . The oxides mentioned above contain cations that form a crosslinking structure between those and a phosphorous ion through an oxygen ion [16]. They are able to improve the water resistance more than the divalent elements. Both slag and fly ash proved to be great and inexpensive sources of polyvalent element oxides. As materials, they are cheap in relation to pure oxides, as they are by-products. Therefore, the price per kg glass decreases as the waste % increases, which replaces K_2O and P_2O_5 , incorporated directly as KPO_3 .

In most of these compositions, P_2O_5 is the main compound, the glass former. Thus its concentration should be significant for building the network of the glass structure. However, phosphorous pentoxide decomposes in water and its content has a strong relation to weight loss of glass in water, as previously indicated in the literature [24] and reinforced by the water resistance tests conducted in this work. Finding a concentration of P_2O_5 low enough to produce a durable material but high enough to build the required glass network was the key. It is clear that the replacement of KPO_3 by Al_2O_3 and other polyvalent element oxides can increase the degree of polymerization of the network. The ideal O/P ratio of 3.76 corresponds to the optimum phosphorous pentoxide percentage in terms of durability, corresponding to the structure Q^1 in which there is one oxygen bridging two PO_4 tetrahedra [24]. As shown in Table 3.7 and calculated in Appendix B,

all the samples produced in this work had a O/P ratio higher than 3.76. Most of the compositions have O/P ratio < 5.

Table 3.7: The O/P ratio of different compositions.

Compositions	60KPO ₃ - 20slag- 20Al ₂ O ₃ (mol%)	70KPO ₃ - 15slag- 15Al ₂ O ₃ (mol%)	50KPO ₃ - 15Slag- 15Al ₂ O ₃ - 20B ₂ O ₃ (mol%)	75KPO ₃ - 12.5slag- 12.5Al ₂ O ₃ 1150C (mol%)	75KPO ₃ - 12.5slag- 12.5Al ₂ O ₃ 1250C (mol%)	70KPO ₃ - 15FA- 20Al ₂ O ₃ (mol%)	60KPO ₃ - 20FA- 20Al ₂ O ₃ (mol%)	40KPO ₃ - 25FA- 15Al ₂ O ₃ - 20B ₂ O ₃ (mol%)
O/P ratio	5.09	4.51	8.21	4.20	4.21	4.73	5.16	7.85

For O/P ratios lower than 3.5 (Q¹ -pyrophosphate), aluminium is assumed as predominantly six-coordinated and completely fully linked to phosphorus (Al(OP)₆ sites). When the O/P ratio gets close to 4, an important structural transformation takes place, with the appearance of additional four- and five-coordinated aluminum species whose second coordination spheres are also entirely dominated by phosphorus [26]. Glasses with an O/P ratio of exactly 4.0 (Q⁰-orthophosphate) have a structure dominated by Al(OP)₄ units. Figure 3.14 illustrates an expected fragment of the network organization in high alumina glasses.

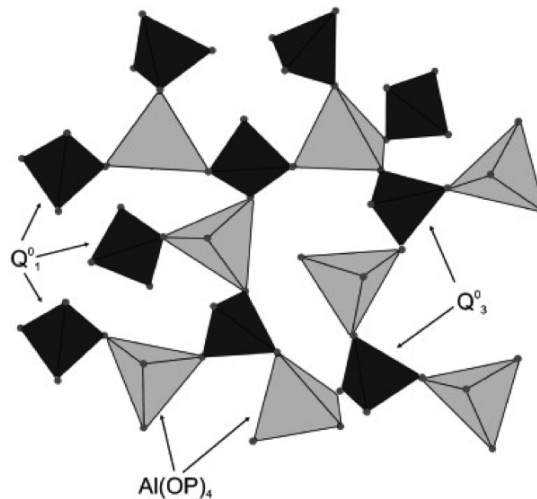


Figure 3.14: Network organization for the high alumina glasses exhibiting Q⁰₃, AlO₄ and Al(OP)₄ as the dominating structural motifs on intermediate length scales [27].

As the O/P ratio increases beyond 4.0, the average extent of Al-O-P connectivity is decreased significantly. Here, new types of five- and six-coordinated aluminum units, which are only weakly connected to phosphorus, are formed, while the network modifier is attracted mainly by the phosphate units [28]. This is probably the structure of most of the glasses obtained in this work, possessing O/P ratios between 4.2 and 5.16.

The glasses containing 20% of B₂O₃ have a O/P ratio higher than all the other compositions. The main components of the sample 50KPO₃-15Slag-15Al₂O₃-20B₂O₃ are B₂O₃

and Al_2O_3 . Both $[\text{BO}_3]$ triangles and $[\text{BO}_4]$ tetrahedron are expected to be present in the structure of this glass [28]. It is suggested that the promotion of the $\text{B}_2\text{O}_3/\text{Al}_2\text{O}_3$ ratio, which for this sample is 1.16, helps in a gradual conversion of $[\text{BO}_4]$ to $[\text{BO}_3]$ units and the formation of boron–oxygen rings. Consequently, this could produce a larger number of bridge oxygen and a lower number of non-bridge oxygen in the network of the glasses, increasing the continuity of the glass network [28]. The sample 40KPO₃-25FA-15Al₂O₃-20B₂O₃ is an admixture of high amounts of different glass formers. B₂O₃ is a well-known glass former, probably also participates in the glass network with triangular boron oxygen units mostly condensed as boroxol rings. A part of the boron transforms into tetrahedral co-ordination in the presence of other glass formers and modifiers. The glass network of such a glass, containing high amounts of B₂O₃, Al₂O₃, SiO₂ and P₂O₅, is probably composed of three dimensional aluminoborate, alumino phosphate and alumino silicate structural units [29]. The confirmation of the structure of the glasses and a deeper understanding of their network can be achieved using techniques such as solid-state nuclear magnetic resonance (NMR). This kind of investigation can determine, for instance, in which coordination (4-,5- or 6-) the Al⁺³ ions are incorporated into the phosphate glass, clarifying the distributions of the diverse Al and P anions.

Glass formation results when the liquid is restrained by an internal structure able to prevent the nucleation and the growth of nuclei into crystals. The diffractograms of the sample developed in this work demonstrated a lack of crystals in their structures, proving the predominance of amorphous structures. The achievement of durable and amorphous samples circumvents two challenges: the poor chemical durability of phosphate glasses and the high tendency to crystallize presented by fly ash and slag.

The achievement of durable glass is closely related to the development of compositions in which the networks are higher polymerized than pure phosphate glass. Nevertheless, this change in the connectivity does not only influence chemical durability. In the following chapters, the relation between the composition of the samples and properties like glass transition temperature and thermal expansion coefficient will be discussed.

REFERENCES

- [1] Hoornweg, D., Bhada-Tata, P., Kenney, C.A. (2015). Peak Waste: When Is It Likely to Occur?. *Journal of Industrial Ecology*, 19: p. 117–128.
- [2] Zhang, J., Dong, W., Li, L., Qiao, L., Zheng, J., Sheng, J. (2007). Utilization of coal fly ash in the glass–ceramic production. *Journal of Hazardous Materials*. v. 149, Issue 2, p. 523-526.
- [3] Dhoble, Y.N., Ahmed, S. (2018). Review on the innovative uses of steel slag for waste minimization. *Journal of Material Cycles and Waste Management*. v. 20, Issue 3, p. 1373-1382.
- [4] Karamanova, E., Avdeev, G., Karamanov, A. (2011). Ceramics from blast furnace slag, kaolin and quartz. *Journal of the European Ceramic Society*. v.31, Issue 6, p. 989-998.
- [5] Zschimmer, E. (2013). *Chemical technology of glass*. Sheffield: Society of Glass Technology.
- [6] Van Wazer, J.R. (1958). *Phosphorus and its compounds*. Vol.1, New York, Interscience Publishers.

- [7] Sales, B.C., Boatner, L.A. (1984). Lead-Iron Phosphate Glass: A Stable Storage Medium for High-Level Nuclear Waste. *Science*, 226 (4670), p. 45-48.
- [8] Almeida, F.J.M. (2006). Obtenção de vidros fosfatos contendo ferro por meio do aquecimento em fornos de micro-ondas (Master's thesis). Retrieved from the database of Universidade de São Paulo (USP).
- [9] Brow, R.K. (2000). Review: the structure of simple phosphate-glasses. *Journal of Non-Crystalline Solids*. 263–264 (1), p. 1-28.
- [10] Karabulut, M., Metwalli, E., Day, D.E., Brow, R.K. (2003). Mossbauer and IR investigations of iron ultraphosphate glasses. *Journal of Non-Crystalline Solids*. v. 328 p. 199–206.
- [11] Mauro, J.C. (2017). Decoding the glass genome. *Current Opinion in Solid State & Materials Science*. v. 22, Issue 2, p. 58-64.
- [12] Poirier, G., Messadeq, Y., Ribeiro, S.J.L., Poulain, M. (2005). Structural study of tungstate fluorophosphate glasses by Raman and X-ray absorption spectroscopy. *Journal of Solid State Chemistry*, v. 178, p. 1533-1538.
- [13] de Lima, C.L.J., Pastena, B., Nardi, R.P.R.D., Gouvea Junior, J.T., Ferrari, J.L., Casanjes, F.C., Poirier, G. (2015). Thermal, structural and crystallization study of niobium potassium phosphate glasses. *Materials Research*. p. 13-16.
- [14] Parsons A.J., Burling L.D., Rudd C.D., Scotchford C.A., Walker G.S. (2004). The effect of production regime and crucible materials on the thermal properties of sodium phosphate glasses produced from salts. *Journal of biomedical materials research*. Part B, *Applied biomaterials*, 71(B), p.22–29.
- [15] Paul, A. (1982). *Chemical Durability of Glass*. Chemistry of Glasses, Springer. p. 108-147.
- [16] Inaba, S. (2016). United States patent application publication. Anisotropic glass. Pub. No.: US 2016/0362328A1.
- [17] Strachan, D.M., Turcotte, R.P., Barnes, B.O.(1982). MCC-1: A Standard leach test for nuclear waste forms, *Nuclear Technology*, v.56, Issue 2, p. 306-312.
- [18] Zhang, B., Chen, Q., Song, L., Li, H.P., Hou, F.Z., Zhang, J.C. (2008). Fabrication and properties of novel low-melting glasses in the ternary system $ZnO-Sb_2O_3-P_2O_5$. *Journal of Non-Crystalline Solids*, 354, p. 1948-1954.
- [19] Karabulut, M., Melnik, E., Stefan, R., Marasinghe, G.K., Ray, C.S., Kurkjian, C.R., Day, D.E. (2001). Mechanical and structural properties of phosphate glasses. *Journal of Non-Crystalline Solids*, 288, p. 8-17
- [20] Brow, R.K., Kirkpatrick, R.J., Turner, G.L. (1993). Nature of alumina in phosphate glass: II, structure of sodium aluminophosphate glass. *Journal of the American Ceramic Society*. p.919-928.
- [21] Metwalli, E., Brow, R.K., Stover, F.S. (2001). Cation Effects on Anion Distributions in Aluminophosphate Glasses. *Journal of the American Ceramic Society*, 84, p. 1025-1032.
- [22] Kim, N.J., Im, S.H., Kim, D.H., Yoon, D.K., Ryu, B.K. (2010). Structure and properties of borophosphate glasses. *Electronic Materials Letters*, 6, p. 103-106.
- [23] Lide, D.R. (2001). *CRC Handbook of Chemistry and Physics*, CRC Press, Boca Raton.
- [24] Marino, A.E., Arrasmith, S.R., Gregg, L.L., Jacobs, S.D., Chen, G., Duc, Y. (2001). Durable phosphate glasses with lower transition temperatures. *Journal of Non-Crystalline Solids*, 289, p. 37-41.

- [25] Day, D.E., Wu, Z., Ray, C.S., Hrma, P. (1998). Chemically Durable Iron Phosphate Glass Waste Forms. *Journal of Non-Crystalline Solids* 241(1): p.1-12.
- [26] Zhang, L., Eckert, H. (2006). Short- and medium-range order in sodium aluminophosphate glasses: new insights from high-resolution dipolar solid-state NMR spectroscopy. *Journal of Physical Chemistry B*. 110 (18), p. 8946–8958.
- [27] Wegner, S., van Wüllen, L., Tricott, G. (2008). The structure of aluminophosphate glasses revisited: application of modern solid state NMR strategies to determine structural motifs on intermediate length scales. *Journal of Non-Crystalline solids*, 354. p. 1703-1714.
- [28] Cheng, Y., Xiao, H., Shuguang, C., Tang, B. (2009). Structure and crystallization of $B_2O_3-Al_2O_3-SiO_2$ glasses. *Physica B: Condensed Matter*. v. 404. p. 1230-1234.
- [29] Jagan Mohini, G., Krishnamacharyulu, N., Sahaya Baskaran, G., Venkateswara Rao, P., Veeraiah, N. (2013). Studies on influence of aluminium ions on the bioactivity of $B_2O_3-SiO_2-P_2O_5-Na_2O-CaO$ glass system by means of spectroscopic studies. *Applied Surface Science*, 287. p. 46-53.

4

THERMAL, CRYSTALLIZATION AND COLORATION STUDIES OF THE GLASSES

The thermal characterization of different types of glass is an important tool to determine its characteristic temperatures and the thermal stability against crystallization. In this work, thermal characterization was performed using the differential scanning calorimetry (DSC) technique and this showed that different compositions generate different thermal behaviors. The variation of compositions also produces different types of glass in a wide range of colorations. Samples containing slag are blue, amber or dark brown, while samples containing fly ash are yellow or green. In order to clarify the origin of coloration of these materials, they were characterized using optical spectroscopy (UV-Vis) and mass spectrometry coupled with thermogravimetric analysis (TGA). The combination of these results with the chemical compositions, deduced from X-ray fluorescence (XRF), allowed a more advanced characterization of coloration. When the glass was produced again, this time in different melting conditions, the results showed that the melting temperature can drastically affect color. Besides a better understanding of the coloration mechanism, these results also helped overcome a major challenge: the production of transparent and colorless glass containing waste materials.

4.1. THERMAL ANALYSIS OF THE SAMPLES

THE DSC-measurements show heat flow (arbitrary units) versus temperature ($^{\circ}\text{C}$), allowing a comparison of characteristic temperatures for the different glass compositions. Experimental details can be found in Appendix A.

4.1.1. THERMAL ANALYSIS OF SAMPLES CONTAINING SLAG

FOR glass containing slag, measurements were taken from samples containing from 12.5% to 20 wt% of slag (Figure 4.1). Through DSC curves, it was possible to determine the characteristic temperatures of the samples. Based on these characteristic temperatures, it was also possible to determine the parameter of thermal stability of the systems, as shown in Table 4.1. This was achieved by comparing the T_g and T_x obtained for each sample. The level of thermal stability against crystallization marks the difference between the starting crystallization temperature and the glass transition temperature ($T_x - T_g$). Both temperatures were determined on the DSC curves using the tangent method. Sample 4 had the highest thermal stability against devitrification, a well-defined glass transition temperature, a sharp exothermic peak related to crystallization, and a sharp endothermic peak related to the melting of the crystalline phase. In samples containing higher amounts of slag and aluminum oxide (particularly samples 1 and 2), the thermal stability appeared to decrease. It was also difficult to precisely locate the transition temperature of these glasses, due to the variation in the slopes of the curves in a range of temperatures being relatively small. As expected, increasing amounts of slag and aluminum oxide tend to result in increased crystallization as reflected in the broadening of the crystallization peaks. The sample with the lowest amount of slag, 75KPO₃-12.5slag-12.5Al₂O₃, was the only sample exhibiting a thermal stability comparable to soda-lime glasses, which is approximately 110 $^{\circ}\text{C}$.

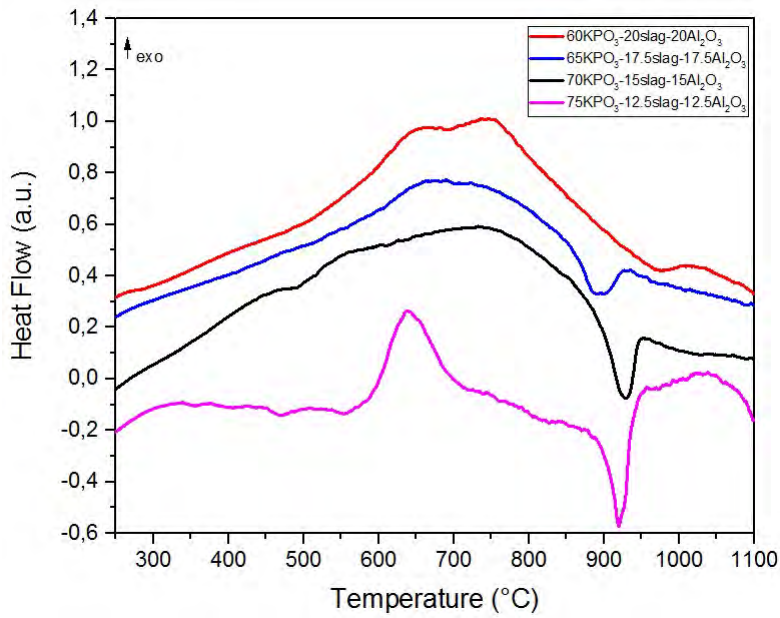


Figure 4.1: DSC curves of the glasses containing slag, in which the amount of slag ranges from 12.5% to 20% (wt).

Table 4.1: Characteristic temperatures and thermal stability of glasses containing slag.

Identification	Sample	T_g (°C)	T_x (°C)	$T_x - T_g$ (°C)
1	60KPO ₃ -20slag-20Al ₂ O ₃	490	526	36
2	65KPO ₃ -17.5slag-17.5Al ₂ O ₃	482	520	38
3	70KPO ₃ -15slag-15Al ₂ O ₃	453	520	67
4	75KPO ₃ -12.5slag-12.5Al ₂ O ₃	443	576	133

Two samples were produced with the addition of B_2O_3 : $60KPO_3-10B_2O_3-15slag-15Al_2O_3$ and $50KPO_3-20B_2O_3-15slag-15Al_2O_3$. While the sample containing 10% (wt) of B_2O_3 has a T_g of around $484^\circ C$ (Figure 4.2), the glass transition temperature of the sample with 20% of B_2O_3 is around $451^\circ C$. Besides decreasing the T_g , the addition of this oxide also decreases the tendency to crystallize. This can be inferred from the large exothermic peak observed around $790^\circ C$ for the sample with 10% B_2O_3 , which is not present in the sample containing 20% of the same oxide.

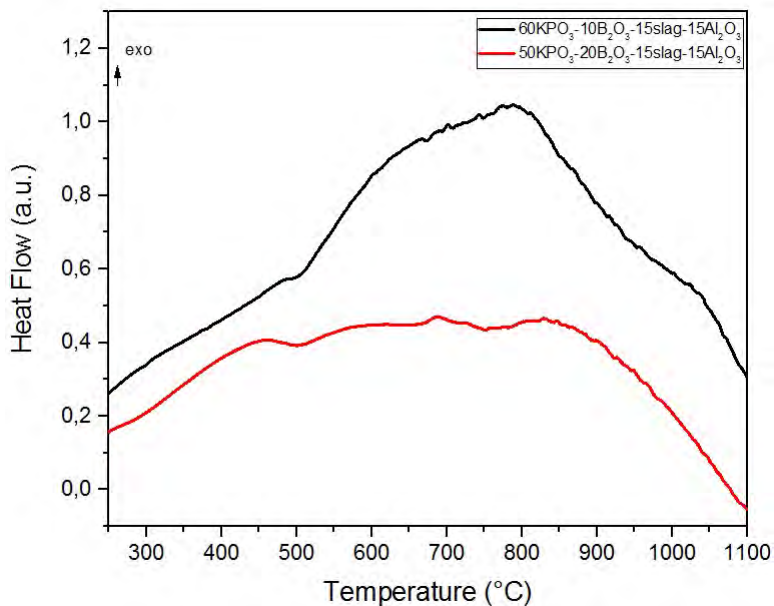


Figure 4.2: DSC curves of the glasses containing slag and B_2O_3 .

4.1.2. THERMAL ANALYSIS OF SAMPLES CONTAINING FLY ASH

THE DSC-curves of the samples containing from 12.5 to 35% of fly ash (Figure 4.3) show that higher concentrations of fly ash and Al_2O_3 correlate with an increase in glass transition temperatures. In addition, thermal stability decreases with increasing concentrations of fly ash (Table 4.2). As the enthalpy of a transition is derived from the area under its curve, the sample with the lowest amount of KPO_3 (Sample 1), shows the crystallization peak with the highest enthalpy. This tendency to crystallize goes with the high concentrations of different oxides present in this sample, due to it containing the highest concentrations of fly ash and aluminum oxide.

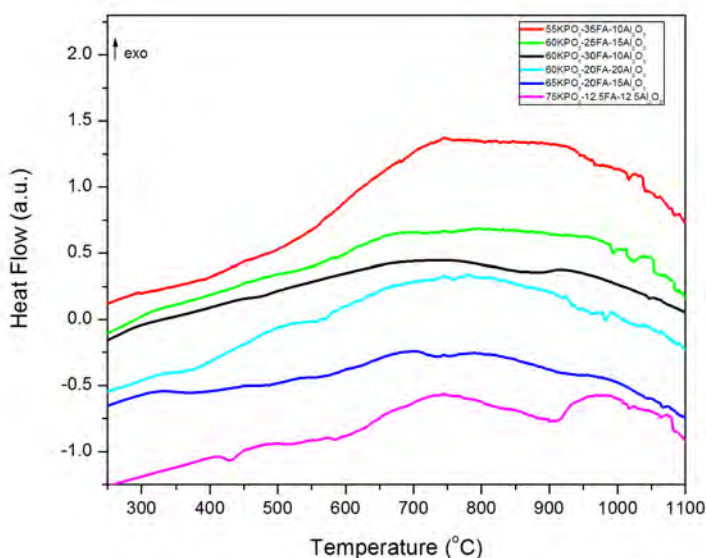


Figure 4.3: DSC curves of the glasses containing fly ash, in which the amount of fly ash ranges from 12.5% to 35% (wt).

Table 4.2: Characteristic temperatures and thermal stability of glasses containing fly ash.

Identification	Sample	T_g (°C)	T_x (°C)	$T_x - T_g$ (°C)
1	55 KPO_3 -35FA-10 Al_2O_3	456	510	54
2	60 KPO_3 -25FA-15 Al_2O_3	458	535	77
3	60 KPO_3 -30FA-10 Al_2O_3	460	530	70
4	60 KPO_3 -20FA-20 Al_2O_3	484	564	80

Two samples were produced with the addition of B_2O_3 : $50KPO_3-10B_2O_3-25fly\ ash-15Al_2O_3$ and $40KPO_3-20B_2O_3-25fly\ ash-15Al_2O_3$. There is a marginal decrease in T_g with the addition of B_2O_3 : the glass transition temperature of the sample with 10% (wt) of B_2O_3 is around $475\text{ }^\circ\text{C}$, while the sample containing 20% (wt) of the same oxide had a glass transition temperature of $472\text{ }^\circ\text{C}$. A meaningful change introduced by increasing the amount of B_2O_3 is the crystallization behavior of the sample. While the sample with the lowest amount of this oxide presents two following crystallization peaks (Figure 4.4), the first starting around $514\text{ }^\circ\text{C}$ and peaking around $650\text{ }^\circ\text{C}$ and the second one peaking around $860\text{ }^\circ\text{C}$, the sample containing 20% of B_2O_3 presents only one peak, starting around $640\text{ }^\circ\text{C}$ and peaking around $810\text{ }^\circ\text{C}$. Thus, the interval between the T_x and T_g is significantly higher for the sample with the highest amount of this oxide, showing that increasing the amount of B_2O_3 produces samples with a higher thermal stability against devitrification.

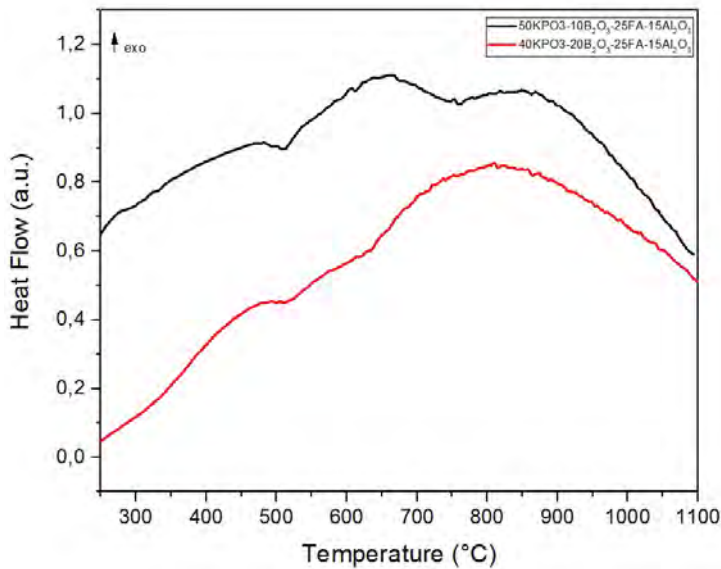


Figure 4.4: DSC curves of the glasses containing fly ash and B_2O_3 .

4.2. THERMAL ANALYSIS OF COMMERCIAL GLASSES

FIGURE 4.5 shows the DSC-curves of two standard glass types used for architectural engineering purposes. Soda-lime glass has a T_g around $560\text{ }^\circ\text{C}$, while B270 (a modified soda-lime glass) has a T_g of around $531\text{ }^\circ\text{C}$. This proves that the new glass compositions containing slag or fly ash have glass transition temperatures lower than the ones of commercial glass currently used for building purposes.

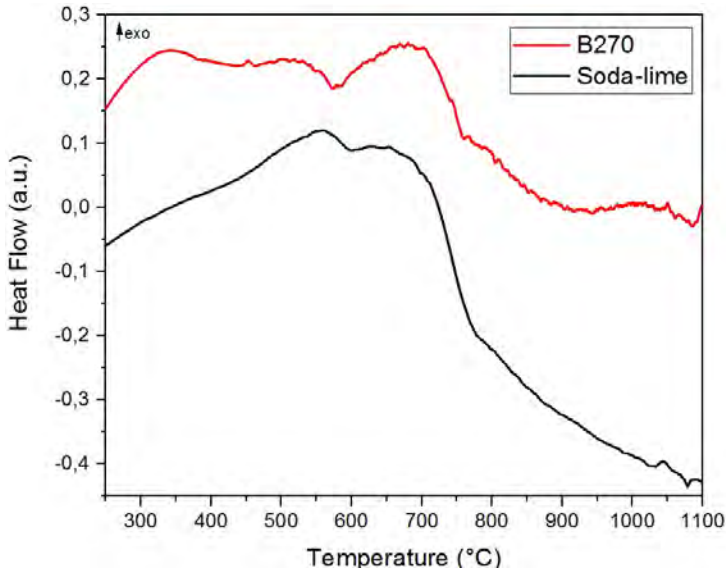


Figure 4.5: DSC curves of two commercial silicate glasses.

4.3. COLORATION OF SAMPLES

If a white beam of light falls on glass, it will transmit light in the same proportion of all the radiations of different wavelengths that make up the beam, making the glass colorless. However, if it absorbs light with unequal intensity and therefore transmit only certain wavelengths, the glass will become colorized as a result of the remaining spectral components that pass through it.

4.3.1. FACTORS DETERMINING THE COLOR OF A GLASS

GENERALLY, the main components of glass are colorless, therefore, it is necessary to add specific coloring agents to produce the desired coloration [1]. It is possible to classify the colored glasses based on the degree of dispersion of the chromophore groups responsible for the selective light absorption. These groups are listed in Table 4.3.

Table 4.3: Classification of chromophores according to their size in colored glasses (adapted from Fernández Navarro [1]).

Degree of division	State	Order of magnitude of the chromophore group	Examples
Ionic or molecular	Dissolution	1 nm	Fe^{2+} , Fe^{3+} , Co^{2+} , Ni^{2+} , Cr^{3+} , Cu^{2+}
Colloidal or microcrystalline	Colloidal or microcrystalline dispersion	1 nm-100 nm	Cu_2O , $\text{Cd}_{(x+y)}\text{S}_x\text{Se}_y$.
Coarse	Crystalline dispersion	>100 nm	Aventurine and hematite glasses (CuO , Cr_2O_3)

Most colored glass belongs to the group of the ionic dyes. In general, they are transition elements, such as iron. The iron present in a glass can be either intentionally added or can be the result of contamination, deriving from raw materials or from refractories. Iron might be present in different oxidation states, however, in phosphate glass, iron appears mainly in Fe(III) or (II) oxidation state. Both states are reported to be chiefly in tetrahedral and octahedral coordination sites [2].

It is not only the amount of a certain metal oxide that influences the color of a glass. The fractions of the metal ion's oxidation state (valence) and the stereochemistry (coordination) also affect it. Charge transfer transitions describe electronic transitions between different ions and may result in coloration if their absorption bands extend from the UV region (10-400 nm) to the visible region (400-750 nm) (Figure 4.6).

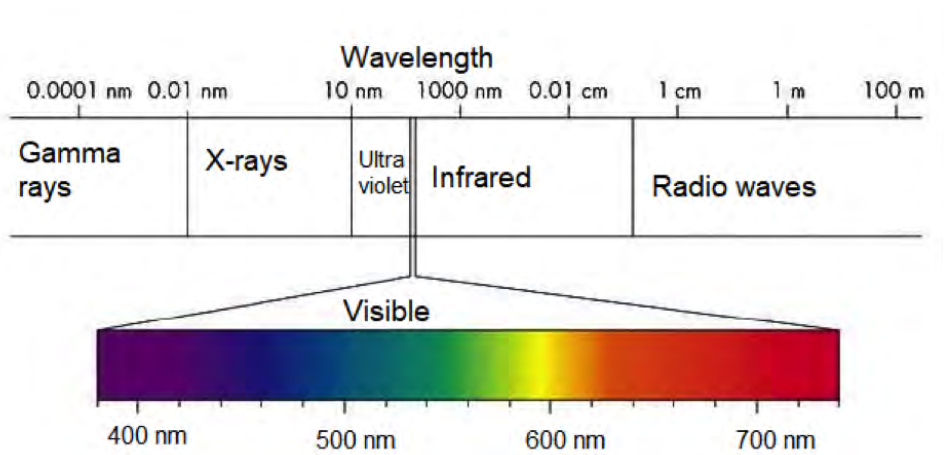


Figure 4.6: The electromagnetic spectrum with the visible region highlighted.

However, most colors are generated by the much weaker electronic transitions between the energy levels of the outer shell or valence electrons – in other words, between the d levels within a transition metal ion [3]. The energy of these weaker transitions can be inferred from the optical absorption spectra by application of the ligand field theory and allowing the computation of the energy levels of the five d orbitals of different symmetry, each of which can be occupied by two electrons of different spin. Usually, the coloring magnitude produced by the d electron transition metal ions, such as Co^{2+} , Cu^{2+} , Fe^{2+} , Fe^{3+} and Mn^{3+} , is various magnitudes lower than those of charge transfer (CT) transitions, as the ones taking place between sulphur and iron in the $[\text{Fe(III)SO}_3]$ -chromophore or of intervalence charge-transfer transitions (IV-CT) as between Fe^{2+} and Fe^{3+} . For this reason, CT transition can strongly affect the color of the glass, even if the concentration of the chromophores is in the order of ppm [3].

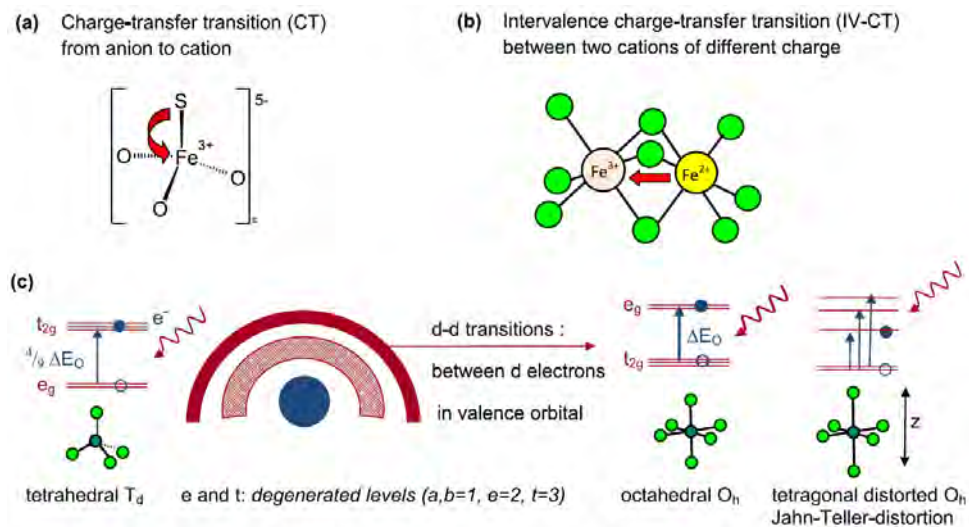


Figure 4.7: Different types of electronic transitions: a) the charge transfer transition in sulphur-amber, b) intervalence charge transfer transition between cations of different valence. c) d-d transitions for different coordinated complexes (adapted from Moncke et. al. [3]).

Optical spectroscopy is a non-destructive tool that can provide information on transition metal ions, mainly if combined with chemical analysis. The spectral transmission can be determined with a UV-VIS spectrophotometer, in which the light transmission is measured as a function of its wavelength. The intensity of transmitted light can be expressed as a percentage of its transmittance (% T) or absorbance (% A). If I_0 is the energy, or radiant power, which reaches the detector when there is no sample in the direction of the beam, and I is the energy detected in the presence of a sample, the transmittance is defined by the relation:

$$T = \frac{I}{I_0} \quad (4.1)$$

And the percentage of transmittance:

$$\%T = \frac{100I}{I_0} \quad (4.2)$$

The absorbance is:

$$A = \log\left(\frac{I_0}{I}\right) = \log\left(\frac{1}{T}\right) \quad (4.3)$$

Strong and weak bands are more easily visualized simultaneously without changing scale when spectra are represented as a function of the transmittance. This is because absorbance ranges from zero to infinity, while transmittance ranges from 0 to 100%T (0%T corresponding to an infinite absorbance). For quantitative analyses, absorbance, or some other scale of intensity proportional to concentration, should be used.

4.3.2. VISUAL ASPECT OF THE GLASSES CONTAINING WASTES AND THEIR MELTING CONDITIONS

TRANSPARENT samples containing slag were obtained with a maximum concentration of 15 wt% of this waste material. The samples consisting of 12.5 wt% of slag showed a blue coloration, while the ones consisting of 15% showed an amber coloration. It is also possible to obtain samples with a higher concentration of slag; however, they are not transparent. All the samples are illustrated in Figure 4.8.



Figure 4.8: The samples containing slag. From the left to the right: $77.5\text{KPO}_3\text{-}10\text{Slag-}12.5\text{Al}_2\text{O}_3$, $75\text{KPO}_3\text{-}12.5\text{Slag-}12.5\text{Al}_2\text{O}_3$, $70\text{KPO}_3\text{-}15\text{Slag-}15\text{Al}_2\text{O}_3$, $65\text{KPO}_3\text{-}17.5\text{Slag-}17.5\text{Al}_2\text{O}_3$, $65\text{KPO}_3\text{-}20\text{Slag-}15\text{Al}_2\text{O}_3$, $60\text{KPO}_3\text{-}20\text{Slag-}20\text{Al}_2\text{O}_3$.

The samples containing slag were very sensitive to certain melting conditions and small variations in composition. The sample consisting of 12.5% slag exhibits different colorations depending on the temperature at which it was melted. Melted at $1150\text{ }^\circ\text{C}$, the sample shows a homogeneous blue coloration. At $1250\text{ }^\circ\text{C}$ it is heterogeneous and reveals two different patterns of coloration: blue and colorless. At $1350\text{ }^\circ\text{C}$ the sample is homogeneous and colorless. The visual aspects of the sample melted at the three temperatures can be found in Figure 4.9.



Figure 4.9: Samples consisting of 12.5% slag melted at different temperatures: 1150 °C, 1250 °C, and 1350 °C, respectively.

The sample consisting of 15% slag is homogenous and has an amber coloration. Tests were made adding Boron oxide (B_2O_3) at the composition to decrease its thermal expansion. The introduction of 10% of B_2O_3 modified the visual aspect of the sample, which became heterogeneous and colorless with light yellow areas. The further addition of 10% B_2O_3 , (totaling 20%) generates two colorations, one colorless and one blue. The three samples are shown in Figure 4.10.



Figure 4.10: Samples consisting of 15% slag, without the addition of B_2O_3 , with the addition of 10% B_2O_3 and 20% B_2O_3 , respectively.

For the samples containing fly ash, transparent samples with a maximum concentration of 35% (wt) of fly ash were obtained. The samples consisting of 35% fly ash showed a green coloration and were produced at 1350 °C. The samples consisting of 15% fly ash

were yellow and can be produced at lower temperatures (1100 °C). Higher concentrations of fly ash made samples become darker, as illustrated in Figure 4.11, and also increased melting temperature. No tests were conducted for fly ash concentrations higher than 35%. It is likely to be possible to produce glass samples with higher concentrations of fly ash. However, the melting temperatures would exceed 1400 °C and the samples would present a very dark coloration.



Figure 4.11: The samples containing fly ash (FA) - From the left to the right: 75KPO₃-12.5FA-12.5Al₂O₃, 70KPO₃-15FA-15Al₂O₃, 65KPO₃-20FA-15Al₂O₃, 60KPO₃-20FA-20Al₂O₃, 60KPO₃-25FA-5Al₂O₃, 60KPO₃-30FA-10Al₂O₃, 55KPO₃-35FA-10Al₂O₃.

4.3.3. OPTICAL SPECTROSCOPY, MASS LOSS AND GAS RELEASE OF THE GLASSES

ULTRAVIOLET-VISIBLE (UV-Vis) spectroscopy and mass spectrometry coupled with thermogravimetric analysis (TGA) were conducted in order to understand the origin of the different colorations of the glasses.

MASS LOSS AND GAS RELEASE OF THE GLASSES CONTAINING SLAG

THE content of sulfur in slag is often expressed as SO₃, assuming a +6 oxidation state. Sulfur shows a broad spectrum of oxidation states, generally from -2 to +6. The actual speciation of sulphur in slag could clarify it. Some tools, as X-ray absorption near edge structure spectroscopy (XANES) could support this analysis. Some references indicate that the sulphur in an anhydrous GGBFS is generally found in reduced form [4]. The presence of reduced sulphur may give rise to coloration. The radical anions S₂⁻ (disulphur) and S₃⁻ (trisulphur) are known to be green and blue chromophores, respectively [4].

The redox state of a glass type can be inferred from the sulphate or sulphide residue in the glass, or by the ratio of ferrous/ferric iron (Fe²⁺/Fe³⁺). This redox state depends, among other aspects, on the redox state of the batch, affected by the presence of reducing agents or by the concentration of oxidants. Among the reducing agents, it is possible to mention carbon, sulphides, ferrous iron, organic contaminants and metals. As SO₃ was detected in the glass types containing slag in concentrations between 0.08 and 0.02% (wt) and the amount of Fe₂O₃ in these glass types is between 0.15 and 0.1% (wt), these compounds can produce a reduced melt. Besides the presence of reducing or oxidant agents, the maximum melting temperature of the batch also affects the redox state. Batches containing reducing components, such as the sulphide containing slag, are ex-

pected to release much more gaseous sulphur components in the temperature range of 900-1400 °C [5].

First, the samples containing slag were analyzed by TGA up to 1100 °C (Figure 4.12). The samples presented a minimum mass loss, the maximum loss found was of 1.35% (wt) for the sample $65\text{KPO}_3\text{-}17.5\text{slag-}17.5\text{Al}_2\text{O}_3$.

For the sample $75\text{KPO}_3\text{-}15\text{slag-}15\text{Al}_2\text{O}_3$, which produced an amber-colored glass, both thermogravimetric analysis and mass spectrometry were used to check levels of gas released. The gas released during glass melting can be caused by the decomposition of raw materials into carbonates, and via reactions of polyvalent species or coke during heating. Excessive gas evolution, combined with meta-stable bubbles, can produce foaming [6]. The main parameters defining the release of gases and foam formation are, according to Beerkens: oxidate state of the melt, water content in the melt (dissolved water), temperature of the melt and concentration of gas forming fining agent.

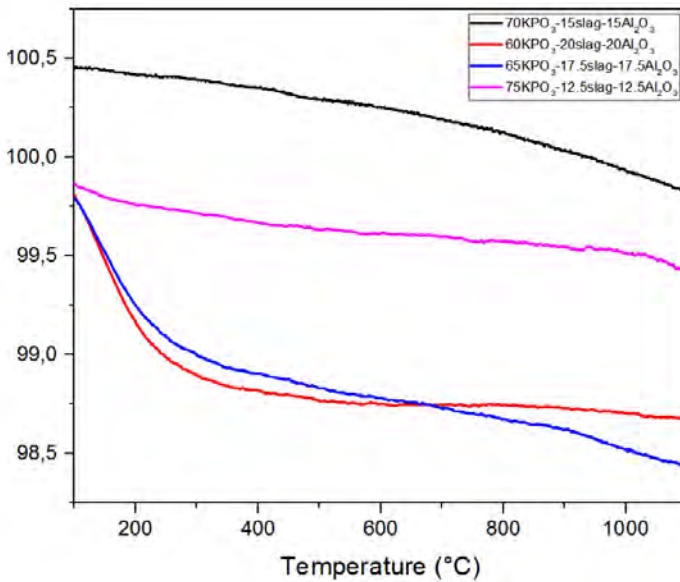


Figure 4.12: Mass loss of the glasses containing slag, in which the amount of slag ranges from 12.5% to 20% (wt).

Reducing components absorb oxygen from other compounds in the batch: polyvalent ions will be converted to their reduced forms. For instance, a ferric iron (Fe^{3+}) can be reduced to ferrous iron (Fe^{2+}). Sulphates (SO_4^{2-}) can react with a reductor to form sulphur dioxide (SO_2 , sulphur (S) or sulphides (S^{2-}). As the valency of polyvalent ions affects the transmission spectrum of the glass, as well as the presence of oxygen during the melting, the existence of reducing agents in the melting affects the rate of degassing and the color of the final product [5].

The sample $75\text{KPO}_3\text{-}15\text{slag-}15\text{Al}_2\text{O}_3$ was analyzed up to 1250°C . The analysis showed that mass loss increases above 1000°C , while at temperatures above 1200°C the amount of SO_2 released also increases (Figure 4.13).

The analysis of the sample $50\text{KPO}_3\text{-}15\text{slag-}15\text{Al}_2\text{O}_3\text{-}20\text{B}_2\text{O}_3$ was then performed at higher temperatures to check levels of gas release and mass loss up to 1400°C . Figure 4.14 shows a drastic mass loss after 1200°C . Between the start of the measurement and 1200°C only 0.5% of the mass of the sample was lost, but between 1200°C and 1400°C , around 5% of its mass is lost. At the same temperature at which this intensification occurs, there is a significant increase in the amount of SO_2 released. It can therefore be inferred that these two events are in some way connected.

In the neighborhood of reducing components, sulphur can be present in different states, but it is only stable in the melt as a sulphide or sulphate. In a reducing melt with ferrous iron as the reductor agent, a considerable part of sulphates will be released as SO_2 gas at high temperatures. The residual sulphate level in the glass tends to decrease by lowering the oxidation state of the batch until stringent reducing conditions are met. In adequate reducing environments, the redox state should allow the production of stable sulphides in the batch, leading to an increase of sulphur retention as sulphide. If some residual ferric iron is present in the batch, the amber chromophore can be formed during the cooling of the glass [5].

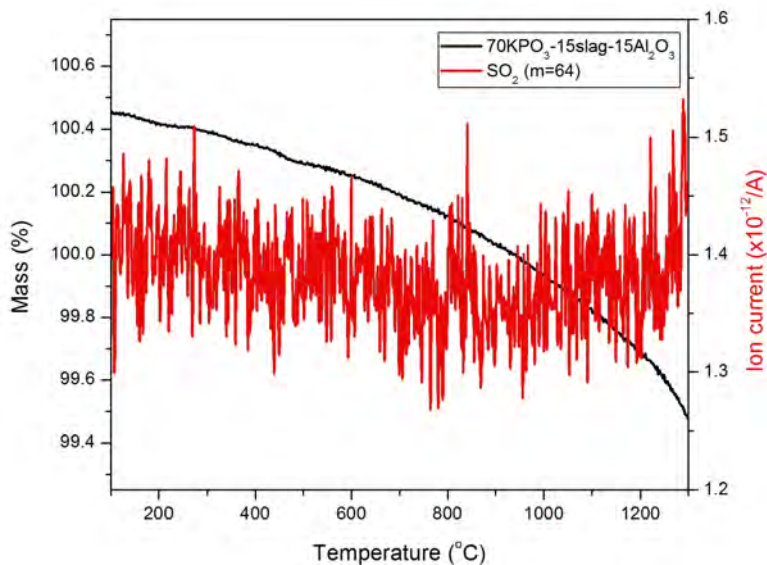


Figure 4.13: Mass loss and SO_2 release (TGA-MS) of the sample $75\text{KPO}_3\text{-}15\text{slag-}15\text{Al}_2\text{O}_3$.

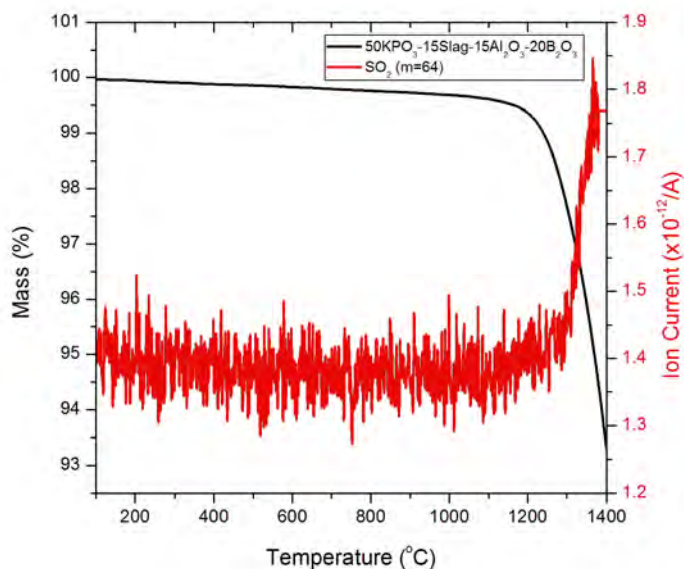


Figure 4.14: Mass loss and SO_2 release (TGA-MS) of the sample $50\text{KPO}_3\text{-}15\text{slag-}15\text{Al}_2\text{O}_3\text{-}20\text{B}_2\text{O}_3$.

OPTICAL SPECTROSCOPY AND GAS RELEASE OF THE GLASSES CONTAINING SLAG





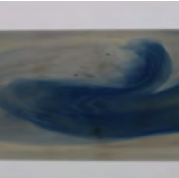
THE colors of all the samples containing slag are summarized in Table 4.4. The amber coloration of the sample $70\text{KPO}_3\text{-}15\text{slag-}15\text{Al}_2\text{O}_3$ connected to the interpretation of the absorption bands of its spectral transmission as determined by UV-Vis spectrophotometry (Figure 4.15) points to the presence of the amber chromophore. The S-Fe^{3+} charge transfer transitions absorbance typically peaks at 410nm in the visible part of the spectrum, and even traces of this complex results in significant coloration [3]. It is estimated that the onset of amber coloration is around a relative Fe^{2+} minimum concentration of 50% of the total iron ions, while best effects are originated at 70–90% of Fe^{2+} . The intensity of the amber absorption at 420 nm should be proportional to the product of the concentration of ferric ion and sulphide ion in the glass [7].

The sample consisting of 12.5% slag exhibits different colorations depending on the temperature at which it is melted. Melted at 1150 °C, the sample shows a homogeneous blue coloration. At 1250 °C, it is heterogeneous, showing two different patterns of coloration, blue and colorless. Comparing the bands of these two samples, the absorption band around 1100 nm related to Fe^{2+} is very similar, both for these two glass types and for the sample containing 20% B_2O_3 , which is also blue. These three blue glasses have also in common a strong absorption band around 580nm, which is probably related to the radical anion S_3^- (trisulfur).

The bright blue color of S_3^- is typically related to a visible absorption band in the range 595–620 nm [8]. This radical anion is present in the naturally occurring mineral lapis lazuli, from which the pigment ultramarine is derived [8]. It is suggested that for the

three samples showing an intense optical absorption at 580nm, mainly the composition containing 20% of B_2O_3 , the coloration is due to the optical absorption of S_3^- anions present in the space between the glass networks, a mechanism that can occur for some borosilicate glasses [9]. Comparing the two samples of composition $75KPO_3 - 12.5slag - 12.5Al_2O_3$, the absorption at 580nm is more intense for the sample melted at a lower temperature. The amount of sulphur in the sample decreases at higher temperatures due to the decomposition of sulphates, and for this reason the sample melted at $1250^\circ C$ shows a less intense band related to the trisulphur. It can be also noticed in the visual aspect of the samples, because the sample melted at $1150^\circ C$ is completely blue while the sample melted at $1250^\circ C$ is partially transparent. The sample containing 20% of B_2O_3 has undoubtedly the most intense absorption band at 580nm, and also the deepest blue color among all the samples.

Table 4.4: Colors of different glasses containing slag as glass beads of 3mm of thickness.

60KPO ₃ -20slag- 20Al ₂ O ₃	50KPO ₃ -20B ₂ O ₃ -15Slag- 15Al ₂ O ₃	70KPO ₃ -15slag- 15Al ₂ O ₃	75KPO ₃ -12.5slag- 12.5Al ₂ O ₃ 1150°C	75KPO ₃ -12.5slag- 12.5Al ₂ O ₃ 1250°C
				

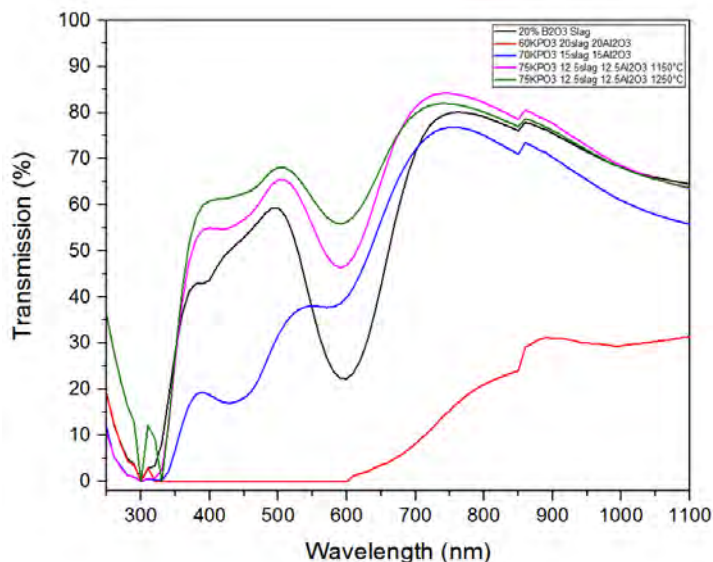


Figure 4.15: Optical spectra of samples containing slag.

The band probably related to the Fe^{3+} , appears around 380 nm for the sample containing B_2O_3 . This band appears at a higher wavelength for the sample containing 12.5% slag melted at 1150 °C and an even higher wavelength for the sample with the same composition but melted at 1250 °C. It is interesting to note that the band related to Fe^{3+} is much more intense for the sample containing 15% slag than any other sample, appearing around 440 nm. An intense band related to Fe^{2+} is also present in the same sample, at around 1100 nm. This corroborates the hypothesis that the formation of an amber chromophore is originating from S- Fe^{3+} charge transfer transitions. During the cooling of this sample, the ferrous iron (Fe^{2+}) probably reacts with sulphite (SO_3^{2-}), increasing the concentration of Fe^{3+} (ferric iron) and S^{2-} (sulphide). If both species coexist in the melt in reasonable proportions, the amber coloration is produced during the cooling. The sample 60KPO₃-20slag-20Al₂O₃ is very dark, absorbing much more light at all wavelengths than all the other samples.

MASS LOSS AND GAS RELEASE OF THE GLASSES CONTAINING FLY ASH

THE samples containing fly ash were analyzed by TGA up to 1100°C (Figure 4.16). The samples presented a low mass loss, the maximum loss found was 1.63% (wt) for the sample 65KPO₃-20FA-15Al₂O₃.

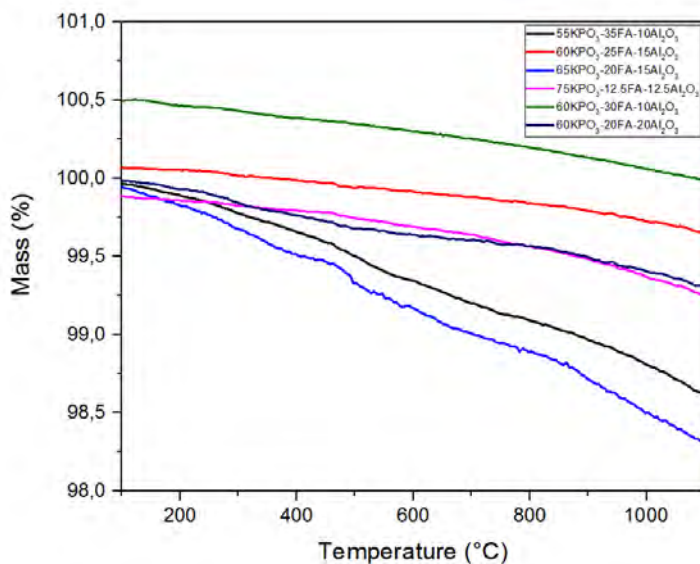


Figure 4.16: Mass loss of the glasses containing fly ash, in which the amount of fly ash ranges from 12.5% to 35% (wt).

The sample 60KPO₃-30FA-10Al₂O₃ was analyzed up to 1250°C. Levels of gas released were also measured. As in the samples containing slag, an increase in the release of SO₂ detected in temperatures around 1200°C was also noted in this sample (Figure 4.17).

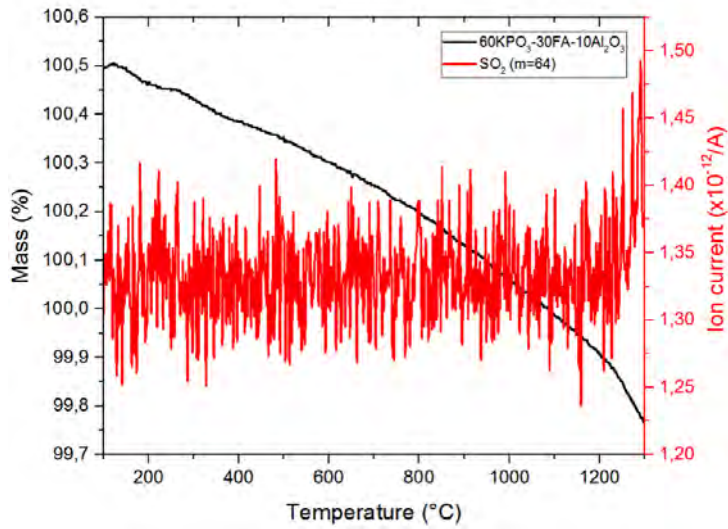


Figure 4.17: Mass loss and SO_2 release (TGA-MS) of the sample $60\text{KPO}_3\text{-}30\text{FA}\text{-}10\text{Al}_2\text{O}_3$.

One sample containing B_2O_3 was analyzed up to 1400°C . The emission of SO_2 showed a significant increase after 1200°C . This is accompanied by an increase in mass loss, but this increase is not as significant as the one presented in the sample containing slag and 20% of B_2O_3 . For the sample containing fly ash and 20% of B_2O_3 , the mass lost between 1200°C and 1400°C is only 1% of the total weight of the sample (Figure 4.18).

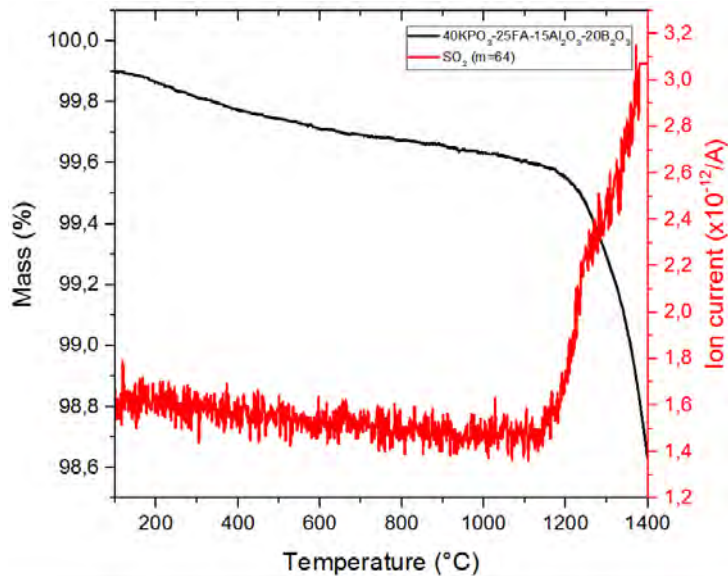


Figure 4.18: Mass loss and SO_2 release (TGA-MS) of the sample $40\text{KPO}_3\text{-}25\text{fly ash}\text{-}15\text{Al}_2\text{O}_3\text{-}20\text{B}_2\text{O}_3$.

OPTICAL SPECTROSCOPY AND GAS RELEASE OF THE GLASSES CONTAINING FLY ASH

THE colors of all the samples containing fly ash are summarized in Table 4.5 and their optical spectra are shown in Figure 4.19. All the analyzed samples had the same thickness. While the samples containing slag contain between 0.15 and 0.1% (wt) of Fe_2O_3 , the samples containing fly ash possess much higher quantities, between 1.3 and 2.5% (wt). The states of transition metals in host glass, and thus the ratio of these two iron species, not only depends on composition but also on the redox conditions of the melt, such as air atmosphere, melting temperature and melting time [10]. It is known that alkali borate and alkali silicate glass types favor the presence of transition metal ions (i.e. iron) in higher oxidation states. On the other hand, alkali phosphate glasses induce a lower oxidation state [11].

Table 4.5: Colors of different glasses containing fly ash as glass beads of 3mm.

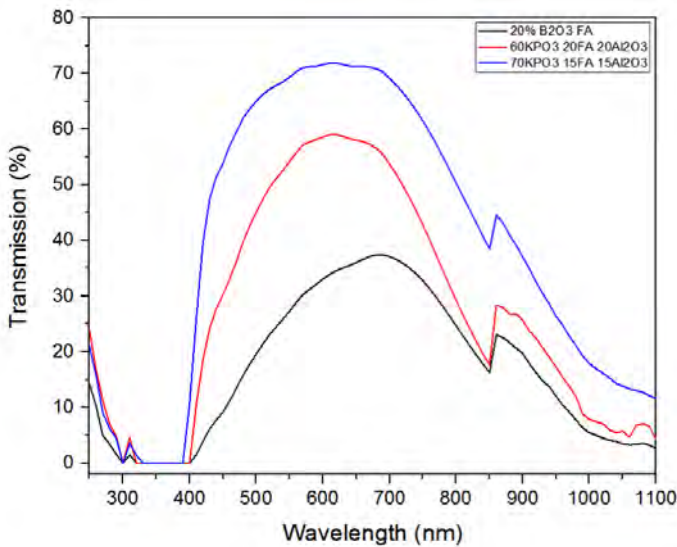
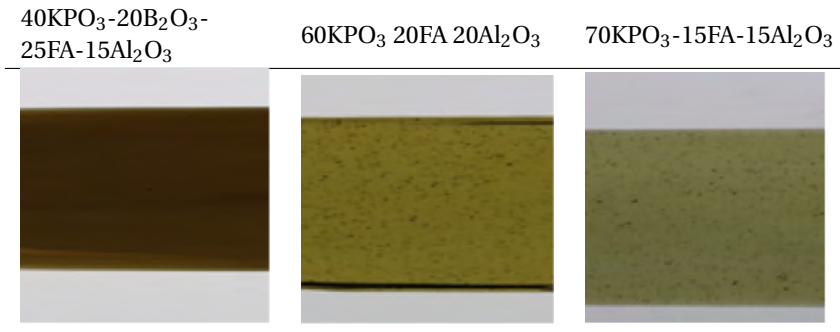


Figure 4.19: Optical spectra of samples containing fly ash.

Fe^{2+} and Fe^{3+} are respectively blue and yellow chromophores. The CT bands of Fe^{2+} are located at higher energies and therefore lower wavelengths than those of Fe^{3+} . Ferric Fe^{3+} is mainly identified by an absorption band at 380nm. Ferrous Fe^{2+} is characterized by a strong absorption band with a maximum of around 1050nm, thus already outside the visible range. The broadness of the band may be indicative of the Jahn–Teller distortion of the octahedrally coordinated ion, an effect often found in octahedral complexes of transition metals. It is expected that the band of tetrahedrally coordinated Fe^{2+} ions would be found around 2000 nm in the near IR [3].

The ratio between $\text{Fe}^{2+}/\text{Fe}^{3+}$ explains the color of the glass types. While the two species can appear simultaneously in a sample, its ratio is affected by the composition of the glass and its melting conditions. The intensity of the absorption at 1050nm is notably higher for the sample 40KPO₃-20B₂O₃-25FA-15Al₂O₃, followed by the sample with 20% of fly ash and then 15% of fly ash. As the ratio $\text{Fe}^{2+}/\text{Fe}^{3+}$ decreases, the color of the glass changes from dark green (20%B₂O₃) to yellow (15% of fly ash). Green-colored glass could therefore be associated with a relative increase in the concentration of ferrous ions, while a yellow color is associated with a lower value of $\text{Fe}^{2+}/\text{Fe}^{3+}$, thus a relative higher amount of ferric ion.

4.4. CRYSTALLIZATION STUDIES

THE T_g of glass containing waste increase with the amount of waste incorporated in the composition. Even the highest T_g , of glass containing the highest concentrations of aluminum oxide and wastes, still have low melting temperatures in comparison to the T_g of commercial silicate glasses. The production of glass with lower melting temperatures demands less energy, and, as a consequence, the environmental impact and manufacturing cost decrease.

The samples containing the highest amounts of waste materials also present the lowest thermal stabilities against crystallization. The crystallization study of the samples is a tool to identify the ideal melting conditions for each sample. For instance, the composition 60KPO₃-20slag-20Al₂O₃ is a dark glass, which already had its amorphous structure confirmed by XRD (Figure 3.9), when produced via the melting-quenching process. However, when melted using the kiln-casting method, which has a slow cooling rate in relation to the traditional melt-quenching method, it becomes a white solid (Figure 4.20). In the kiln-casting method, the melting, pouring and annealing of the glass took place in the same kiln. The kiln-casting is the process of creating a glass object in a kiln by heating glass above or inside a refractory mold until it flows to fill the void. This process employs a single kiln for the melting of the glass into the moulds and for the subsequent annealing process. As the investment moulds remain in the kiln throughout the whole process, they determine the maximum heating rate and maximum temperature that can be used. This kiln-casting method was used to evaluate the thermal stability of the samples and their potential to be prepared even with slow cooling rates. The glass was melted from the batch raw materials at 970 °C and cooled inside of the oven at a rate of around 2.66 °C/minute. This accords with the DSC-curve of this sample (Figure 4.1) that present the lowest thermal stability against crystallization among all the samples containing slag.



Figure 4.20: The sample $60\text{KPO}_3\text{-}20\text{slag-}20\text{Al}_2\text{O}_3$ produced, respectively, via the melt-quenching and the kiln-casting method.

The diffractogram of the sample made by the kiln-casting method is presented in Figure 4.21. A phase related to the Potassium Calcium Magnesium Phosphate $\text{Ca}_9\text{MgK}(\text{PO}_4)_7$ was identified. The red sticks give the peak positions and intensities of the crystalline phase identified as $\text{Ca}_9\text{MgK}(\text{PO}_4)_7$. The presence of this phase could be related to the high amounts of CaO and MgO present in the composition of the slag. Both oxides act like network modifiers, which when added to a glass matrix can induce crystallization.

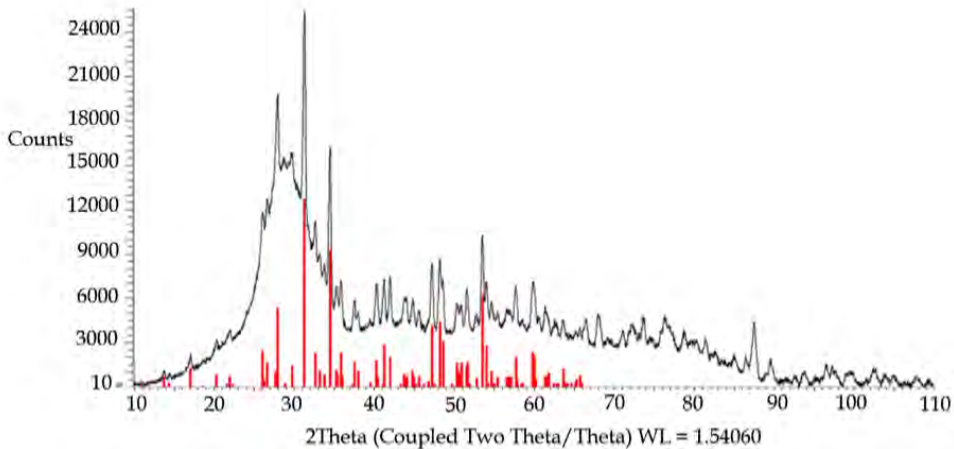


Figure 4.21: X-ray diffraction pattern of the sample $60\text{KPO}_3\text{-}20\text{slag-}20\text{Al}_2\text{O}_3$, produced by the kiln casting method, after background subtraction.

High stability is required from the composition in order to prevent crystallization upon slow cooling. A sample consisting of $60\text{KPO}_3\text{-}30\text{FA-}10\text{Al}_2\text{O}_3$ was also melted from the batch raw materials at 970°C and cooled at a rate of around $2.66^\circ\text{C}/\text{minute}$ via the kiln-casting method. The visual aspect of this sample is glassy, similar to the same composition melted by the melt-quenching method, as shown in Figure 4.22.



Figure 4.22: The sample $60\text{KPO}_3\text{-}30\text{FA-}10\text{Al}_2\text{O}_3$ produced, respectively, via the melt-quenching and the kiln-casting method.

The XRD pattern of the sample produced by a fast cooling has already been shown (Figure 3.8), and is amorphous. Figure 4.23 shows the structure of the sample produced by slow cooling. The identified phase is related to quartz. The blue sticks give the peak positions and intensities of the crystalline phase identified as SiO_2 , quartz. However, the low intensity of the peaks suggests that the sample is essentially amorphous. The results of these tests are in accord with the DSC-curve of this sample (Figure 4.3), as the enthalpy of the phenomenon of crystallization of this composition should be the lowest of all the samples containing fly ash.

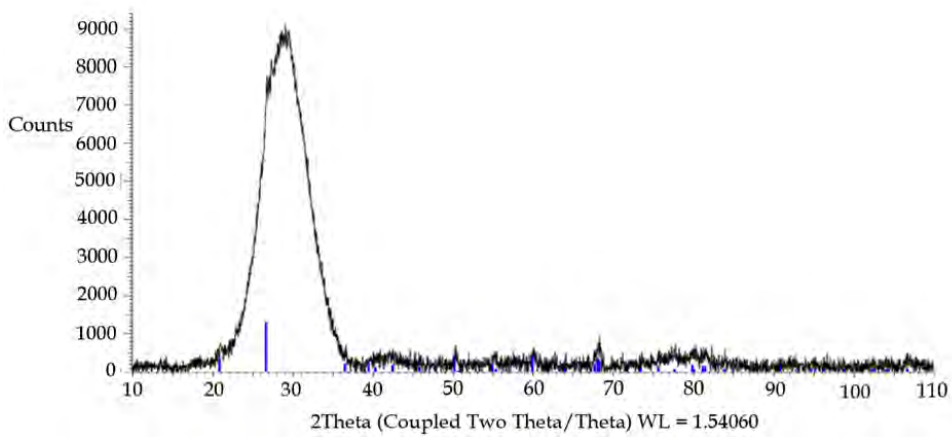


Figure 4.23: X-ray diffraction pattern of the sample $60\text{KPO}_3\text{-}30\text{FA-}10\text{Al}_2\text{O}_3$, produced by the kiln-casting method, after background subtraction.

All the studied compositions form a glass when melted by the melt-quenching technique, overcoming the highly-likely tendency to crystallize exhibited by pure waste materials. For instance, pure slag does not form a glass when prepared by the same technique (Figure 4.24).



Figure 4.24: Pure slag melted at $1500\text{ }^\circ\text{C}$ using the melt-quenching technique.

During melting, glass types containing wastes presented a maximum mass loss of 1.63 wt % when melted at temperatures up to 1100 °C. This rate of loss is higher than that found in commercial glasses. As shown in Figure 4.25, commercial silicate glass presents a maximum loss of 0.24, for the glass type B270. However, this is still acceptable and expected, due to the presence of various compounds and impurities in the composition of the wastes.

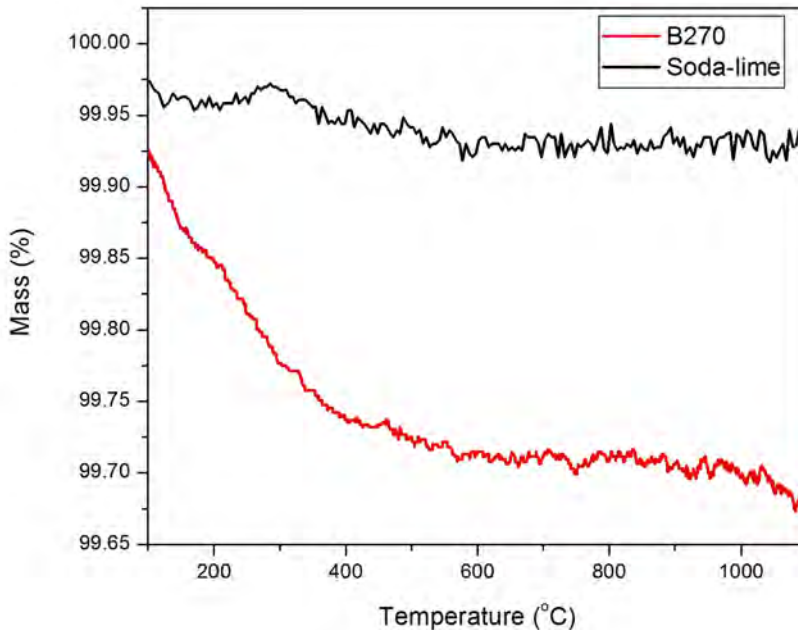


Figure 4.25: Mass loss of two commercial silicate glasses.

4.5. DISCUSSION AND CONCLUSIONS

The samples containing slag display a variety of colors, depending on their composition and the temperatures in which they are melted. For instance, the sample 50KPO₃-20B₂O₃-15Slag-15Al₂O₃ is blue when melted at 1150 °C and a mixture of blue and colorless when melted at 1250 °C (Figure 4.26). This sample has an O/P ratio=8.21, the highest among all the samples containing slag or fly ash (Table 3.7). It was already proposed that for borosilicate glasses, low-molecular-weight sulphur anions, such as S₃⁻, occupy the space between the glass networks without forming Si-S and B-S bonds, originating blue glasses [9]. As discussed in Chapter 3, it is expected that this sample presents a larger number of bridge oxygen and a lower number of non-bridge oxygen. Thus, it is expected that the blue coloration originates from the optical absorption of S₃⁻ anions present in

the space between the glass networks.



Figure 4.26: The sample $50\text{KPO}_3\text{-}20\text{B}_2\text{O}_3\text{-}15\text{Slag-}15\text{Al}_2\text{O}_3$ melted at 1150°C , and 1250°C .

After these conclusions, colored glass types containing slag, previously melted at the maximum temperature of 1250°C , were melted in 1500°C . Due to the expected mass loss, the melting time was reduced from 1 hour to 30 minutes. This temperature was chosen because it is expected that at this point, the SO_2 would be already released as gas. The increasing gas release could be an indication of decomposition of sulphates, which can occur according to the following reaction:



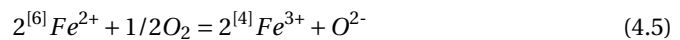
All samples melted at 1500°C were transparent and colorless, even the sample containing 20% of slag, which was dark brown when melted at 1250°C (Figure 4.27). Due to the expected mass loss, the melting time was reduced from 1 hour to 30 minutes.



Figure 4.27: The sample $60\text{KPO}_3\text{-}20\text{slag-}20\text{Al}_2\text{O}_3$, melted at temperatures varying from 1250°C to 1500°C .

For glasses containing slag, the chemical analysis showed a concentration of SO_3 between 0.08 and 0.02 wt % which proved to affect the final color of the glass. The band related to S_3 originates the color of blue samples. For the amber sample, it coexists with the band related to Fe^{3+} . Melting the glass at 1500°C leads to a higher release of SO_2 , thus limiting the concentration of sulphite. This way, the amber chromophore cannot be formed during the cooling.

After releasing SO_2 all the samples become colorless, despite the concentration of iron in the samples, in concentrations between 0.15 and 0.1 wt%. One explanation is that the formed oxygen gas could enable the conversion from Fe^{2+} to Fe^{3+} according to the following equation:



Another hypothesis is that the manganese, which is present in the slag and works like a decolorizing agent, could oxidize the iron to Fe^{3+} , a yellow color less intense than the characteristic color of Fe^{2+} (blue chromophore). Meanwhile, the manganese would be converted to Mn^{2+} , producing a colorless glass according to the following reaction:



Chemical analysis showed that glass types containing fly ash possess a lower amount of SO_3 than those with slag: a maximum concentration of 0.02 wt %. The color of these glass types is mainly determined by the ratio $\text{Fe}^{2+}/\text{Fe}^{3+}$. The amount of Fe_2O_3 in these glass types is between 1.3 and 2.5 wt % thus much higher than the amount of Fe_2O_3 in slag.

For these reasons, the melting of these glass types between 1200°C and 1400°C does not cause a loss in mass as intense as in the glasses containing slag, releasing a lower amount of SO_2 . In order to prove that the color of these glass types is not affected by the

presence of sulphur, all samples containing fly ash were melted at 1500 °C, temperature at which point the SO₂ should be already released. In contrast to the samples containing slag, melting the samples containing fly ash at a higher temperature did not affect the final color of the glasses, which kept the same colors than when melted between 1100 °C and 1350 °C, ranging from yellow to dark green. Attempts can be done to decolorize the glasses containing fly ash. In some cases, decolorizing agents, such as manganese dioxide (MnO₂), can be added to glasses containing iron to eliminate the green color. In fact, these glasses already possess between 0.01 and 0.02% of MnO in their compositions. However, these concentrations are insufficient to decolourise the glasses. Due to the high amounts of Fe₂O₃ present on these glasses, attempts to add higher amounts of decolorizing agents are more likely to work for the glasses with the lowest amounts of fly ash, such as the sample 70KPO₃-15FA-15Al₂O₃.

The fact that the compositions containing slag are so susceptible to changes in melting conditions and to the introduction of further elements demonstrates that their use could produce glass with interesting and unique colorations. However, this would be a drawback of producing glass on a commercial scale, considering the fact that slag is not a homogeneous material and its composition can vary widely, as already shown in Table 3.4. The presence of impurities in the melting or the use of a furnace with a non-tightly controlled temperature could also produce glass samples with undesirable properties. Melting at higher temperatures offers an alternative method and a way of avoiding these variations in the final color of the glass. Furthermore, it allows the production of colorless glass. In this case, an estimation of the mass loss should be taken into account during the batch calculation.

REFERENCES

- [1] Fernández Navarro, J. M. (1991). *El Vidrio*. Consejo Superior de Investigaciones Científicas. Fundación Centro Nacional Del Vidrio. Madrid.
- [2] Mandal, A.K., Sinha, P.K., Das, D., Guha, C., Sen, R. (2015). Higher Fe²⁺ /total Fe ratio in iron doped phosphate glass melted by microwave heating. *Materials Research Bulletin*, 63, p. 141–146.
- [3] Möncke, D., Papageorgiou, M., Winterstein-Beckmann, A., Zacharias, N. (2014). Roman glasses coloured by dissolved transition metal ions: redox-reactions, optical spectroscopy and ligand field theory. *Journal of Archaeological Science*, 46. p. 23-36.
- [4] Chaouche, M., Gao X.X., Cyr M., Cotte M., Frouin L. (2017) On the origin of the blue/green color of blast-furnace slag-based materials: sulfur K-edge XANES investigation. *Journal of the American Ceramic Society*, 100. p. 1707–1716.
- [5] Beerkens, R.C.G. (1999). Redox and sulphur reactions in glass melting processes. *Ceramics-Silikáty*, 43, p. 123-131.
- [6] Beerkens, R.C.G., van der Schaaf, J. (2006). Gas release and foam formation during melting and fining of glass. *Journal of the American Ceramic Society*, 89 [1]. p.24-35.
- [7] Bamford, C.R. (1977). *Colour Generation and Control in Glass*. Glass Sciences and Technology, 2, Elsevier Scientific Publishing Company, Amsterdam.
- [8] Chivers, T., Elder, P J. W. (2013). ElderUbiquitous trisulfur radical anion: fundamentals and applications in materials science, electrochemistry, analytical chemistry and geochemistry. *Chemical Society Reviews*, 42, p. 5996-6005.

- [9] Saiki, K., Sakida, S., Benino, Y., Nanba, T. (2010). Phase separation of borosilicate glass containing sulfur. *Journal of the Ceramic Society of Japan* 118 [7]. p. 603-607.
- [10] Babadzhanova, O.E, Yashchishin, I.N. (2000). Low-melting glasses based on phosphate ore processing products. 57, Issue 5–6, p. 149–151.
- [11] ElBatal, F.H., Hamdy, Y.M., Marzouk, S.Y. (2009). UV-visible and infrared absorption spectra of transition metals-doped lead phosphate glasses and the effect of gamma irradiation. *Journal of Non-Crystalline Solids*, 355, p. 2439-2447.

5

COMPOSITIONAL DEPENDENCE OF THE COEFFICIENT OF THERMAL EXPANSION OF THE GLASSES

Determining the thermal expansion coefficient of a glass is fundamental in order to predict the susceptibility to thermal shocks and the crack propagation after rapid cooling. Pyrex glass is the most typical example of low-expansion glass, used for laboratory and kitchen ware. It consists of a borosilicate glass, in which the boron oxide plays an important role to decrease the thermal expansion. The lower melting phosphate glasses possess a high thermal expansion coefficient. For this reason, the boron oxide was added to the glasses in this study, as an attempt to decrease the thermal expansion of the samples. This chapter describes the measurement of the coefficient of thermal expansion of the glasses. The preparation of the setup using strain gauges was reported. Results were analyzed, correlated with the compositions and compared with each other. Different applications were suggested for different compositions, according to their coefficients of thermal expansion.

5.1. PREPARATION OF THE SAMPLES

NINE glass samples containing fly ash or slag had their coefficient of thermal expansion (CTE) determined. The preparation of the samples consisted of attaching the gauges type ZFLA-6-11 to the surfaces of the samples. First, the surfaces of the samples were made flat using sandpaper and cleaned with acetone. Next, the gauges were attached using a special glue, the NP-50B adhesives for high temperatures. This two-component room-temperature-curing polyester adhesive is specific for bonding QE, ZF and BF series of strain gauges. The glue was always applied while using a mask and inside a ventilated fume cabinet. An analytical balance was used to measure the two components of the glue in a proportion 33 parts of component A to 1 part of component B (Figure 5.1). Then, they were mixed. The drying process, at environmental temperature, took four hours and during this process weights were kept above the samples to apply a constant pressure.

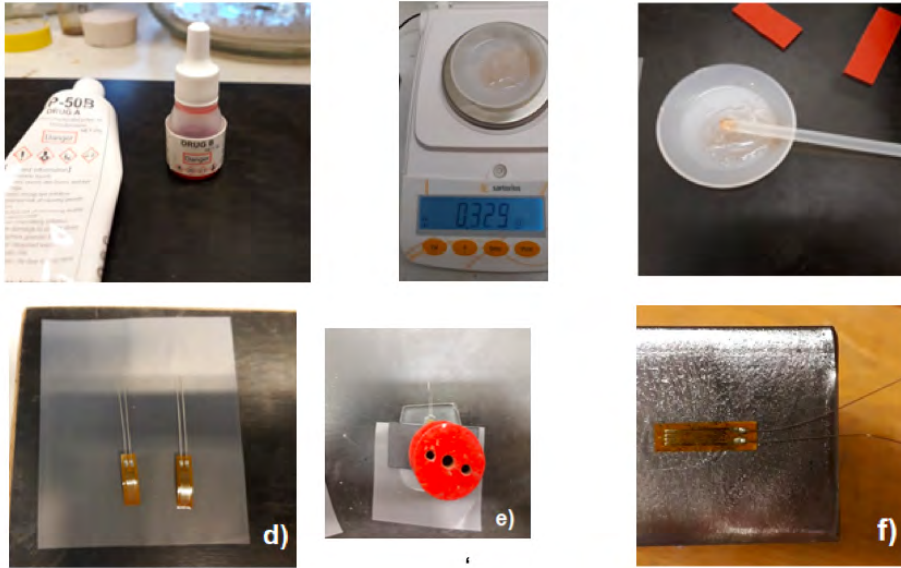


Figure 5.1: Preparing samples a) components of glue: component A and component B (red liquid) b) weighing the glue c) glue ready d) strain gauges e) drying process: weights pressurising samples f) gauge glued to a steel sample.

5.2. EXPERIMENTAL SETUP

THE gauges attached to the samples were connected to wires of a DAQ device of three channels. The device was also connected to a computer. The samples were placed inside a Heraeus oven type UT 12P, shown in Figure 5.2, which is operational up to 250 °C. A bridge-compensation circuit was used outside the oven while inside it used a quarter bridge sensing gauge.

The first experiments were conducted up to 240 °C. In the first test, channel 1 was connected to a steel sample, by a white wire, and channels 2 and 3 were connected to the surface (blue wire) and bottom (red wire) of a sample of composition $40\text{KPO}_3\text{-}20\text{B}_2\text{O}_3\text{-}25\text{FA-}15\text{Al}_2\text{O}_3$ (Figure 5.3). After reaching 240 °C, the furnace was kept equal to this temperature for approximately 15 minutes to achieve a strain stability. Subsequently, the furnace was turned off. The furnace door was closed during the whole process, enabling a slow cooling. A temperature sensor was connected to the DAQ device and placed inside the oven. Since a difference exists between the temperature measured by the sensor and the temperature shown on the display of the furnace, only the temperature detected by the sensor was considered for the measurements.



Figure 5.2: The setup a) connexion between wire and gauge b) connexion wire and gauge c) DAQ device d) furnace Heraeus.

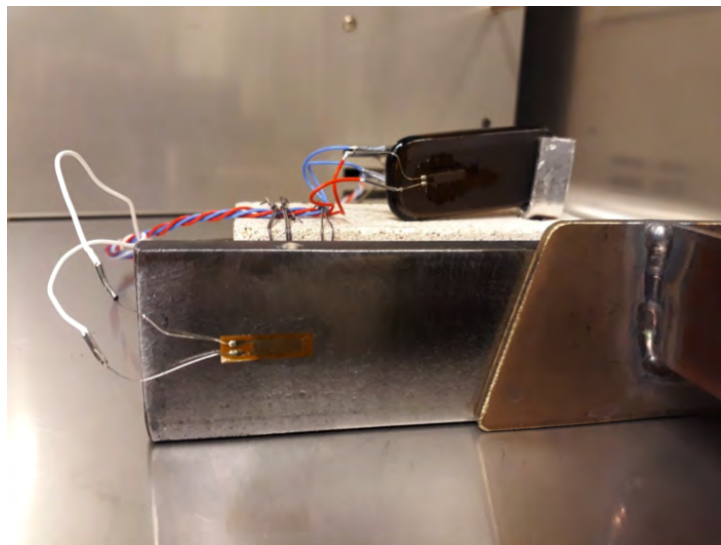


Figure 5.3: Testing steel (channel 1) and a glass $40\text{KPO}_3\text{-}20\text{B}_2\text{O}_3\text{-}25\text{FA-}15\text{Al}_2\text{O}_3$ (channels 2 and 3).

The results of the first test demonstrate that the two sides of the glass show very similar behaviour by expanding less than the metal (Figure 5.4).

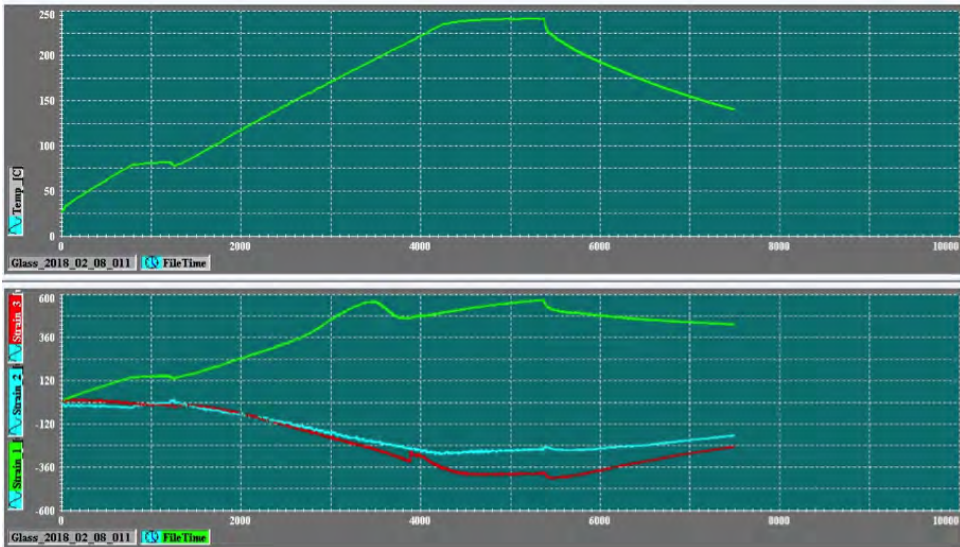


Figure 5.4: Channel 1 is connected to the steel, while the surface and bottom of a glass show similar behaviours (channels 2 and 3).

However, the samples exhibited divergent behaviors when the test was repeated, particularly above 200 °C (Figure 5.5). The glue and the gauges should be operational up to 300 °C, however the creep effect may be caused by the combination of glue and gauge, or a drip effect caused by the use of excessive glue. The next tests were performed at lower temperatures to prevent any such effects.

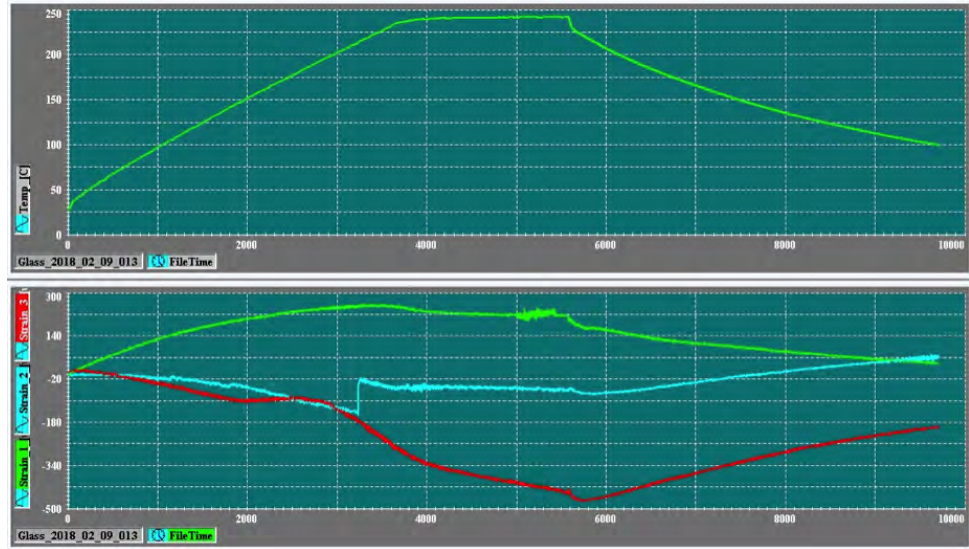


Figure 5.5: Channel 1 is connected to the steel, while the surface and bottom of a glass show different behaviours (channels 2 and 3).

The coefficient of thermal expansion (CTE) of the glasses was measured from the environmental temperature, ranging from 24 °C to 160 °C. Next, the temperature was kept at 160°C to derive a stable value for strain at the maximum temperature, which presented small fluctuations. In the calculations, the strain value at 30°C was applied as the strain at minimum temperature and the strain at 163°C was used as the strain at maximum temperature. This temperature was the maximum temperature achieved during the fluctuations, when the programmed temperature was kept constant. The developed glasses containing slag and fly ash and also the standard soda-lime and borosilicate glasses were tested, in order to compare the CTE of them. In all tests, two channels were connected to the surfaces of glass samples while channel 1 was connected to a piece of steel (Figures 5.6 and 5.7). The tests were performed under the same conditions, and each sample was tested three times. The steel was used to ensure the replicability of the results.



Figure 5.6: Setup of test 5, steel (channel 1), $75\text{KPO}_3\text{-}12.5\text{Slag-}12.5\text{Al}_2\text{O}_3$ (channel 2) and $60\text{KPO}_3\text{-}20\text{Slag-}20\text{Al}_2\text{O}_3$ (channel 3).



Figure 5.7: Setup of test 7, steel (channel 1), $50\text{KPO}_3\text{-}10\text{B}_2\text{O}_3\text{-}25\text{FA-}15\text{Al}_2\text{O}_3$ (channel 2) and soda-lime (channel 3).

Strain gauges are designed for specific applications and materials. After analyzing the datasheet of the gauges used in these tests, it was noticed that they were intended for steel, as they were tested on AISI 400 stainless steel with a CTE of $11.8 \times 10^{-6} / ^\circ\text{C}$. Hence, they possess a compensation for this material and intend not to display strain if there is no applied load, even when the temperature is changing. With the strain gauge technique, the active gauge used to measure the thermal expansion must be compensated

for the effects of apparent thermal strain. This can be done by using a gauge identical to the active one on a reference material [1]. For all experiments, a piece of steel was used as a reference and the similar values of CTE obtained for steel in the different tests ensured the replicability of the tests. During the measurements, the strain of some samples appeared as negative values, probably as a result of the large difference between the expansion rate of the gauge, prepared for steel with a higher expansion, and the glasses. Hence, the negative values of strain of the glasses were considered positive for the calculations below.

The correction may be executed according to the equation for apparent strain (ϵ_{app}), listed in the datasheet of the gauges (Appendix C) and displayed below:

$$\epsilon_{app} = -2.27 \times 10^1 + 1.35 \times T^1 - 1.07 \times 10^{-2} \times T^2 + 8.57 \times 10^{-6} \times T^3 + 1.7 \times 10^{-8} \times T^4 (\mu m/m) \quad (5.1)$$

For instance, for the initial temperature of 30°C, the apparent strain is calculated as follows:

$$\epsilon_{app} = -2.27 \times 10 + 1.35 \times 30 - 1.07 \times 10^{-2} \times 30^2 + 8.57 \times 10^{-6} \times 30^3 + 1.7 \times 10^{-8} \times 30^4 = 8.42 \mu m/m \quad (5.2)$$

It follows that the gauge shows 8.42 μ Strain even when there is no stress applied. In other words, the strain exceeded 8.42 μ Strain.

Considering a maximum temperature of 163°C, the apparent strain is:

$$\epsilon_{app} = -2.27 \times 10^1 + 1.35 \times 163 - 1.07 \times 10^{-2} \times 163^2 + 8.57 \times 10^{-6} \times 163^3 + 1.7 \times 10^{-8} \times 163^4 = -37.82 \mu m/m. \quad (5.3)$$

In this case, the gauge displays a negative strain. This implies that the display indicates a strain which is 37.82 μ Strain lower than expected. This is in accordance with the temperature compensation curve of the gauges. The plot shows that temperatures below 125°C require a negative correction, and temperatures above this value require a positive correction (Figure 5.8).

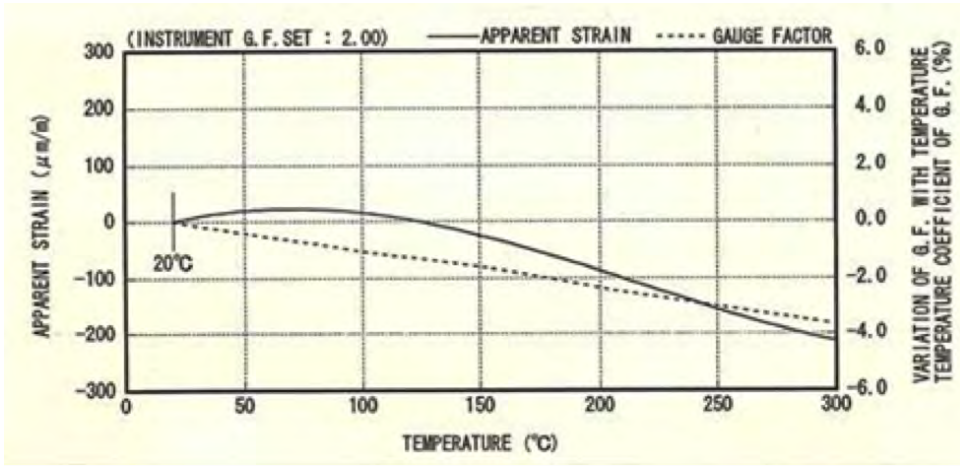


Figure 5.8: Temperature compensation curve of the gauges.

The results obtained from the measurements were corrected in line with the equation for the apparent strain. Subsequently, the gauge factor should be considered. These gauges have a gauge factor of 2.01, which should be understood as an amplification. The increasing temperature could lower the gauge factor, and, as a consequence, it will display a lower strain than expected. The correction could be executed by multiplying the apparent strain by the gauge factor (β):

$$\varepsilon_{compensated} = (\varepsilon - \varepsilon_{app}) \times \beta \quad (5.4)$$

Using these values, the uncorrected CTE was calculated for all the samples in the different tests, according to the equation:

$$\alpha' = \varepsilon' / \Delta T \quad (5.5)$$

In which α' is the uncorrected coefficient of thermal expansion, ε' is the measured strain of the sample and ΔT corresponds to the variation of temperature (°C). Next, the average uncorrected expansion was calculated for each sample, based on the results of three tests. As a last step, the CTE of each sample (α) was calculated considering the uncorrected coefficient of thermal expansion (α') and the CTE of the compensating material (α_c , the steel) by applying the following formula:

$$\alpha = \alpha' + \alpha_c \quad (5.6)$$

The results of the calculations are presented in Appendix C. To validate the measurements, two pieces of aluminium with a known CTE of $24.8 \times 10^{-6} / ^\circ\text{C}$ measured between 20 °C-200 °C [2] were also evaluated. In this test, channel 1 of the DAQ device was connected to a piece of steel, the same piece that was used as a reference for the measurements of all glasses, and channels 2 and 3 were connected to the surfaces of two pieces of aluminium. The results of the test are presented below in Tables 5.1 and 5.2.

Table 5.1: Calculation of uncorrected coefficients of thermal expansion of aluminium samples.

Sample	ϵ at Max T	ϵ at Min T	ϵ_{app} at max T	ϵ_{app} at min T	$\epsilon - \epsilon_{app}$ (max)	$\epsilon_{compensated}$ (max)	$\epsilon - \epsilon_{app}$ (min)	$\epsilon_{compensated}$ (min)	$\epsilon_{compensated}$ max - $\epsilon_{compensated}$ min	Δ	α'
steel	218.9313	3.6774	-37.83	8.57	256.7613	516.0902	-4.8926	-9.83413	525.9243	132.7975	3.960348
Aluminium 1	1379.4911	-1.6636	-37.83	8.57	1417.321	2848.815	-10.2336	-20.5695	2869.385	132.7975	21.60722
Aluminium 2	1226.8303	7.3608	-37.83	8.57	1264.66	2541.967	-1.2092	-2.43049	2544.398	132.7975	19.15998

Table 5.2: Calculation of the coefficient of thermal expansion of aluminium samples.

Sample	Average α'	α
Steel	3.960348	-
Aluminium	20.3836	24.34395

The value of the average CTE derived for the two tested pieces of aluminium is $24.34 \times 10^{-6}/^{\circ}\text{C}$. This implies a deviation of 1.8% in relation to the nominal CTE of the aluminium, indicating a good fit between the reference values and the CTE values measured with strain gauges.

5.3. DISCUSSION AND CONCLUSIONS

TABLE 5.3 shows the values of the CTE obtained for 9 glasses containing fly ash or slag and 3 commercial glasses. The addition of B_2O_3 to the glasses clearly changes the CTE, as the glasses with 20% of B_2O_3 possess the lowest CTE among the tested glasses. The CTE of the glass containing 20% of B_2O_3 and slag is similar to the expansion coefficient of a borosilicate glass, while the expansion of the glass containing 10% of B_2O_3 and slag has a coefficient of expansion comparable to a flat soda-lime glass. The CTE of the glasses containing 20% and 10% of B_2O_3 and fly ash are even lower than the coefficient of expansion of a borosilicate glass. Samples without B_2O_3 expand more than the other glasses. The CTE increases with the increasing amount of KPO_3 , thus with higher amounts of K_2O and P_2O_5 . The samples with 60% of KPO_3 have a CTE slightly above the one of soda-lime glasses. However, the glasses containing 70% or 75% of KPO_3 have a CTE much higher than borosilicate or soda-lime glasses, which limit their applications in architectural engineering as they will be sensitive to temperature shocks.

Matching thermal expansion between different kinds of materials is critical in modern engineering. Hence, research on thermal expansion of materials is becoming increasingly significant in both scientific and technological fields [3]. These investigations are also important in the development of other fields, such as the thermal strengthening of glass.

Table 5.3: CTE obtained for different glasses.

Sample	$\alpha \times 10^{-6} / ^\circ\text{C}$
70KPO ₃ -15slag-15Al ₂ O ₃	12.8±0.4
40KPO ₃ -20B ₂ O ₃ -25FA-15Al ₂ O ₃	5.71±0.2
75KPO ₃ -12.5Slag-12.5Al ₂ O ₃	15.22±0.8
60KPO ₃ -20Slag-20Al ₂ O ₃	10.26±0.4
50KPO ₃ -10B ₂ O ₃ -25FA-15Al ₂ O ₃	6.19±0.7
Flat glass	9.02±0.2
50KPO ₃ -20B ₂ O ₃ -15slag-15Al ₂ O ₃	7.50±0.0
60KPO ₃ -10B ₂ O ₃ -15slag-15Al ₂ O ₃	8.62±0.2
Flat glass	8.99±0.5
60KPO ₃ -30FA-10Al ₂ O ₃	10.42±0.3
Borosilicate	7.62±0.9
70KPO ₃ -15FA-15Al ₂ O ₃	14.07±0.8

Due to the brittleness of glass, the existent superficial micro-cracks are sensitive to mechanical and thermal stresses. Fracture will start at a critical surface flaw. When a thermal shock occurs, a transient temperature gradient occurs, producing thermal strain which induces local stress. The shock intensity is directly associated with the level of temperature difference between the initial temperature and the environment. A difference exists between a cold-hot and a hot-cold thermal shock test. The latter, which occurs for instance in the melt quenching technique, is more harmful for brittle materials because it generates tensile stresses on the quickly cooled surface. These stresses may be sufficient to activate pre-existing micro-cracks, leading to fracture [4].

Soda-lime glasses are inexpensive, chemically durable and relatively easily melted and formed. The main composition is 70% silica, 15% soda, 10% calcium oxide and magnesium oxide and 5% other oxides. Small additions to the main composition improve the properties of soda-lime glasses: alumina improves the chemical durability and provides higher stability against crystallization, zinc oxide is used to lower the melting point, arsenic and antimony oxides are used for fining and borates are applied for easier working and lower thermal expansion [5]. Pyrex-borosilicate glass was developed by Corning to create more resistance to thermal shocks and to be more chemically durable than soda-lime glass, while preserving a similar melting and working temperature. The borate decreases the viscosity and the coefficient of thermal expansion of this glass. Furthermore, it allows for a lower sodium content, increasing the chemical durability [5]. Table 5.4 compares CTE of phosphate and silicate glasses reported in the literature. These reference values of CTE are a good fit with the CTE measured for borosilicate and soda-lime glasses in the tests using strain gauges.

Typically, alkali aluminophosphate glasses have glass transition temperatures under 400°C and thermal expansion coefficients higher than $15 \times 10^{-6} / ^\circ\text{C}$ [9]. Recently, research was performed on improving the physical properties of alkali phosphate glasses by adding different metal oxides with high valence cations, like Al³⁺ or Ti⁴⁺. These ions modify thermo-mechanical, physical and structural properties, mainly due to changes in the glass structural network, thereby forming cross-linked bonds. Sodium aluminophos-

phate (NAP) glasses have been the subject of numerous research. It was found that additions of Al₂O₃ up to 10 mol % to sodium phosphate glasses, converts P-O-Na and some P-O-P linkages to P-O-Al linkages. This results in improved thermal and chemical durability due to modification of thermophysical properties like the thermal expansion coefficient [10]. As discussed in chapter 3, the chemical durability of phosphate glasses can be improved with the addition of oxide components as B₂O₃, CaO, SiO₂ and Al₂O₃.

Table 5.4: CTE of some phosphate and silicate glasses reported in the literature.

Composition (wt%)	$\alpha \times 10^{-6} / ^\circ\text{C}$	Reference
Soda-lime (72SiO ₂ - 15Na ₂ O-5CaO-4MgO-2Al ₂ O ₃ - 1B ₂ O ₃)	9	[1]
Borosilicate crown (65.6SiO ₂ -13B ₂ O ₃ -12.1K ₂ O-7.6Na ₂ O-1.2ZnO-0.5As ₂ O ₃)	7.6×10^{-6}	[6, 7]
25K ₂ O-22P ₂ O ₅ -53WO ₃	24.4	[8]
40K ₂ O-60P ₂ O ₅	24	[8]
41K ₂ O-2.5ZnO-1.5Al ₂ O ₃ -55P ₂ O ₅	28.6	[8]
37K ₂ O-4.5Al ₂ O ₃ -58.5P ₂ O ₅	24.1	[8]
33K ₂ O-7Al ₂ O ₃ -60P ₂ O ₅	21.4	[8]

The analysis of the CTE of the phosphate glasses listed in Table 5.4 suggests that the increasing CTE when alkalis are added to phosphate glasses is probably caused by the depolymerization of anions. On the other hand, additions of Al₂O₃ and WO₃ increase the degree of polymerization. Linear relations were already found between the expansion coefficient and the radius of alkali cations for a series of compositions in the systems R₂O-Al₂O₃-P₂O₅ and R₂O-WO₃-P₂O₅: the expansion increases with increasing radius, similar to the case of silicate glasses. This trend suggests that the increase in expansion is a result of the decrease in the strength of the cationic field and the expansion would mainly be determined by the interaction between cations and nonbridging oxygens [8]. Similar trends are found for the glasses containing fly ash and slag, developed in this work. Table 5.5 shows the CTE measured in the expansion tests as a function of the compositions of the samples (wt%). The components present in concentrations lower than 1.5% were omitted.

Table 5.5: CTE obtained for phosphate glasses as a function of the chemical composition.

Sample	$\alpha \times 10^{-6} / ^\circ\text{C}$
28.4K ₂ O-5.19SiO ₂ -5.85CaO-17.58Al ₂ O ₃ -40.17P ₂ O ₅	12.76913
18.54K ₂ O-13.86SiO ₂ -14.32B ₂ O ₃ -2.5Fe ₂ O ₃ -21.75Al ₂ O ₃ -26.64P ₂ O ₅	5.711153
29.83K ₂ O-4.29SiO ₂ -4.89CaO-14.68Al ₂ O ₃ -42.1P ₂ O ₅	15.21695
26.66K ₂ O-7.48SiO ₂ -1.7MgO-7.87CaO-18.95Al ₂ O ₃ -35.19P ₂ O ₅	10.25915
21.18K ₂ O-5.49SiO ₂ -17.77B ₂ O ₃ -6.52CaO-22.5Al ₂ O ₃ -24.77P ₂ O ₅	7.503744
27.96K ₂ O-8.36SiO ₂ -19.55Al ₂ O ₃ -38.29P ₂ O ₅	14.06547

The glass with the highest thermal expansion coefficient is also the glass containing the highest amount of K₂O and P₂O₅. It is the sample 75KPO₃-12.5Slag-12.5Al₂O₃ with a composition 29.83K₂O-4.29SiO₂-4.89CaO-14.68Al₂O₃-42.1P₂O₅. This is also the only tested sample which shows low chemical durability. This is consistent with studies reporting an increase in expansion coefficient together with the increase of the dissolution

rate of a phosphate glass, indicating that both properties are controlled primarily by the interaction of cations with nonbridging oxygens [8].

High expansion glasses with good chemical durability are desirable for applications such as bonding with plastics or metals, since the thermal expansion coefficient of the joining materials should be proximate. However, high values of CTE mean sensitivity to thermal shock which limits the applications of phosphate glasses in other areas, such as building materials. The development of new glass compositions, containing lower amounts of phosphate and higher amounts of other oxides, present in fly ash and slag, or B_2O_3 , demonstrated the possibility to decrease the CTE of the glasses, producing samples with a coefficient of expansion comparable to the coefficient of soda-lime and borosilicate glasses, or even lower. It expands the range of applications of typical phosphate glasses, showing potential uses in construction, such as bricks, or even in more advanced technologies which require a combination of low melting temperatures and low thermal expansion, such as 3D printing.

REFERENCES

- [1] Valentich, J. (1985). Thermal expansion of solids from $-261\text{ }^\circ\text{C}$ to $173\text{ }^\circ\text{C}$ using strain gauges. *Cryogenics*, v. 25. p.63-67.
- [2] Hidnert, P., Krider, H.S. (1952). Thermal expansion of aluminum and some aluminum alloys. *Journal of research of the national bureau of standards*. v.48, 3, research paper 2308.
- [3] Zeng, H., Ye, F., Li, X., Wang, L., Yang, B., Chen, J., Zhang, X., Sun, L. (2016). Calculation of thermal expansion coefficient of glasses based on topological constraint theory. *Chemical Physics Letters*, v. 662, p. 268-272.
- [4] Malou, Z., Hamidouche, M., Bouaouadja, N., Chevalier, J., Fantozzi, G. (2013). Thermal shock resistance of a soda lime glass. *Ceramics–Silikáty*, v. 57, 1, p. 39–44.
- [5] Moavenzadeh, F. (1990). *Concise encyclopedia of building & construction materials*. 1st ed., Pergamon Press.
- [6] Stephens, R.E., Rodney, W.S. (1954). Refractive indices of five selected optical glasses. *Journal of research of the national bureau of standards*. v. 52, 6, research paper 2504.
- [7] Hidnert, P. (1954). Thermal expansion of five selected optical glasses. *Journal of research of the national bureau of standards*. v. 52, 6, research paper 2507.
- [8] Minamf, T., Mackenzie, J.D. (1977). Thermal Expansion and Chemical Durability of Phosphate Glasses. *Journal of the American ceramic society*. v.60, p.232-235.
- [9] Brow, R.K. (2000). Review: the structure of simple phosphate glasses. *Journal of non-crystalline solids*. v.263-264. p.1-28.
- [10] Tiwari, B., Dixit, A., Kothiyal, G.P., Pandey, M., Deb, S.K. (2007). Preparation and characterization of phosphate glasses containing titanium. *BARC Newsletter*, v. 285, p. 167-173.

6

MECHANICAL PROPERTIES OF THE PRODUCED GLASSES: ELASTIC MODULUS, HARDNESS AND INDENTATION TOUGHNESS

Nanoindentation has been extensively applied in the last decades as a high spatial resolution micro-probe for measuring the mechanical properties of glasses at the micro-level. Among the mechanical properties that can be measured by this technique are: hardness, elastic modulus and fracture toughness [1]. A crucial factor in the expansion of the use of nanoindentation is the simple sample preparation. A small glass sample requires only grinding and polishing, achieving a surface free of scratches. Besides, most indentation equipment offers control of test parameters, which is necessary for the exploration of different deformation modes by changing experimental time scale, indenter tip geometry and loading conditions [2]. This chapter reports some mechanical properties of the produced glasses, obtained using the nanoindentation technique. The Oliver and Pharr method is the base of the measurements for both elastic modulus and hardness, and the indentation toughness is determined using approaches based on crack length or energy-methods.

6.1. ELASTIC MODULUS AND HARDNESS

AMONG other reasons, the development of innovative glasses is possible in connection with the evolution of the understanding of the property response as a function of the chemical composition. Therefore, it is important to determine the quantitative relation of each constituent element and its contribution to the final properties of the glass.

The Makishima-Mackenzie (MM) model provides a direct calculation of the Young's modulus of oxide glasses from chemical compositions. The prediction is based on an assessment of the dissociation energy of the oxide constituents and the packing density [3].

The model relates the bulk stiffness to the strength of the bonds and their density. The strength of the bonds is estimated from the dissociation energy, while the bond density is related to the combination of specific bond energy and atomic packing fraction [4]. Work by Yamane and Mackenzie provides evidence that the Vickers hardness of the glasses is directly related to their bond strengths and the elastic moduli [5]. Considering the packing density of atoms and bond energy in unit volume, it is possible to calculate the elastic moduli of a glass, according to the Makishima-Mackenzie (MM) model [6]. The model posits:

$$E = 2V_t \sum_i G_i x_i \quad (6.1)$$

In which E is the Young's modulus, V_t is the atomic packing fraction (fraction of space filled with atoms), G_i is the dissociation energy per unit volume of component i , and x_i the mole fractions [4]. Silicate glasses are well described by this model, with a precision of approximately 20%. However, borate glasses are very poorly described by the model with an error of a factor of 5, mainly due to the lack of consideration of network topology in the MM model [4]. In this case, using the packing fraction as a descriptor of structure leads to inaccurate results, as the average coordination of this glass is only 2.4. The elastic moduli also depends on the coordination, on the polymerization degree (cross linking) and the molecular organization, including the forming of rings, chains or layers units [7]. Both elastic modulus and hardness can be obtained from the nanoindentation curve.

The calculation of E using nanoindentation is not straightforward. A reduced Young's modulus, $E_r = E/(1 - \nu^2)$, is obtained and these methods usually consider arbitrary values for ν , which can be a significant source of uncertainties [7]. Poisson's ratio is the negative of the ratio of transverse contraction strain to longitudinal extension strain in the direction of elastic loading, expressing the resistance of a material opposes to volume change with respect to shape change. It is associated with the glass network connectivity. If there are four bridging oxygen per glass-forming atom, a 3D network is achieved and Poisson's ratio is as low as $\nu = 0.15$, such as SiO_2 . Differently, glasses with $n_{\text{BO}} = 3$, such as B_2O_3 or P_2O_5 have ν around 0.3 [7] as shown in Figure 6.1. Therefore, Poisson's ratio correlates with the atomic packing density and with the polymerization degree.

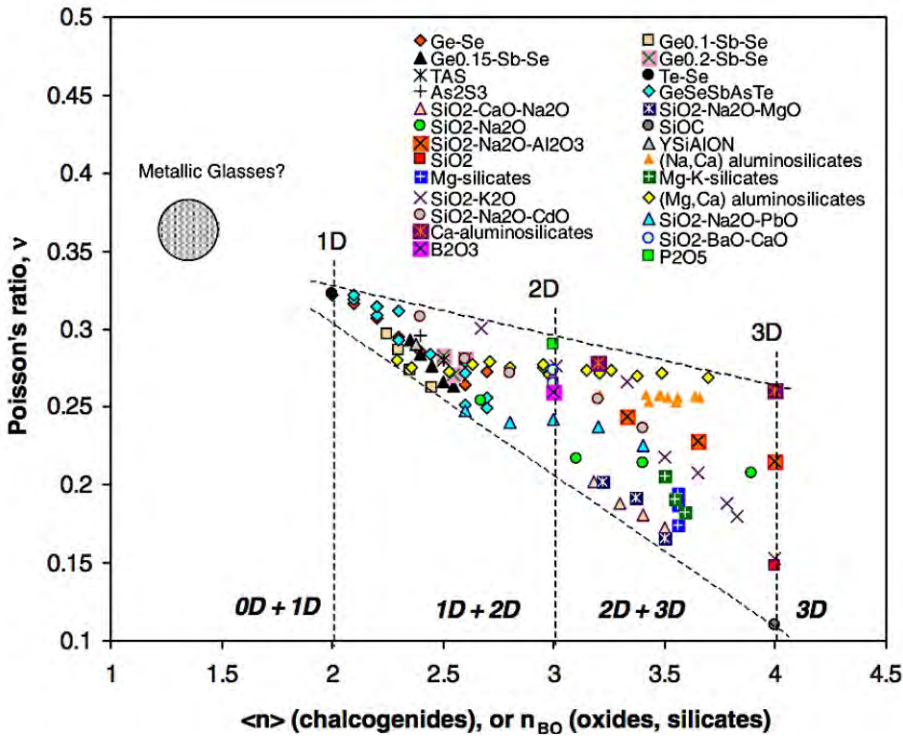


Figure 6.1: Poisson's ratio related to the average coordination number $\langle n \rangle$ or the number of bridging oxygen per glass-forming cation n_{BO} [7].

6.2. INDENTATION TOUGHNESS

INDENTATION have also been used to estimate fracture toughness. Usually, a sharper cube corner diamond tip is preferred, as due to the high stress concentrations that it generates below the tip, it can initiate fracture at lower critical loads [8]. Traditional testing methods for fracture toughness determination are generally based on macroscopic crack extension experiments. However, evaluating the fracture toughness of glasses and ceramics is still problematic. Consequently, a mechanism for measuring fracture toughness of these materials has not been well determined. The nano-indentation test is an option that has been used in order to assess the fracture toughness of brittle materials, such as glasses, ceramics, films and coatings. As long as the materials exhibit brittle fracture with minimal crack tip plasticity, this crack pattern can be used to establish fracture toughness values [9]. This property can be estimated by either crack-length-based method or crack-energy-based method, providing useful partially quantitative information.

6.3. MATERIALS AND METHODS

BERKOVICH nano-indentation was used for the measuring of elastic modulus and hardness of the samples. Each test was repeated 25 times as 5×5 indents, as shown in Figure 6.2.

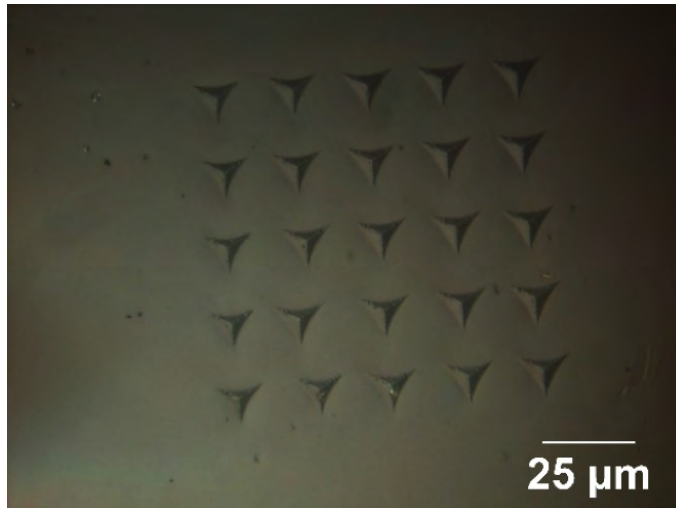


Figure 6.2: Indents in the sample $40\text{KPO}_3\text{-}20\text{B}_2\text{O}_3\text{-}25\text{fly ash-}15\text{Al}_2\text{O}_3$ under 400 mN.

The load on sample was 400mN and the average values of both properties were calculated based on the load-displacement curves of the samples, via the Oliver-Pharr method [10]. For calculations, the values between 1000nm and 1400nm were considered, this is an interval in which the results are more stable. Examples of curves obtained for elastic modulus and hardness are shown in Figures 6.3 and 6.4.

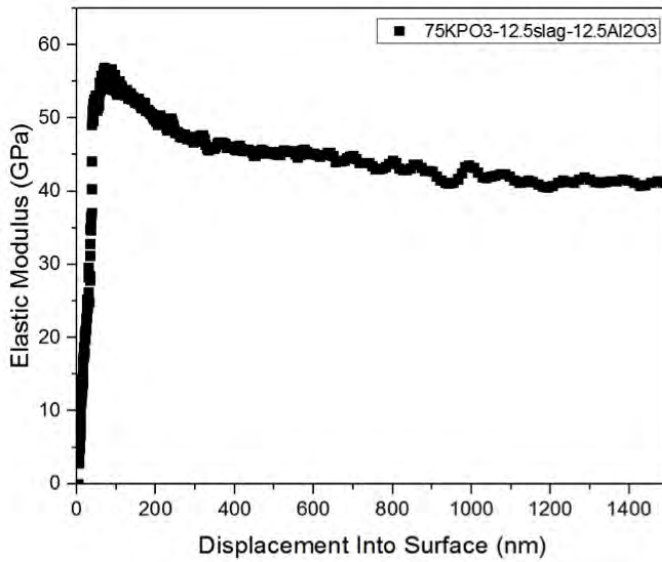


Figure 6.3: Elastic modulus versus penetration depth curve.

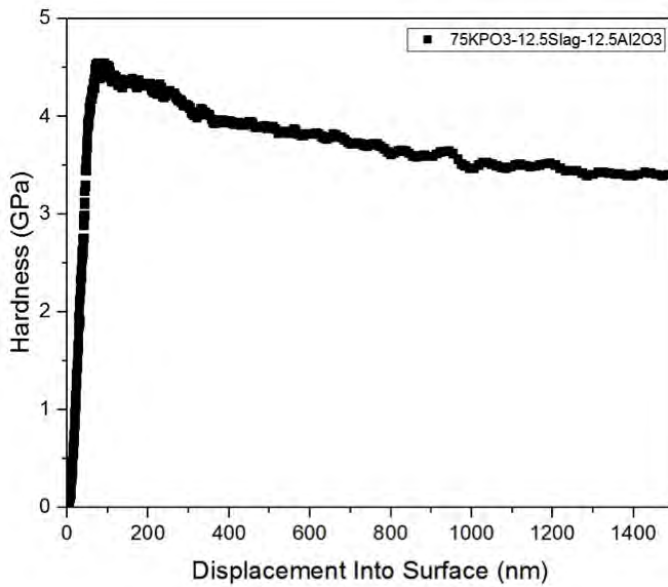


Figure 6.4: Hardness versus penetration depth curve.

High loads were used in order to produce controlled cracks and estimate the fracture toughness of the samples, also using a Berkovich indenter. The crack lengths were evaluated using optical microscopy. The first load-controlled experiments were performed using a load of 32 mN, loading and unloading time of 5 seconds, and hold time of 10 seconds (Figure 6.5). To help to locate their positions, these indents were made between two indents of 2.5 N.

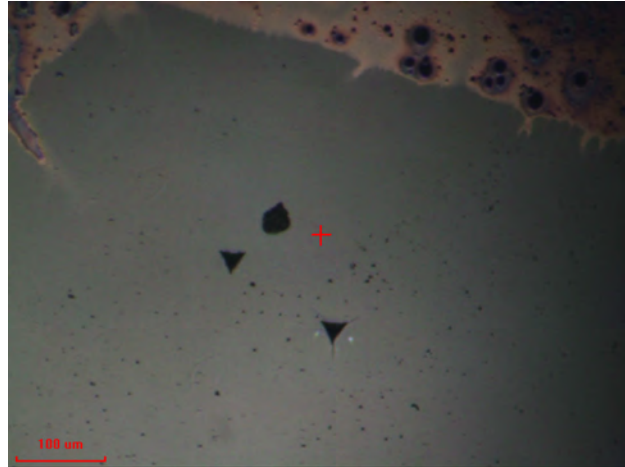


Figure 6.5: Ten indents under 32 mN between two indents under 2.5 N in a soda-lime glass.

As these first tests did not generate visible cracks, the load was increased from 32 mN to 2.5 N, consisting of 30 seconds loading, 10 seconds unloading and hold time of 15 seconds. Each test was repeated at least 4 times, with a distance of 100 μm between each indent. However, while some samples did not present visible cracks, other samples exhibited long cracks, which overlapped each other, as shown in Figure 6.6.

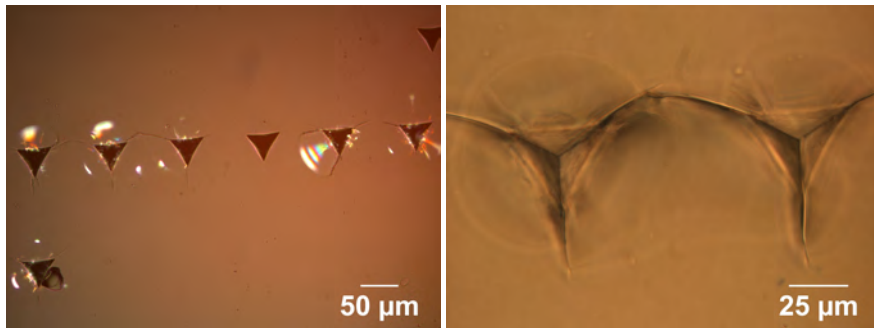


Figure 6.6: Cracks in the sample $70\text{KPO}_3\text{-15slag-15Al}_2\text{O}_3$ induced by a load of 2.5 N using a Berkovich indenter: a) all the indents b) details of 2 indents.

For this reason, new tests were performed, under 2N and with a distance of 200 μm between the indents. The indents were performed close to a scratch to help to locate them in the further microscopy analysis (Figures 6.7 and 6.8).

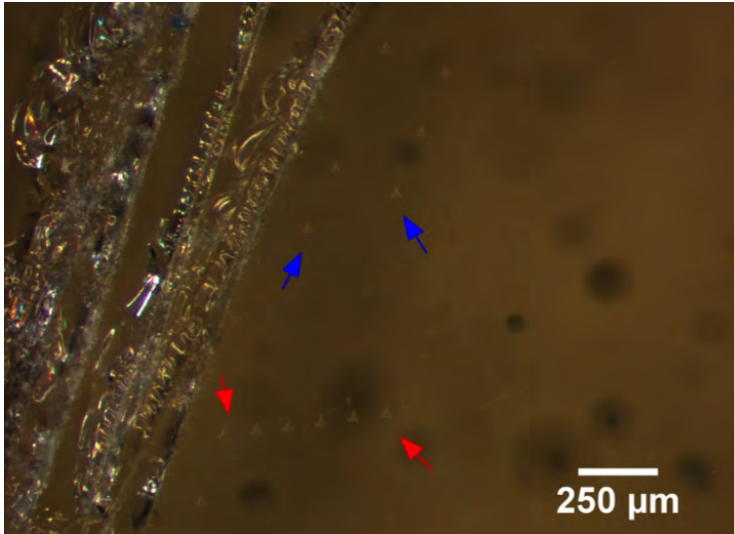


Figure 6.7: Indents under 2.5 N (red arrows) and 2N (blue arrows) in the sample $60\text{KPO}_3\text{-}20\text{FA-}20\text{Al}_2\text{O}_3$.

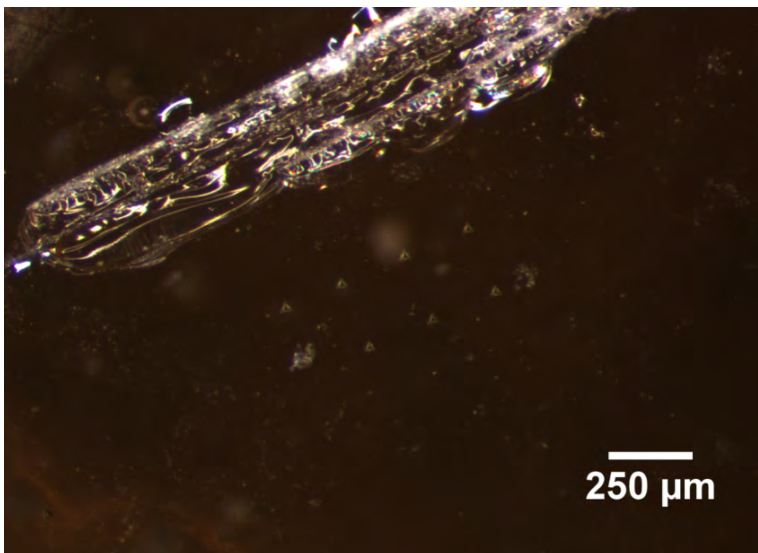


Figure 6.8: Indents under 2 N.

As some samples did not crack under these conditions, new tests were performed with a Knoop indenter under a load of 8.5 N. All the tests were performed using a Nano Indenter MTS G200.

6.4. RESULTS AND DISCUSSION

There is a trend of increasing both elastic modulus and hardness with amounts of slag and Al_2O_3 . The values are quite lower than the values presented by the standard glasses. A standard borosilicate glass has an elastic modulus of approximately 63 GPa and a hardness of 6.4 GPa while for a soda-lime glass these values are 74 GPa and 5.5 GPa, respectively [11]. The results of the samples consisting of slag are shown in Table 6.1, and the results of the samples consisting of fly ash are presented in Table 6.2.

Considering samples with the same amount of KPO_3 , the addition of waste is more effective in increasing both properties than the addition of Al_2O_3 . It can be observed comparing samples 4 and 5 from Table 6.1 or samples 1 and 2 from Table 6.2. Comparing Table 6.1 and Table 6.2 it is noticeable that glasses containing slag possess slightly higher elastic modulus and hardness than the glasses containing fly ash. The different compositions of the raw waste materials could be a possible explanation for this difference. The slag contains 39.17% of CaO (Calcium oxide), while the fly ash contains 4.23% of it. The hardness of a phosphate glass can increase with the CaO content due to densification [12]. Furthermore, the CaO is easily crystallized, and it could explain the fact that materials containing slag can form glasses in a shorter range of compositions than the ones containing fly ash.

Table 6.1: Average elastic modulus and hardness of the samples consisting of slag, based on 25 indents.

Sample	Composition	Average E (Gpa)	Average H (GPa)	Std. Dev. E (GPa)	Std. Dev. H (GPa)
1	75KPO ₃ -12.5Slag-12.5Al ₂ O ₃	41.6	3.42	1.3	0.22
1	75KPO ₃ -12.5Slag-12.5Al ₂ O ₃	41.6	3.42	1.3	0.22
2	70KPO ₃ -15Slag-15Al ₂ O ₃	43.7	4.19	1.6	0.30
3	50KPO ₃ -20B ₂ O ₃ -15Slag-15Al ₂ O ₃	45.5	4.67	2.2	0.51
4	65KPO ₃ -17.5Slag-17.5Al ₂ O ₃	46.7	4.59	0.4	0.08
5	65KPO ₃ -20Slag-15Al ₂ O ₃	49.2	4.85	2.5	0.53
6	60KPO ₃ -20Slag-20Al ₂ O ₃	52.6	5.14	0.9	0.21

Table 6.2: Average elastic modulus and hardness of the samples consisting of fly ash, based on 25 indents.

Sample	Composition	Average E (GPa)	Average H (GPa)	Std. Dev. E (GPa)	Std. Dev. H (GPa)
1	60KPO ₃ -20FA-20Al ₂ O ₃	41.6	3.94	0.9	0.19
2	60KPO ₃ -25FA-15Al ₂ O ₃	42.3	3.99	0.6	0.10
3	55KPO ₃ -35FA-10Al ₂ O ₃	43.5	4.18	0.9	0.18
4	60KPO ₃ -30FA-10Al ₂ O ₃	45.2	4.56	3.1	0.59
5	40KPO ₃ -20B ₂ O ₃ -25FA-15Al ₂ O ₃	48.4	5.02	0.7	0.13

Although somewhat problematic, fracture toughness evaluation can be quickly performed using indentation. If a sharp tip is forced into a bulk sample of a brittle material, radial cracking usually occurs after a critical load has been reached, originating from stress concentrations at the diamond facet edges, which allows an estimate of the fracture toughness based on the maximum indentation load and the crack length [13].

In indentation-based methods with sharp pyramidal indenters, the fracture toughness can be determined from measurements of the lengths of cracks emerging from the residual indentation impression [1].

An equation proposed by Evans [14] and Lawn [15] allows the calculation of K_C based on indentation tests, measuring the length of cracks originating from the edges of the indent impression, determining that:

$$K_C = A \left(\frac{E}{H} \right)^{1/2} \frac{P}{c^{3/2}} \quad (6.2)$$

In which E = Young's modulus, H = hardness, P =load, c = crack length measured from the center of the indent to the crack tip. A is an empirical constant, which varies according to the indenter and the crack geometry [13]. For Berkovich indenter, $A=0.016$ [16]. The representative dimensions of pyramidal indentation fracture testing method are shown in Figure 6.9.

A crack is classified as well developed if $c \gg a$. However, if the radial cracks are not well developed (Figure 6.10), the relation between K_C and $P/c^{3/2}$ stops [17].

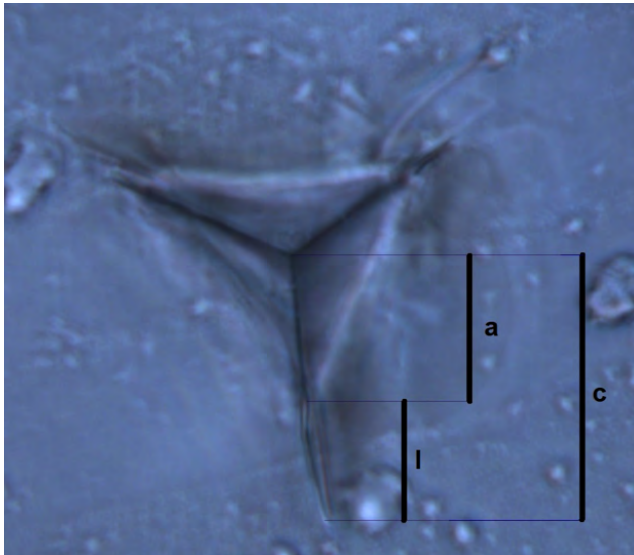


Figure 6.9: Dimensions of a crack induced by a Berkovich indenter, in which $c=a+l$.

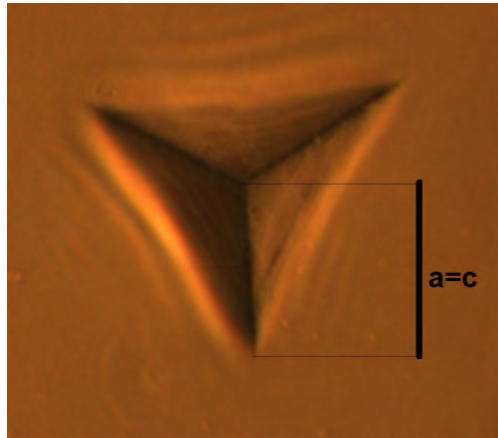


Figure 6.10: Dimensions of a crack induced by a Berkovich indenter, in which $c=a$.

The method presented above can be applied only to well-developed radial cracks. Some authors reported that the linear relation between K_{IC} and $P/c^{3/2}$ stops when $c < 2.5a$ [18, 19]. Other authors claimed that the relation is valid even when c is down to $1.1a$ [20, 21]. The different glass compositions were analysed by optical microscopy and presented huge variations in crack lengths (Appendix E). Some samples, such as $40KPO_3-20B_2O_3-25\text{fly ash}-15Al_2O_3$ showed a crack length equivalent to the impression diagonal, as presented in Figure 6.11.

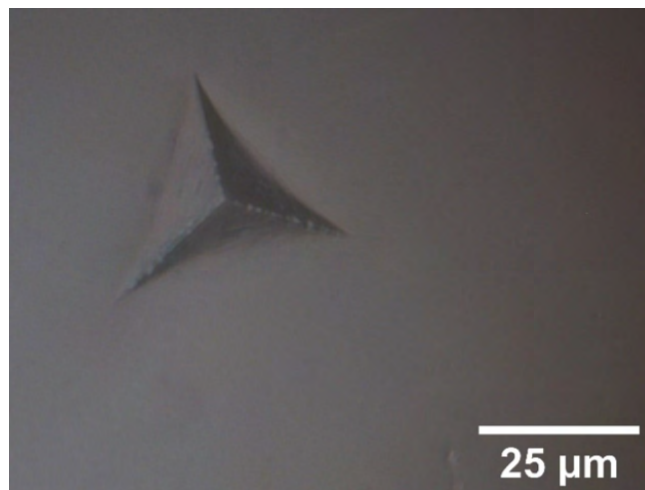


Figure 6.11: Indent in the sample $40KPO_3-20B_2O_3-25\text{fly ash}-15Al_2O_3$.

Other samples, such as $75\text{KPO}_3\text{-}12.5\text{slag-}12.5\text{Al}_2\text{O}_3$, exhibited well developed cracks (Figure 6.12).



Figure 6.12: Indent of the sample $75\text{KPO}_3\text{-}12.5\text{slag-}12.5\text{Al}_2\text{O}_3$.

At least 5 indents were made in each sample. The average dimensions of c and a are shown in Table 6.3. Twelve measurements were used to calculate the average a and c .

Table 6.3: Average dimensions of the crack lengths made with a Berkovich indenter and K_{Ic} calculation based on the equation of Lawn and Evans.

Sample	Sample size	Average a (nm)	Std. Dev. (a)	Average c (nm)	Std. Dev. (c)	c/a	E (GPa)	H (GPa)	K_{Ic} ($\text{MPa} \sqrt{m}$)
$60\text{KPO}_3\text{-}20\text{slag-}20\text{Al}_2\text{O}_3$	6	19.97	1.50	33.70	6.79	1.69	52.6	4.85	0.54
$75\text{KPO}_3\text{-}12.5\text{slag-}12.5\text{Al}_2\text{O}_3$	6	20.17	2.31	41.02	5.30	2.03	41.6	3.42	0.42
$70\text{KPO}_3\text{-}15\text{slag-}15\text{Al}_2\text{O}_3$	6	21.40	1.07	36.69	9.09	1.71	43.7	4.19	0.46
$60\text{KPO}_3\text{-}20\text{FA-}20\text{Al}_2\text{O}_3$	5	19.13	1.13	30.30	7.98	1.58	41.6	3.94	0.62
Soda-lime (reference)	7	14.33	0.48	24.84	7.70	1.73	74.0	5.50	0.94

For the fracture toughness estimation based on the length of the cracks, only defined cracks, with $c/a > 1.1$, were considered. Those were the samples $75\text{KPO}_3\text{-}12.5\text{slag-}12.5\text{Al}_2\text{O}_3$, $70\text{KPO}_3\text{-}15\text{slag-}15\text{Al}_2\text{O}_3$, $60\text{KPO}_3\text{-}20\text{FA-}20\text{Al}_2\text{O}_3$, $60\text{KPO}_3\text{-}20\text{slag-}20\text{Al}_2\text{O}_3$ and soda-lime. For bulk brittle materials, this method provides a calculation within 40% accuracy [8]. The most significant source of error is probably the unknown crack geometry. The models make presumptions about crack geometry, halfpenny type or Palmquist, and this assumption influences the crack area considered. If the real crack geometry is

different than the assumed geometry, the model yield to wrong conclusions [22].

In the case of non-developed cracks, an energy-based model was used, based on the load-displacement curve (Appendix D) associated with fracture. In this work, the shapes of the indentation load-displacement (P-h) curves reveal predominant elastic-plastic deformation, in which the hysteresis is caused mainly by plastic deformation mechanisms. It is opposed to the brittle behaviour, in which the indentation hysteresis is mostly generated by fracture [2]. The maximum displacement into surface of the samples containing fly ash and slag is significantly higher than the soda-lime sample. It agrees with the lower hardness values of these materials, which should allow a higher penetration depth under the same load. In many cases, the images obtained with the use of microscopy can be related to the load-displacement curves. For instance, the sample $40\text{KPO}_3\text{-}20\text{B}_2\text{O}_3\text{-}25\text{FA}\text{-}15\text{Al}_2\text{O}_3$, in which the microscopy does not reveal the presence of cracks, and the load-displacement curve does not show any significant pop-in (Figure 6.13). The sample $60\text{KPO}_3\text{-}20\text{FA}\text{-}20\text{Al}_2\text{O}_3$ shows long cracks, which can be related to the pop-ins of high energy, clearly present in the load-displacement curve of the sample (Figure 6.14).

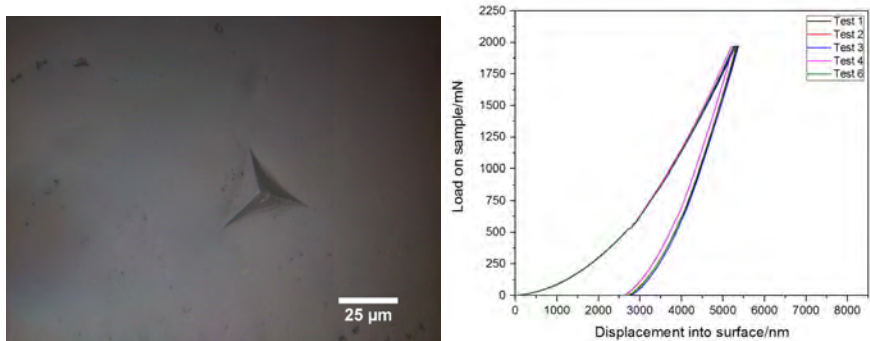


Figure 6.13: Microscopic image and load-displacement curve of the sample $40\text{KPO}_3\text{-}20\text{B}_2\text{O}_3\text{-}25\text{FA}\text{-}15\text{Al}_2\text{O}_3$ under 2N, using a Berkovich indenter.

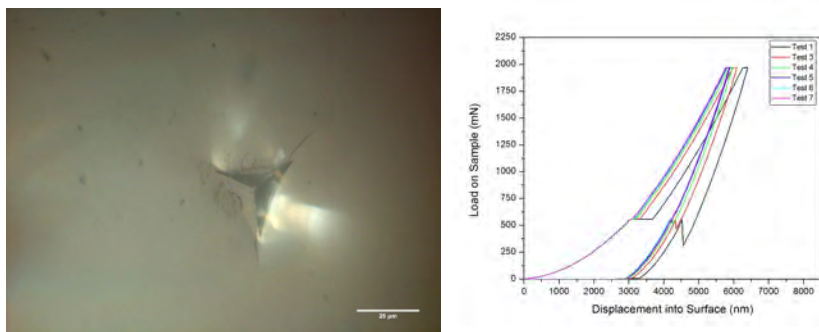


Figure 6.14: Microscopic image and load-displacement curve of the sample $60\text{KPO}_3\text{-}20\text{FA}\text{-}20\text{Al}_2\text{O}_3$ under 2N, using a Berkovich indenter.

Energy-based models can be used to deal with various cracking patterns. A largely applied energy-based model was proposed by Li [23], consisting in extrapolating the loading curve where there is a fracture-induced pop-in. The $P-\delta$ curve is extrapolated from the start point (onset of fracture) to its end point. The area under the load-displacement curve corresponds to the work performed by the indenter during elastic-plastic deformation of the system [23]. The difference between the extrapolated curve and the measured curve is considered as the fracture dissipated energy [17]. The crack formation shifts the loading curve OAB into OAC (Figure 6.13). At the point B, the elastic energy stored in the system is equivalent to OBE. At point C, this energy should correspond to OACE. Thus, the energy difference before and after the crack generation corresponds to the area of ABC [23] shown in Figure 6.15.

This energy difference (U) was calculated for all the tests of all the samples. An example of calculation of U for one glass sample is shown in Figure 6.16. The average value of U for each sample was calculated.

Figure 6.17 shows some important points in the load-displacement curve. In the loading, the curve reaches its maximum depth. During the unloading the elastic recovery, which can be related to the distance between the total indentation depth, (h_t) and residual indentation depth (h_r), takes place. The pop-in, related to the crack formation, occurs at a critical displacement (h_{crit}) point that can be recognized by a horizontal plateau on the curve.

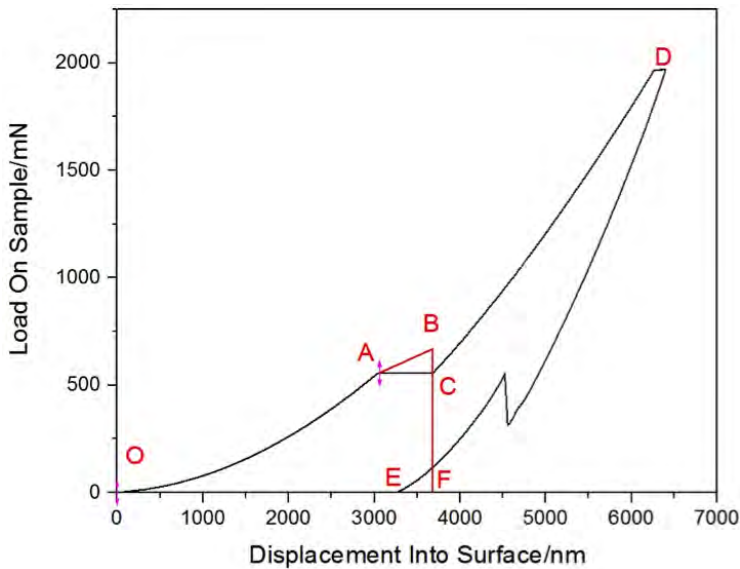


Figure 6.15: Schematic of a load-displacement curve.

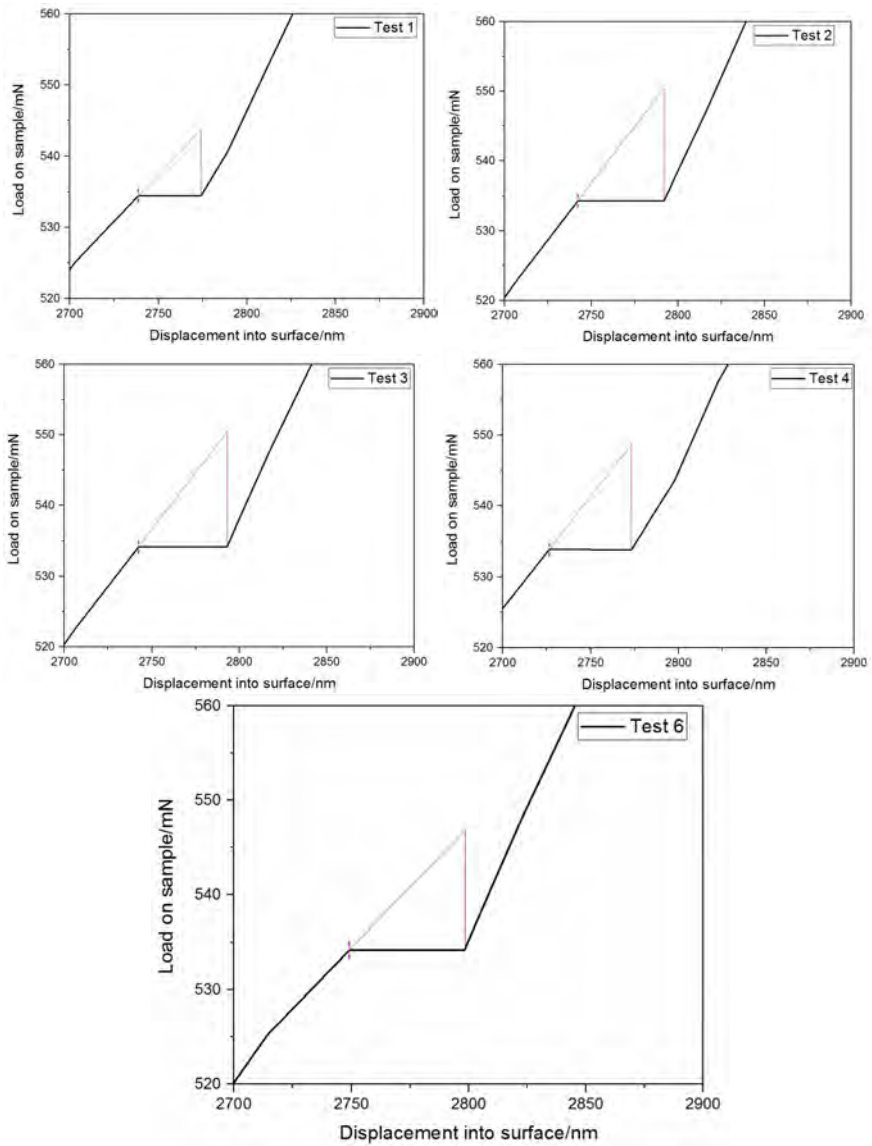


Figure 6.16: Calculation of fracture dissipated energy from the sample $50\text{KPO}_3\text{-}20\text{B}_2\text{O}_3\text{-}15\text{Slag-}15\text{Al}_2\text{O}_3$.

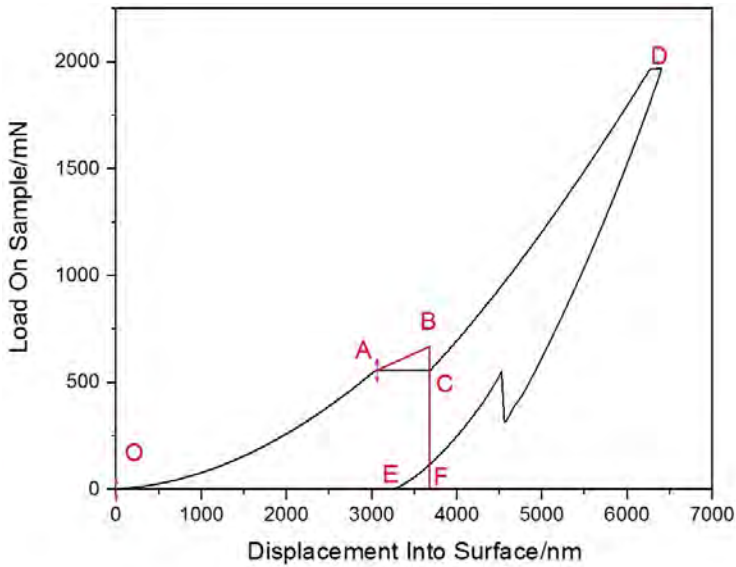


Figure 6.17: Schematics of indentation load-displacement curve with pop-in.

Table 6.4 shows that the elastic recovery of the glasses containing fly ash and slag is higher than the elastic recovery of a silicate glass. The average h_t and average h_r were calculated based on six indentations. The new glasses also present a higher total indentation depth, which is in accordance with their lower hardness, and higher critical displacement, meaning that the formation of cracks starts at higher penetration depths.

Table 6.4: Values of total indentation depth (h_t), residual indentation depth (h_r) and critical displacement (h_{crit}) of the samples.

Sample	Average h_t (nm)	Std. Dev. (h_t)	Average h_r (nm)	Std. Dev. (h_r)	h_t-h_r (nm)	h_{crit} (nm)
40KPO ₃ -20B ₂ O ₃ -25FA-15Al ₂ O ₃	6890	53.18	2899	99.78	3991	3038
60KPO ₃ -20slag-20Al ₂ O ₃	5382	115.72	2624	120.55	2758	2689
55KPO ₃ -35FA-10Al ₂ O ₃	5608	74.56	2812	125.65	2796	2868
75KPO ₃ -12.5slag-12.5Al ₂ O ₃	5746	94.52	2904	97.93	2848	2972
50KPO ₃ -20B ₂ O ₃ -15Slag-15Al ₂ O ₃	5320	44.97	2601	72.16	2719	2739
70KPO ₃ -15slag-15Al ₂ O ₃	5469	71.67	2764	229.14	2705	2836
60KPO ₃ -20FA-20Al ₂ O ₃	6012	208.63	2780	61.98	3232	3051
60KPO ₃ -30FA-10Al ₂ O ₃	5343	36.27	2500	58.91	2843	2601
Soda-lime (reference)	4075	78.45	1948	115.30	2127	2135

Calculating the fracture toughness by measuring the fracture energy requires an estimate of the area F of the crack. For a Berkovich indenter, it can be adapted to [22]:

$$F = \frac{\pi c^2}{4} - \frac{a^2}{2} \tag{6.3}$$

Estimating the fracture toughness can be done according to the following equation, which applies to any crack shape [23]:

$$K_c = \sqrt{\frac{E}{1-\nu^2} \frac{U}{F}} \tag{6.4}$$

In which E= Young's modulus, ν = Poisson ratio, U= crack energy from pop-in and F=crack area. In this work, it was assumed a ν =0.35 for phosphate glasses and ν =0.25 for soda-lime glass. The calculated values of fracture toughness can be found in Table 6.5.

Table 6.5: Kc calculation based on the equation of Li.

Sample	Average a	Average c	c/a	F	U	E	Kc (MPa \sqrt{m})
40KPO ₃ -20B ₂ O ₃ -25FA-15Al ₂ O ₃	17.91	19.53	1.09	139.03	0.52	48.4	0.42
60KPO ₃ -20slag-20Al ₂ O ₃	19.97	33.7	1.69	692.11	0.95	52.6	0.29
*55KPO ₃ -35FA-10Al ₂ O ₃	18.15	18.15	1	93.22	0.49	43.5	*0.51
75KPO ₃ -12.5slag-12.5Al ₂ O ₃	20.17	41.02	2.03	1117.4	3.05	41.6	0.36
*50KPO ₃ -20B ₂ O ₃ -15slag-15Al ₂ O ₃	19.93	19.93	1	111.39	0.32	45.5	*0.39
70KPO ₃ -15slag-15Al ₂ O ₃	21.4	36.69	1.71	827.75	0.71	43.7	0.2
60KPO ₃ -20FA-20Al ₂ O ₃	19.13	30.3	1.58	537.7	7.26	41.6	0.8
*60KPO ₃ -30FA-10Al ₂ O ₃	20.31	20.31	1	117.56	0.186	45.2	*0.28
Soda-lime (reference)	14.33	24.84	1.73	381.69	0.96	74	0.44

*As c=a there is no crack. Therefore, these Kc are not reliable and reflect a pessimistic lower boundary.

Due to the absence of developed cracks in the samples 55KPO₃-35fly ash-10Al₂O₃, 60KPO₃-30fly ash-10Al₂O₃, reference (soda-lime), 50KPO₃-20B₂O₃-15slag-15Al₂O₃ and 50KPO₃-20B₂O₃-15slag-15Al₂O₃, new tests were performed on these samples, using a higher load and another indenter geometry, the Knoop indenter. The cracks were analysed with optical microscopy and scanning electron microscopy. Table 6.6 shows the average dimensions (Figure 6.18) of the indents produced for different samples. The average was calculated based on three indentations.

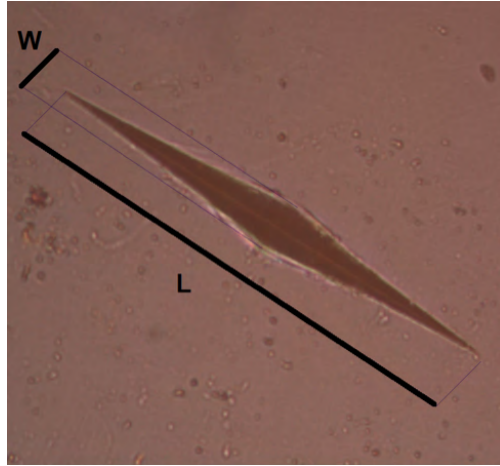


Figure 6.18: Dimensions of a Knoop indent.

Table 6.6: Average dimensions of the Knoop indent in the samples.

Sample	Sample size	L (μm)	Std. Dev. (L)	W (μm)	Std. Dev. (W)
50KPO ₃ -20B ₂ O ₃ -15Slag-15Al ₂ O ₃	4	189.90	6.87	22.00	0.94
40KPO ₃ -20B ₂ O ₃ -25FA-15Al ₂ O ₃	4	261.20	0.09	9.25	0.52
60KPO ₃ -30FA-10Al ₂ O ₃	6	209.20	3.85	21.00	1.17
55KPO ₃ -35FA-10Al ₂ O ₃	5	208.10	1.82	21.46	0.76
Soda-lime (reference)	6	162.42	2.66	21.32	0.11

The dimensions of the samples varied among the different compositions. Remarkably, the soda-lime sample has a low value of L, while the sample containing fly ash and 20% of B₂O₃ has a remarkably low W. Different patterns of cracks were associated to different glass compositions. The sample containing fly ash and 20% of B₂O₃ has radial cracks (Figure 6.19) and an indentation pattern of an arrow, in which the dimension W is kept almost constant for all the extension of the sample.

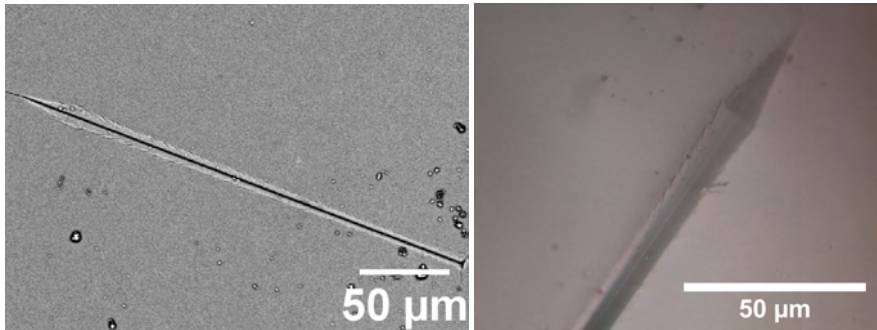


Figure 6.19: Crack pattern of the sample $40\text{KPO}_3\text{-}20\text{B}_2\text{O}_3\text{-}25\text{fly ash-}15\text{Al}_2\text{O}_3$ induced by a load of 8.5N using a Knoop indenter a) indent analysed by SEM b) close-up of the cracks analysed by optical microscopy.

This pattern differs significantly from typical Knoop indents, and no reports of it were found in the literature. Then, new indentation tests were performed under the same conditions as the previous one, but in 4 different directions, as indicated in Figure 6.20. Three indents were performed in each direction, and their load-displacement curves can be found in Appendix D (Figures D15-D18).



Figure 6.20: Sample $40\text{KPO}_3\text{-}20\text{B}_2\text{O}_3\text{-}25\text{fly ash-}15\text{Al}_2\text{O}_3$ divided in four areas tested in different directions in the indentation test.

The different results obtained for different directions strongly indicate an anisotropic behaviour of this glass, as observed in Figure 6.21. More pictures are shown in appendix E (Figure E3).

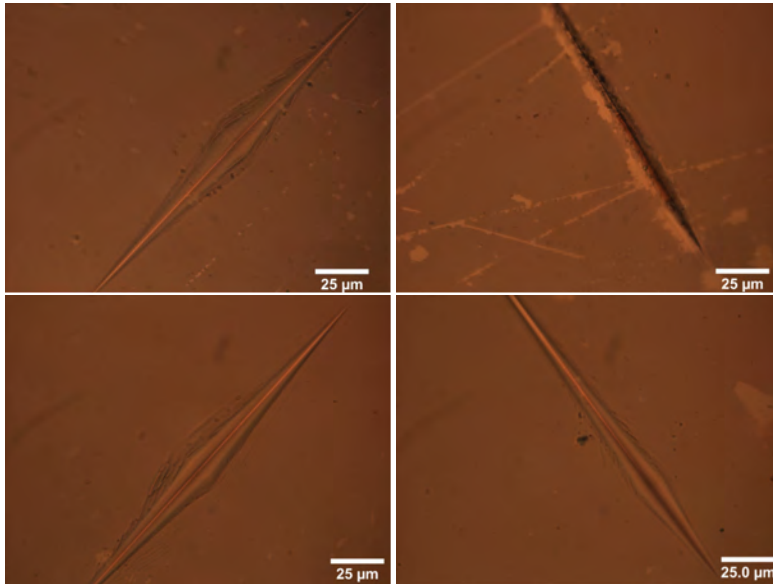


Figure 6.21: Crack patterns of the sample $40\text{KPO}_3\text{-}20\text{B}_2\text{O}_3\text{-}25\text{fly ash-}15\text{Al}_2\text{O}_3$ induced by a load of 8.5N using a Knoop indenter and measured in 4 different orientations.

Anisotropy was already reported for some glasses, such as a metaphosphate glass of composition $12.5\text{Li}_2\text{O-}12.5\text{Na}_2\text{O-}12.5\text{K}_2\text{O-}12.5\text{Cs}_2\text{O-}50\text{P}_2\text{O}_5$ (mol%). In this case, the enhancement of the mechanical properties was attributed to the orientation of -P-O-Ps chains in the glass [24]. Alkali metaphosphate glasses, $50\text{R}_2\text{O-}50\text{P}_2\text{O}_5$ (mol%), in which R2O represents an alkali oxide, possess a structure mainly formed by one-dimensional -P-O-P- chains because their PO_4 tetrahedral units are connected by two oxygen atoms ($n=2$). If these chains are randomly organized, the metaphosphate glasses will be isotropic. However, NaPO_3 and KPO_3 metaphosphate crystals are anisotropic. Both have uniaxially oriented P-O-P chains, NaPO_3 in a spiral orientation and KPO_3 in a zigzag manner. When the chains in glass are uniaxially organized, such as in metaphosphate crystals, anisotropic glasses can be formed [24].

Another work from the same authors reports the occurrence of entropic elasticity in phosphate glasses with highly anisotropic structures [25]. Oxide glasses generally possess three-dimensional networks, consisting of oxygen polyhedra surrounding network-forming cations such as Si^{4+} , B^{3+} and P^{5+} . However, metasilicate and metaphosphate glasses are usually based on chain structures in which oxygen tetrahedra are connected by their two corners and the chains are composed of covalent bonds, with some degree of ionic character. Typical metaphosphate glasses have chains containing between 40 and 100 P-tetrahedra, ended by hydroxyl groups or modifiers such as alkali ions [25]. The chains connect with each other by ionic bonding through modifiers. It is expected that oxide glasses with a rubberlike structure containing highly polymerized chains with strong (covalent) intrachain bonds, weaker interchain interactions and moderate crosslinking may show entropic elasticity [25]. These glasses can self-organize into oriented structures by application of uniaxial stress, and then return to their original configurations

when the stress is removed. Figure 6.22 shows a molecular model and a possible change in structure under deformation.

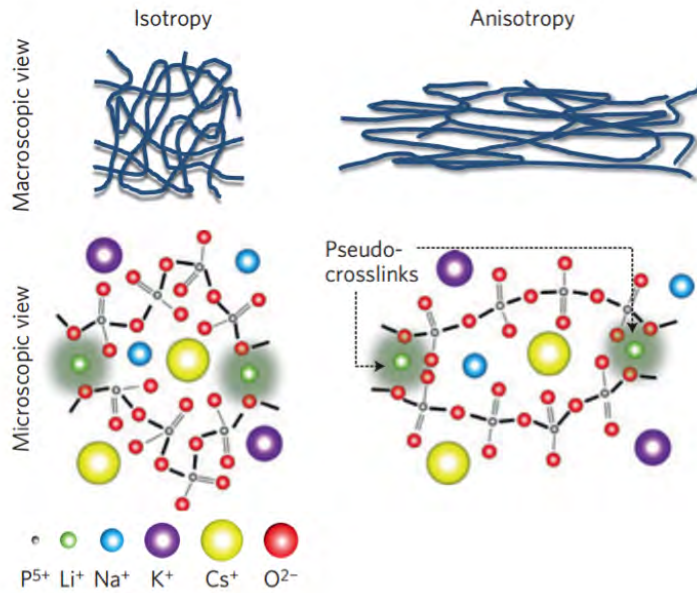


Figure 6.22: Model structure of an oxide glass with a preferentially oriented one-dimensional structure [25].

Further investigation is required to understand the anisotropic behaviour of the sample containing 20% of B_2O_3 and fly ash. One hypothesis is that, like in the case of the rubbery glass reported by Inaba, the addition of modifiers weakly bonded with oxygen could reduce interchain interactions and increase the flexibility of the chains. These modifiers are mainly the compounds with lower bond strength, such as MgO , CaO and SrO . Some indents in the soda-lime glass possess extended cracks on both sides with interference fringes, indicating the presence of lateral cracks (Figure 6.23).

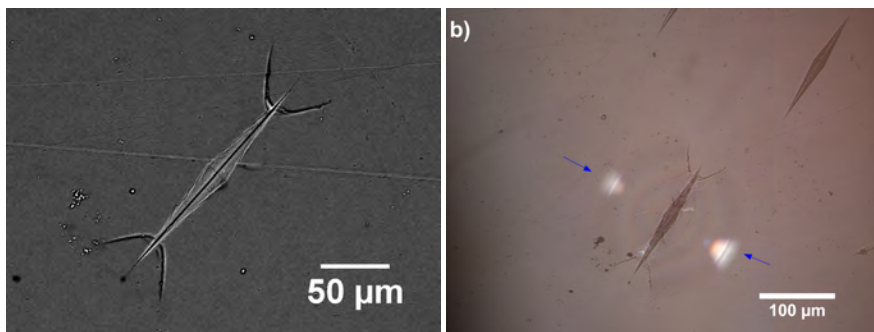


Figure 6.23: Crack pattern of a silicate glass induced by a load of 8.5 N using a Knoop indenter a) indent analysed by SEM b) interference fringes (blue arrows).

The samples containing 30% and 35% of fly ash present similar patterns of cracks with edge cracks (Figures 6.24 and 6.25).

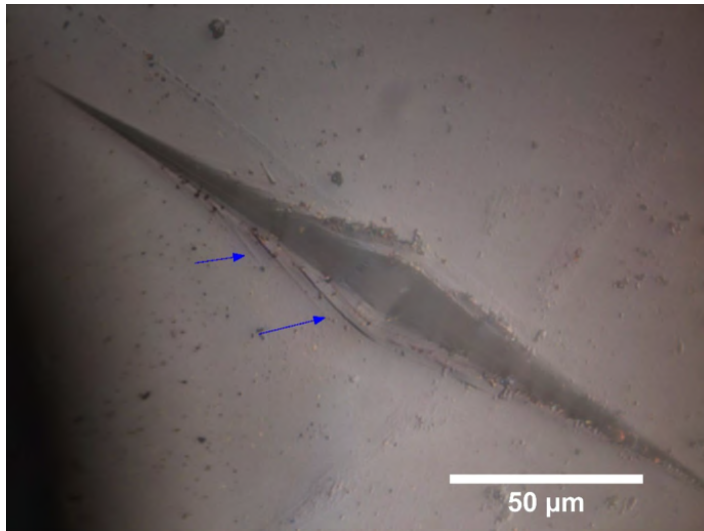


Figure 6.24: Crack pattern of $60\text{KPO}_3\text{-}30\text{FA-}10\text{Al}_2\text{O}_3$ induced by a load of 8.5 N using a Knoop indenter. Arrows point to the edge cracks.

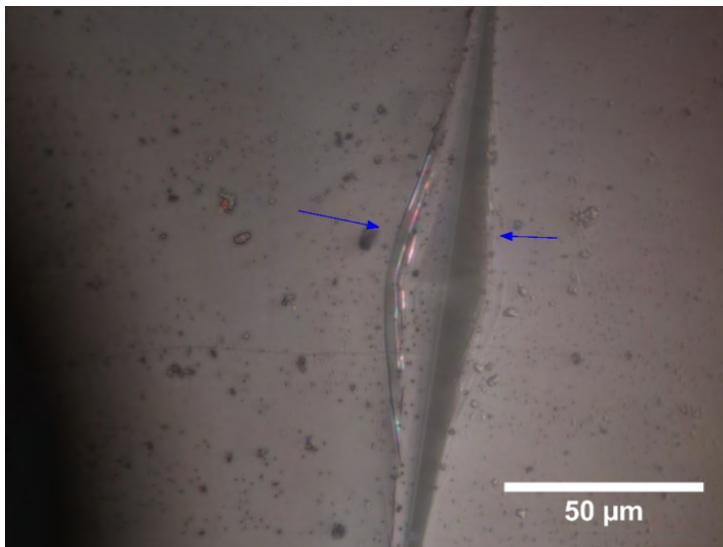


Figure 6.25: Crack pattern of $55\text{KPO}_3\text{-}35\text{FA-}10\text{Al}_2\text{O}_3$ induced by a load of 8.5 N using a Knoop indenter. Arrows point to the edge cracks.

Analysing the load-displacement curves of the samples (appendix D) it is possible to note that for some samples, as $40\text{KPO}_3\text{-}20\text{B}_2\text{O}_3\text{-}25\text{FA-}15\text{Al}_2\text{O}_3$, there are no long steps in the loading curves, while other samples, such as $50\text{KPO}_3\text{-}20\text{B}_2\text{O}_3\text{-}15\text{Slag-}15\text{Al}_2\text{O}_3$, show a long step. The length of the step can be related to how much the indenter abruptly advances into the material. While brittle fracture is associated to systems with an indentation hysteresis caused mainly by fracture, for the elastic-plastic systems the hysteresis is caused primarily by plastic deformation mechanisms [2]. The cracking pattern of the sample containing 20% of B_2O_3 and slag is characterized by a well-defined L dimension and medium and lateral cracks forming the W dimension (Figure 6.26). However, for the same sample and also other samples in this work, the indent looks asymmetric, as can be observed in Figure 6.26 and in Figure E1. It can be an indication that the samples may not have been sufficiently flat. Thus, it is recommended to repeat the nanoindentation test for these samples.

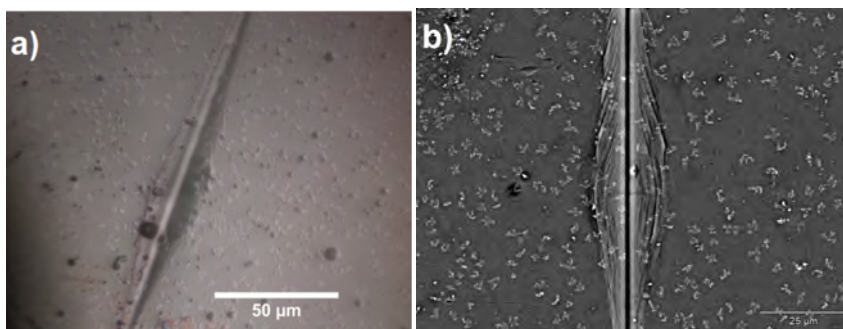


Figure 6.26: Crack pattern of $50\text{KPO}_3\text{-}20\text{B}_2\text{O}_3\text{-}15\text{Slag-}15\text{Al}_2\text{O}_3$ induced by a load of 8.5N using a Knoop indenter analysed by a) optical microscope b) scanning electron microscope.

6.5. CONCLUSIONS

DUE to its flaw geometry, the Knoop indenter produces a relatively clean crack. These controlled flaws allow the observation of different mechanical responses for glasses with distinct compositions. In this work, the Knoop indenter was used to produce controlled cracks. However, it can also be used to measure fracture toughness with bars in bending, a method known as Surface Crack in Flexure (SCF) [26]. In this test, loads of 19.6N to 29.4N are used to induce cracks. The indentation residual stress and lateral cracks are removed by polishing and subsequently the sample is broken in flexure [26]. Fractography is used to measure the flaw size, and the fracture toughness can be calculated from it. This test was the primary method used to prepare the world's first standard reference material for fracture toughness, K_{IC} [26] and its application is suggested as a direction for future works about the same topic.

The calculation of the fracture toughness based on nanoindentation without fractographic analysis provides a straightforward examination and the evaluation of a mechanical property related to toughness, the indentation toughness K_c . However, the results should be carefully interpreted instead of directly being associated to results obtained from other techniques. They should not be related to K_{IC} as the removal of resid-

ual stresses and damage zones is not performed. The indentation technique assumes that the indentation deformation energy per unit area absorbed to a critical penetration depth could be related to the fracture energy needed for fracture initiation.

Low brittleness glasses could be developed by modifying the chemical composition to improve the glass deformation ability. The permanent deformation in glass can be associated with densification and flow. The glass composition or the shape of the indenter can influence the mechanism of deformation and indentation performed with a Knoop indenter highlighted the different patterns of crack exhibited by the glasses. The glasses containing boron oxide, mainly the one containing fly ash, showed a cracking pattern significantly different than the patterns usually found for silicate glasses. For this glass, the minor diagonal is not developed.

Crack-resistant glasses generally have enough free space to release the mechanical stress without cracking by atom displacements. It results in plastic deformation chiefly by densification and, to lesser extent, by shear deformation [27]. Thus, crack-resistant oxide glasses should be related to less-packed structures. The Poisson's ratio (ν) was already used to represent the available free volume in the structures of glasses [28]. In addition to the packing (atomic level) structure, the electronic structure and chemical bonding also affect the mechanical properties [29]. The calculation of the indentation toughness using Berkovich indentation varied widely between the method that considers the fracture dissipated energy and the crack length and the method that considers only the crack lengths. However, the results from both tests points that the glasses with higher amounts of KPO_3 have a lower indentation toughness, which however increases with the addition of the waste material, mainly fly ash. Using the energy-based model, some glasses containing fly ash presented a higher indentation toughness than the silicate glass, due to their small crack lengths in relation to their high fracture dissipated energy.

REFERENCES

- [1] Sebastiani, M., Johanns, K.E., Herbert, E.G., Pharr, G.M. (2015). Measurement of fracture toughness by nanoindentation methods: Recent advances and future challenges. *Current opinion in solid state and materials science* 19, p. 324-333.
- [2] Oyen, M.L., Cook, R.F. (2009). A practical guide for analysis of nanoindentation data. *Journal of the mechanical behavior of biomedical materials* 2, p. 396-407.
- [3] Makishima, A., Mackenzie, J.D. (1973). Direct calculation of Young's modulus of glass. *Journal of non-crystalline solids*, 13. p. 35-45.
- [4] Plucinski, M., Zwanziger, J.W. (2015). Topological constraints and the Makishima Mackenzie Model. *Journal of non-crystalline solids* 429, p. 20-23.
- [5] Yamane, M., Mackenzie, J.D. (1974). Vickers Hardness of glass. *Journal of non-crystalline solids* 15, p.153-164.
- [6] Makishima, A., Mackenzie, J.D. (1975). Calculation of bulk modulus, shear modulus and poisson's ratio of glass. *Journal of non-crystalline solids* 17, p.147-157.
- [7] Rouxel, T. (2007). Elastic properties and short-to medium-range order in glasses. *Journal of the american ceramic society*, 90 [10]. p. 3019-3039.
- [8] Volinsky, A.A., Vella, J.B., Gerberich, W.W. (2003). Fracture toughness, adhesion and mechanical properties of low-K dielectric thin films measured by nanoindentation. *Thin*

solid films, 429. pp.201-210.

- [9] Guo, H., Jiang, C.B., Yang, B.J., Wang, J.Q. (2018). On the fracture toughness of bulk metallic glasses under Berkovich nanoindentation. *Journal of Non-Crystalline Solids*, 481, p.321-328.
- [10] Oliver, W.C., Pharr, G.M. (1992). An improved technique for determining hardness and elastic modulus using load and displacement sensing indentation experiments. *Journal of Materials Research*, 7, p. 1564-1583.
- [11] Chorfa A., Madjoubi, M.A., Hamidouche, M., Bouras, N., Rubio, J., Rubio, F. (2010). Glass hardness and elastic modulus determination by nanoindentation using displacement and energy methods *Ceramic-Silikaty*, 54, p. 225-234.
- [12] Rao, G.V., Shashikala, H.D. (2014). Optical and mechanical properties of calcium phosphate glasses. *Glass Physics and Chemistry*, 40, p. 303-309.
- [13] Vella, J.B., Adhichetty, I.B., Junker, K., Volinsky, A.A. (2003). Mechanical properties and fracture toughness of organo-silicate glass (OSG) low-k dielectric thin films for microelectronic applications, 120, p. 487-499.
- [14] Evans, A.G., Charles, E.A. (1976). Fracture Toughness Determination by Indentation. *Journal of the American ceramic society*, 59. p. 371-372.
- [15] Lawn, B.R., Evans, A.G., Marshall, D.B. (1980). Elastic/Plastic Indentation Damage in Ceramics: The Median/Radial Crack System. *Journal of the American ceramic society*, 63. pp.574-581.
- [16] Chen, J., Bull, S.J. (2006). Assessment of the toughness of thin coatings using nanoindentation under displacement control. *Thin solid films*, 494. p.1-7.
- [17] Chen, J. (2012). Indentation-based methods to assess fracture toughness for thin coatings. *Journal of physics D: applied physics*, 45. p.1-15.
- [18] Laugier, M. T. (1987). Palmqvist indentation toughness in Wc-Co composites. *Journal of materials science letters*. v.6, p.897-800.
- [19] Niihara, K., Morena, R., Hasselman, D.P.H. (1982). Evaluation of K_{Ic} of brittle solids by the indentation method with low crack-to-indent ratios. *Journal of materials science letters*. V.1, p.13-16.
- [20] Jang, J., Wen, S., Lance, M.J., Anderson, I.M., Pharr, G.M. (2004). Cracking and phase transformation in silicon during nanoindentation. *MRS Proceedings*, v.795, U8.15.
- [21] Scholz, T., Schneider, G.A., Munoz-Saldana, J., Swain, M.V. (2004). Fracture toughness from submicron derived indentation cracks. *Applied Physics Letters*, v.84, issue 16, p. 3055-3057.
- [22] Schiffmann, K.I. (2011). Determination of fracture toughness of bulk materials and thin films by nanoindentation: comparison of different models. *Philosophical magazine*, v.91:7-9. p. 1163-1178.
- [23] Li, X., Diao, D., Bhushan, B. (1997). Fracture mechanisms of thin amorphous carbon films in nanoindentation. *Acta materialia*, v.45, 11. p. 4453-4461.
- [24] Endo, J., Inaba, S., Ito, S. (2015). Mechanical properties of anisotropic glass. *Journal of the american ceramic society*. v. 98, p. 2767-2771.
- [25] Inaba, S., Hosono, H., Ito, S. (2015). Entropic shrinkage of an oxide glass. *Nature Materials*, v. 14, p. 312-317.
- [26] Quinn, G.D. (2016). *Fractography of ceramics and glasses*. National Institute of Standards and Technology.

- [27] Rosales-Sosa, G.A., Masuno, A., Higo, Y., Inoue, H. (2016). Crack resistant Al_2O_3 - SiO_2 glasses. Scientific reports, p. 1-8.
- [28] Rouxel, T., Ji, H., Hammouda, T., Moréac, A. (2008). Poisson's ratio and the densification of glass under high pressure. Physical Review Letters, 100, 225501.
- [29] He, Q., Cheng, Y., Ma, E., Xu, J. (2011). Locating bulk metallic glasses with high fracture toughness: Chemical effects and composition optimization. Acta Materialia 59, p. 202-215.

7

CONCLUSION AND PERSPECTIVES FOR FUTURE WORK

This chapter summarizes the importance of the innovative low-melting glasses containing oxides present in fly ash and blast furnace slag and suggests applications for the developed glasses based on their measured properties. Furthermore, it suggests some directions for future research.

7.1. SUMMARIZING THE PROPERTIES

TABLE 7.1 compares the properties of soda-lime glass with other construction materials. Besides transparency, which is a feature only provided by glass, this material possesses as a benefit a thermal expansion coefficient lower than concrete and steel. However, the high price and the lower fracture toughness of glass are considerable drawbacks. The low values of fracture toughness exhibited by glass and concrete are related to the low resistance of these materials to brittle fracture when a crack is present. On the other hand, the high fracture toughness of steel is related to its capacity to undergo ductile fracture. In practice, it means that when a structure slowly reaches the limits of its carrying capacity it provides warn by deformation, instead of suddenly collapses [1].

Table 7.1: The properties of different construction materials: soda-lime glass, stee and concrete [2].

Property/Material	Soda-lime glass	Steel, mild 1020	Concrete
Price	\$ 1.35/kg	\$ 0.50/kg	\$ 0.05/kg
Young's Modulus (E, GPa)	65	210	48
Poisson's ratio (ν)	0.23	0.29	0.20
Fracture Toughness (K_{Ic} , MN m ^{-3/2})	0.71	140	0.75
Thermal expansion (α , 10 ⁻⁶ /C)	8.8	14	11

Based on the results obtained from the characterization techniques, the properties of the phosphate glasses developed in this work are compared to the properties of benchmark glasses in Table 7.2. However, we recommend the repetition of the preparation of samples and the nanoindentation tests, in order to confirm that preparation procedures, such as polishing and annealing, did not affect the results. The price was calculated based on the use of pure compounds, assuming that fly ash and slag are free of cost. The addition of B₂O₃ increases the final price due to the price of this compound. However, even with the addition of B₂O₃, the final price of the phosphate glasses is still significantly lower than the price of the silicate glasses.

The glass transition temperature of the glasses containing wastes increases with the amount of waste incorporated in the composition. As a consequence, the melting temperature also increases. For the phosphate glasses, the melting temperature, which is presented in Table 7.2, corresponds to the temperature in which the viscosity of the liquid is low enough to be quenched from the crucible to the mould.

Table 7.2: The properties of the phosphate glasses containing wastes in relation to the properties of soda-lime and borosilicate glasses.

Property	Phosphate glasses containing waste	Soda-lime glass	Borosilicate glass
Price	€ 63-93/kg	€ 166/kg	€ 180/kg
Melting temperature	1100 °C- 1350 °C	1500 °C	1650 °C
Glass transition temperature	443 °C- 490 °C	572 °C	545 °C
Elastic modulus	41.6 GPa- 52.6 GPa	74 GPa	63 GPa
Hardness	3.94 GPa- 5.15 GPa	5.5 GPa	6.4 GPa
Thermal expansion	$5.71 \times 10^{-6} /^{\circ}\text{C}$ - $14.06 \times 10^{-6} /^{\circ}\text{C}$	$9 \times 10^{-6} /^{\circ}\text{C}$	$7.65 \times 10^{-6} /^{\circ}\text{C}$
Fracture Toughness	0.2-0.8 MPa \sqrt{m}	0.44 MPa \sqrt{m}	*

*not measured.

For the benchmark glasses, the exhibited melting temperatures are related to temperatures in which these glasses are industrially melted and possess a viscosity low enough to be moulded. The melting temperatures of silicate and borosilicate glasses were obtained from the literature [3]. The melting temperatures of all the developed compositions are still are low in relation to the melting temperature of borosilicate and soda-lime glasses, as shown in Table 7.2. The production of glasses with lower melting temperatures demands less energy, and, as a consequence, the environmental impact and manufacturing cost decrease. All the produced glasses possess lower elastic modulus and hardness than the values presented for the standard silicate glasses, which were obtained from the literature [4]. The fracture toughness of the developed glasses can reach higher values than the fracture toughness of a standard silicate glass, in a situation where both values were experimentally measured. It is one of the main drawbacks of using glass as a construction material.

The properties of the glasses developed in this work vary in a large range, proving that the development of compositions with designed properties turns glass into a versatile material, able to fulfill many different demands. Table 7.3 summarizes the properties measured for some of these samples.

Table 7.3: Properties of glasses of different compositions.

Compositions Mol(%)	60KPO ₃ -20slag-20Al ₂ O ₃	70KPO ₃ -15slag-15Al ₂ O ₃	50KPO ₃ -15Slag-15Al ₂ O ₃ -20B ₂ O ₃	75KPO ₃ -12.5slag-12.5Al ₂ O ₃	60KPO ₃ -20FA-20Al ₂ O ₃	40KPO ₃ -25FA-15Al ₂ O ₃ -20B ₂ O ₃	60KPO ₃ -30FA-10Al ₂ O ₃	70KPO ₃ -15FA-15Al ₂ O ₃
Sample	1	2	3	4	5	6	7	8
O/P ratio	5.09	4.51	8.21	4.21	5.16	7.85	*	4.73
T _g (°C)	490	453	451	443	484	472	460	*
T _x -T _g (°C)	36	67	190	133	80	168	70	*
$\alpha \times 10^{-6} /^{\circ}\text{C}$	10.26	12.77	7.50	15.22	*	5.71	10.42	14.06
K _c	0.29	0.2	0.39	0.36	0.8	0.42	0.28	*
Color	Brown/Colorless	Amber/Colorless	Blue/Colorless	Blue/Colorless	Yellow	Green	Green	Yellow

*not measured.

In most of these compositions, P_2O_5 is the main compound, the glass former. The addition to other components, such as aluminium oxide, boron oxide or other oxides originated from the by-products, produce glasses with a higher O/P ratio. Investigations of the short- and intermediate-range structure of the glasses were not performed, but are encouraged, mainly in order to support a better understanding of the mechanical and optical properties.

These multicomponent glasses were not previously reported and the complexity of the compositions leads to unique properties, such as the blue colour shown by sample 3, possibly related to the S_3^- occupying the space between the glass networks, which is a scenario reported only a few times in the literature. The mechanical measurements of sample 6 suggest that it is an anisotropic glass. While glasses are mostly isotropic materials, anisotropy is not incompatible with a lack of crystalline order.

7.2. ANISOTROPIC GLASSES

BRITTLENESS is the main drawback of glass, since the presence of very small defects has a drastic effect on its strength. In order to enhance the fracture toughness, glasses have been used as a basis for composites. In the composites, anisotropic particles are dispersed or precipitated uni-directionally in the glass matrix. Nevertheless, these types of composites are hardly transparent. For the plastics composed of molecules with chain structures, the strength and Young's modulus increase when the molecules are oriented uni-axially [5]. It is predicted that the fracture toughness of glass can be improved, while keeping the transparency, by aligning nano-meter-sized chain molecules in the glass.

Despite the assumption that an anisotropic structure influences the mechanical properties of a glass, a deeper understanding of this relationship remains unknown. As the indentation measurements show that sample 6 behaves differently when indented in different directions, we suggest for future works an investigation about how this singularity could be used to enhance the mechanical performance of a glass. The anisotropy could optimize the performance of the glass if the main loading direction applied to it could be arranged along the tougher direction of the glass, achieving advantageous properties in relation to isotropic materials. As only sample 6 and sample 3 had indentations measures performed in multiple directions and the other samples had their fracture toughness measured only in one direction, it is recommended to measure this property in different orientations for all the samples. Figures 7.1 and 7.2 show the contrast between the indentation patterns in an anisotropic glass, $40KPO_3-20B_2O_3-25FA-15Al_2O_3$, and an isotropic glass, $50KPO_3-15Slag-15Al_2O_3-20B_2O_3$.

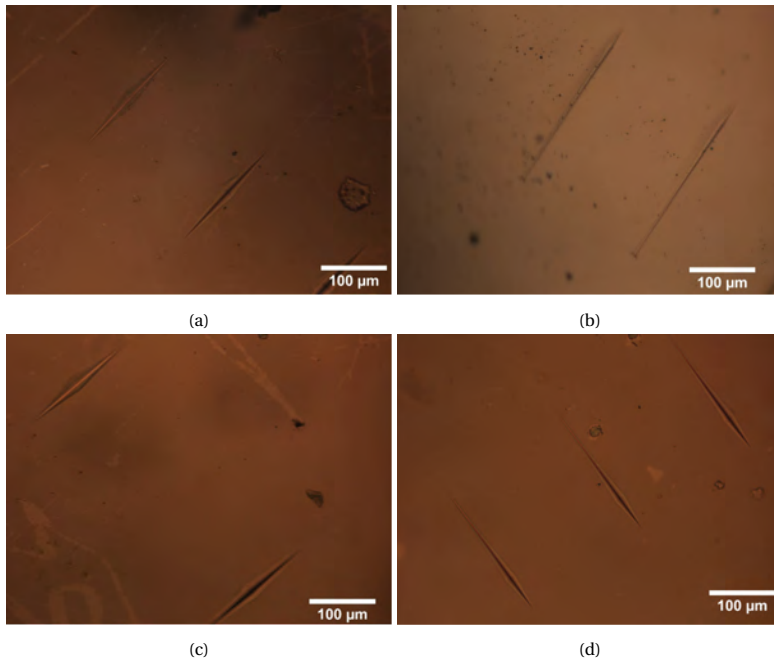


Figure 7.1: Crack patterns of the sample $40\text{KPO}_3\text{-}20\text{B}_2\text{O}_3\text{-}25\text{FA-}15\text{Al}_2\text{O}_3$ induced by a load of 8.5N using a Knoop indenter and performed at every 90 degrees: 1 (a), 2(b), 3(c) and 4 (d).

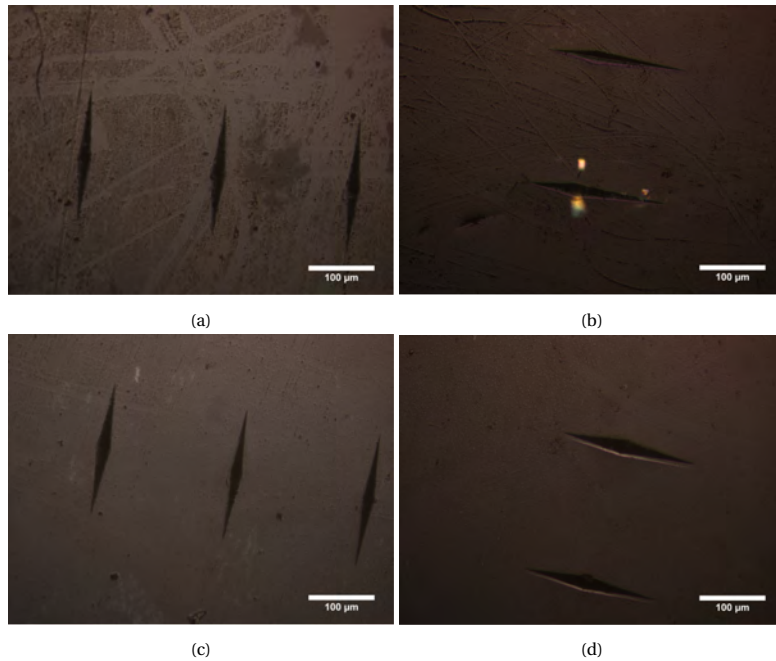


Figure 7.2: Crack patterns of the sample $50\text{KPO}_3\text{-}15\text{Slag-}15\text{Al}_2\text{O}_3\text{-}20\text{B}_2\text{O}_3$ induced by a load of 8.5N using a Knoop indenter and performed at every 90 degrees: 1 (a), 2(b), 3(c) and 4 (d).

7.3. LOW-MELTING POINT GLASSES, COLORLESS GLASSES AND COMPOSITIONS PRODUCED WITH PURE REAGENTS

ALL the produced samples have a low T_g in relation to a soda-lime or a borosilicate glass. The drastic reduction of the melting temperature allows to save energy during the manufacture process. Along with the incorporation of by-products, it contributes to fill a current appeal for a more sustainable glass manufacturing process. Combined with a high thermal stability and a coefficient of thermal expansion comparable or lower than the standard glasses, these compositions are candidates to applications in building engineering. The samples 1, 3, 6 and 7 combine all these properties and could be used, for instance, for the manufacturing of glass bricks.

Although advantageous from a perspective of saving emissions and energy, the addition of by-products to the glass can be problematic as it introduces to the batch many components usually avoided by glass manufacturers, such as iron oxide. An alternative to avoid the contamination of furnaces, is to melt the glasses excluding the components present in the lowest concentrations. Table 7.4 shows some compositions, excluding the components existing in concentrations lower than 0.02 mol%, as it is assumed that they do not add beneficial properties to the material. It is suggested to test melt the compositions excluding even more compounds. Furthermore, the sample $60\text{KPO}_3\text{-}20\text{slag-}20\text{Al}_2\text{O}_3$ is a promising result, as it shows that the glasses containing slag can be colorless, when melted in certain conditions.

Table 7.4: Compositions of the samples expressed in mol%, excluding components present in concentrations lower than 0.02 mol%.

Sample/ Compound	70KPO ₃ - 15FA- 15Al ₂ O ₃	60KPO ₃ - 20FA- 20 Al ₂ O ₃	40KPO ₃ - 25FA- 15Al ₂ O ₃ - 20B ₂ O ₃	60KPO ₃ - 20slag- 20Al ₂ O ₃	70KPO ₃ - 15slag- 15Al ₂ O ₃	50KPO ₃ - 15Slag- 15Al ₂ O ₃ - 20B ₂ O ₃	75KPO ₃ - 12.5slag- 12.5Al ₂ O ₃
SiO ₂	14.97	17.47	21.17	12.06	8.78	8.15	7.53
B ₂ O ₃			18.88			22.79	
Al ₂ O ₃	20.62	24.40	19.57	18.01	17.52	19.71	15.19
Na ₂ O			0.26	0.10	0.08	0.09	0.09
K ₂ O	31.92	27.53	18.06	27.42	30.63	20.08	33.42
MgO	0.65	0.72	0.86	4.08	3.07	2.80	2.68
CaO	1.33	1.42	1.89	13.60	10.59	10.39	9.21
SrO	0.02	0.02	0.03				
TiO ₂	0.23	0.30	0.39	0.26	0.22	0.20	0.18
MnO	0.02	0.02	0.02	0.09	0.06	0.06	0.06
SO ₃	0.02	0.02	0.01	0.10	0.08	0.02	0.04
Fe ₂ O ₃	0.85	1.05	1.44	0.09	0.07	0.07	0.06
P ₂ O ₅	29.01	26.69	17.22	24.03	28.74	15.58	31.30
GeO ₂		0.03					
BaO				0.02		0.02	0.20
ZnO				0.10			

Besides forming glass in a larger range of compositions, the samples consisting of fly ash are also less susceptible to changes in melting conditions and to the introduction of further elements. As suggestion for future work, we propose the development of glass-ceramics consisting of fly ash and slag. It is an alternative to incorporate even higher amounts of wastes than the amounts incorporated by glasses. Despite a possible loss in the transparency, the improved mechanical strength and an attractive visual aspect could find application in construction, as the manufacture of tiles and the replacement of natural stones. The colour of the samples containing slag originates principally from the presence of sulfur. Eliminating the SO₃, and other components present in low concentrations in the formula, would be an attempt to produce colourless glasses, even at melting temperatures as low as 1250 °C. In contrast to the samples containing slag, melting the samples containing fly ash at a higher temperature did not affect the final color of the glasses. Eliminating all the components present in concentrations lower than 1 mol%, the Fe₂O₃ would be eliminated from the sample 8. It brings a possibility to produce colorless glasses containing fly ash, and simplifying the composition to a formula containing only SiO₂, Al₂O₃, K₂O, CaO and P₂O₅. We encourage the reproduction of the samples using pure reagents and eliminating the impurities present in the by-products, as well as a comparison of the properties of these glasses with the ones produced with the incorporation of fly ash and slag.

The combination of low glass transition temperatures, high thermal stability and low thermal expansion, along with the production of samples based on the nominal composition excluding impurities and using high purity reagents, instead of the by-products, could produce samples used for more advanced technologies. For instance, these glasses

are candidates to be 3D printed, mainly samples 3 and 6, with the lowest coefficients of thermal expansion. This promising process has distinct advantages over traditional methods of fabrication. Notably, the fact that 3D printing is capable of producing complex shapes that other manufacturing methods cannot handle, allows the production of components such as glass connectors. 3D printing can design and print components with variable thicknesses and complex inner features, unlike glassblowing, where the inner features reflect the outer shape [6]. However, glass is inherently a very difficult material to work with. It requires a high-temperature system, above 1000°C, and the viscosity changes significantly with temperature, requiring precise control of the temperature at all stages of the process [6]. The high melting temperature of glasses as fused silica combined with a high thermal expansion, that can lead to cracking, are drawbacks that have made standard glass compositions unreachable to three-dimensional printing.

7.4. HIGH EXPANSION GLASSES

HIGH expansion glasses with good chemical durability, such as samples 2 and 8, are desirable for applications such as bonding with plastics or metals, since the thermal expansion coefficient of the joining materials should be very similar. For instance, the samples have a CTE very similar to a 446 stainless steel, which possess an expansion coefficient of about $11.4 \times 10^{-6} / ^\circ\text{C}$ [7]. Samples with concentrations of KPO_3 higher than 70 mol%, such as sample 4, should not be designed to applications that require a high water resistance. Finding a concentration of P_2O_5 low enough to produce a durable material but high enough to keep the high expansion is a key for applications like glass-to-metal seals. Glasses with high thermal expansion could have the potential to optimize the effect of the tempering process, that uses the stress introduced during the cooling of the glass to create compression at the surface and to keep the glass interior under tension, increasing its strength. Thin borosilicate glass cannot be tempered in an ordinary tempering furnace because it requires very high temperatures and the very low coefficient of expansion of the glass limits the residual stresses that can be obtained. The temperature difference that can be achieved by a traditional air quench is not enough to cause high stress levels in the finished glass. An increased thermal expansion could favour this process.

REFERENCES

- [1] Nijssse, R. 2003. Glass in structures: Elements, concepts, designs. Birkhäuser.
- [2] Roylance, D. 1996. Mechanics of Materials. Wiley.
- [3] de Jong, B. H. W. S. 1989. Glass. In: Ullmann's Encyclopedia of Industrial Chemistry"; 5th edition, v. A12, VCH Publishers, Weinheim, Germany.
- [4] Chorfa A., Madjoubi, M.A., Hamidouche, M., Bouras, N., Rubio, J., Rubio, F. 2010. Glass hardness and elastic modulus determination by nanoindentation using displacement and energy methods Ceramic-Silikaty, 54, p. 225-234.
- [5] Endo, J., Inaba, S., Ito, S. 2015. Mechanical properties of anisotropic metaphosphate glass. Journal of the American ceramic society. p. 1-5.
- [6] Bradley, D. 2015. 3D printing transparent glass. Materials today, v.18, Issue 10. p. 531-532.

[7] Brow, R.K., Watkins, R.D. 1991. High expansion, lithium corrosion resistant sealing glasses. United States patent.

ACKNOWLEDGEMENTS

MY PhD research was possible due to a grant from the Brazilian National Council for Scientific and Technological Development (CNPq), to which I am immensely grateful. The guidance of Dr. Fred Veer was the other determinant factor that made this research possible, and I am equally grateful to him. I want to express my gratitude to his availability to supervise this work, all the discussions along these years, from which I learned a lot, and for being a great supervisor, giving the freedom that a PhD deserves but at the same time being able to scope the research and focus in what is important, helping me to finish it on a reasonable time.

I want to express my gratitude to Dr. Oguzhan Copuroglu, for the advises along these years which certainly contributed to improve the quality of this work and for introducing me in the Microlab. I extend my gratitude to all my colleagues from the Microlab, who make it an amazing working environment.

I am grateful to Prof. Rob Nijse, who welcomed me in the Glass & Transparency Research Group. I am glad for the opportunity to have been able to work alongside talented colleagues there : Ate, Christian, Faidra, Kees, Lida, Tommaso and Rong. Special thanks to Telesilla Bristogianni, not only for the times that we collaborated, but also for the great company. In addition to my supervisors, I would like to thank the other members of my thesis committee for their availability and the insightful comments, which contributed to improve the quality of this work.

I owe my interest in glass to my master supervisors, Dr. Fabia Castro Cassanjes and Dr. Gael Poirier. I am eternally grateful for all that I learned from them, for introducing me to research, to the laboratory and for all the opportunities that I had during my master. This positive experience was crucial in order to motivate me to pursue a PhD.

I am thankful to everyone who made technical contributions to the experiments done in this thesis: thanks to John van den Berg, Ron Penners and Maiko van Leeuwen for the assistance in the laboratory. Thanks to Hans van Limpt for the UV-VIS measurements and Paul Vermeulen for all his help with the thermal expansion tests and for the constructive discussions about the results. Many thanks to Gabriela Ricci for her help formatting this thesis.

I am also grateful for the technical support from my colleagues from Microlab: to Branko and Hongzhi for the many times that they helped me with the indentation tests, to Fernando for his support with the microscope and to Stefan, not only for the many times that he clarified my doubts about tests but also for his friendship.

I want to express my gratitude to my current employer, American Glass Research, represented by Peter de Haan and Jennifer Hu-a-ng, for being so understandable and offering me flexibility during the period of conclusion of this thesis.

In my first months in Delft I was lucky to make some friends who filled my life with joy. Wesley, Luana, Paulo, Eva and Simone, I have good memories from the nights at Be-bops, dinners together and all the moments spent together. Special thanks to Fernanda,

one of the warmest and most welcoming people that I ever met, Eni, the best flatmate that I could ever get and Larissa, who is present in my best memories from Delft. You definitely made the Netherlands a warmer place to me.

I am also grateful to the other friends that I met along the years of the PhD and who shared great moments with me: Gláucia, Romina, Violetta, Vitória, Camila, Safaa, Abel, Vanessa, Tania, Lucas, Thiago, Bianca and Nestor. Thank you for the friendship. I am thankful to Karoline, Tales, Mohammed and Maria for the meetings at the faculty of Civil Engineering. Having lunch or coffee with you always made my days better. I am grateful to Rita, Francesco, Greet and the entire lunch group for the many meals that we shared and to Weijian, Haohui and Martin, for the nice company at the office.

During the last years I dedicated part of my time to APEB, the Association of Brazilian Students and Researchers in the Netherlands. There I met and worked with some amazing people. It was great to have them around to be able to discuss about our country, specially the surreal times that Brazil is facing, and I am grateful to everybody that I met there: Ana Clara, Carol, David, Andréa and especially to Regiane, who is the great responsible for keeping the association alive.

I am especially grateful to my boyfriend Marijn, who during the last years has been cheerfully sharing life with me, being the most supportive and wonderful partner that I could ever find, particularly with this PhD. I am also thankful to all his family for being so welcoming and attentive to me, mainly to his parents, Anja and Jacques.

I want to express my gratitude to all my friends and family in Brazil, mainly to my grandmother, Luiza, and my aunts and uncle, Lurdes, Natalina and Valmiro, who always supported me.

I learned a lot during my formative years at school and later at the university, but it was from home that I took the most important teachings, such as trusting in myself, pursuing my goals and being independent. Without these lessons, I would hardly manage to move to another country and make it a nice experience. I am particularly grateful to my mother for her endless optimism and for being a great teacher to my brother and I during our childhood. I am sure that my interest in science is related to the long evenings that she dedicated to our homeworks, the hundreds of books that we read together and for always feeding our curiosity. My deepest acknowledges goes to my parents, Graça and José Francisco and to my brother, Bruno. Muito obrigada por tudo.

A

APPENDIX A

The experimental conditions of the measurements and a brief report of the preparation of the samples is provided in order to ensure the reproducibility of the tests.

MAKING THE SAMPLES

The glasses were melted in a Carbolite high temperature box furnace, model HTF 17/10, which can operate up to 1.700°C. The samples were prepared in a 30 milliliters platinum crucible. The crucible was cleaned with HF (Hydrofluoric acid) between each batch.

X-RAY FLUORESCENCE (XRF)

The investigated samples were flat, dimensions about 2.5 × 5 cm, and thickness of approximately 0.5 cm. The measurements were performed with a Panalytical Axios Max WD-XRF spectrometer and data evaluation was done with SuperQ5.0i/Omnian software.

X-RAY POWDER DIFFRACTION (XRD)

The samples were investigated as fine powder, homogeneized in a ceramic mortar. A thin layer of sample powder was deposited on a Si510 wafer from a powder-ethanol suspension and fixed in PMMA sample holder L510. The instrument used in the analysis was a Bruker D8 Advance diffractometer Bragg-Brentano geometry and Lynxeye position sensitive detector, using Cu $K\alpha$ radiation. Divergence slit V12, scatter screen height 5 mm, 45 kV 40 mA. Sample spinning. Detector settings: LL 0.19, W 0.06. Coupled $\theta - 2\theta$ scanning among $10^\circ - 110^\circ$, step size $0.034^\circ 2\theta$, counting time per step 2 s. The data evaluation was done with a Bruker software DiffracSuite.EVA vs 4.3.

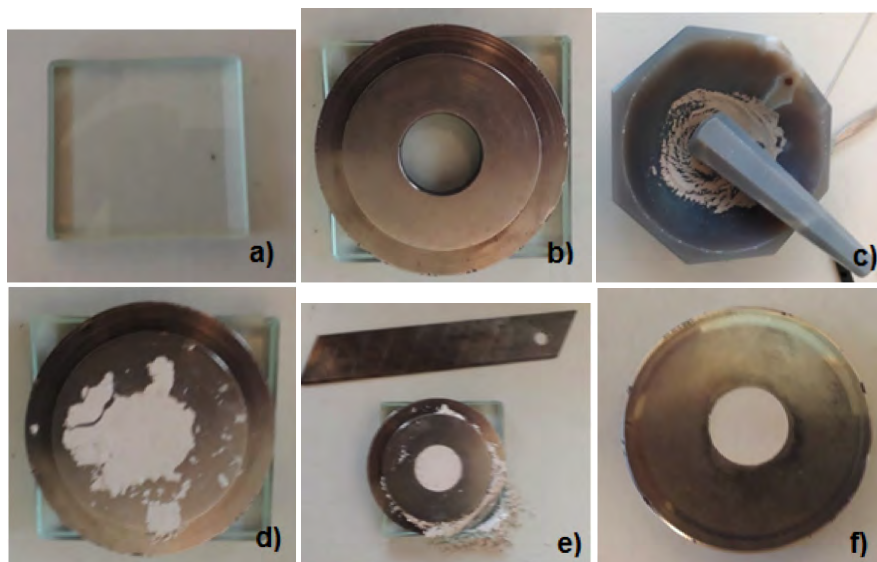


Figure A.1: Preparing a sample for XRD a) Clean a piece of flat glass b) place the sample holder ring on the glass. The surface of the sample holder should be in contact with the surface of the glass c) grind the sample to obtain a fine powder d) spread the powder in the sample holder and press it using a weight e) clean the excess of powder with a knife blade f) Turn the sample holder upside down and remove the glass.

DIFFERENTIAL SCANNING CALORIMETRY AND THERMOGRAVIMETRY ANALYSIS (DSC-TGA)

Differential Scanning Calorimetry and thermogravimetry were performed using a Netzsch STA F3 Jupiter. The data was analysed using the Proteus Software for Thermal Analysis Version 5.2.1. The DSC-TGA measurements were performed with a correction of a blank sample, under an argon atmosphere, using a heating rate of 10K/minute. Most measurements were performed up to 1100°C. The samples had an approximated weight of 60mg. All the samples were measured as bulk and placed in alumina pans.

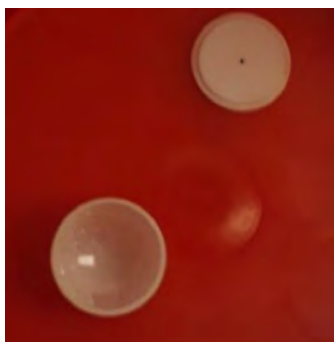


Figure A.2: Alumina pan and lid.



Figure A.3: Sample carrier with two alumina pans: one for the measured glass and another to be used as a reference.

EVOLVED GAS ANALYSIS (EGA)

The evolved gas analysis was performed with a QMS403C Aëolos gas analysis system coupled with the DSC-TGA instrument. Coupling both instruments, the detection of gas, separation and identification of the separated components is possible in exact time correlation with the other thermal analysis signals. The result of the analysis provides information about the mass numbers of the compositions of the evolved gases, allowing the identification of them. The results were analysed using the software Aëolos QuadStar-Version 7.02/32 Bit.

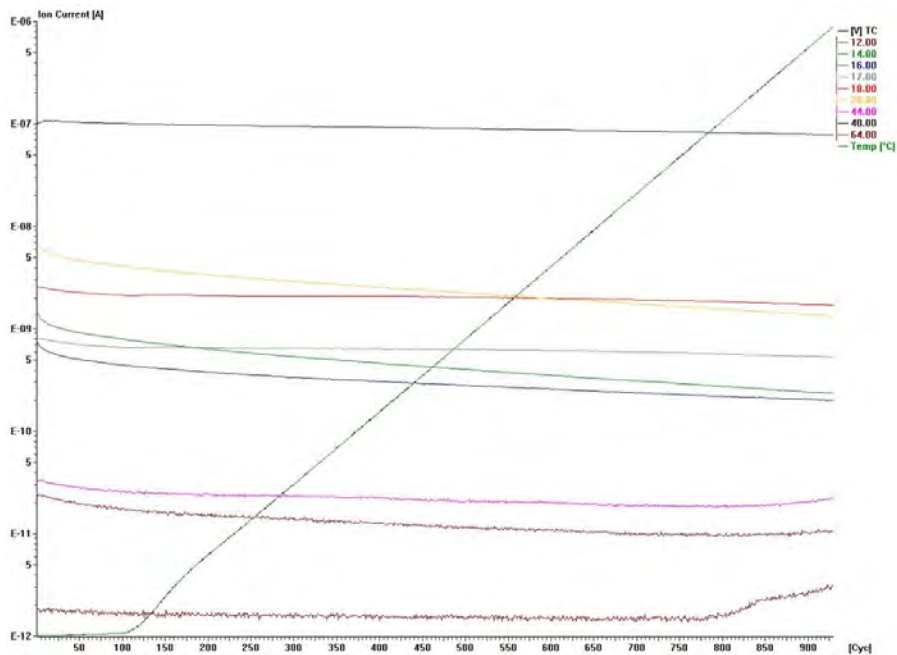


Figure A.4: Evolved gas analysis of a glass sample. The lines are identified by numbers, related to the mass of the components (in atomic mass unit): C=12, N=14, = 16, =17, H₂O= 18, CO=28, CO₂= 44, NO₂= 46, SO₂= 64.

UV/VIS SPECTROSCOPY

The UV/VIS spectroscopy was performed with a spectrophotometer is a Perkin-Elmer Lambda 950 UV-VIS-NIR.

NANOINDENTATION

The measures of elastic modulus, hardness and fracture toughness were conducted with a Nano Indenter MTS G200. The prepared glass samples had their surfaces polished, and then the samples were reannealed.

The measurements of elastic modulus and hardness were performed 25 times per sample, using a surface approach velocity of 10 nm/s, depth limit of 2000 nm, strain rate target of 0.05 1/s, surface approach distance of 1000 nm, harmonic displacement target of 2 nm, frequency target of 45 Hz, minimum depth for average of 1000 nm, maximum depth for average of 1400 nm.

Knoop measurements were performed using a Surface Approach Velocity of 100 nm/s, maximum load of 8.5 N, approach distance to store of 1000 nm, peak hold time of 30 s, time to load of 60 s. Berkovich measurements were performed using Surface Approach Velocity of 10 nm/s, maximum load of 2 N, approach distance to store of 1000 nm, peak hold time of 15 s, time to load of 30 s, surface approach distance of 1000 nm, surface approach sensitivity of 40%.



Figure A.5: Polished glass samples in the sample holder.

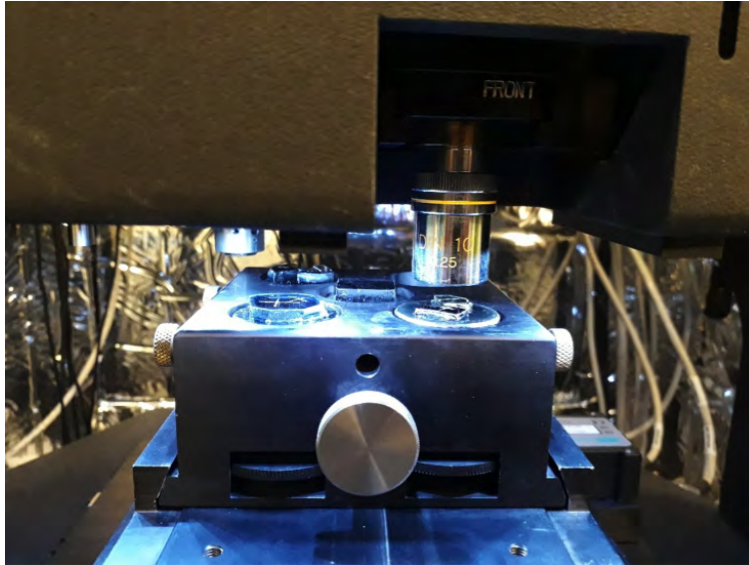


Figure A.6: Setup of the nanoindentation test.

MICROSCOPY

Microscopic images were obtained with an Environmental Scanning Electron Microscope (ESEM) Philips XL30 ESEM and a Polarisation and Fluorescence Microscope. The samples analysed by SEM were coated with a thin carbon layer.

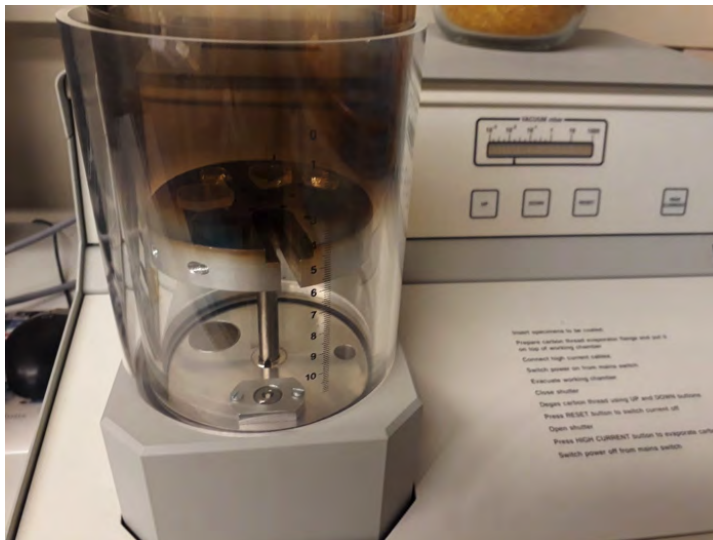


Figure A.7: Coating the samples for SEM.

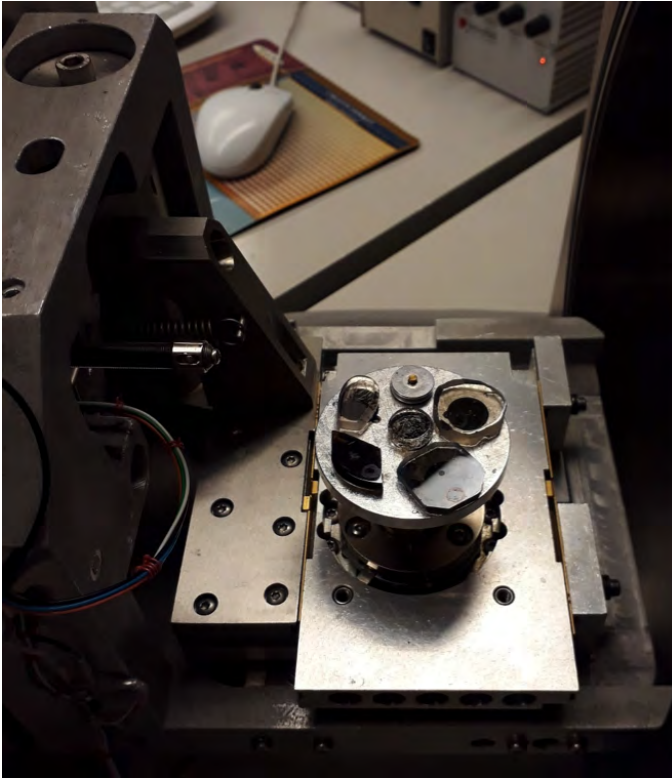


Figure A.8: Set up of the SEM.

B

APPENDIX B

Example of conversion of a glass composition from weight (%) to mol (%). The composition in weight (%) was obtained from XRF and placed in the 4th column. Then, this concentration in weight is multiplied by 100, divided by the molecular weight of the element (MW) and divided by the sumproduct of the molecular weight¹.

Table B.1: Conversion from weight percentage to molar percentage.

		Total	100.82	100
1/MW	Element	Molecular weight(MW)	concentration in	
		in g/mol	wt%	mol%
0.0166	SiO ₂	60.084	10.312	17.470
0.0098	Al ₂ O ₃	101.961	24.443	24.403
0.0106	K ₂ O	94.195	25.471	27.526
0.0248	MgO	40.304	0.286	0.722
0.0178	CaO	56.077	0.780	1.416
0.0097	SrO	103.619	0.026	0.025
0.0081	ZrO ₂	123.219	0.185	0.153
0.0123	ZnO	81.379	0.111	0.139
0.0021	Bi ₂ O ₃	465.959	0.003	0.001
0.0125	TiO ₂	79.879	0.232	0.296
0.0141	MnO	70.937	0.015	0.021
0.0125	SO ₃	80.064	0.018	0.023

The phosphate glass structure depends on the O/P molar ratio of oxygen to phosphorus. The chemical equations of the components of the glasses were balanced and their coefficients were used to calculate the O/P ratio.

¹The sumproduct of the molecular weight is calculated by multiplying the weight percentage by the 1/MW for each element. Next, the outcomes of the individual multiplications are summed to derive a total value.

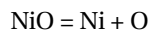
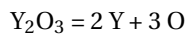
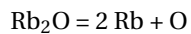
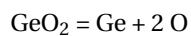
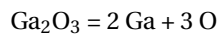
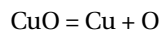
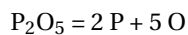
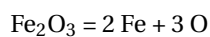
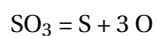
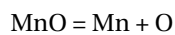
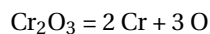
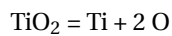
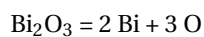
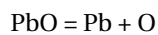
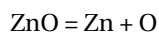
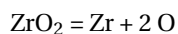
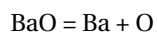
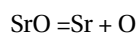
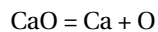
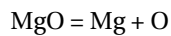
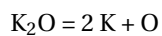
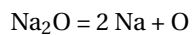
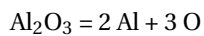
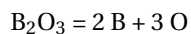
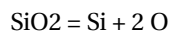


Table B.2: Compositions of the glasses containing slag in mol.% and their O/P ratios.

Compound	Coefficient	60KPO ₃ - 20slag- 20Al ₂ O ₃ (mol%)	70KPO ₃ - 15slag- 15Al ₂ O ₃ (mol%)	50KPO ₃ - 15Slag- 15Al ₂ O ₃ - 20B ₂ O ₃ (mol%)	75KPO ₃ - 12.5slag- 12.5Al ₂ O ₃ 1150 °C (mol%)	75KPO ₃ - 12.5slag- 12.5Al ₂ O ₃ 1250 °C (mol%)
SiO₂	1	12.063	8.778	8.154	7.812	7.528
Si	1	12.063	8.778	8.154	7.812	7.528
O	2	24.126	17.556	16.308	15.624	15.056
B₂O₃	1	0	0	22.795	0	0
B	2	0	0	45.59	0	0
O	3	0	0	68.385	0	0
Al₂O₃	1	18.008	17.517	19.712	14.859	15.189
Al	2	36.016	35.034	39.424	29.718	30.378
O	3	54.024	52.551	59.136	44.577	45.567
Na₂O	1	0.1	0.087	0.088	0	0.087
Na	2	0.200	0.174	0.176	0	0.174
O	1	0.100	0.087	0.088	0	0.087
K₂O	1	27.423	30.629	20.083	32.393	33.417
K	2	54.846	61.258	40.166	64.786	66.834
O	1	27.423	30.629	20.083	32.393	33.417
MgO	1	4.083	3.067	2.798	2.557	2.681
Mg	1	4.083	3.067	2.798	2.557	2.681
O	1	4.083	3.067	2.798	2.557	2.681
CaO	1	13.599	10.594	10.387	8.842	9.212
Ca	1	13.599	10.594	10.387	8.842	9.212
O	1	13.599	10.594	10.387	8.842	9.212
SrO	1	0.014	0.012	0.012	0.01	0.009
Sr	1	0.014	0.012	0.012	0.010	0.009
O	1	0.014	0.012	0.012	0.010	0.009
BaO	1	0.019	0	0.018	0.219	0.204
Ba	1	0.019	0	0.018	0.219	0.204
O	1	0.019	0	0.018	0.219	0.204
ZrO₂	1	0.007	0.117	0.006	0.006	0.006
Zr	1	0.007	0.117	0.006	0.006	0.006
O	2	0.014	0.234	0.012	0.012	0.012
ZnO	1	0.105	0	0	0.123	0
Zn	1	0.105	0	0	0.123	0
O	1	0.105	0	0	0.123	0

Compound	Coefficient	60KPO ₃ - 20slag- 20Al ₂ O ₃ (mol%)	70KPO ₃ - 15slag- 15Al ₂ O ₃ (mol%)	50KPO ₃ - 15Slag- 15Al ₂ O ₃ - 20B ₂ O ₃ (mol%)	75KPO ₃ - 12.5slag- 12.5Al ₂ O ₃ 1150 °C (mol%)	75KPO ₃ - 12.5slag- 12.5Al ₂ O ₃ 1250 °C (mol%)
Bi₂O₃	1	0	0	0	0.001	0
Bi	2	0	0	0	0.002	0
O	3	0	0	0	0.003	0
TiO₂	1	0.257	0.217	0.198	0.192	0.185
Ti	1	0.257	0.217	0.198	0.192	0.185
O	2	0.514	0.434	0.396	0.384	0.370
MnO	1	0.089	0.064	0.065	0.065	0.062
Mn	1	0.089	0.064	0.065	0.065	0.062
O	1	0.089	0.064	0.065	0.065	0.062
SO₃	1	0.102	0.076	0.024	0.041	0.039
S	1	0.102	0.076	0.024	0.041	0.039
O	3	0.306	0.228	0.072	0.123	0.117
Fe₂O₃	1	0.092	0.070	0.066	0.077	0.065
Fe	2	0.184	0.140	0.132	0.154	0.130
O	3	0.276	0.210	0.198	0.231	0.195
P₂O₅	1	24.026	28.742	15.583	30.856	31.297
P	2	48.052	57.484	31.166	61.712	62.594
O	5	120.130	143.710	77.915	154.28	156.485
CuO	1	0	0.004	0	0.005	0
Cu	1	0	0.004	0	0.005	0
O	1	0	0.004	0	0.005	0
Rb₂O	1	0.001	0	0.001	0	0.001
Rb	2	0.002	0.000	0.002	0	0.002
O	1	0.001	0.000	0.001	0	0.001
Y₂O₃	1	0.001	0	0	0.001	0.001
Y	2	0.002	0.000	0.000	0.002	0.002
O	3	0.003	0.000	0.000	0.003	0.003
NiO	1	0.010	0.008	0.008	0.014	0.017
Ni	1	0.010	0.008	0.008	0.014	0.017
O	1	0.010	0.008	0.008	0.014	0.017
Total O		244.836	259.388	255.882	259.465	263.495
O/P		5.095	4.512	8.210	4.204	4.210

Table B.3: Compositions of the glasses containing fly ash in mole% t and their O/P ratios.

Compound	Coefficient	70KPO ₃ -15FA-15Al ₂ O ₃ (mo%)	60KPO ₃ -20FA-20Al ₂ O ₃ (mo%)	40KPO ₃ -25FA-15Al ₂ O ₃ -20B ₂ O ₃ (mol%)
SiO₂	1	14.967	17.470	21.169
Si	1	14.967	17.470	21.169
O	2	29.934	34.940	42.338
B₂O₃	1	0	0	18.879
B	2	0	0	37.758
O	3	0	0	56.637
Al₂O₃	1	20.625	24.403	19.572
Al	2	41.250	48.806	39.144
O	3	61.875	73.209	58.716
Na₂O	1	0	0	0.261
Na	2	0	0	0.521
O	1	0	0	0.260
K₂O	1	31.925	27.526	18.064
K	2	63.850	55.052	36.128
O	1	31.925	27.526	18.064
MgO	1	0.654	0.722	0.856
Mg	1	0.654	0.722	0.856
O	1	0.654	0.722	0.856
CaO	1	1.331	1.416	1.888
Ca	1	1.331	1.416	1.888
O	1	1.331	1.416	1.888
SrO	1	0.022	0.025	0.035
Sr	1	0.022	0.025	0.035
O	1	0.022	0.025	0.035
BaO	1	0.195	0	0.059
Ba	1	0.195	0	0.059
O	1	0.195	0	0.059
ZrO₂	1	0.006	0.153	0.082
Zr	1	0.006	0.153	0.082
O	2	0.012	0.306	0.164
ZnO	1	0.116	0.139	0.009
Zn	1	0.116	0.139	0.009
O	1	0.116	0.139	0.009

Compound	Coefficient	70KPO ₃ -15FA-15Al ₂ O ₃ (mol%)	60KPO ₃ -20FA-20Al ₂ O ₃ (mol%)	40KPO ₃ -25FA-15Al ₂ O ₃ -20B ₂ O ₃ (mol%)
PbO	1	0.001	0	0.002
Pb	1	0.001	0	0.002
O	1	0.001	0	0.002
Bi₂O₃	1	0	0.001	0
Bi	2	0	0.002	0
O	3	0	0.003	0
TiO₂		0.234	0.296	0.392
Ti	1	0.234	0.296	0.392
O	2	0.468	0.592	0.784
Cr₂O₃	1	0	0	0.007
Cr	2	0	0	0.014
O	3	0	0	0.021
MnO	1	0.018	0.021	0.025
Mn	1	0.018	0.021	0.025
O	1	0.018	0.021	0.025
SO₃	1	0.025	0.023	0.008
S	1	0.025	0.023	0.008
O	3	0.075	0.069	0.024
Fe₂O₃	1	0.849	1.047	1.442
Fe	2	1.698	2.094	2.884
O	3	2.547	3.141	4.326
P₂O₅	1	29.012	26.693	17.220
P	2	58.024	53.386	34.440
O	5	145.060	133.465	86.100
CuO	1	0.005	0.006	0.008
Cu	1	0.005	0.006	0.008
O	1	0.005	0.006	0.008
Ga₂O₃	1	0	0.001	0.001
Ga	2	0	0.002	0.002
O	3	0	0.003	0.003
GeO₂	1	0	0.027	0
Ge	1	0	0.027	0
O	2	0	0.054	0
Rb₂O	1	0.002	0.002	0.003
Rb	2	0.004	0.004	0.006
O	1	0.002	0.002	0.003
Y₂O₃	1	0	0	0.001
Y	2	0	0	0.002
O	3	0	0	0.003
NiO	1	0.011	0.011	0.016
Ni	1	0.011	0.011	0.016
O	1	0.011	0.011	0.016
Total O		274.251	275.650	270.342
O/P		4.726	5.163	7.850

C

APPENDIX C

Data graphs and calculations related to the measurements of coefficient of thermal expansion of the glasses (Chapter 5) are reported.

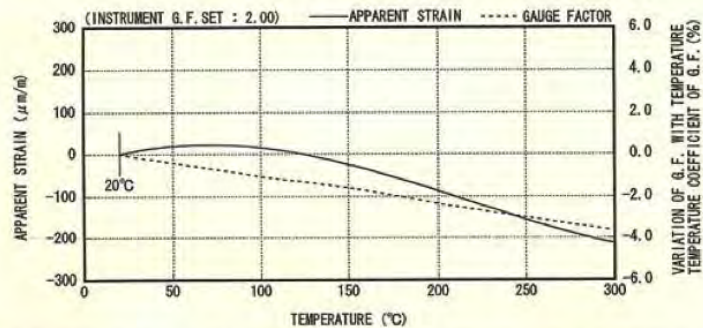
TML STRAIN GAUGE TEST DATA

GAUGE TYPE	: ZFLA-6-11	TESTED ON	: SS 400
LOT NO.	: S505711	COEFFICIENT OF THERMAL EXPANSION	: 11.8 $\times 10^{-6}/^{\circ}\text{C}$
GAUGE FACTOR	: 2.01 $\pm 1\%$	TEMPERATURE COEFFICIENT OF G.F.	: $-0.13 \pm 0.05 \%$ / 10°C
ADHESIVE	: NP-50	DATA NO.	: 10017

THERMAL OUTPUT (ϵ_{app} : APPARENT STRAIN)

$$\epsilon_{app} = -2.27 \times 10^{-1} + 1.35 \times T^1 - 1.07 \times 10^{-2} \times T^2 + 8.57 \times 10^{-6} \times T^3 + 1.70 \times 10^{-8} \times T^4 \quad (\mu\text{m/m})$$

TOLERANCE : ± 0.85 [$(\mu\text{m/m})/^{\circ}\text{C}$], T : TEMPERATURE



ひずみゲージ取扱いの注意事項

- 上記の特性データは、リード線の取付けによる影響を含んでおりません。裏面記載のリード線の測定値への影響に従って補正してください。
- ゲージの使用温度は、接着剤の耐熱温度などにより変わります。
- 絶縁抵抗などの点検は、印加電圧を50V以下にしてください。
- ゲージリード線に無理な力を加えないでください。
- ゲージ裏面に接着剤を塗布して接着してください。
- ひずみゲージの裏面は脱脂洗浄してありますので、汚さないように取扱いしてください。
- ゲージの包装を開封後は、乾燥した場所で保管してください。
- ご使用に際してご不明な点がございましたら、当社までお問い合わせください。

CAUTIONS ON HANDLING STRAIN GAUGES

- The above characteristic data do not include influence due to lead wires. Correct the data in accordance with the influence of lead wires on measured values described overleaf.
- The service temperature of strain gauge depends on the operating temperature of adhesive, etc.
- Check of insulation resistance, etc. should be made at a voltage of less than 50V.
- Do not apply an excessive force to the gauge leads.
- Apply an adhesive to the back of a strain gauge and stick the gauge to a specimen.
- As the back of strain gauge has been degreased and washed, do not contaminate it.
- After unpacking, store strain gauges in a dry place.
- If you have any questions on strain gauges or installation, contact TML or your local agent.

Made in Japan

TML 株式会社 東京測器研究所

〒140-8560 東京都品川区南大井 6-8-2
TEL 03-3763-5811
FAX 03-3763-6128

Tokyo Sokki Kenkyujo Co., Ltd.

8-2, Minami-Ohi 6-Chome
Shinagawa-ku, Tokyo 140-8560

Figure C.1: Data sheet of the strain gauges used in the measurements of coefficient of thermal expansion.

Table C.1: Calculation of apparent strain of maximum and minimum temperature for the 18 tests.

Test	Reference (datafile)	Sample	Max T	Min T	ΔT	ϵ_{app} at max T	ϵ_{app} at min T
1	Glass_2018_02_14_016	1a: steel/ reference	163.824	30.025	133.799	-38.78	8.43
		1b: 70KPO ₃ - 15slag-15Al ₂ O ₃					
		1c: 40KPO ₃ - 20B ₂ O ₃ -25FA- 15Al ₂ O ₃					
2	Glass_2018_02_14_017	2a: steel/ reference	163.635	30.087	133.548	-38.56	8.48
		2b: 70KPO ₃ - 15slag-15Al ₂ O ₃					
		2c: 40KPO ₃ - 20B ₂ O ₃ -25FA- 15Al ₂ O ₃					
3	Glass_2018_02_15_020	3a: steel/ reference	163.119	30.116	133.003	-37.96	8.50
		3b: 70KPO ₃ - 15slag-15Al ₂ O ₃					
		3c: 40KPO ₃ - 20B ₂ O ₃ -25FA- 15Al ₂ O ₃					
4	Glass_2018_02_16_021	4a: steel/ reference	163.021	30.039	132.983	-37.85	8.44
		4b: 75KPO ₃ - 12.5Slag-12.5Al ₂ O ₃					
		4c: 60KPO ₃ - 20Slag-20Al ₂ O ₃					
5	Glass_2018_02_20_021	5a: steel/ reference	162.881	30.065	132.817	-37.69	8.46
		5b: 75KPO ₃ - 12.5Slag-12.5Al ₂ O ₃					
		5c: 60KPO ₃ - 20Slag-20Al ₂ O ₃					
6	Glass_2018_02_20_022	6a: steel/ reference	163.216	30.127	133.089	-38.07	8.51
		6b: 75KPO ₃ - 12.5Slag-12.5Al ₂ O ₃					
		6c: 60KPO ₃ - 20Slag-20Al ₂ O ₃					
7	Glass_2018_02_21_023	7a: steel/ reference	163.688	30.087	133.601	-38.62	8.48
		7b: 50KPO ₃ - 10B ₂ O ₃ -25FA- 15Al ₂ O ₃					
		7c: Flat glass/ soda-lime					
8	Glass_2018_02_21_024	8a: steel/ reference	163.592	30.017	133.576	-38.51	8.43
		8b: 50KPO ₃ - 10B ₂ O ₃ -25FA- 15Al ₂ O ₃					
		8c: Flat glass/ soda-lime					
9	Glass_2018_02_21_025	9a: steel/ reference	163.996	30.083	133.913	-38.98	8.48
		9b: 50KPO ₃ - 10B ₂ O ₃ -25FA- 15Al ₂ O ₃					
		9c: Flat glass/ soda-lime					

10	Glass_2018_02_23_027	10a: steel/ reference	163.959	30.145	133.813	-38.94	8.52
		10b: 50KPO ₃ - 20B ₂ O ₃ -15slag- 15Al ₂ O ₃					
		10c: 60KPO ₃ - 10B ₂ O ₃ -15slag- 15Al ₂ O ₃					
11	Glass_2018_02_26_028	11a: steel/ reference	163.566	30.074	133.492	-38.48	8.47
		11b: 50KPO ₃ - 20B ₂ O ₃ -15slag- 15Al ₂ O ₃					
		11c: 60KPO ₃ - 10B ₂ O ₃ -15slag- 15Al ₂ O ₃					
12	Glass_2018_02_26_029	12a: steel/ reference	163.527	30.063	133.465	-38.44	8.46
		12b: 50KPO ₃ - 20B ₂ O ₃ -15slag- 15Al ₂ O ₃					
		12c: 60KPO ₃ - 10B ₂ O ₃ -15slag- 15Al ₂ O ₃					
13	Glass_2018_02_27_029	13a: steel/ reference	163.102	30.018	133.084	-37.94	8.43
		13b: Flat glass/ soda-lime					
		131c: 60KPO ₃ - 30FA-10Al ₂ O ₃					
14	Glass_2018_02_27_031	14a: steel/ reference	163.949	30.017	133.932	-38.93	8.43
		14b: Flat glass/ soda-lime					
		14c: 60KPO ₃ - 30FA-10Al ₂ O ₃					
15	Glass_2018_02_27_032	15a: steel/ reference	163.454	30.001	133.453	-38.35	8.42
		15b: Flat glass/ soda-lime					
		14c: 60KPO ₃ - 30FA-10Al ₂ O ₃					
16	Glass_2018_02_28_033	16a: steel/ reference	162.702	30.045	132.658	-37.48	8.45
		16b: Borosilicate					
		16c: 70KPO ₃ - 15FA-15Al ₂ O ₃					
17	Glass_2018_02_28_034	17a: steel/ reference	162.626	30.267	132.360	-37.39	8.61
		17b: Borosilicate					
		17c: 70KPO ₃ - 15FA-15Al ₂ O ₃					
18	Glass_2018_03_02_037	18a: steel/ reference	162.920	30.038	132.882	-37.73	8.44
		18b: Borosilicate					
		18c: 70KPO ₃ - 15FA-15Al ₂ O ₃					

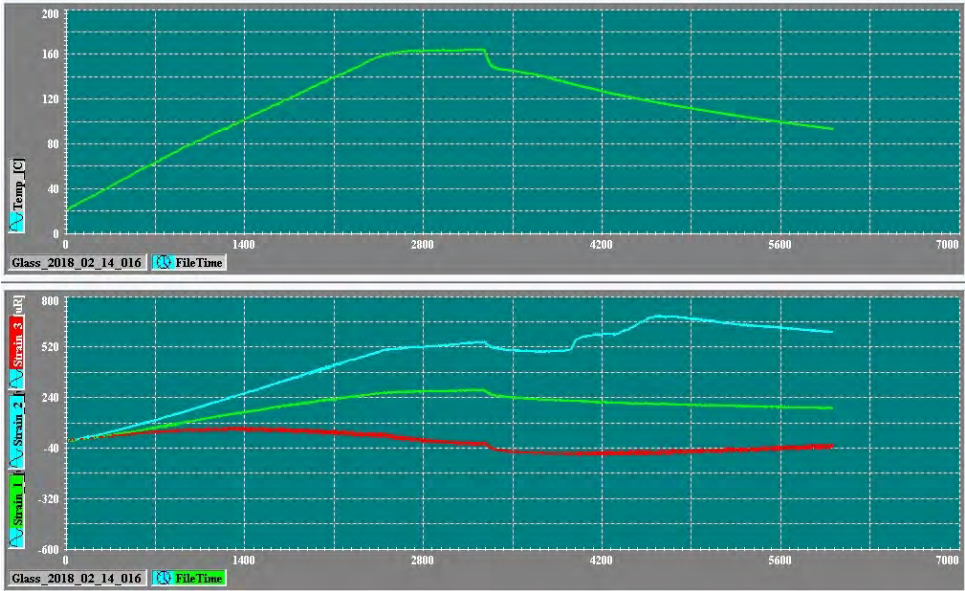


Figure C.2: Test 1, in which strain 1= steel, strain 2= 70KPO₃-15slag-15Al₂O₃, strain 3= 40KPO₃-20B₂O₃-25FA-15Al₂O₃.

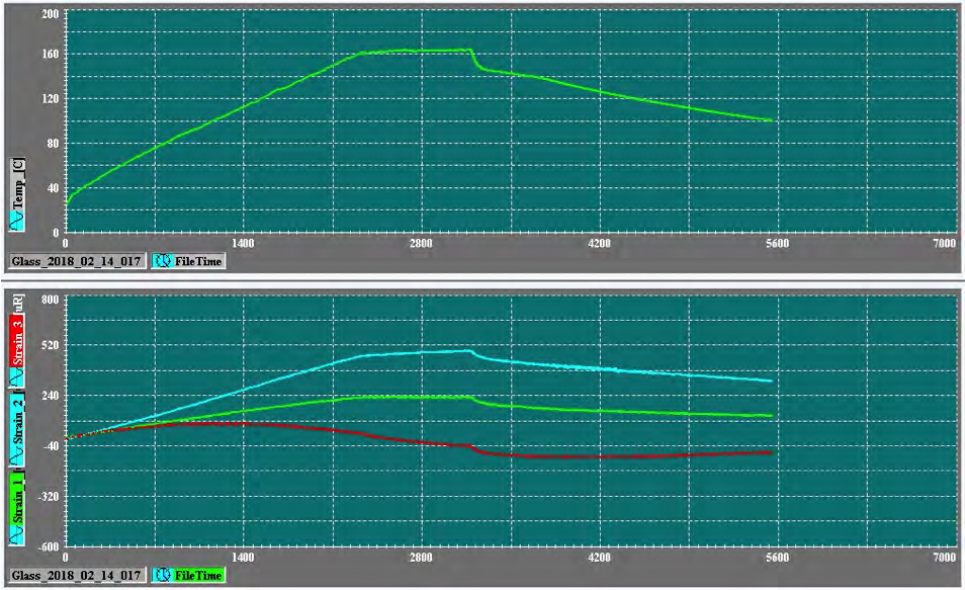


Figure C.3: Test 2, in which strain 1= steel, strain 2= 70KPO₃-15slag-15Al₂O₃, strain 3= 40KPO₃-20B₂O₃-25FA-15Al₂O₃.

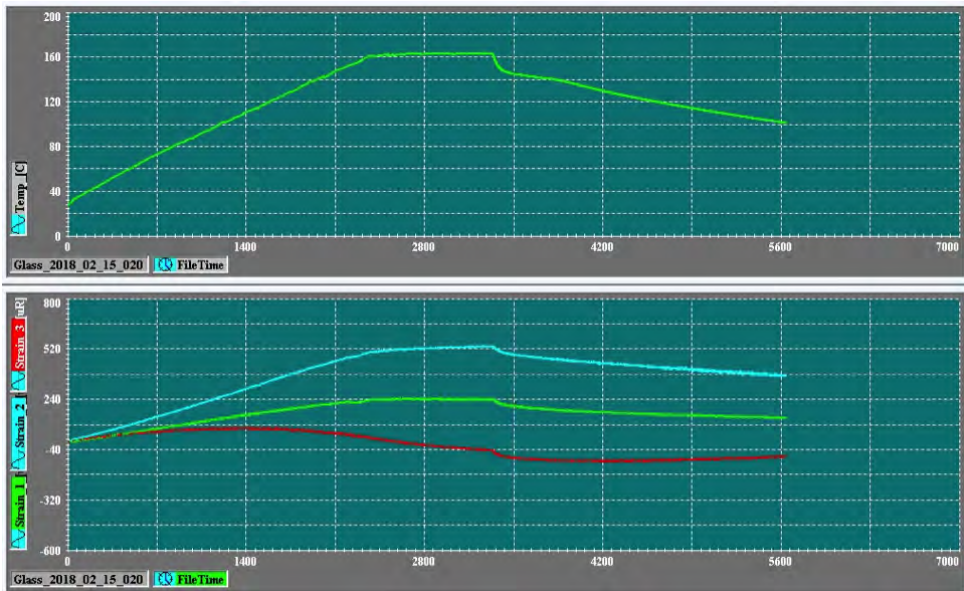


Figure C.4: Test 3, in which strain 1= steel, strain 2= 70KPO₃-15slag-15Al₂O₃, strain 3= 40KPO₃-20B₂O₃-25FA-15Al₂O₃.

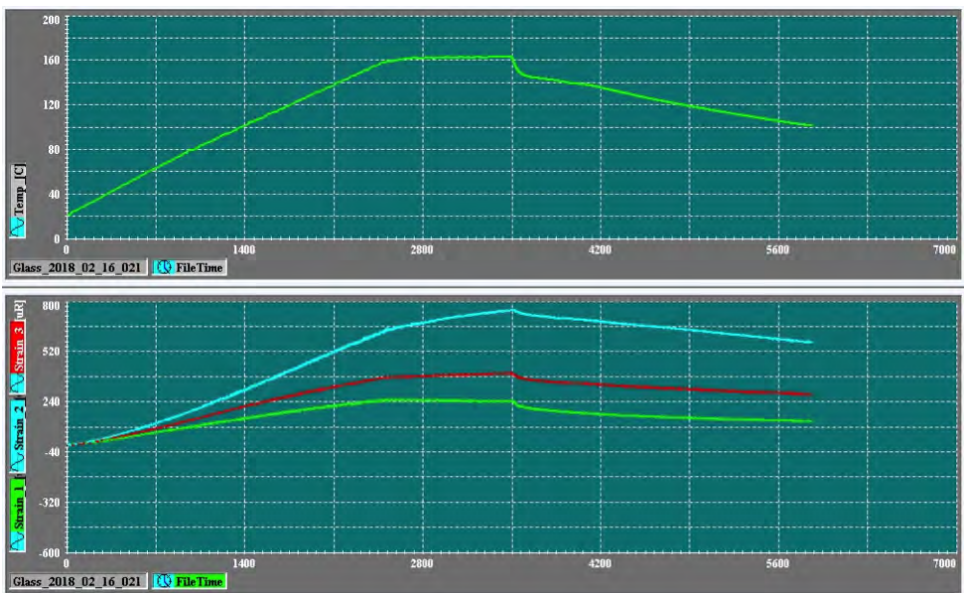


Figure C.5: Test 4, in which strain 1= steel, strain 2= 75KPO₃-12.5Slag-12.5Al₂O₃, strain 3= 60KPO₃-20Slag-20Al₂O₃.

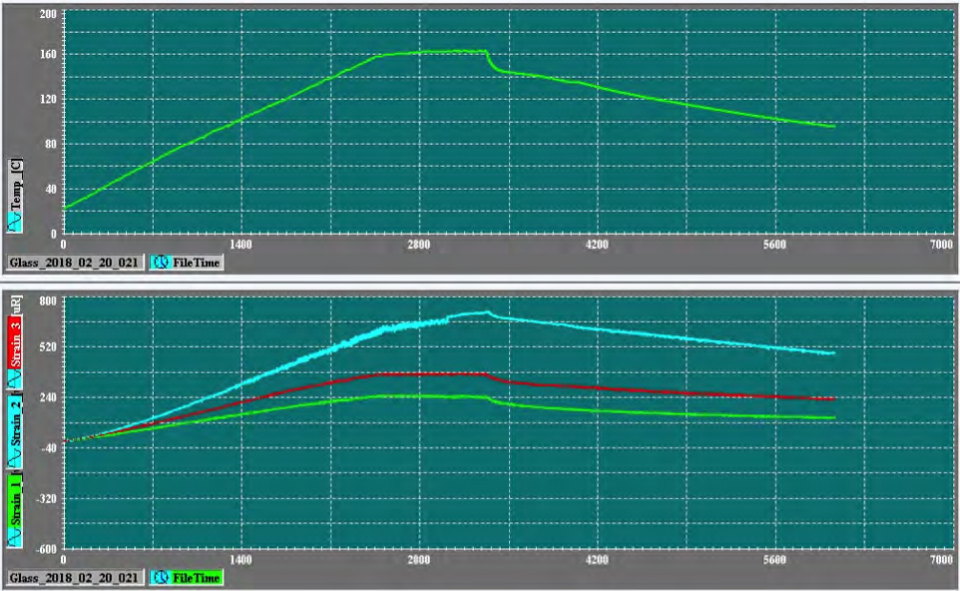


Figure C.6: Test 5, in which strain 1= steel, strain 2= 75KPO₃-12.5Slag-12.5Al₂O₃, strain 3= 60KPO₃-20Slag-20Al₂O₃.

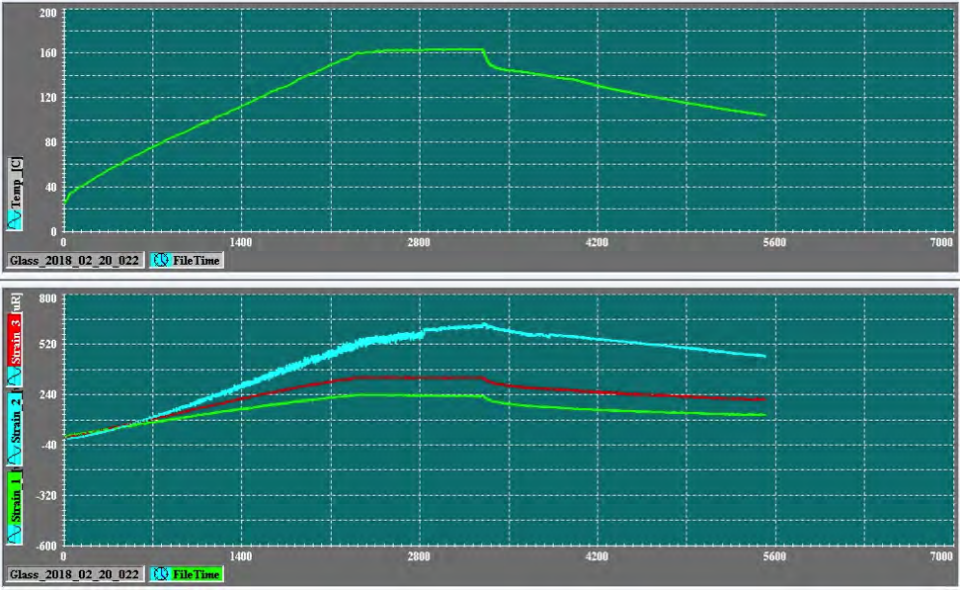


Figure C.7: Test 6, in which strain 1= steel, strain 2= 75KPO₃-12.5Slag-12.5Al₂O₃, strain 3= 60KPO₃-20Slag-20Al₂O₃.

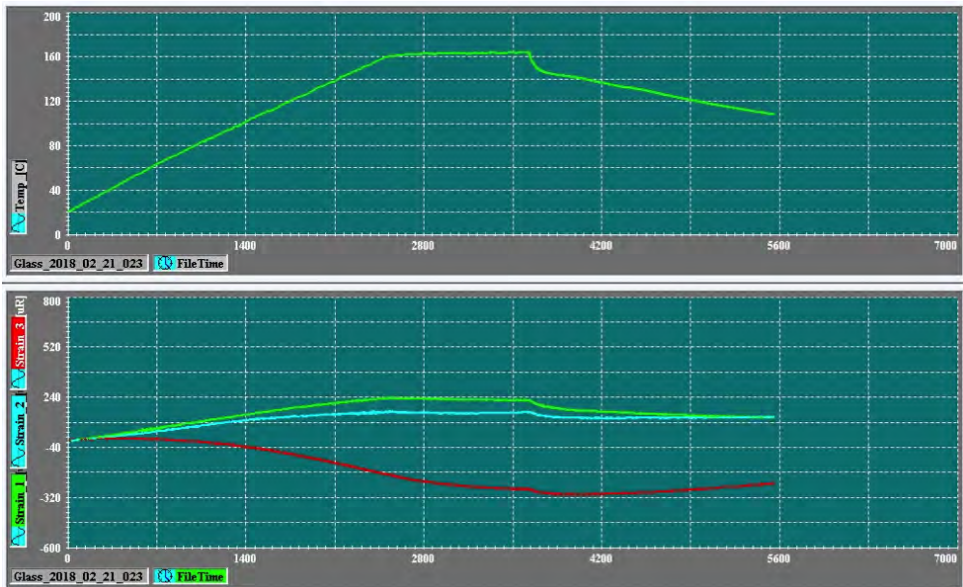


Figure C.8: Test 7, in which strain 1= steel, strain 2= $50\text{KPO}_3\text{-}10\text{B}_2\text{O}_3\text{-}25\text{FA-}15\text{Al}_2\text{O}_3$, strain 3= flat glass.

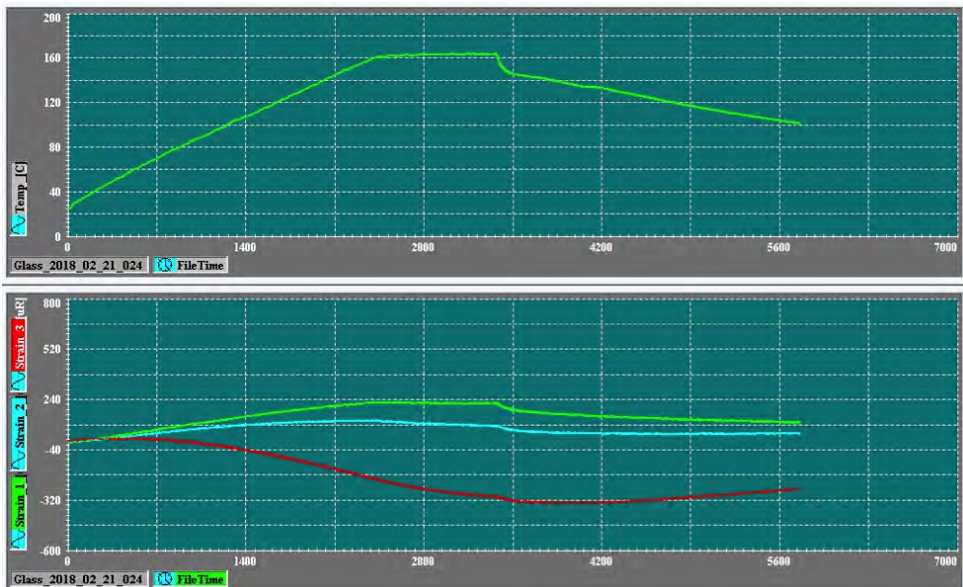


Figure C.9: Test 8, in which strain 1= steel, strain 2= $50\text{KPO}_3\text{-}10\text{B}_2\text{O}_3\text{-}25\text{FA-}15\text{Al}_2\text{O}_3$, strain 3= flat glass.

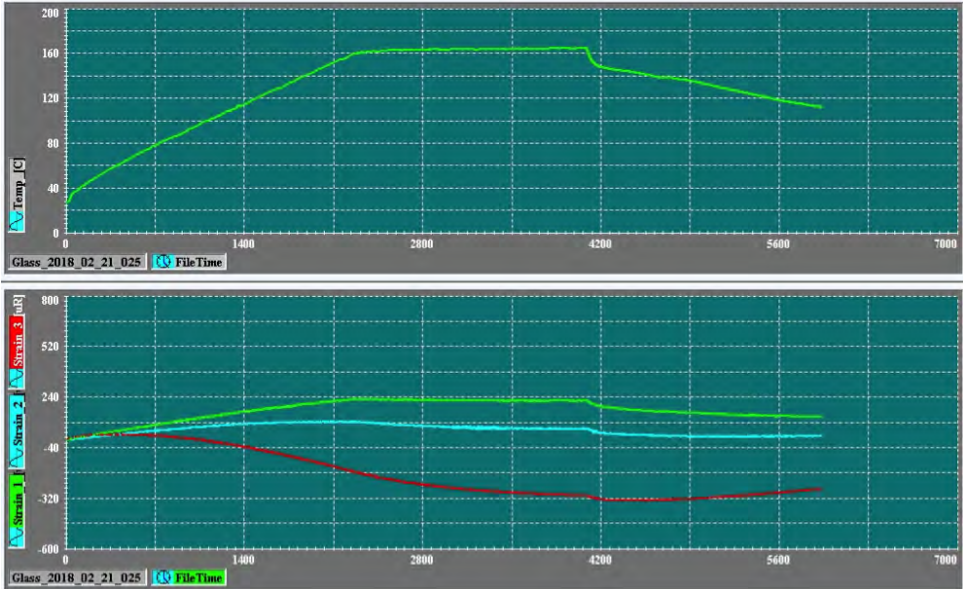


Figure C.10: Test 9, in which strain 1= steel, strain 2= 50KPO₃-10B₂O₃-25FA-15Al₂O₃, strain 3= flat glass.

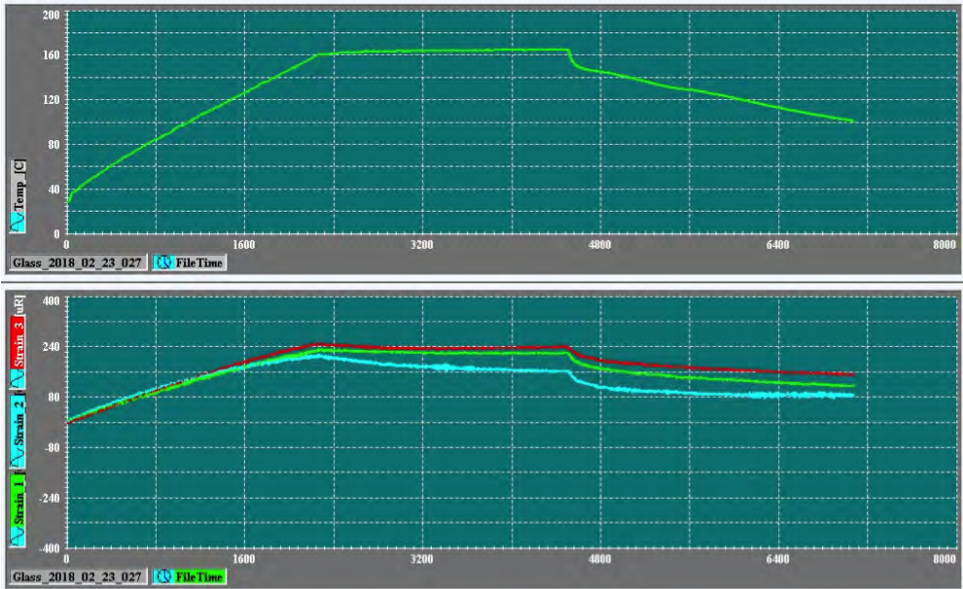
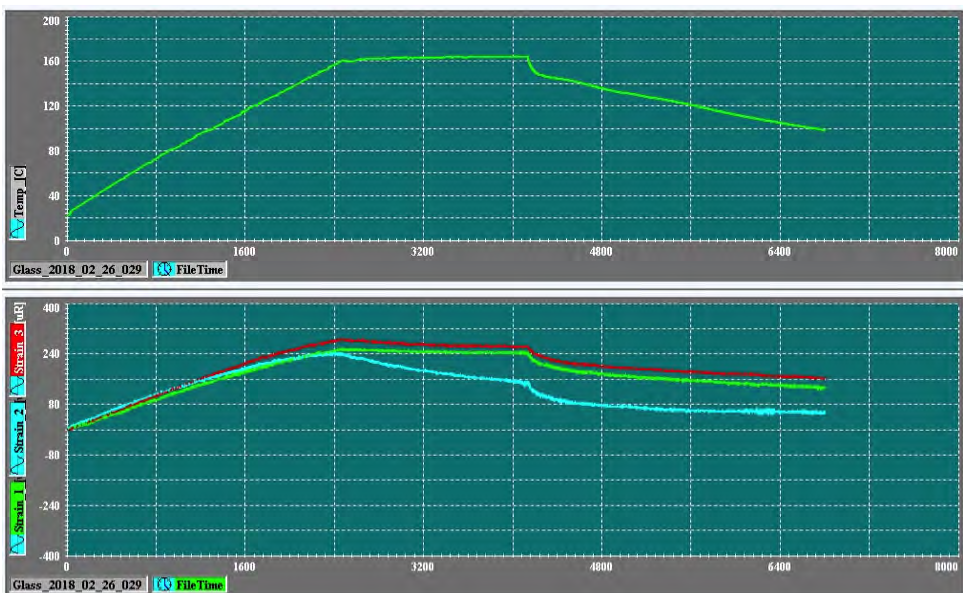
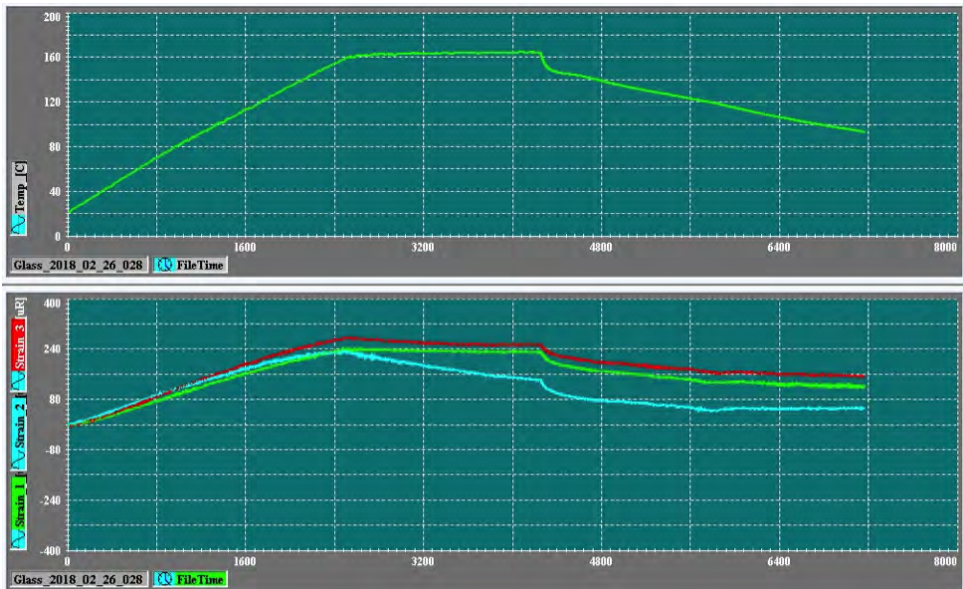


Figure C.11: Test 10, in which strain 1= steel, strain 2= 50KPO₃-20B₂O₃-15slag-15Al₂O₃, strain 3: 60KPO₃-10B₂O₃-15slag-15Al₂O₃.



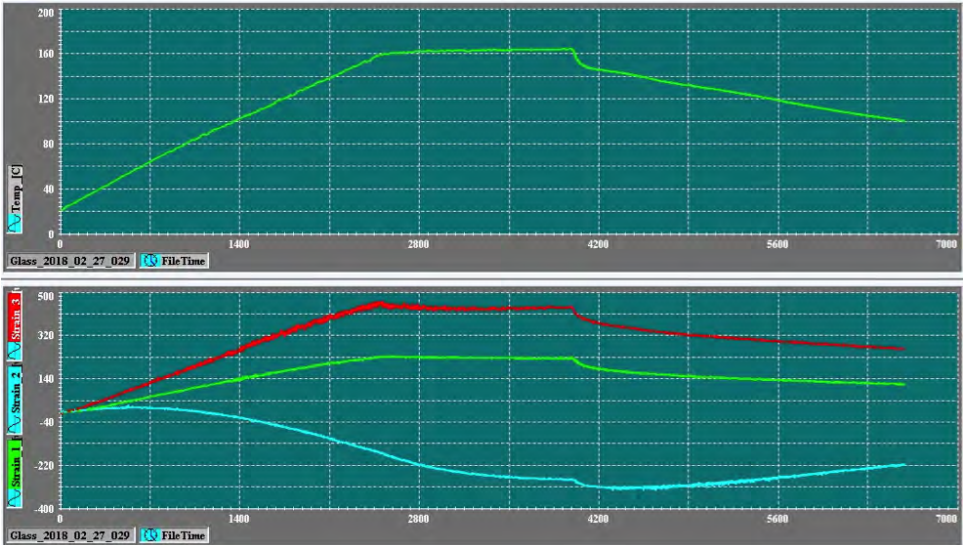


Figure C.14: Test 13, in which strain 1= steel, strain 2= flat glass, strain 3= 60KPO₃-30FA-10Al₂O₃.

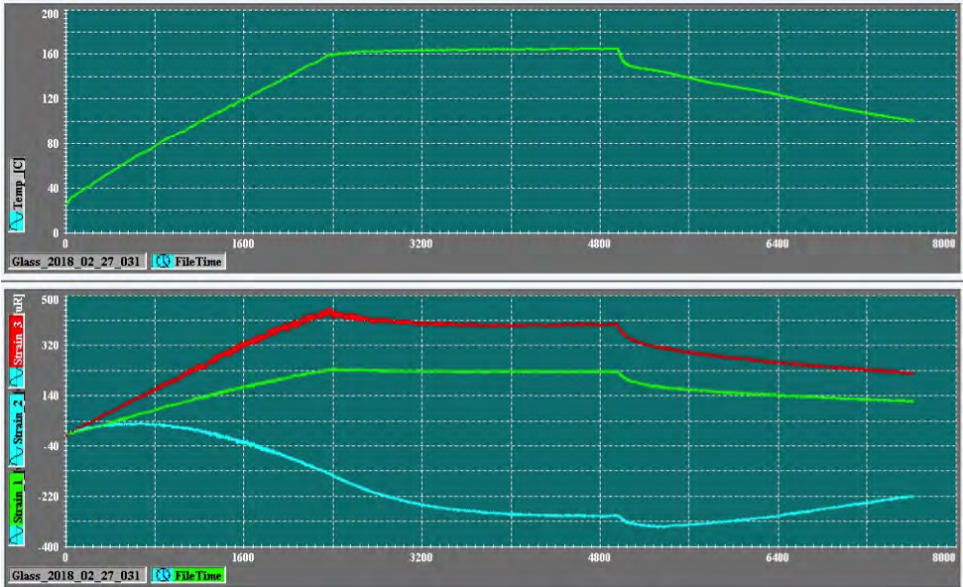


Figure C.15: Test 14, in which strain 1= steel, strain 2= flat glass, strain 3= 60KPO₃-30FA-10Al₂O₃.

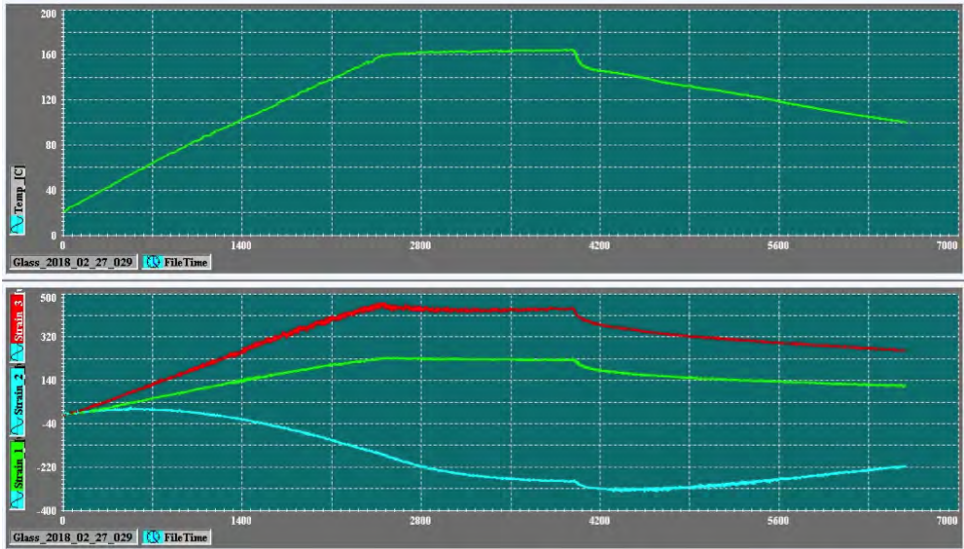


Figure C.16: Test 15, in which strain 1= steel, strain 2= flat glass, strain 3= $60\text{KPO}_3\text{-}30\text{FA-}10\text{Al}_2\text{O}_3$.

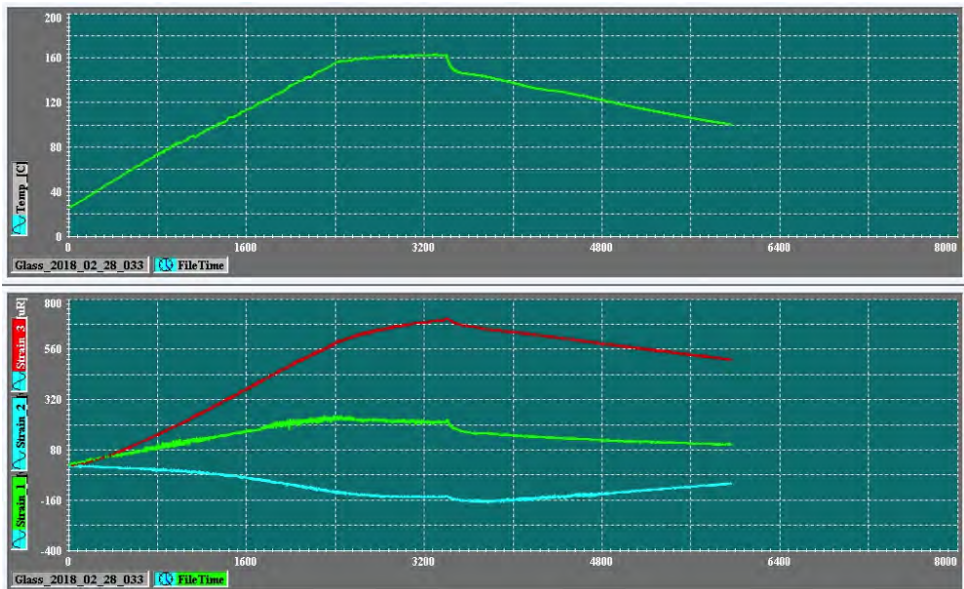


Figure C.17: Test 16, in which strain 1= steel, strain 2= borosilicate, strain 3= $70\text{KPO}_3\text{-}15\text{FA-}15\text{Al}_2\text{O}_3$.

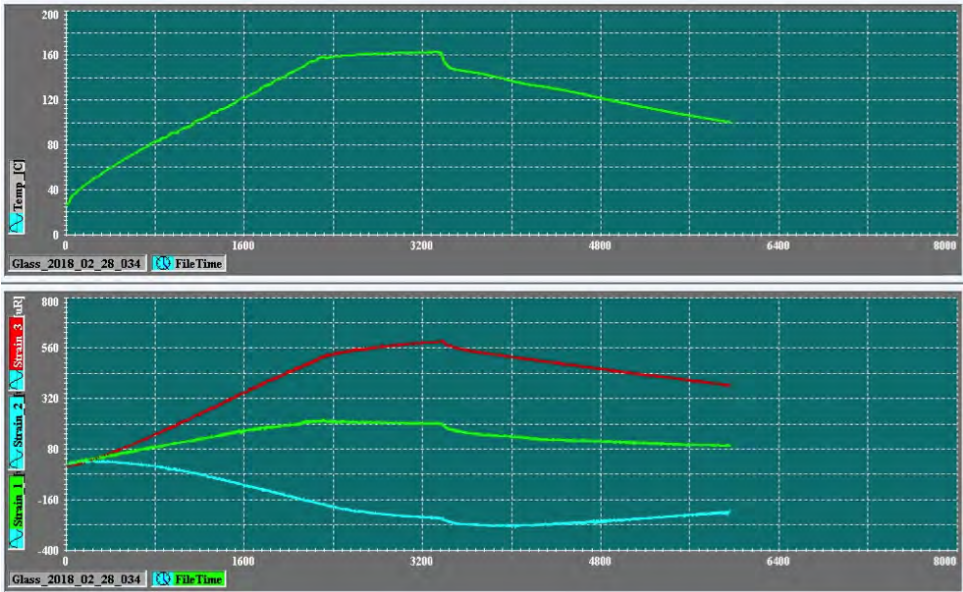


Figure C.18: Test 17, in which strain 1= steel, strain 2= borosilicate, strain 3: 70KPO₃-15FA-15Al₂O₃.

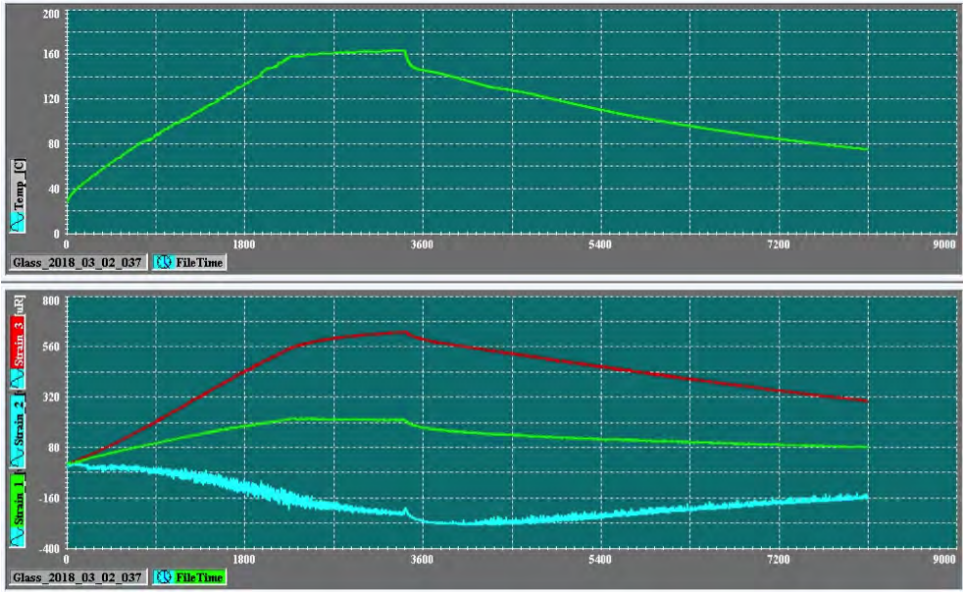


Figure C.19: Test 18, in which strain 1= steel, strain 2= borosilicate, strain 3: 70KPO₃-15FA-15Al₂O₃.

Table C.2: Calculation of uncorrected coefficient of thermal expansion for the tests 1,2 and 3.

Sample	ϵ at Max T	ϵ at Min T	ϵ_{app} at Max T	ϵ_{app} at Min T	$\epsilon - \epsilon_{app}$ (max)	$\epsilon_{compensated}$ (max)	$\epsilon - \epsilon_{app}$ (min)	$\epsilon_{compensated}$ (min)	$\epsilon_{compensated}$ max - $\epsilon_{compensated}$ min	ΔT	α'
1a	282.478	10.689	-38.780	8.430	321.258	645.728	2.259	4.540	641.188	133.799	4.792
1b	544.386	17.076	-38.780	8.430	583.166	1172.164	8.646	17.378	1154.786	133.799	8.631
1c	17.000	-10.824	-38.780	8.430	55.780	112.118	-19.254	-38.7011	150.8193	133.799	1.127
2a	229.992	7.148	-38.560	8.480	268.552	539.790	-1.332	-2.678	542.468	133.548	4.062
2b	484.770	2.221	-38.560	8.480	523.330	1051.894	-6.259	-12.580	1064.474	133.548	7.971
2c	41.277	-8.602	-38.560	8.480	79.837	160.472	-17.082	-34.334	194.807	133.548	1.459
3a	240.185	4.094	-37.960	8.500	278.146	559.072	-4.406	-8.855	567.928	133.003	4.270
3b	532.507	11.106	-37.960	8.500	570.467	1146.639	2.606	5.238	1141.402	133.003	8.582
3c	40.165	-7.561	-37.960	8.500	78.125	157.032	-16.061	-32.283	189.314	133.003	1.423

Table C.3: Calculation of the average uncorrected CTE and the CTE of samples 1, 2 and 3.

Sample	Average α'	α
1	4.375	-
2	8.394	12.769
3	1.336	5.711

Table C.4: Calculation of uncorrected coefficient of thermal expansion for the tests 4, 5 and 6.

Sample	ϵ at Max T	ϵ at Min T	ϵ_{app} at Max T	ϵ_{app} at Min T	$\epsilon - \epsilon_{app}$ (max)	$\epsilon_{compensated}$ (max)	$\epsilon - \epsilon_{app}$ (min)	$\epsilon_{compensated}$ (min)	$\epsilon_{compensated}$ max - $\epsilon_{compensated}$ min	ΔT	α'
4a	241.567	9.715	-37.850	8.440	279.417	561.627	1.275	2.563	559.065	132.982	4.204
4b	743.894	14.295	-37.850	8.440	781.744	1571.305	5.855	11.770	1559.536	132.983	11.727
4c	397.326	10.970	-37.850	8.440	435.176	874.703	2.530	5.085	869.618	132.983	6.539
5a	240.246	8.327	-37.890	8.460	277.936	558.652	-0.133	-0.267	558.919	132.817	4.208
5b	708.118	12.420	-37.890	8.460	745.808	1499.074	3.960	7.960	1491.113	132.817	11.227
5c	363.224	6.456	-37.890	8.460	400.914	805.837	-2.004	-4.027	809.864	132.817	6.098
6a	231.361	10.894	-38.070	8.510	269.431	541.556	2.384	4.792	536.764	133.089	4.033
6b	622.411238	-9.781627	-38.07	8.51	660.4812	1327.567	-18.2916	-36.7662	1364.333	133.0891	10.25128
6c	333.293	2.777	-38.070	8.510	371.363	746.439	-5.733	-11.524	757.963	133.089	5.695

Table C.5: Calculation of the average uncorrected CTE and the CTE of samples 4, 5 and 6.

Sample	Average α'	α
4	4.148	-
5	11.069	15.217
6	6.111	10.259

Table C.6: Calculation of uncorrected coefficient of thermal expansion for the tests 7, 8 and 9.

Sample	ϵ at Max T	ϵ at Min T	ϵ_{app} at Max T	ϵ_{app} at Min T	$\epsilon - \epsilon_{app}$ (max)	$\epsilon_{compensated}$ (max)	$\epsilon - \epsilon_{app}$ (min)	$\epsilon_{compensated}$ (min)	$\epsilon_{compensated}$ max - $\epsilon_{compensated}$ min	ΔT	α'
7a	224.064	8.604	-38.620	8.480	262.684	527.994	0.124	0.249	527.746	133.601	3.950
7b	155.685	4.721	-38.620	8.480	194.305	390.552	-3.759	-7.556	398.109	133.601	2.980
7c	275.556	-5.137	-38.620	8.480	314.176	631.494	-13.617	-27.371	658.865	133.601	4.932
8a	216.018	3.400	-38.510	8.430	254.529	511.602	-5.030	-10.111	521.713	133.576	3.906
8b	101.040	2.429	-38.510	8.430	139.550	280.496	-6.001	-12.062	292.558	133.576	2.190
8c	281.079	-12.495	-38.510	8.430	319.589	642.374	-20.925	-42.059	684.432	133.576	5.124
9a	219.418	9.783	-38.980	8.480	258.398	519.380	1.303	2.620	516.760	133.913	3.859
9b	65.297	0.278	-38.980	8.480	104.277	209.597	-8.202	-16.487	226.084	133.913	1.688
9c	294.419	-9.718	-38.980	8.480	333.399	670.132	-18.198	-36.578	706.710	133.913	5.277

Table C.7: Calculation of the average uncorrected CTE and the CTE of samples 7, 8 and 9.

Sample	Average α'	α
7	3.905	-
8	2.286	6.191
9	5.111	9.016

Table C.8: Calculation of uncorrected coefficient of thermal expansion for the tests 10, 11 and 12.

Sample	ϵ at Max T	ϵ at Min T	ϵ_{app} at Max T	ϵ_{app} at Min T	$\epsilon - \epsilon_{app}$ (max)	$\epsilon_{compensated}$ (max)	$\epsilon - \epsilon_{app}$ (min)	$\epsilon_{compensated}$ (min)	$\epsilon_{compensated}$ max - $\epsilon_{compensated}$ min	ΔT	α'
10a	222.881	9.089	-38.940	8.520	261.821	526.261	0.569	1.144	525.116	133.813	3.924
10b	178.765	3.818	-38.940	8.520	217.705	437.588	-4.702	-9.452	447.040	133.813	3.341
10c	234.195	-1.527	-38.940	8.520	273.135	549.001	-10.047	-20.194	569.196	133.813	4.254
11a	233.703	5.135	-38.480	8.470	272.183	547.087	-3.335	-6.704	553.792	133.492	4.148
11b	190.271	11.729	-38.480	8.470	228.751	459.790	3.259	6.551	453.238	133.492	3.395
11c	262.082	4.164	-38.480	8.470	300.562	604.129	-4.306	-8.654	612.783	133.492	4.590
12a	248.548	10.963	-38.440	8.460	286.988	576.847	2.503	5.031	571.815	133.465	4.284
12b	196.303	16.240	-38.440	8.460	234.743	471.833	7.780	15.638	456.195	133.465	3.418
12c	270.753	9.231	-38.440	8.460	309.193	621.478	0.771	1.550	619.927	133.465	4.645

Table C.9: Calculation of the average uncorrected CTE and the CTE of samples 10,11 and 12.

Sample	Average α'	α
10	4.119	-
11	3.385	7.504
12	4.496	8.615

Table C.10: Calculation of uncorrected coefficient of thermal expansion for the tests 13,14 and 15.

Sample	ϵ at Max T	ϵ at Min T	ϵ_{app} at Max T	ϵ_{app} at Min T	$\epsilon - \epsilon_{app}$ (max)	$\epsilon_{compensated}$ (max)	$\epsilon - \epsilon_{app}$ (min)	$\epsilon_{compensated}$ (min)	$\epsilon_{compensated}$ max - $\epsilon_{compensated}$ min	ΔT	α'
13a	224.752	5.620	-37.940	8.430	262.692	528.010	-2.810	-5.648	533.658	133.084	4.010
13b	263.734	-8.268	-37.940	8.430	301.674	606.364	-16.698	-33.562	639.926	133.084	4.808
13c	430.453	15.063	-37.940	8.430	468.393	941.469	6.633	13.332	928.137	133.084	6.974
14a	226.000	5.134	-38.930	8.430	264.930	532.509	-3.296	-6.624	539.133	133.932	4.025
14b	280.254	-10.629	-38.930	8.430	319.184	641.560	-19.059	-38.308	679.868	133.932	5.076
14c	389.680	7.981	-38.930	8.430	428.610	861.507	-0.449	-0.902	862.408	133.932	6.439
15a	178.391	4.925	-38.350	8.420	216.741	435.650	-3.495	-7.024	442.674	133.453	3.317
15b	328.195	-5.765	-38.350	8.420	366.545	736.755	-14.186	-28.513	765.268	133.453	5.734
15c	390.203	5.344	-38.350	8.420	428.553	861.392	-3.076	-6.183	867.575	133.453	6.501

Table C.11: Calculation of the average uncorrected CTE and the CTE of samples 13, 14 and 15.

Sample	Average α'	α
13	3.784	-
14	5.206	8.990
15	6.638	10.422

Table C.12: Calculation of uncorrected coefficient of thermal expansion for the tests 16,17 and 18.

Sample	ϵ at Max T	ϵ at Min T	ϵ_{app} at Max T	ϵ_{app} at Min T	$\epsilon - \epsilon_{app}$ (max)	$\epsilon_{compensated}$ (max)	$\epsilon - \epsilon_{app}$ (min)	$\epsilon_{compensated}$ (min)	$\epsilon_{compensated}$ max - $\epsilon_{compensated}$ min	ΔT	α'
16a	212.948	13.321	-37.480	8.450	250.428	503.361	4.871	9.790	493.571	132.658	3.721
16b	143.454	2.846	-37.480	8.450	180.934	363.678	-5.604	-11.263	374.941	132.658	2.826
16c	699.384	8.472	-37.480	8.450	736.864	1.481.097	0.022	0.044	1.481.053	132.658	11.164
17a	203.307	11.794	-37.390	8.610	240.697	483.801	3.184	6.401	477.400	132.360	3.607
17b	246.681	-10.825	-37.390	8.610	284.071	570.983	-19.435	-39.064	610.047	132.360	4.609
17c	586.718	-3.124	-37.390	8.610	624.108	1.254.458	-11.734	-23.585	1.278.043	132.360	9.656
18a	211.426	0.763	-37.730	8.440	249.157	500.805	-7.677	-15.430	516.235	132.882	3.885
18b	238.737	5.760	-37.730	8.440	276.467	555.699	-2.680	-5.386	561.085	132.882	4.222
18c	627.635	1.874	-37.730	8.440	665.365	1.337.384	-6.566	-13.197	1.350.581	132.882	10.164

Table C.13: Calculation of the average uncorrected CTE and the CTE of samples 16, 17 and 18.

Sample	Average α'	α
16	3.737	-
17	3.915	7.652
18	10.328	14.065

Table C.14: CTE values of all the glass samples.

Sample	Average α'	α	Std. Dev.
steel/ reference	4.375	-	0.376
70KPO ₃ -15slag-15Al ₂ O ₃	8.394	12.769	0.368
40KPO ₃ -20B ₂ O ₃ -25FA-15Al ₂ O ₃	1.336	5.711	0.182
steel/ reference	4.148	-	0.100
75KPO ₃ -12.5Slag-12.5Al ₂ O ₃	11.069	15.217	0.751
60KPO ₃ -20Slag-20Al ₂ O ₃	6.111	10.259	0.422
steel/ reference	3.905	-	0.046
50KPO ₃ -10B ₂ O ₃ -25FA-15Al ₂ O ₃	2.286	6.191	0.651
Flat glass	5.111	9.016	0.173
steel/ reference	4.119	-	0.182
20%B ₂ O ₃ -slag	3.385	7.504	0.040
10%B ₂ O ₃ -slag	4.496	8.615	0.212
steel/ reference	3.784	-	0.405
Flat glass	5.206	8.990	0.476
60KPO ₃ -30FA-10Al ₂ O ₃	6.638	10.422	0.293
steel/ reference	3.737	-	0.140
Borosilicate	3.886	7.623	0.938
70KPO ₃ -15FA-15Al ₂ O ₃	10.328	14.065	0.768

D

APPENDIX D

Load-displacement curves obtained from Berkovich (Figures D.1 to D.9) and Knoop (Figures D.10 to D.18) indentation.

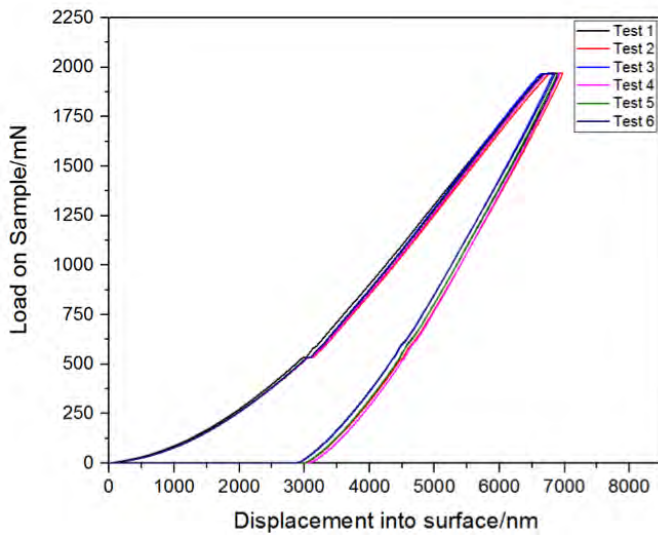
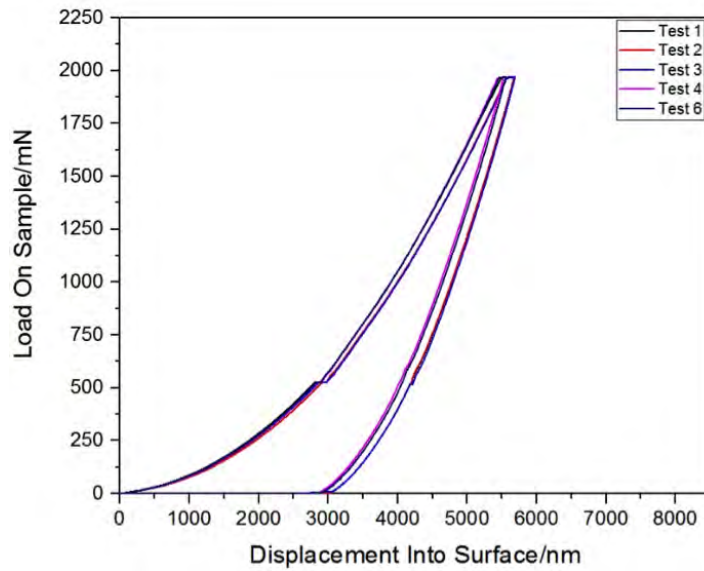
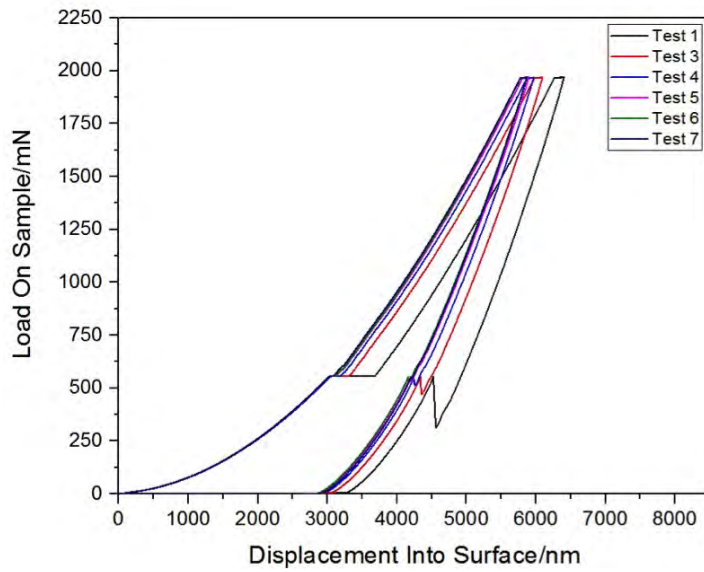
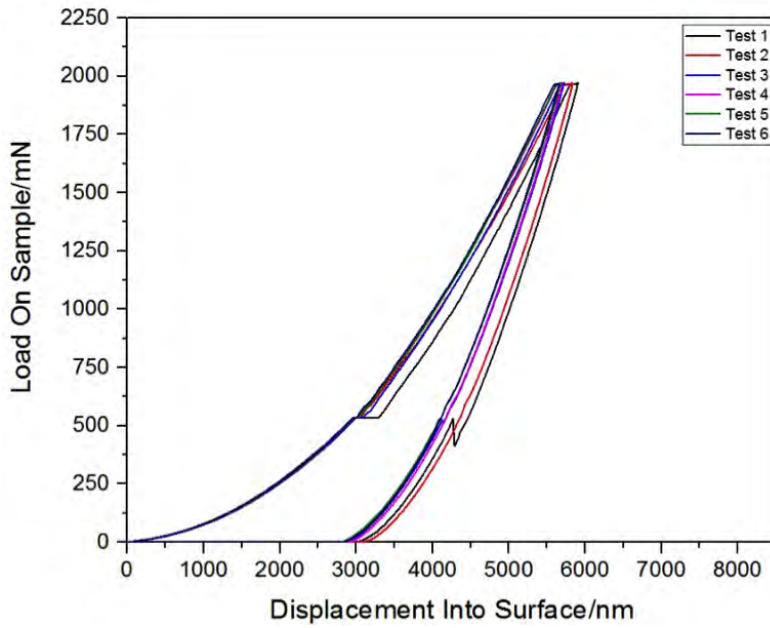
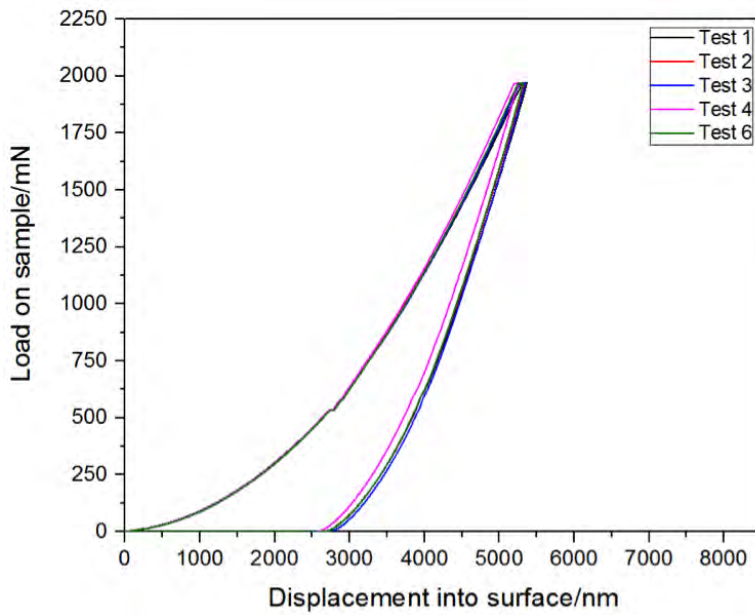
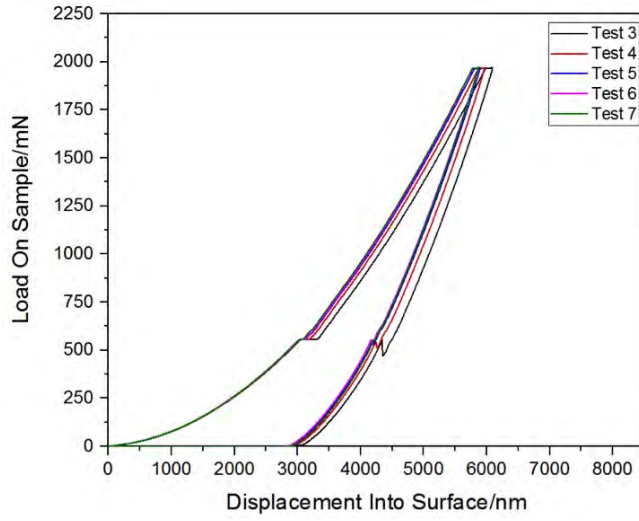
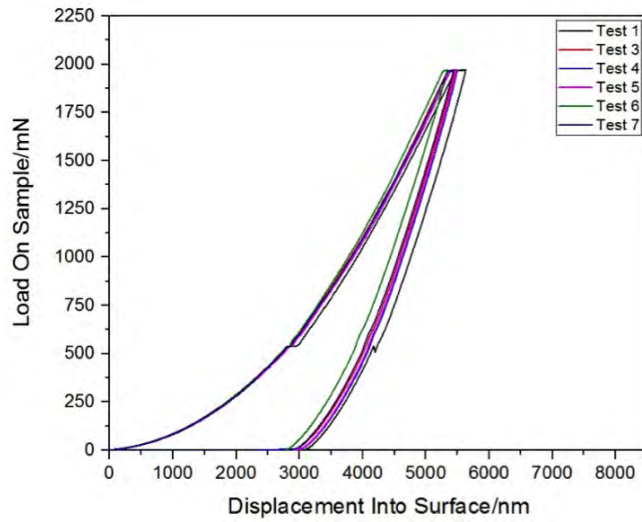


Figure D.1: Sample $40\text{KPO}_3\text{-}20\text{B}_2\text{O}_3\text{-}25\text{FA-}15\text{Al}_2\text{O}_3$.

Figure D.2: Sample 55KPO₃-35FA-10Al₂O₃.Figure D.3: Sample 60KPO₃-20slag-20Al₂O₃.

Figure D.4: Sample 75KPO₃-12.5slag-12.5Al₂O₃.Figure D.5: Sample 50KPO₃-20B₂O₃-15Slag-15Al₂O₃.

Figure D.6: Sample 60KPO₃-20FA-20Al₂O₃.Figure D.7: Sample 70KPO₃-15slag-15Al₂O₃.

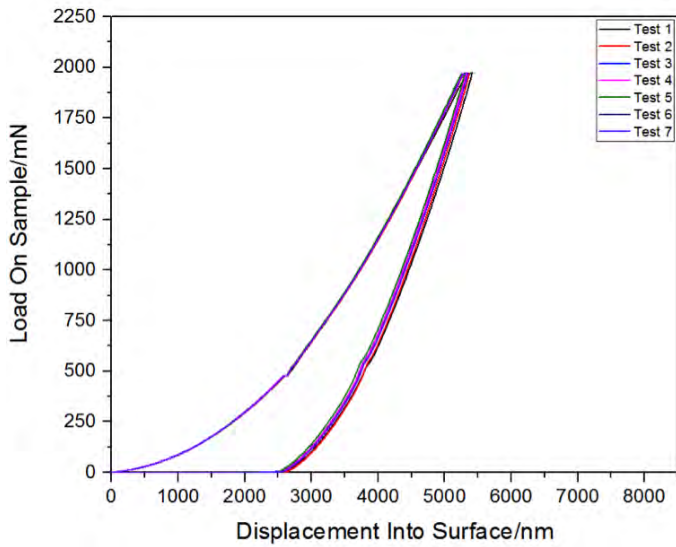
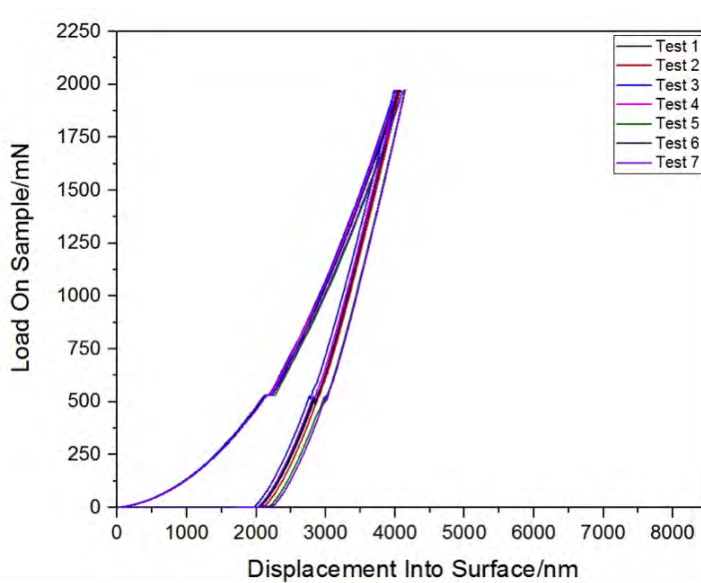
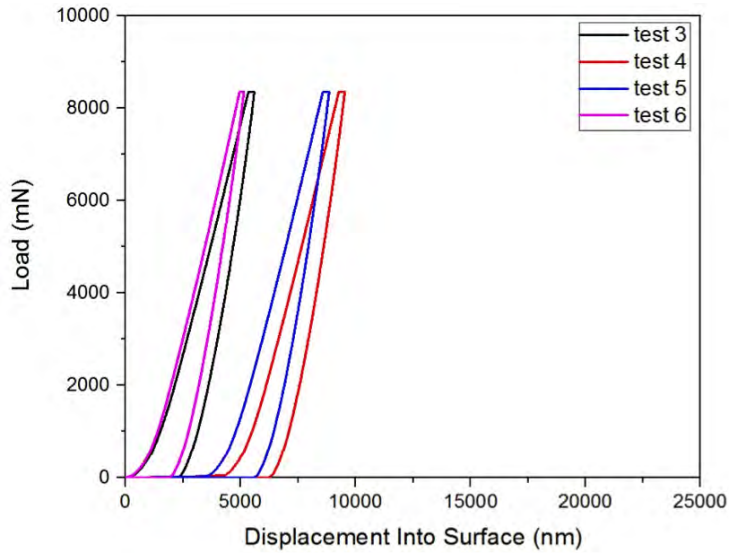
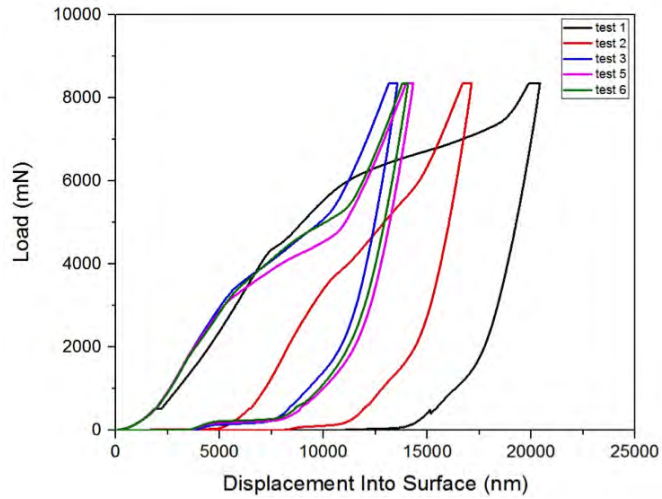
Figure D.8: Sample 60KPO₃-30FA-10Al₂O₃.

Figure D.9: Sample soda-lime (reference).

Figure D.10: Sample $40\text{KPO}_3\text{-}20\text{B}_2\text{O}_3\text{-}25\text{FA-}15\text{Al}_2\text{O}_3$.Figure D.11: Sample $55\text{KPO}_3\text{-}35\text{FA-}10\text{Al}_2\text{O}_3$.

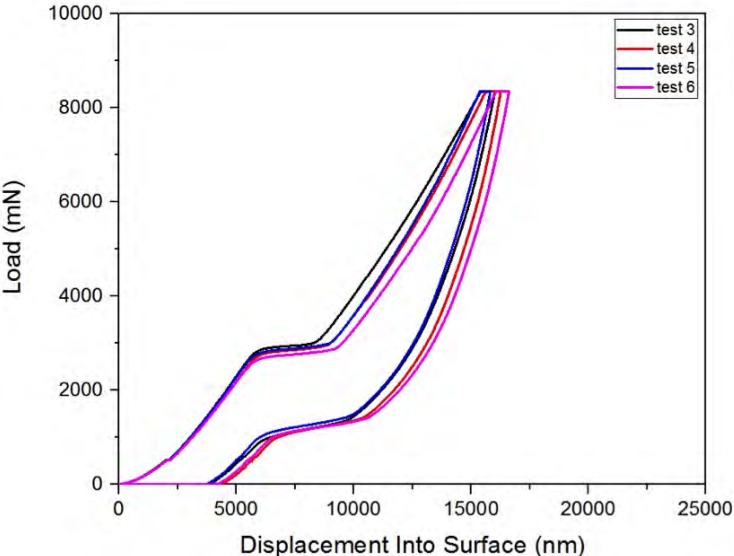


Figure D.12: Sample $50\text{KPO}_3\text{-}20\text{B}_2\text{O}_3\text{-}15\text{Slag-}15\text{Al}_2\text{O}_3$.

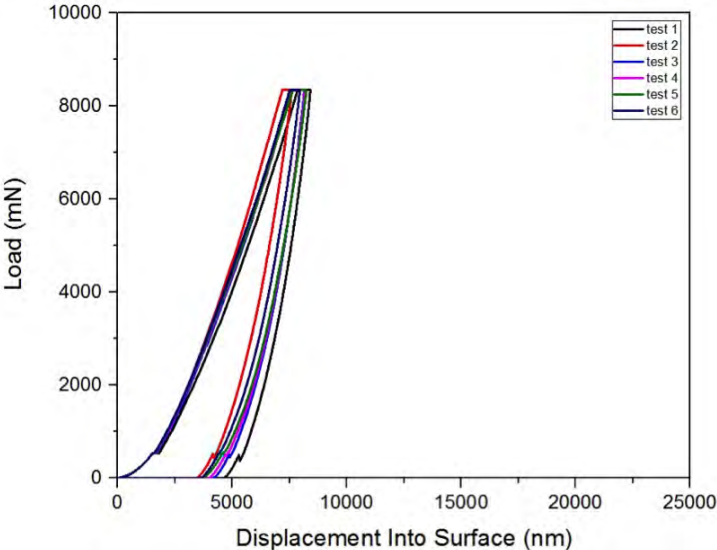
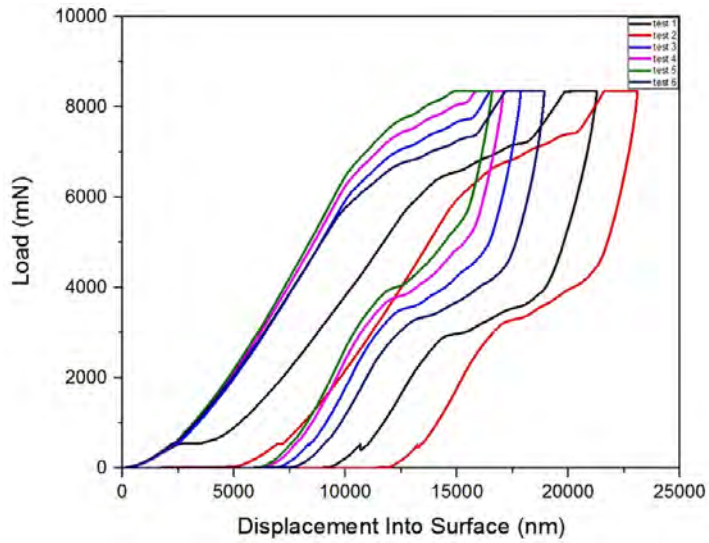
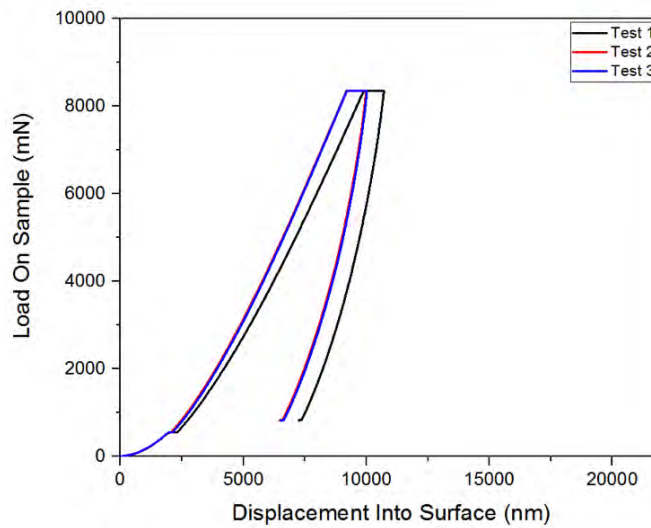


Figure D.13: Sample soda-lime (reference).

Figure D.14: Sample 60KPO₃-30FA-10Al₂O₃.Figure D.15: Side 1 of the sample 40KPO₃-20B₂O₃-25FA-15Al₂O₃.

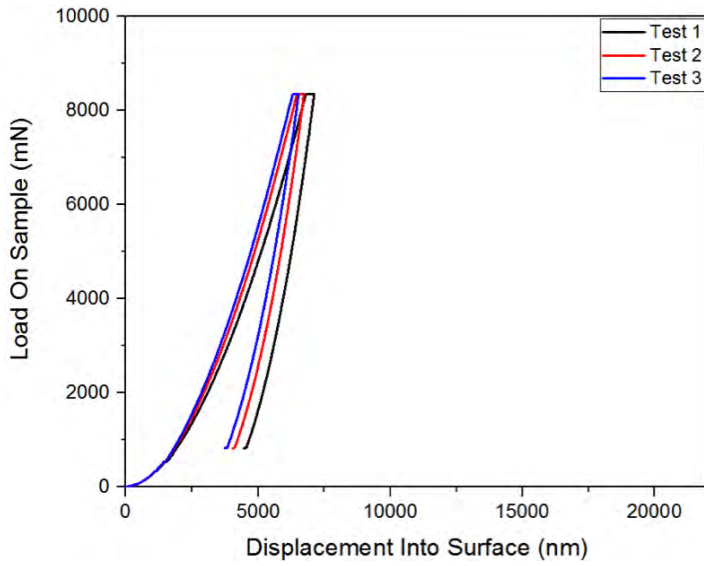


Figure D.16: Side 2 of the sample $40\text{KPO}_3\text{-}20\text{B}_2\text{O}_3\text{-}25\text{FA-}15\text{Al}_2\text{O}_3$.

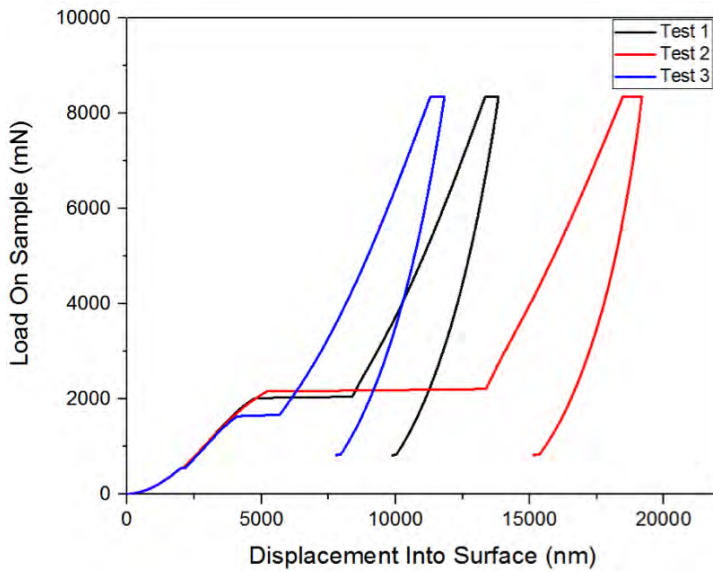


Figure D.17: Side 3 of the sample $40\text{KPO}_3\text{-}20\text{B}_2\text{O}_3\text{-}25\text{FA-}15\text{Al}_2\text{O}_3$.

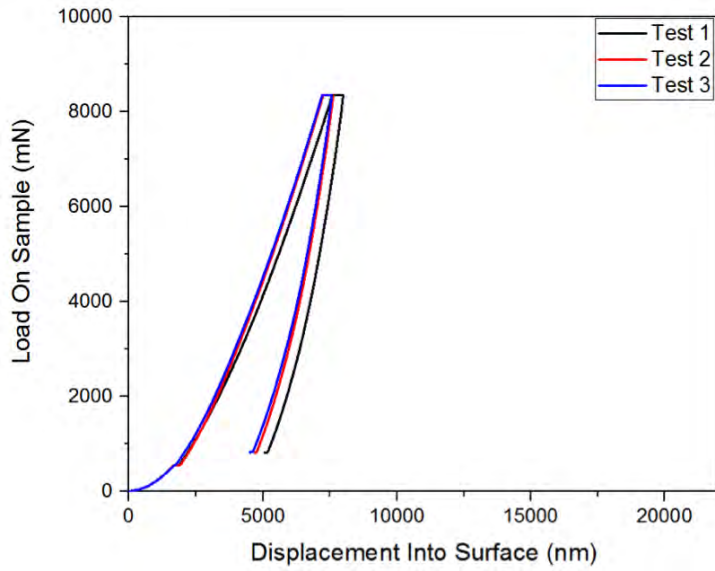


Figure D.18: Side 3 of the sample $40\text{KPO}_3\text{-}20\text{B}_2\text{O}_3\text{-}25\text{FA-}15\text{Al}_2\text{O}_3$.

E

APPENDIX E

Microscopic images from the indents obtained from Berkovich (Figures E.1 to E.6) and Knoop (Figures E.7 to E.32) indentation.

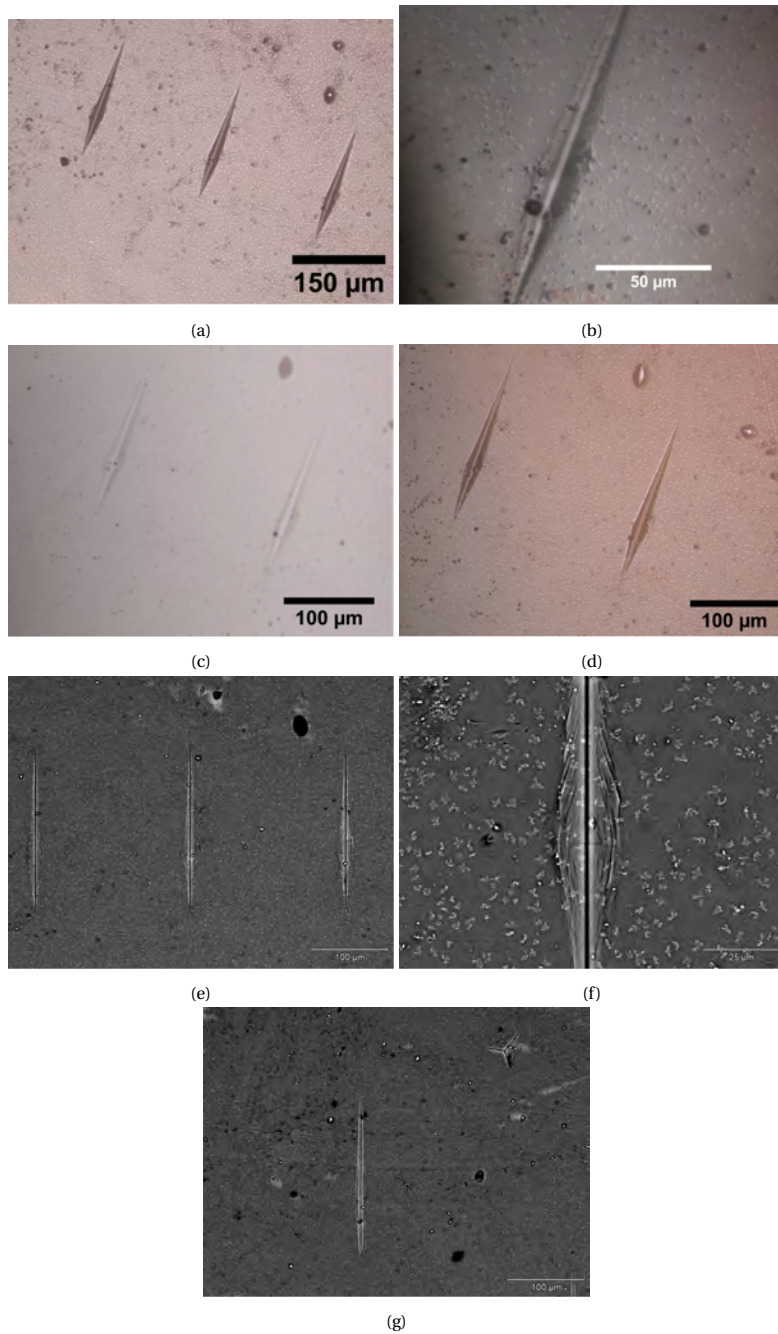


Figure E.1: Crack patterns of the sample $50\text{KPO}_3\text{-}20\text{B}_2\text{O}_3\text{-}15\text{Slag-}15\text{Al}_2\text{O}_3$ induced by a load of 8.5N using a Knoop indenter analysed by optical microscopy (a,b,c,d) and scanning electron microscopy (e,f,g).

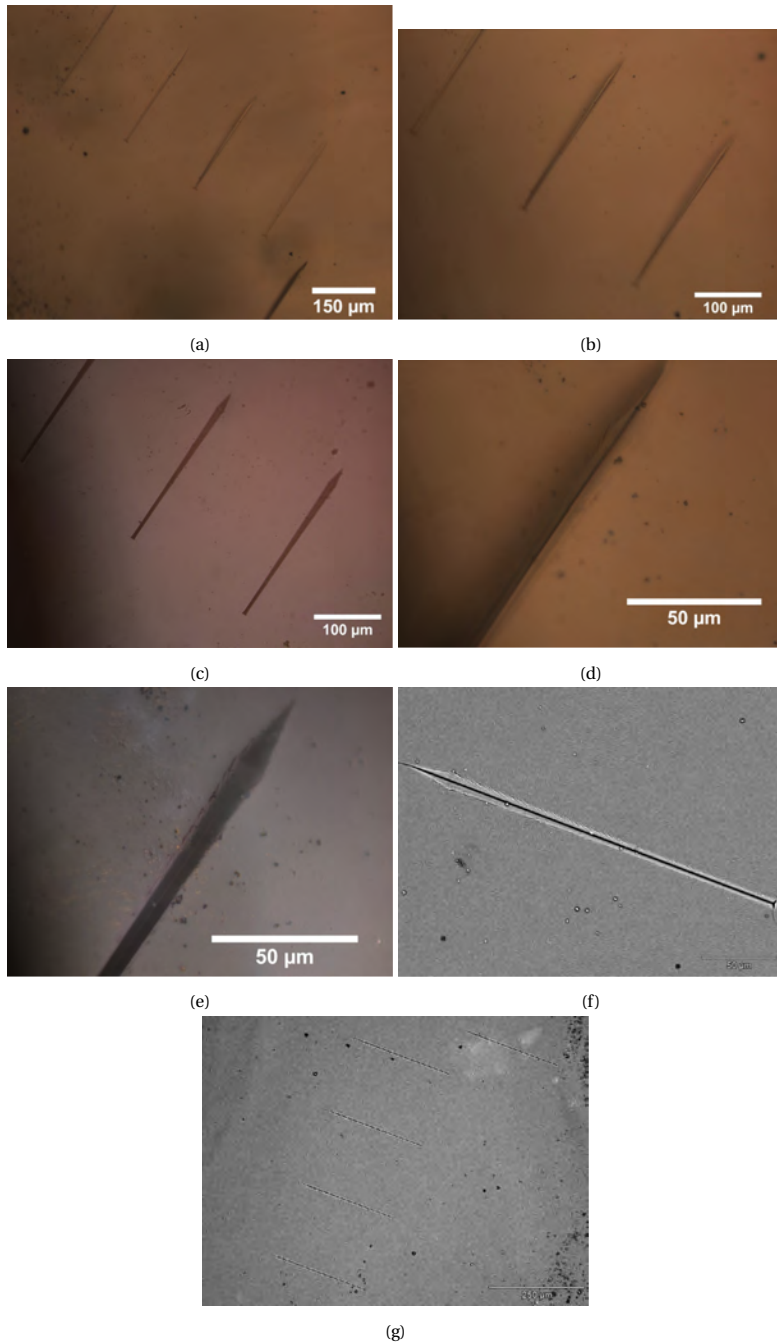


Figure E.2: Crack patterns of the sample $40\text{KPO}_3\text{-}20\text{B}_2\text{O}_3\text{-}25\text{FA-}15\text{Al}_2\text{O}_3$ induced by a load of 8.5N using a Knoop indenter analysed by optical microscopy (a,b,c,d,e) and scanning electron microscopy (f,g).

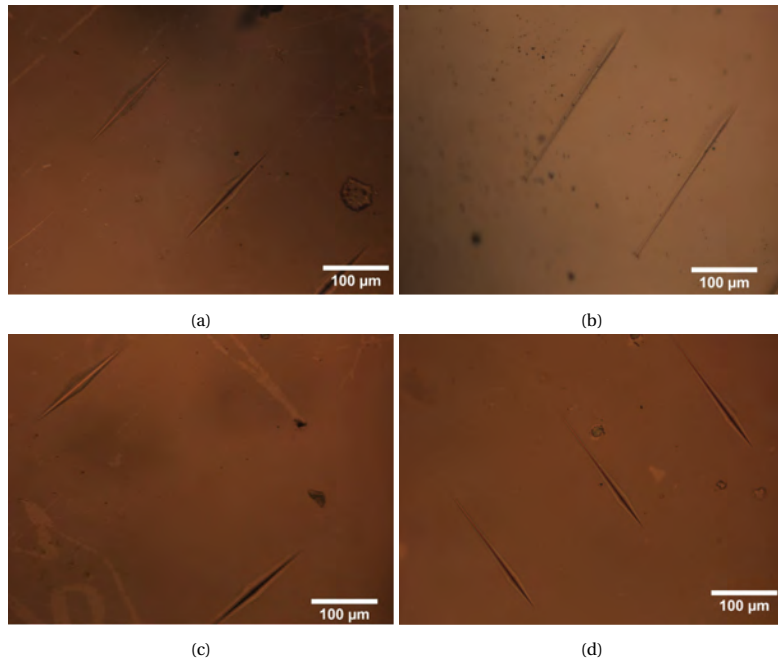


Figure E.3: Crack patterns of the sample $40\text{KPO}_3\text{-}20\text{B}_2\text{O}_3\text{-}25\text{FA-}15\text{Al}_2\text{O}_3$ induced by a load of 8.5N using a Knoop indenter and performed at every 90 degrees: 1 (a), 2(b), 3(c) and 4 (d).

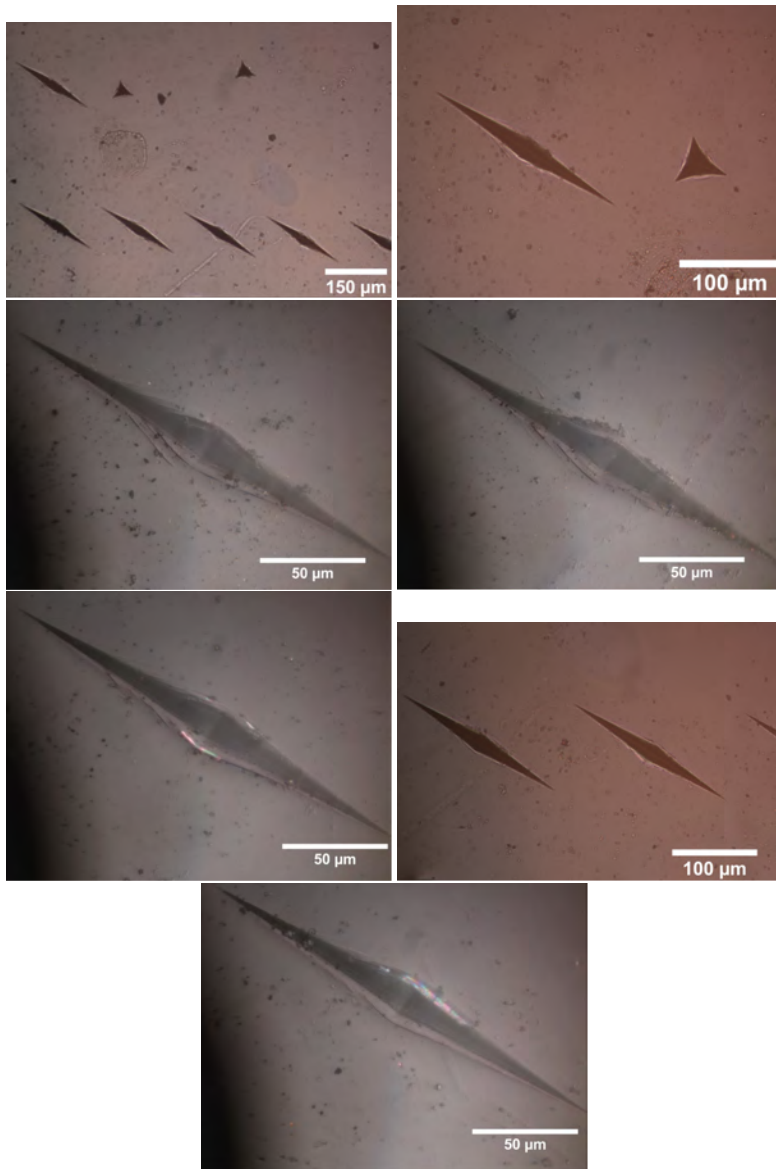


Figure E.4: Crack patterns of the sample $60\text{KPO}_3\text{-}30\text{FA-}10\text{Al}_2\text{O}_3$ induced by a load of 8.5N using a Knoop indenter analysed by optical microscopy.

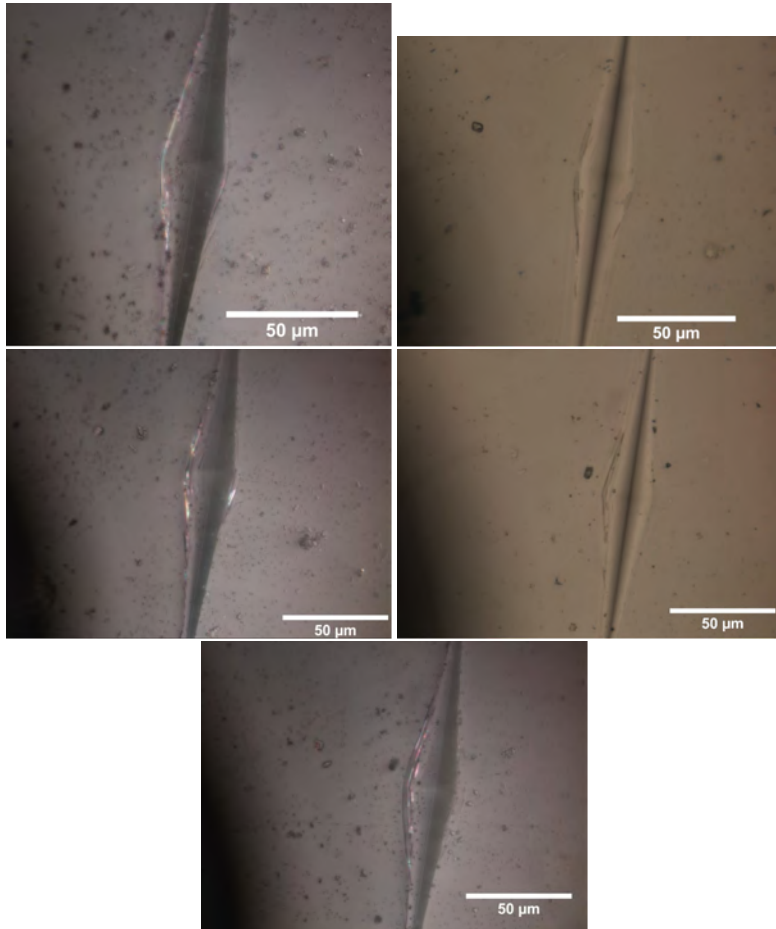


Figure E.5: Crack patterns of the sample $55\text{KPO}_3\text{-}35\text{FA-}10\text{Al}_2\text{O}_3$ induced by a load of 8.5N using a Knoop indenter analysed by optical microscopy.

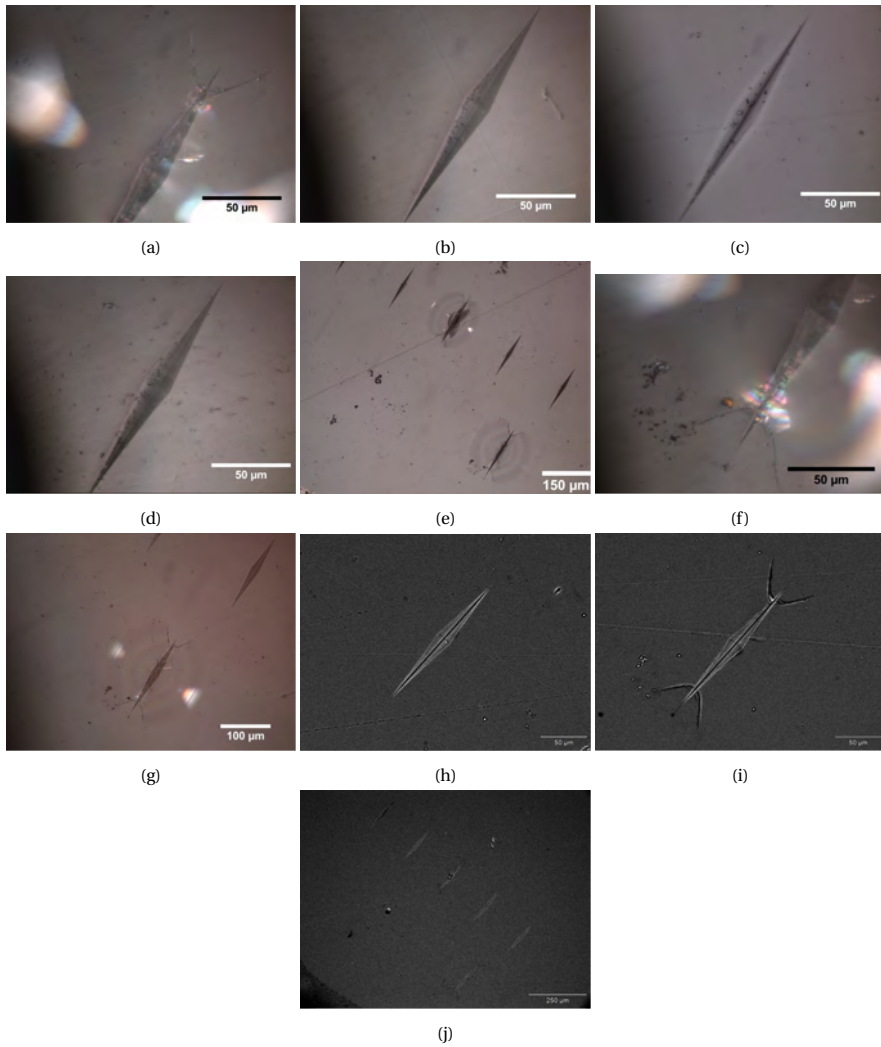


Figure E.6: Crack patterns of the soda-lime sample induced by a load of 8.5N using a Knoop indenter analysed by optical microscopy (a,b,c,d,e,f,g) and scanning electron microscopy (h,i,j).

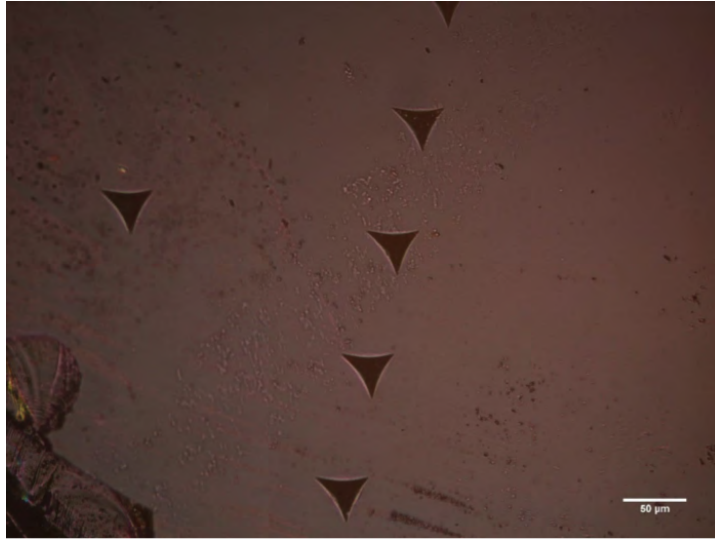


Figure E.7: Sample $40\text{KPO}_3\text{-}20\text{B}_2\text{O}_3\text{-}25\text{FA-}15\text{Al}_2\text{O}_3$ under 2.5N.



Figure E.8: Sample $40\text{KPO}_3\text{-}20\text{B}_2\text{O}_3\text{-}25\text{FA-}15\text{Al}_2\text{O}_3$ under 2.N.

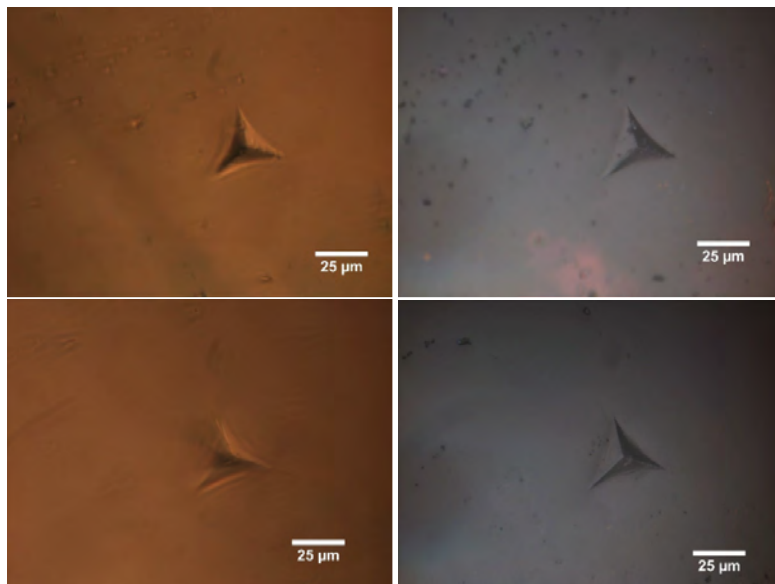


Figure E.9: Two indents of the sample $40\text{KPO}_3\text{-}20\text{B}_2\text{O}_3\text{-}25\text{FA}\text{-}15\text{Al}_2\text{O}_3$ under 2.N, analysed by transmitted (left) and reflected (right) light.

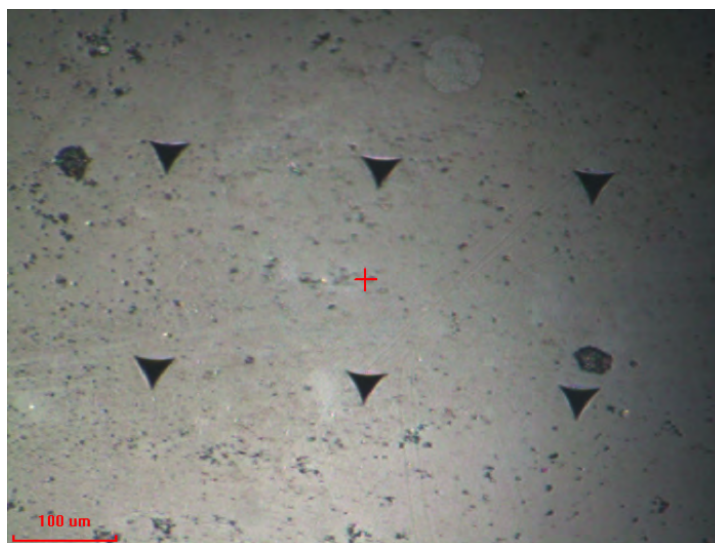


Figure E.10: Sample $55\text{KPO}_3\text{-}35\text{FA}\text{-}10\text{Al}_2\text{O}_3$ under 2.N.

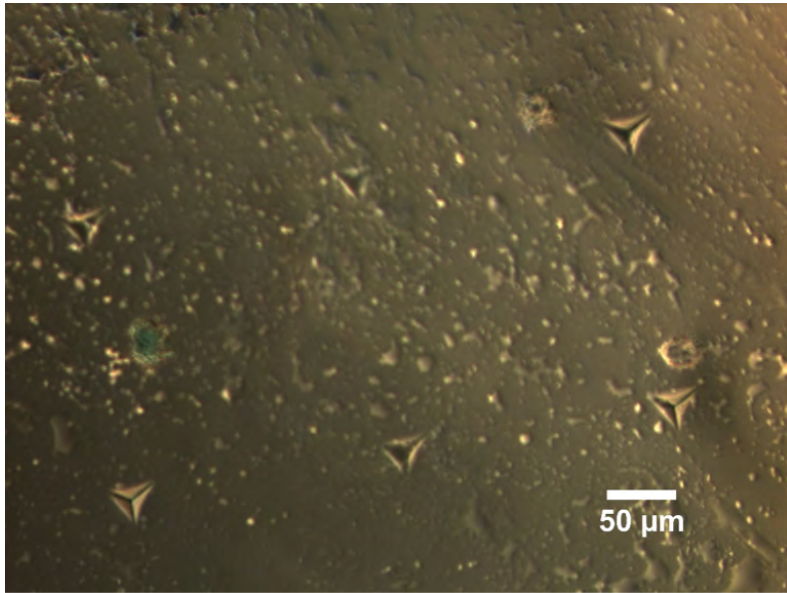


Figure E.11: Sample 55KPO₃-35FA-10Al₂O₃ under 2.N.

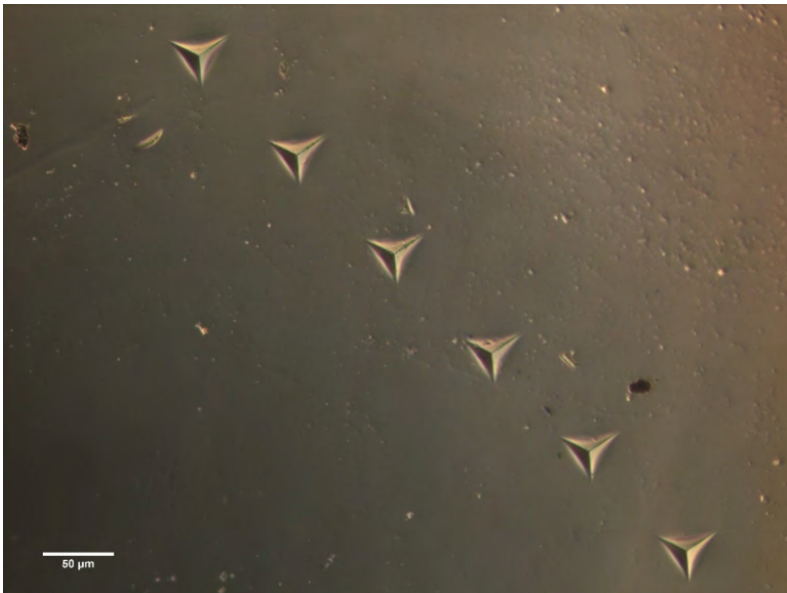


Figure E.12: Sample 60KPO₃-20FA-20Al₂O₃ under 2.5N.

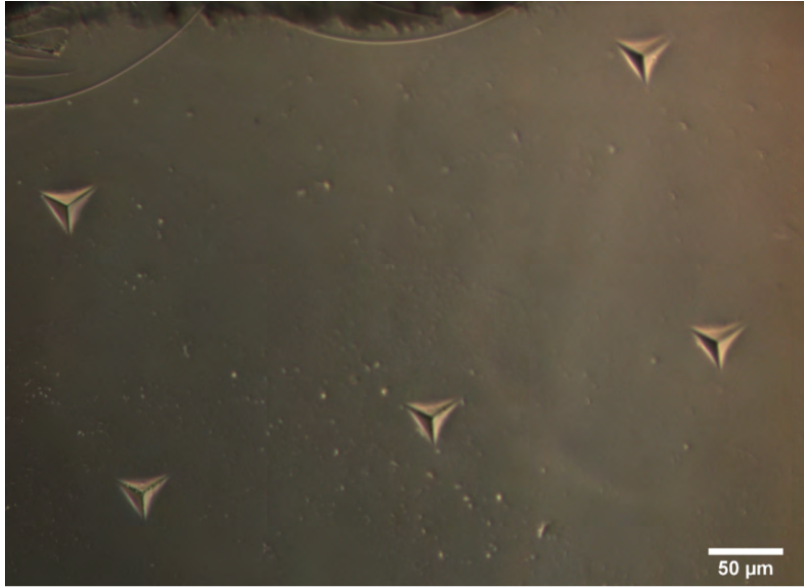


Figure E.13: Sample $60\text{KPO}_3\text{-}20\text{FA-}20\text{Al}_2\text{O}_3$ under 2N.



Figure E.14: Four indents of the sample $60\text{KPO}_3\text{-}20\text{FA-}20\text{Al}_2\text{O}_3$ under 2.N, analysed by reflected light.

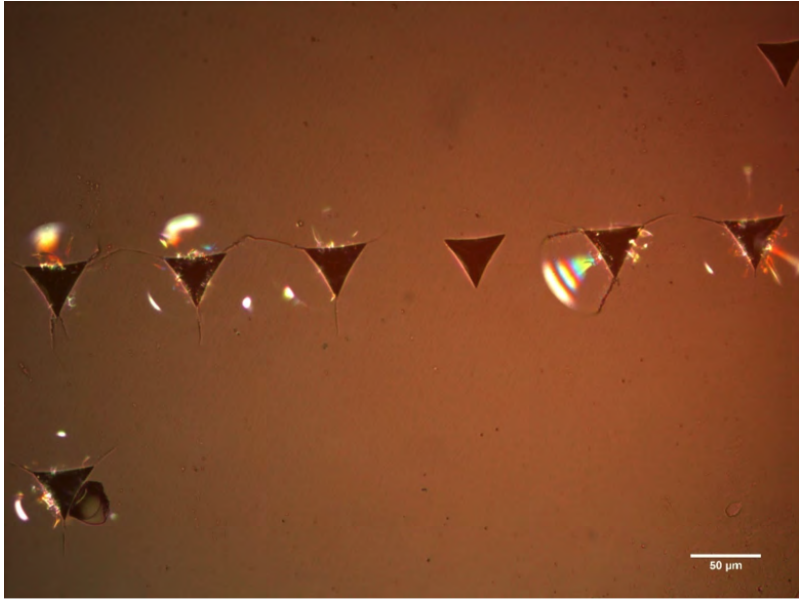


Figure E.15: Sample 70KPO₃-15slag-15Al₂O₃ under 2.5N.

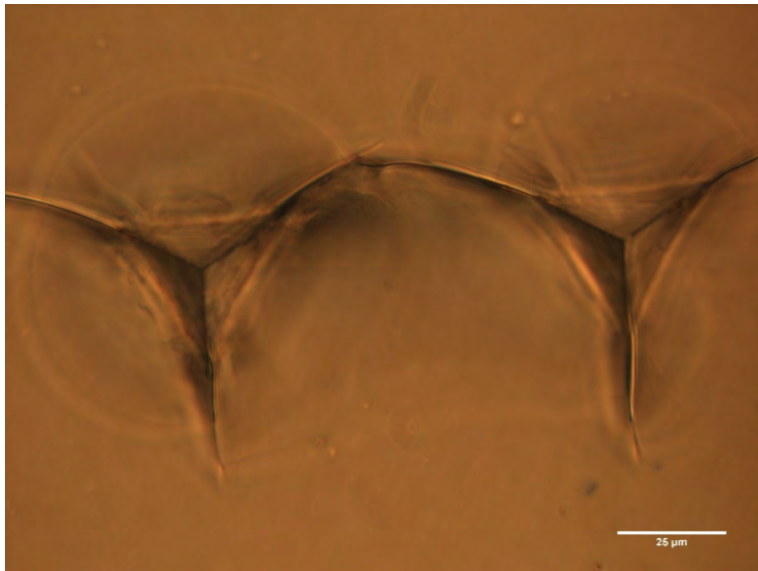


Figure E.16: Two indents of the sample 70KPO₃-15slag-15Al₂O₃ under 2.5N.

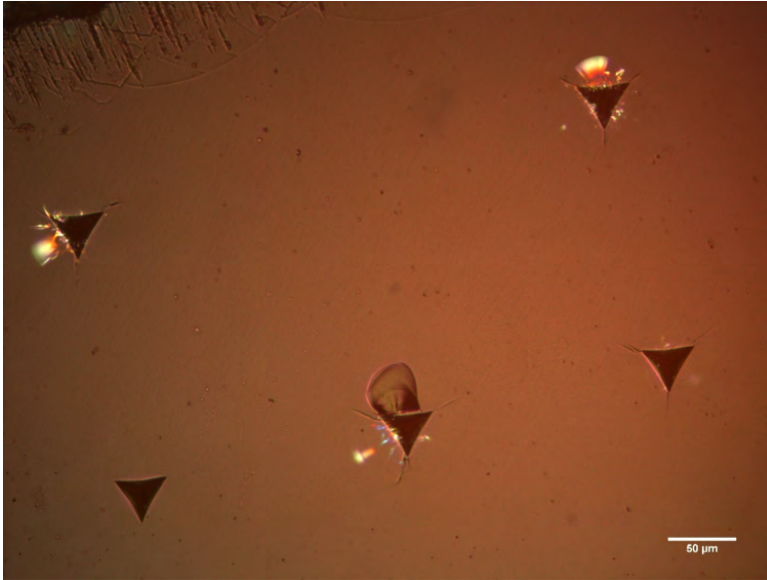


Figure E.17: Sample 70KPO₃-15slag-15Al₂O₃ under 2N.

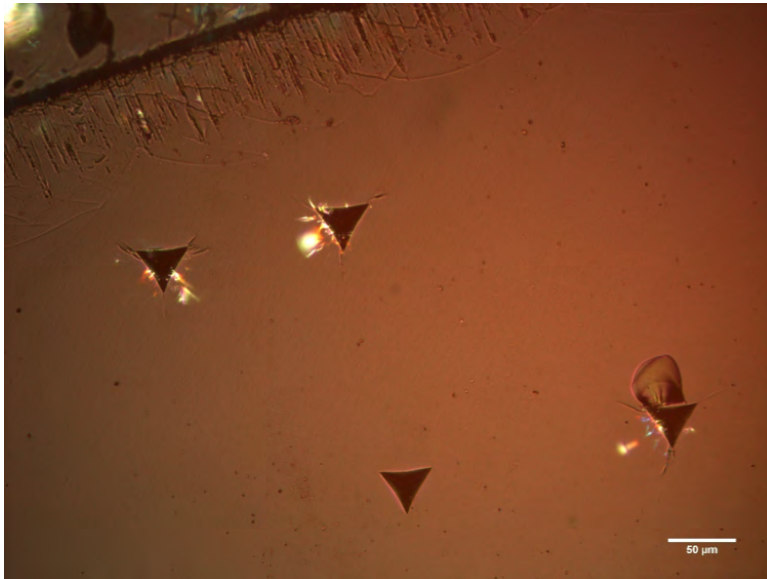


Figure E.18: Sample 70KPO₃-15slag-15Al₂O₃ under 2N.

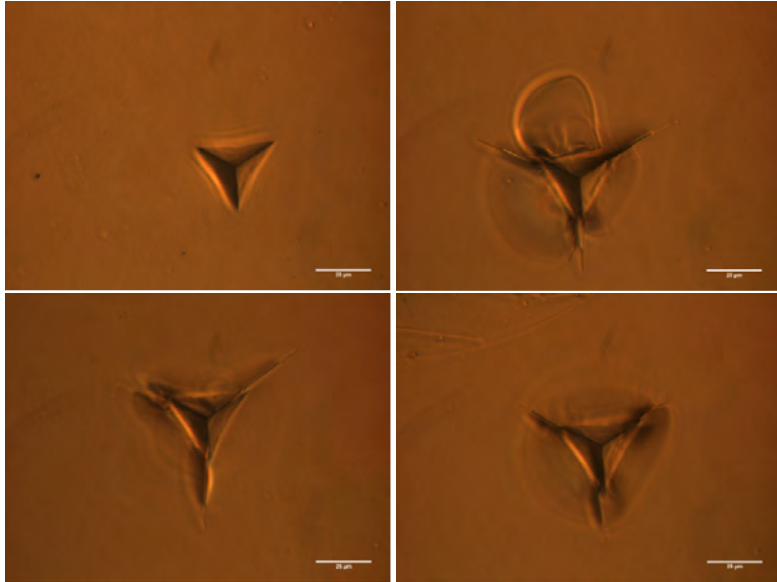


Figure E.19: Four indents of the sample $70\text{KPO}_3\text{-}15\text{slag-}15\text{Al}_2\text{O}_3$ under 2N, analysed by transmitted light.

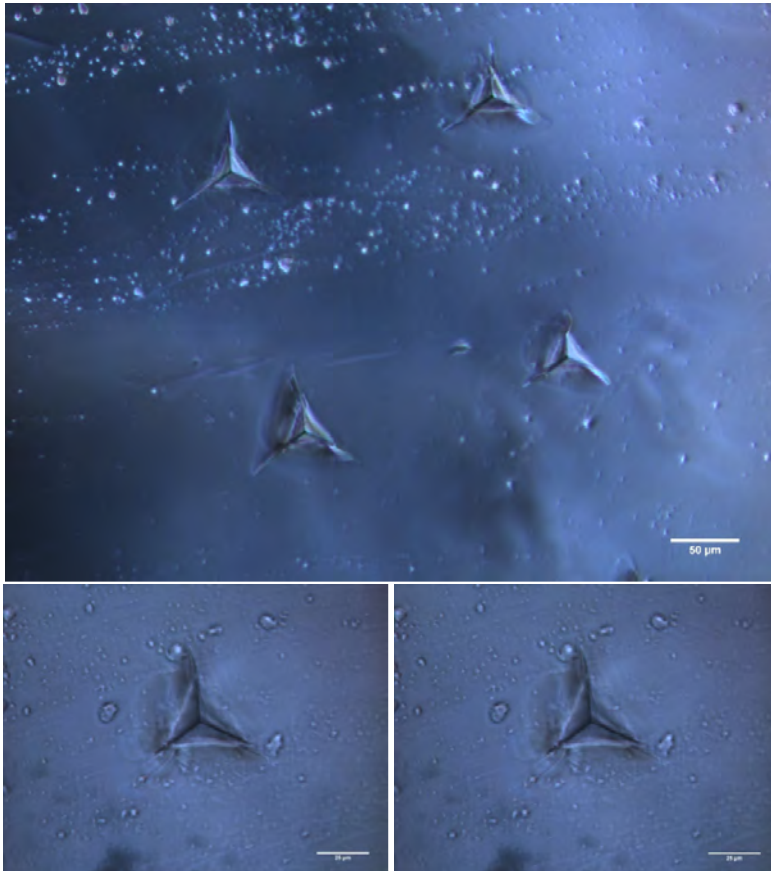


Figure E.20: Sample $75\text{KPO}_3\text{-}12.5\text{slag-}12.5\text{Al}_2\text{O}_3$ under 2.N analysed by transmitted light and two indents in details.



Figure E.21: Sample 75KPO₃-12.5slag-12.5Al₂O₃ under 2N analysed by reflected light.



Figure E.22: Four indents of the sample 75KPO_3 - 12.5slag - $12.5\text{Al}_2\text{O}_3$ under 2.N analysed by reflected light.

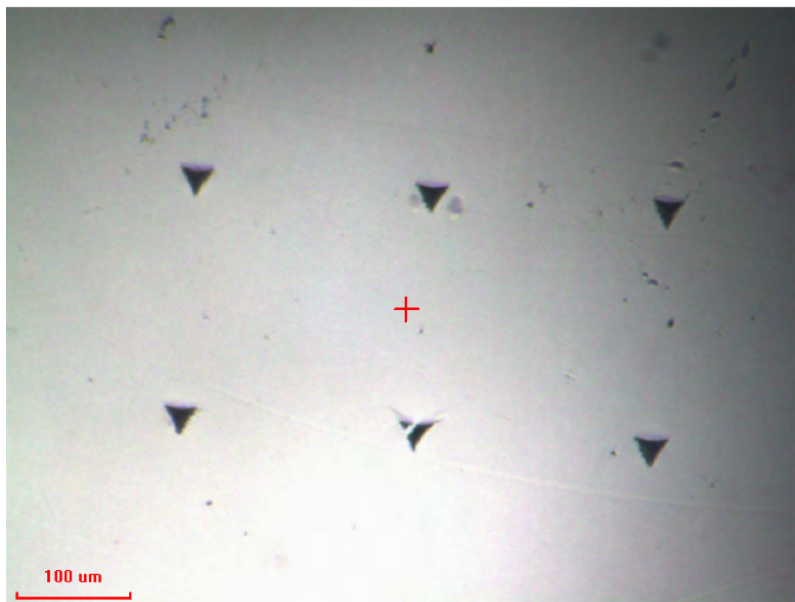


Figure E.23: Soda-lime glass under 2N.

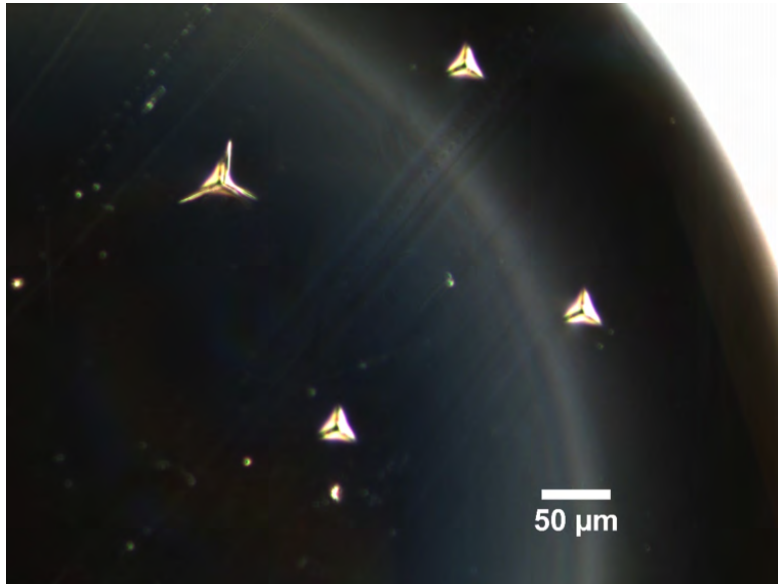


Figure E.24: Four indents of soda-lime glass under 2N.

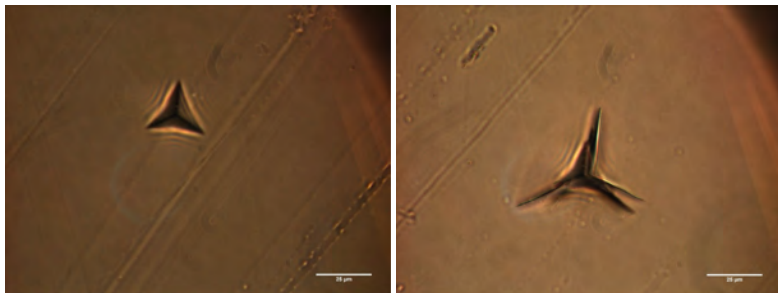


Figure E.25: Two indents of the soda-lime sample under 2.N analysed by transmitted light.

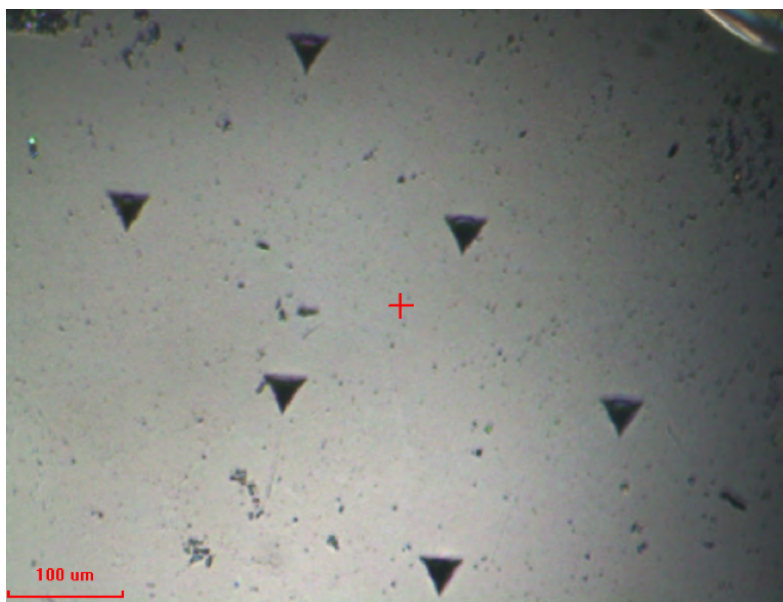


Figure E.26: The sample $60\text{KPO}_3\text{-}30\text{FA-}10\text{Al}_2\text{O}_3$ under 2N.

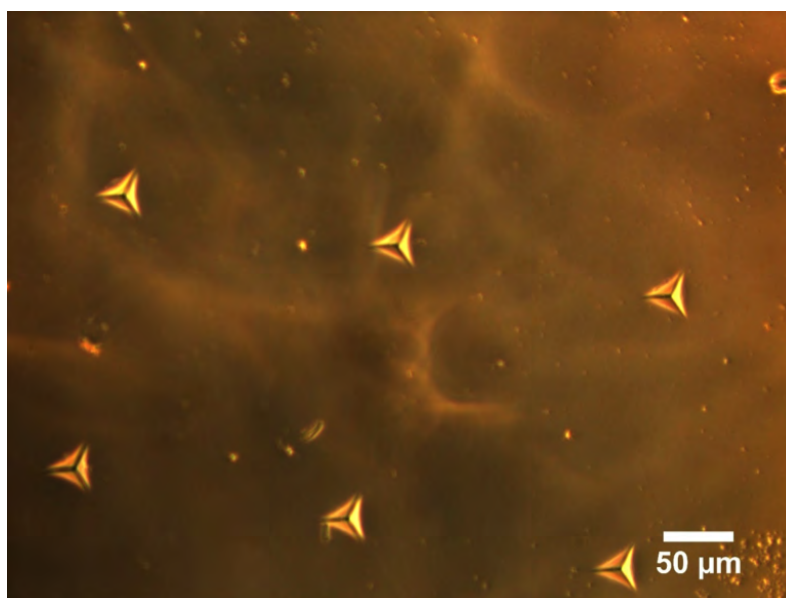


Figure E.27: The sample $60\text{KPO}_3\text{-}30\text{FA-}10\text{Al}_2\text{O}_3$ under 2N analysed under transmitted light.

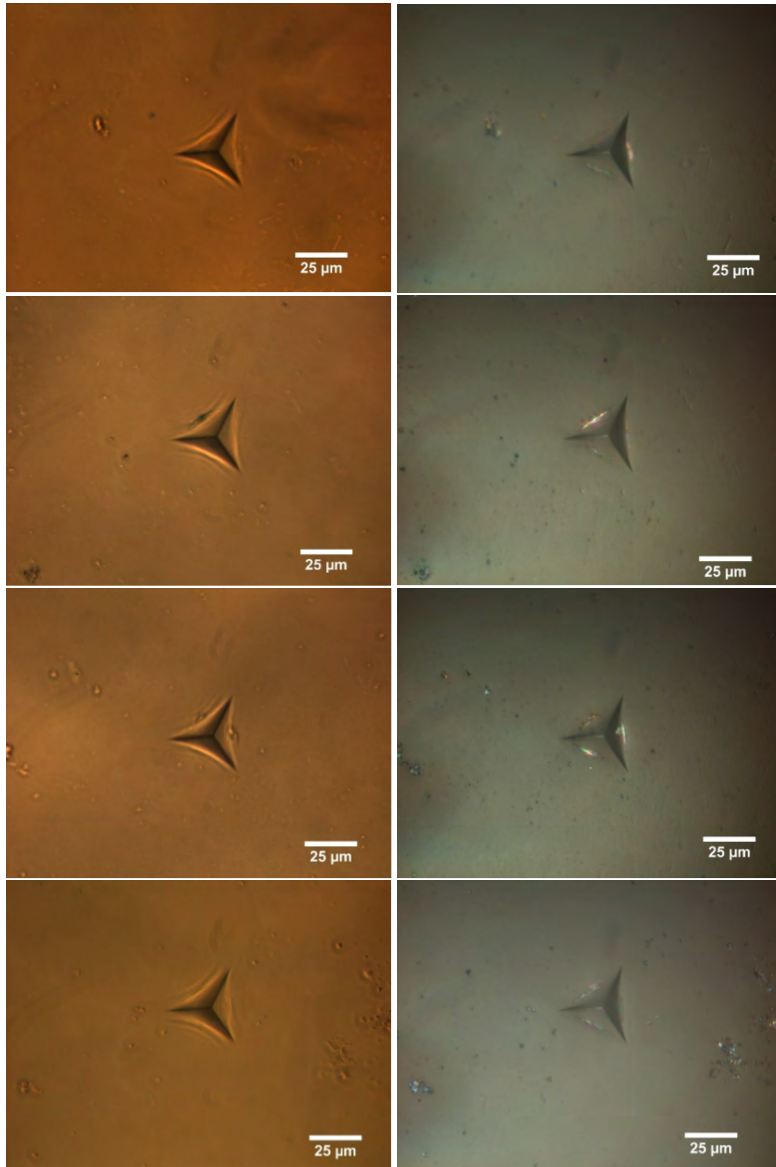


Figure E.28: Four indents of the sample $60\text{KPO}_3\text{-}30\text{FA-}10\text{Al}_2\text{O}_3$ under 2N, analysed by transmitted (left) and reflected (right) light.

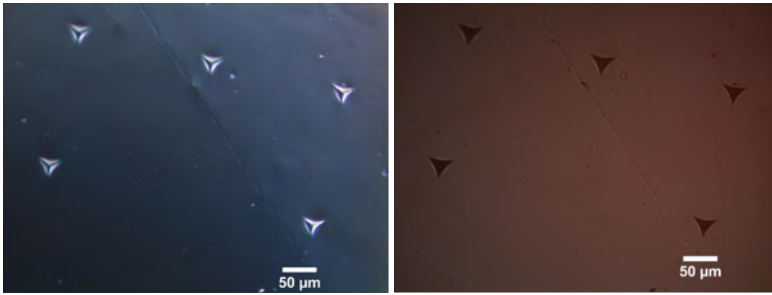


Figure E.29: The sample 50KPO₃-20B₂O₃-15Slag-15Al₂O₃ under 2N analysed by transmitted (left) and reflected (right) light.



Figure E.30: Three indents of the sample 50KPO₃-20B₂O₃-15Slag-15Al₂O₃ under 2N, analysed by reflected light.

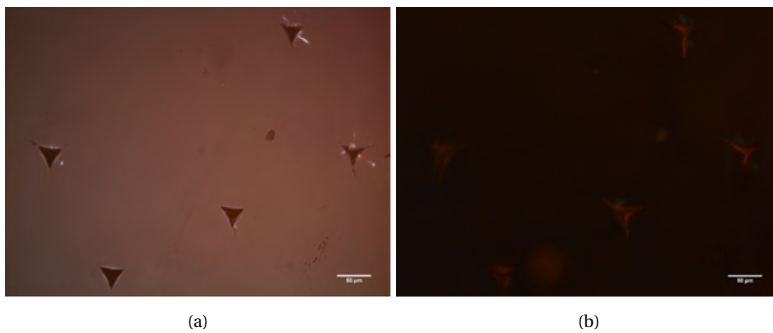


Figure E.31: The sample 60KPO₃-20slag-20Al₂O₃ under 2N analysed by reflected light (left) and transmitted light (right).



Figure E.32: Three indents of the sample $60\text{KPO}_3\text{-}20\text{slag-}20\text{Al}_2\text{O}_3$ under 2N, analysed by transmitted (left) and reflected light (right).

SUMMARY

The investigation of new glass compositions is crucial to expand the possible applications of glass, from the typical applications for building engineering, in the form of cast blocks or floated glass, to more advanced technologies, such as 3D-printed glass or glass to metal connections. Despite the intense research activity and new glass compositions being investigated every day, there has been little innovation or evolution in the composition of architectural glass. This is partially explained by the fact that a substantial part of glass research is not relevant to practical large-scale applications. This thesis is more concerned about the development of compositions with optimized properties than the studies of the short- and intermediate-range structure of a theoretical glass that would hardly find a practical application. Thus, these compositions are inexpensive and appropriate to mass production, utilizing conventional melting techniques. Since the high melting temperatures and the brittleness are two important drawbacks of glass, this work aims to improve both properties. The modification of the properties is achieved via changes in the composition of the glass, using compounds such as phosphorus pentoxide, aluminium oxide and boron oxide. Then, the choice of different glass formers and modifiers contributes to the development of compositions with lower melting and glass transition temperatures. The reduction of the melting temperature allows a saving of energy during the manufacturing and recycling processes. The structures of the glasses differ from the standard soda-lime and borosilicate glasses, leading to a different mechanical behaviour. For instance, an anisotropic structure, which could exhibit a better mechanical performance than standard glasses. Furthermore, these new compositions incorporate up to 35% of slag and fly ash in their formulas. The valorization of these by-products that would otherwise have been previously discarded reduces costs and gas emission. The developed compositions have high water resistance, amorphous structure proved by x-ray diffraction and indentation toughness comparable to a standard soda-lime glass. The coloration of the samples varies depending on the composition and, for the samples containing slag, depending on the melting temperature. In this case, melting at higher temperatures allows the production of colorless glass. The color of the glasses is mainly influenced by the presence of sulfur and iron oxide. In conclusion, this thesis describes the development of new glass compositions containing fly ash and slag. The focus of the work is on the improvement of the properties and a comparison of performance of these new compositions with the glasses currently used in building engineering. The promising results point to the possibility of expansion of the current applications of glass.

SAMENVATTING

Het onderzoek naar nieuwe samenstellingen is cruciaal om de toepassingen van glas te vergroten. Het behelst de typische toepassingen van bouwkunde, in de vorm van blokken of platen, maar ook de meer geavanceerde technologieën zoals 3D geprint glas of glas op metaalverbindingen. Ondanks intensieve onderzoeksactiviteit en het dagelijkse onderzoek naar nieuwe glassamenstellingen, is er weinig innovatie of evolutie in de samenstelling van architecturaal glas. Dit wordt deels verklaard door het feit dat een substantieel deel van glasonderzoek niet relevant is voor praktische toepassingen op grote schaal. Dit proefschrift is meer gericht op de ontwikkeling van samenstellingen met geoptimaliseerde eigenschappen dan op de studies naar de korte en middellange afstand structuren van theoretisch glas die nauwelijks een praktische toepassing hebben. Derhalve zijn deze samenstellingen goedkoop en geschikt voor massaproductie, gebruikmakend van conventionele smelttechnieken. Aangezien de hoge smeltemperatures en de broosheid twee tekortkomingen zijn van glas, heeft dit werk ten doel om beide eigenschappen positief te beïnvloeden. De wijziging van de eigenschappen wordt bereikt via veranderingen in de samenstelling van het glas, gebruikmakend van verbindingen zoals fosforpentoxide, aluminiumoxide en booroxide. Hierna draagt de keuze van verschillende glasvormers en modificatoren bij aan de ontwikkeling van samenstellingen met lagere smelt- en glasovergangstemperaturen. De vermindering van de smeltemperatuur maakt het mogelijk om energie te besparen tijdens het productieproces. De structuren van de glazen verschillen van de standaard; natronkalk glas en borosilicaatglas, wat leidt tot een ander mechanisch gedrag. Bijvoorbeeld een anisotrope structuur, die een betere mechanische prestatie zou kunnen vertonen dan een standaard glas. Bovendien bevatten deze nieuwe composities tot 35% slak en vliegas in hun formules. De valorisatie van deze bijproducten die anders in een eerder stadium zouden zijn weggegooid, vermindert kosten en gasemissie. De ontwikkelde samenstellingen hebben een hoge waterbestendige, amorfe structuur wat bewezen wordt middels röntgendiffractie en een inkepingsterkte die vergelijkbaar is met een natronkalkglas. De kleuring van de monsters varieert afhankelijk van de samenstelling en van de smeltemperatuur voor de monsters die slak bevatten. In dit geval maakt het smelten bij hogere temperaturen het mogelijk om kleurloos glas te produceren. De kleur van het glas wordt voornamelijk beïnvloed door de aanwezigheid van zwavel en ijzeroxide. Concluderend beschrijft dit proefschrift de ontwikkeling van nieuwe glassamenstellingen die vliegas en slak bevatten. De focus van het werk ligt op de verbetering van de eigenschappen en een vergelijking van de prestaties van deze nieuwe samenstellingen met de glassamenstellingen die momenteel worden gebruikt in de bouwtechniek. De veelbelovende resultaten wijzen op de mogelijkheid van uitbreiding van de huidige toepassingen van glas.

CURRICULUM VITÆ

Clarissa Luiza JUSTINO DE LIMA

16-01-1991 Born in Monte Santo de Minas, Brazil.

WORK EXPERIENCE AND EDUCATION

- 2008–2011 BSc. Telecommunications
University of Campinas, São Paulo, Brazil
- 2010–2010 Teaching Assistant – Applied Physics
University of Campinas, São Paulo, Brazil
- 2012–2014 Msc. Materials Science and Engineering
Federal University of Alfenas, Minas Gerais, Brazil
- 2013–2013 Teaching Assistant – Experimental Chemistry II
Federal University of Alfenas, Minas Gerais, Brazil
- 2015–2020 PhD. Candidate
Department of Materials, Mechanics, Management and Design (3Md)
Delft University of Technology, Delft, The Netherlands
- 2019–present Senior Scientist
American Glass Research (Agr), Delft, The Netherlands

LIST OF PUBLICATIONS

JOURNAL PUBLICATIONS

4. C.L. Justino de Lima, F.A. Veer, O. Copuroglu, R. Nijse. New phosphate glasses containing industrial waste and their applications for building engineering. *Heron*, v. 63, p. 31-56, 2018.
3. T. Bristogianni, F. Oikonomopoulou, C.L. Justino de Lima, F.A. Veer, R. Nijse. Structural cast glass components manufactured from waste glass: Diverting everyday discarded glass from the landfill to the building industry. *Heron*, v. 63, p. 57-102, 2018.
2. F.A. Veer, T. Bristogianni, C.L. Justino de Lima. An overview of some recent developments in glass science and their relevance to quality control in the glass industry. *Heron*, v. 63, p. 15-30, 2018.
1. C.L.J. de Lima, B. Pastena, R.P.R.D. Nardi, J.T. Gouvêa Junior, J.L. Ferrari, F.C. Casanjes, G. Poirier. Thermal, Structural and Crystallization Study of Niobium Potassium Phosphate Glasses. *Materials Research (São Carlos. On-line)*, v. 18, p. 13-16, 2015.

CONFERENCE PUBLICATIONS

12. C.J. de Lima, F. Veer, O. Copuroglu, H. Zhang, R. Nijse. Fracture analysis of phosphate and silicate glasses by microscopy and nanoindentation: comparison of different glasses utilized for building engineering. 17th Euroseminar on Microscopy Applied to Building Materials- EMABM. p. 42-46. Toronto, Canada (2019).
11. T. Bristogianni, F. Oikonomopoulou, C. Justino de Lima, F. Veer, R. Nijse. Cast Glass Components out of Recycled Glass: Potential and Limitations of Upgrading Waste to Load-bearing Structures. *Challenging Glass 6 Conference Proceedings*. v. 6. p. 151-174. Delft, The Netherlands (2018).
10. C. Justino de Lima, F. Veer, O. Copuroglu, R. Nijse. Innovative Glass Recipes Containing Industrial Waste Materials. *Challenging Glass 6 Conference Proceedings*. v. 6. p. 533-542. Delft, The Netherlands (2018).
9. F. Veer, T. Bristogianni, C. Justino de Lima. A Re-evaluation of the Physiochemistry of Glass on the Basis of Recent Developments and its Relevance to the Glass Industry. *Challenging Glass 6 Conference Proceedings*. v. 6. p. 769-776. Delft, The Netherlands (2018).
8. C.L. Justino de Lima, F. Veer, O. Copuroglu, R. Nijse. Advancements and Challenges in Glass Concepts, Manufacturing and Applications. *Proceedings of 13th International Congress on Advances in Civil Engineering- ACE 2018*. v. 13. Izmir, Turkey (2018).
7. C.L. Justino de Lima, F. Veer, O. Copuroglu, R. Nijse. Designing an architectural glass composition. *XI Brazilian Symposium on Glass and Related Materials: Book of Abstracts: UEPG-PROEX*. p. 55-55. Curitiba, Brazil (2017).

6. C.L.J. de Lima, O. Copuroglu, F.A. Veer. Crystallization Studies and Mechanical Properties of New $KPO_3-Ta_2O_5-Al_2O_3$ Glasses. Borate 9 and Phosphate 2 International Conferences. p. 88-89. Oxford, England (2017).
5. C.L.J. de Lima, B. Pastena, F.C. Cassanjes, G. Poirier. Crystallization study of niobium potassium phosphate glasses. 21^o Brazilian Materials Science and Engineering Congress- CBECIMAT. p. 1219-1226. Cuiabá, Brazil (2014).
4. C. Braz, C.L.J. de Lima, S. Ribeiro, A.S. Camargo, H. Eckert, F.C. Cassanjes, G. Poirier. Propriedades térmicas e luminescentes de vidros de fosfato de tungstênio contendo fluoreto de chumbo. Proceedings of the 37^a Reunião anual da sociedade brasileira de Química. Natal, Brazil (2014) (In Portuguese).
3. C.L.J. de Lima, C. Pereira, F.C. Cassanjes, G. Poirier. Synthesis and properties of phosphate glasses containing Nb_2O_5 and WO_3 . Proceedings of the X BraSGlass- Brazilian Symposium on Glass and Related Materials. P.159-160. São Carlos, Brazil (2014).
2. C.L.J. de Lima, F.C. Cassanjes, G. Poirier. Novel Nb_2O_5 and WO_3 based phosphate glasses. Proceedings of the Humboldt Kolleg 2013- Sciences & Technology in contemporary life 'Impacts and horizons'. p. 143-143. Campos do Jordão, Brazil (2013).
1. C.L.J. de Lima, F.C. Cassanjes, G. Poirier. Glasses and optical fiber in phosphate matrix containing transition metals. Proceedings of the XII Brazilian MRS (Materials Research Society) Meeting. Campos do Jordão, Brazil (2013).